UNSTEADY FLUID DYNAMICS OF A CIRCULAR CYLINDER UNDERGOING YAW OSCILLATION AT SUBCRITICAL FLOW

VAHID NASR ESFAHANI

A DISSERTATION SUBMITTED TO THE FACULTY OF GRADUATE STUDIES
IN PARTIAL FULFILLMENT OF THE REQUIREMENTS
FOR THE DEGREE OF
DOCTOR OF PHILOSOPHY

GRADUATE PROGRAM IN MECHANICAL ENGINEERING
YORK UNIVERSITY
TORONTO, ONTARIO

MARCH 2022

Abstract

The yaw oscillation of a bluff body is a fundamental part of the motion yielding the complex unsteady flow that occurs past athletes in many examples of competitive sports such as cycling. While the impact of the motion of limbs of athletes on the drag and large-scale flow structures over cyclists, as an example, has received recent and increasing attention, little is known about the underlying flow physics. In this thesis, a canonical case of a circular cylinder is used as a low-order model of an athlete's limb to better understand the flow behavior associated with the yaw oscillation component of motion in a controlled experimental setting.

An experimental study is carried out to characterize the spanwise variation of the near wake of a cylinder yaw-oscillating about its mid-span between the yaw angles of $\theta = 0^\mathrm{o}$ (unyawed case) and 30° at two subcritical Reynolds numbers of 5×10^3 and 1.5×10^4. For these tests, cylinders with aspect ratios of 13 and 20 are immersed into a water channel. The yaw oscillation frequencies (K) have the values of 0.5 (low), 1.3 to 2 (moderate), and 4 (high). Planar Particle Image Velocimetry measurements are performed in a vertical symmetry plane and horizontal planes to investigate the flow structure in the near wake. The time-varying flow behavior such as the vortex shedding is studied using Constant Temperature Anemometry measurements.

For a cylinder undergoing yaw oscillation, the near wake is found to be highly three-dimensional. The spanwise variation in the near wake increases substantially as the reduced frequency is changed from low to moderate values, while at high K, the flow becomes relatively uniform again. The spanwise flow topology is mostly independent of the Reynolds number in the subcritical range considered. The cylinder's direction of motion, its accel-

eration/deceleration, and the axial flow developing as a result of large yaw are identified as factors impacting the flow behavior. At large yaw angles, high-magnitude axial flow originating from the bottom free end develops over larger spanwise sections of the cylinder, turning into the most influential parameter controlling the flow topology in addition to the cylinder's direction of motion effect.

Acknowledgements

This Ph.D. has been a journey that I would not have been able to complete without the support of so many people. First, I have to gratefully thank my supervisor, Prof. Ronald Hanson, for all his support and ideas he provided for my research and for granting me the space to experience different related topics that have helped me grow as both a researcher and a person. I would also like to thank my examination committee; Prof. Joseph Hall, Prof. Pouya Rezai, Prof. Peter Taylor, and Prof. Alidad Amirfazli for their invaluable comments and support.

I would like to express special gratitude to Prof. Alis Ekemkci from the University of Toronto for providing the facility to conduct the experiments. I also want to acknowledge Prof. Ekmekci, for all her time and effort in reviewing the publications related to this research and all her detailed analysis that was a valuable help for me during my research.

Finally, I would like to thank my family and my partner for all their love and unconditional support during my Ph.D. studies, and many thanks to all my close friends who became my new family here in Canada.

Table of Contents

List of Tables

List of Figures

Chapter 1

Introduction

Flow past cylindrical bodies has been given extensive attention in fluid dynamics research due to its fundamental significance to numerous engineering applications and flow phenomena. Many studies have focused on the flow past isolated and stationary cylinders over various flow regimes [1, 2]. One of the main aspects of these studies is related to the periodic vortex shedding causing fluctuating forces on the cylinder in the streamwise and crossflow directions known as fluctuating drag and lift force, respectively. These time-varying forces induce vibrations, which may lead to the failure of the related engineering systems or structures. Therefore cylinders undergoing free or forced oscillations in crossflow have received significant attention in the literature, which has improved the understanding of the underlying flow phenomena from tests performed in controlled laboratory settings. It has been shown that different types of flow phenomena can be observed based on various ranges of oscillation frequency to the vortex shedding frequency ratio. In addition to stationary and freely vibrating cylinders in crossflow [3, 4], flow past cylinders undergoing forced inline [5], rotational [6], and transversal oscillations [7] have been the subject of numerous studies.

In many applications, such as flow past cables, subsea pipelines, aircraft landing gear structures, etc., the direction of the flow may not be perpendicular to the cylindrical structure. When the flow is not perpendicular (crossflow), the orientation of the cylinder is described as yawed or inclined. The yaw angle (θ) is often defined as the angle between the longitudinal axis of the cylinder and the direction orthogonal to the freestream. Several studies of stationary

1

yawed cylinders have shown that the yaw angle is an important parameter that affects the characteristics of the flow [8]. Regarding the yawed cylinders undergoing oscillation, studies are limited to traversal vibrations or oscillatory flows past stationary cylinders [9]. Research directed towards the yaw-oscillating cylinders has received far less attention despite its relevance to complex flows such as that experienced in many examples of sport where aerodynamics plays a key role. With respect to yaw-oscillation, herein lies a critical gap in the literature that will be addressed in the present research.

The flow past a cylinder undergoing yaw-oscillation at moderate Reynolds numbers is the focus of the present study to provide insight into the flow past the limb of an athlete during a sports activity, among other possible engineering applications such as the flow variation in the vicinity of the deploying landing gear of an aircraft. Examples of such limb motions are the legs of the cyclist while pedaling or the arm motion of the Paralympic wheelchair racer that involves a dominant yaw oscillation in addition to other simultaneous motions. In cycling, the aerodynamic drag accounts for around 90% of the resistance experienced by the cyclist at racing speeds (around 15 m/s) [10] and only a minor reduction in the drag can have a major impact on the outcomes of competitions. As an example, in the cycling track women's team pursuit racing at the 2020 Olympic games, the time difference between the gold medalist team (Germany) and the team in 4th place (Canada) was only around 3.09 seconds [11]. For team Canada, the average team speed (V) in the 4 km race is calculated to be around 16.17 m/s. Considering the drag area (C_dA) of 0.25 for the athletes [12], the power of a rider (P) is estimated to be around 630 watts ($P = 0.5\rho C_d A V^3$, where ρ is the density of air). Assuming that the athlete's power is unchanged, a minor 5% reduction in the drag coefficient could increase the average speed of team Canada to around 16.31 m/s at the same power. With this average speed, team Canada could have reduced the total race time by around 4 seconds and won the gold medal by setting a new world record [11].

The impact of leg motion and crank position of the cyclist on the aerodynamic drag was first investigated by Crouch *et al.* [13]. Their quasi-steady analysis on different static leg positions revealed that changing the leg position while pedaling can change the aerodynamic

drag up to 20% while the frontal area changes only around 2%. However, the focus of their study was mainly on large-scale wake caused by the torso and hips, which did not resolve regions near the moving limb. Thus, the flow features near the moving limb of an athlete remain an open question. While the flow over a real moving limb of an athlete is more complex than flow past a simple yaw-oscillating cylinder model [14], the near wake of the limb is shown to have the typical bluff body characteristics such as the reverse flow region bounded by two shear layers [15]. Therefore, studying the flow past the yaw-oscillating cylinder can improve our understanding of flow behavior in the vicinity of a moving limb of an athlete.

The present work investigates the unsteady fluid dynamics of a circular cylinder undergoing yaw oscillation in subcritical Reynolds numbers to build knowledge that can support the understanding of more complex systems. The focus is primarily on determining the similarities and or differences between the flow past a yaw-oscillating and a static yawed cylinder. The analysis is conducted by evaluating the influence of parameters such as yaw angle, frequency of oscillation, Reynolds number, and cylinder aspect ratio on the near-wake region of the cylinder. The experimental methods used herein include Particle Image Velocimetry (PIV) and Constant Temperature Anemometry (CTA). In particular, for the PIV method, the use of phase averaging is extensively applied to explore and compare the yaw-oscillating cylinder with its static counterpart in different yaw angles. While the PIV results provide information about the mean flow topology and parameters such as wake closure length and wake width, the CTA methodology is applied to enable the analysis of time-varying flow phenomena such as vortex shedding.

The structure of this thesis is as follows. Chapter 2 of this thesis provides a summary of related past works. The experimental setup and the different analysis techniques employed are described in Chapter 3. Chapter 4 is devoted to the results and findings on the static yawed cylinder. Then, the impact of reduced frequency on the yaw-oscillating cylinder is evaluated in Chapter 5. The effect of Reynolds number and the aspect ratio of the cylinder is analyzed in detail in Chapters 6 and 7, respectively. Finally, Chapter 8 concludes the thesis and presents recommendations for future work on the subject.

Chapter 2

Background

2.1 Flow Past Circular Cylinders in Crossflow

2.1.1 Overview of Flow Regimes Around Stationary Cylinders

The flow past circular cylinders is a canonical problem in fluid mechanics and has relevance to many engineering applications. A vast number of studies have been done on the classical problem of flow past a stationary cylinder (see for example [1, 16]). The characteristics of the flow past a circular cylinder strongly depend on the oncoming flow Reynolds number, which is defined as:

$$\mathrm{Re} = \frac{\rho U_\infty D}{\mu},\tag{2.1}$$

where ρ is the density of the fluid, U_∞ is the freestream velocity, D is the cylinder diameter and μ is the fluid dynamic viscosity. Flow past a stationary cylinder is categorized into various regimes based on the Reynolds number (see for example [1, 17]). As shown in Figure 2.1, unseparated or potential flow occurs over the cylinder for very small Reynolds numbers of $\mathrm{Re} \leqslant 5$. For Reynolds numbers in the range of approximately $5 < \mathrm{Re} < 40$, the flow is laminar and the wake is considered to be steady with a pair of vortices placed in the near wake of the cylinder. Figure 2.1 indicates that for $40 \leqslant \mathrm{Re} \leqslant 150$, as the vortices become unstable, alternating vortex street forms downstream the cylinder. As the wake instability grows in this

regime, the Reynolds stresses in the near-wake region increase leading to a decrease in the formation length and a consistent increase in the base suction. The transition regime occurs in the range of $150 < \mathrm{Re} < 260$ with two continuous changes in the wake formation. At around $\mathrm{Re} = 180$ to 194, in the first discontinuity (known as Mode A), the primary vortices are deformed and vortex loops and pair of streamwise vortices with a spanwise length scale of around 3-4 diameters are formed. In the second discontinuity around $\mathrm{Re} = 230$ to 250 (known as Mode B), three-dimensional flow structures occur in the near wake consisting of fine-scale streamwise vortices with the spanwise length-scale of one diameter. In the range of $260 \leqslant \mathrm{Re} \leqslant 1000$, the three-dimensional structure of the fine-scaled streamwise vortices becomes disordered and results in the reduction in Reynolds stress, base suction, and an increase in the vortex formation length. For a Reynolds number range of $1000 \leqslant \mathrm{Re} \leqslant 3 \times 10^5$, the wake regime is referred to as the shear-layer transition regime. Increasing Reynolds number in this regime leads to an increase in two-dimensional Reynolds stresses and reduction in the Strouhal number and the vortex formation length. In this regime, the transition to turbulence in the wake occurs at upstream locations in the shear layers where Kelvin-Helmholtz instability (shear-layer instability) increases. The Kelvin-Helmholtz instability is primarily two-dimensional and leads to an increase in the two-dimensional Reynolds stress and therefore increase in the base suction. The critical transition occurs at Reynolds numbers larger than 3×10^5, where the onset of transition to turbulence occurs at further upstream locations in the separating shear layers and reaches the boundary layer separation points at either side of the cylinder. The drag and base suction is drastically reduced. The interesting phenomenon in this regime, which is the separation-reattachment on only one side of the body, causes a large mean lift force. Beyond this regime, in the supercritical regime, the boundary layer separation is turbulent on both sides of the cylinder. However, the boundary layer transition to turbulence has not occurred and the transition to turbulence is located between the stagnation point and the separation point. The organized vortex shedding is suppressed and the drag is increased compared to that of the critical regime (see Figure 2.2). Beyond the Reynolds number of 3.5×10^6, referred to as the post-critical

regime, the boundary layer around the cylinder becomes fully turbulent over the surface of the cylinder itself. The turbulent vortex shedding occurs with the quasi-constant frequency and the drag is slightly increased.

The focus of the current study is on the subcritical flow regime ($260 \leqslant \mathrm{Re} \leqslant 3 \times 10^5$), due to the comparable Reynolds numbers achieved in the sports application. In this regime and beyond, the fluid dynamics are dominated by the process of vortex shedding. Vortex shedding occurs when the boundary layer detaches from the surface of the cylinder and causes instability in the shear layer. The detached layers roll up in the wake region of the cylinder that eventually leading to vortices that are shed from alternating sides of the cylinder, which is termed vortex shedding or the Karman vortex street. Shedding frequency is among the prominent characteristics of this phenomenon and is often represented using a non-dimensional number called the Strouhal number:

$$\mathrm{St} = \frac{f_s D}{U_\infty}, \tag{2.2}$$

where f_s is the vortex shedding frequency, D is the diameter of the cylinder or characteristic length of non-cylindrical bodies. In the subcritical regime, large transition waves within the shear layers roll up first and then turn to small-scale vortices that shed from the cylinder at certain frequencies with a nearly constant Strouhal number of 0.2. Moreover, the behavior of the vortices behind the cylinder can highly influence the aerodynamic drag of a cylinder. The drag coefficient (C_D) for a stationary cylinder in this flow regime is around 1.2. As discussed earlier, past the subcritical flow regime the drag coefficient changes abruptly to approximately 0.5, owing to the narrowing of the detached wake caused by the transition of the surface boundary layer from laminar to turbulent.

2.1.2 Flow Past Oscillating Cylinders

The effects of vortex-induced vibrations (VIV) and forced oscillations on the cylinder body are important in a variety of engineering applications ranging from cables and towers to offshore
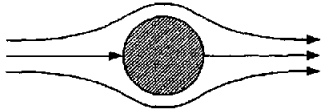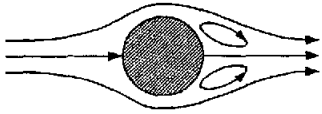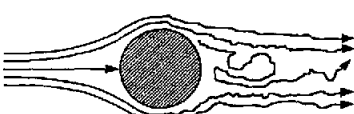
	$R_e<5$: Regime of unseparated or potential flow.
	$5<R_e<40$: a pair of Föppl vortices in the wake and attached to the cylinder.
	$40<R_e<150$: alternating vortex street forms where the vortices and streamlines are laminar. (known as the Von Kármán vortex street)
	$150<R_e<300$: Transition range. $300<R_e<300,000$: vortex street is completely turbulent.
	$300,000<R_e<3,500,000$: laminar boundary layer undergoes turbulent transition and wake is narrower and disorganized. (completely turbulent)
	$R_e>3,500,000$: turbulent vortex street is reestablished but is narrower than in previous cases.

Figure 2.1: Schematics and description of different flow regimes over a two-dimensional cylinder. Reprinted with permission from Blevins [17].
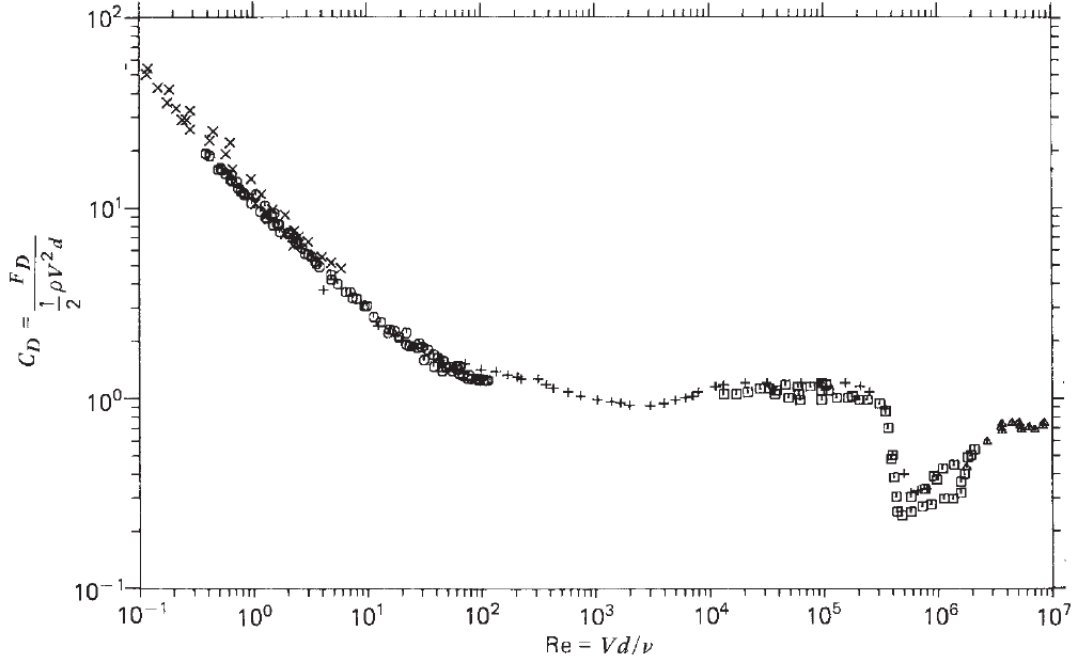
Figure 2.2: Variation of the drag coefficient for a two-dimensional cylinder with Reynolds number. Reprinted with permission from Panton [18].

structures. The alternate vortex shedding from the cylinder causes a large pressure imbalance and thereby unsteady forces on the body. The vibrations may cause failure. Therefore, the vibrations need to be comprehensively studied and controlled. The investigations on the forced oscillations, which occur at velocities and amplitudes that are preset and can be controlled independently of fluid velocity, are mainly associated with the flow past cylinders with inline [19, 5], rotational [6, 20] and lateral oscillations [7, 21] or the oscillating flow over stationary cylinders [22, 23]. Past research has shown that oscillations can alter the wake structure and vortex shedding phenomenon (amplitude and frequency). It has been shown that oscillation frequency and vortex shedding can synchronize within and beyond the natural shedding frequency depending on the frequency ratio of $F = f_s/f_v$, where f_s is the fixed cylinder vortex shedding frequency and f_v is the oscillation frequency. The synchronization process is commonly referred to as lock-in, which is the situation where the cylinder oscillation frequency is synchronized with the vortex shedding frequency ($F=1$) [21]. Studies have shown that there are significant changes in the forces and the vortex patterns of

the near-wake around $F = 1$ based on the type of cylinder oscillation. For example, in the lock-in condition of the cylinder with lateral oscillation, a sudden increase in the amplitude of the vortex-induced force, and a phase angle between the cylinder frequency and the lift force were observed and the extensive mapping of vortex shedding modes also showed a change in the mode of vortex shedding from 2P to 2S [24]. Changes in the wake of the oscillating cylinders are often explained based on the timing and the sign of the initially formed vortex (see for example [25, 19]).

2.2 Flow Over Static Yawed Cylinders

A cylinder is considered to be yawed or inclined when the longitudinal axis of the cylinder is not normal to the incoming flow. The yaw angle (θ) is often measured as the angle between the direction orthogonal to the incoming flow and the longitudinal axis of the cylinder, as shown in Figure 2.3. The flow past the stationary yawed cylinder has been the subject of numerous studies owing to its broad range of applications from cables and heat exchangers to aircraft landing gear structures.

2.2.1 Independence Principle

Early studies of yawed cylinders showed that non-dimensionalizing the Strouhal number and force coefficients by the normal component of the freestream velocity ($U_N = U_\infty \cos\theta$, see Figure 2.3) makes them approximately independent of the yaw angle under some conditions. This concept is commonly referred to as the Independence Principle (IP) [26]. Past experimental studies have shown that the local flow around a yawed cylinder remains normal to the axis of the cylinder and that the normal component of the freestream velocity independently controls the flow physics around the cylinder [27, 28].

The validity of IP for stationary yawed cylinders has received significant attention. In one of the early studies, Van Atta [29] showed that for high aspect ratios stationary cylinders (around 600) in the low Reynolds number range of 50 to 150, the Strouhal number based
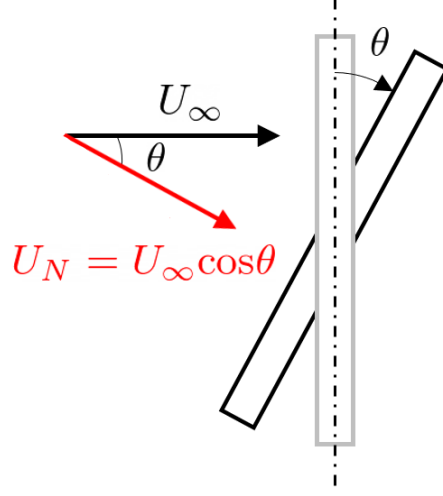
Figure 2.3: Cylinder yaw angle (θ) and the normal component (U_N) of the freestream velocity (U_∞).

on the normal component of the freestream velocity ($\mathrm{St}_N = f_s D/U_N$) was approximately constant for $\theta < 35^\text{o}$ and that the ratio of $\mathrm{St}/\mathrm{St}_N$ should vary as $\cos\theta$ as long as the IP is valid.

Ramberg [8] conducted experiments on finite yawed cylinders with aspect ratios of 20 to 100 for various end conditions (free ended and endplate bounded) in the Reynolds number range of 160 to 1100 and yaw angle range of -10° to 60°. The behavior of flow over the yawed cylinder was found to be sensitive to the end conditions. This sensitivity was more pronounced for low Reynolds numbers. Ramberg demonstrated that the Strouhal number and wake parameters, such as formation length and wake width, cannot be predicted properly by IP for free-ended finite cylinders (see Figure 2.4). For a finite cylinder with endplates, Ramberg showed that inclined endplates approximately simulate an infinitely long cylinder, where the proper amount of inclination for the endplates would depend on the yaw angle. Although the predictions of the values of shedding frequency, vortex formation length, wake width, and base pressure by IP failed for finite yawed cylinders even when appropriate endplates simulating an infinitely long cylinder were used, the universal Strouhal number [30, 31] computed based on the projected values by IP for such configurations with appropriate end conditions agreed well with the previously reported values on non-yawed cylinders. Ramberg concluded that, for
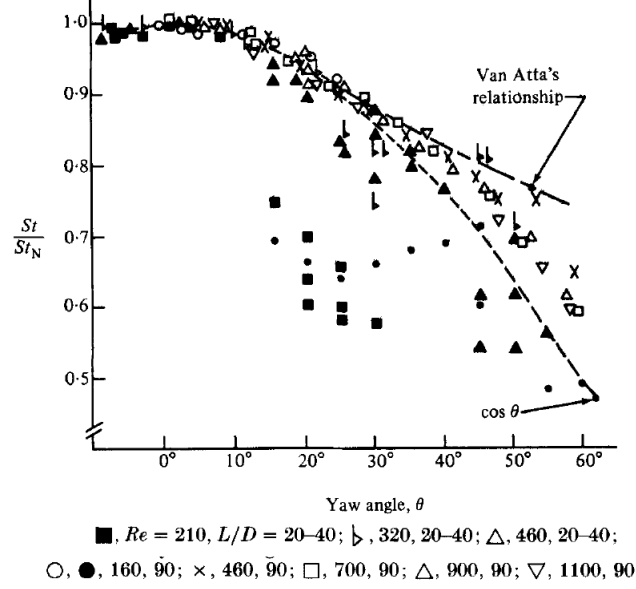
Figure 2.4:   Normalized Strouhal number with yaw angle for various free-ended inclined cylinders. Reprinted with permission from Ramberg [8].

the universal Strouhal number, which directly depends on the Strouhal number, wake width, cylinder diameter, and the base pressure coefficient, variations in these parameters offset. For the flow past a finite-length yawed cylinder near the plane wall with the gap-to-ratio of $0<e/D<1.8$, Kozakiewicz *et al.* [27] showed that IP remained valid up to $\theta = 45^{\text{o}}$ to predict the force coefficients in the Reynolds number range of 3×10^4 to 7×10^4.

Numerical simulation of Zhao *et al.* [32] at a Reynolds number of 1000 in the range of $\theta = 0^{\text{o}}$ to 60° further showed the valid range of IP for $\theta \leqslant 30^{\text{o}}$ for prediction of Strouhal number and drag coefficient values of an infinite cylinder. The discrepancy occurs when $\theta > 30^{\text{o}}$ and it increases with the increase of yaw angle. The computed Storuhal number at $\theta = 60^{\text{o}}$ is 20% smaller than the measured values by Ramberg [8], as shown in Figure 2.5. In another numerical study on an infinitely long cylinder, Lucor and Karniadakis [33] reported that the IP failed for large yaw angles (namely, $\theta = -60^{\text{o}}$ and-70°).

11
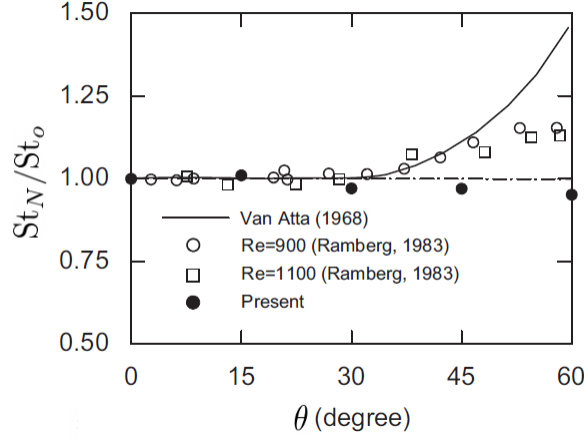
Figure 2.5: The variation of Strouhal number with yaw angle. St_o is the Strouhal number at $\theta = 0^o$. Reprinted with permission from Zhao *et al.* [32].

2.2.2   Structure of the Wake and Vortex Shedding

2.2.2.1   Infinite Yawed Cylinders

Several studies have investigated the structure of flow and vortex shedding process of stationary yawed cylinders to explain the validity or breakdown of the IP. The validity of IP has generally been associated with the parallel vortex shedding at a shedding angle approximately the same as the cylinder yaw angle [8, 32].

For infinitely long yawed cylinders, Zhao *et al.* [32] showed that at high yaw angles, near the center of the principal spanwise vortex, the helical shape streamlines are in the spanwise direction of the cylinder, as shown in Figure 2.6. The flow at the center of the principal vortex is also in the spanwise direction. Further downstream of the cylinder, however, the vortices are convected in the direction of the freestream. Lucor and Karniadakis [33] further proved that the breakdown of IP at high yaw angles is accompanied by a vortex shedding at angles less than the yaw angle. Wang *et al.* [34] simulated the flow structure over an infinite cylinder for $\theta = 0^o$ to 60° at $Re = 1.4 \times 10^4$. They found that for yaw angles above $\theta = 30^o$, the axial flow has a stabilizing effect on the separated shear layer. Figure 2.7 depicts the thinning of the shear layers and more inward curving that precedes the suppression of vortex

(a)   (b)
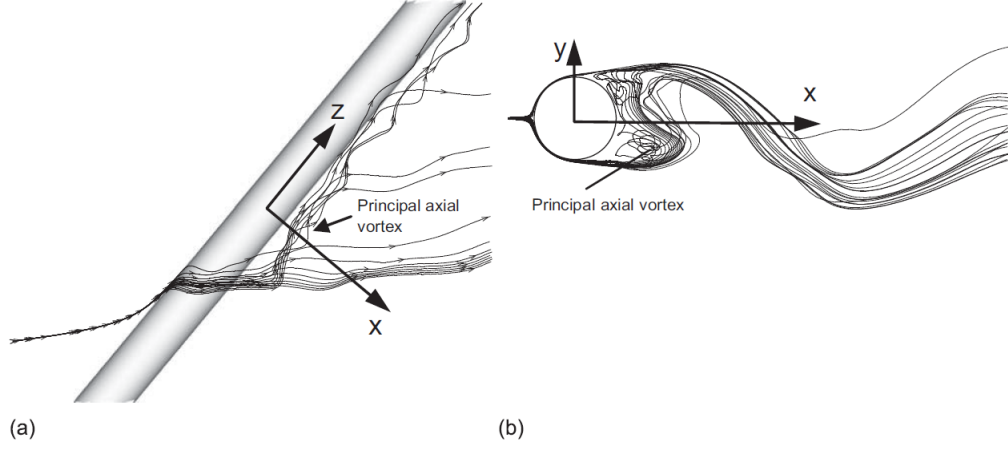
Figure 2.6:   Streamlines for a yawed cylinder with $\theta = 45^o$. a) side view and b) top down view at $z = 0$. Reprinted with permission from Zhao *et al.* [32].

(a)   (b)   (c)
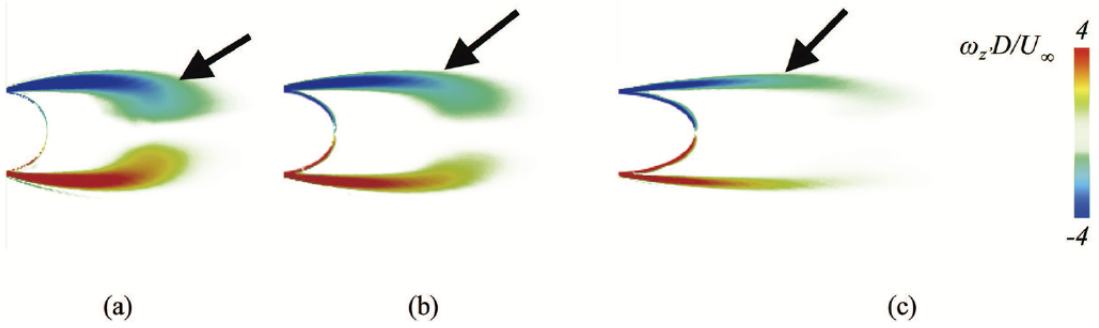
Figure 2.7:   Time-averaged vertical vorticity $\langle \omega_z \rangle D/U_\infty$ for yaw angles of a) $\theta = 30^o$, b) $\theta = 45^o$, and c) $\theta = 60^o$. Flow is from left to right. Reprinted with permission from Wang *et al.* [34].

shedding for $\theta = 30^o$. This effect was likened to that of a wake splitter plate, eventually leading to the suppression of vortex shedding.

2.2.2.2   Finite Yawed Cylinders

For finite-length yawed cylinders, the flow structure is highly dependent on the end conditions. When the free end of a finite yawed cylinder is near a wall, Kozakiewicz *et al.* [27] observed that in the range of yaw angles where the IP is valid (*i.e.*, $\theta = 0^o$ to $\theta = 45^o$), the streamlines near the cylinder are deflected roughly perpendicular to the cylinder axis as demonstrated

in Figure 2.8. The validity of IP for force coefficients was attributed to this observation, which was aligned with the previously mentioned scaling of the force coefficient by the normal velocity component of the freestream velocity.

Marshall [36] simulated the flow over a finite yawed cylinder and showed that at yaw angles near the breakdown of IP, thin sheets of cross-stream vorticity roll up around the Karman wake vortices and destabilize the wake vortices, inducing an axial flow deficit within the vortex cores. The resulting induced axial velocity deficit within the Karman vortex cores is about 20–30% of the spanwise component of the freestream and extends downstream for about 10 cylinder diameters. Both the cross-stream vortex sheets in the cylinder near-wake region and the axial flow deficit within the downstream vortex cores may lead to instability of the vortex street and breakdown of the IP at large yaw angles.

For finite-length yawed cylinders with a free end, Ramberg [8] showed that the vortices near the upstream free end of the cylinder are shed at an angle different than the cylinder yaw angle, leading to a deviation of the Strouhal number and wake parameters from the IP near the upstream end. As shown in Figure 2.9 (a), near the top free end of the cylinder the wake vortices are approximately parallel to each other, but they occur at an angle that is greater than the cylinder yaw angle (the region is marked in Figure 2.9 (a)). A transition then occurs at a specific location along the cylinder, such that beyond this point the wake vortices
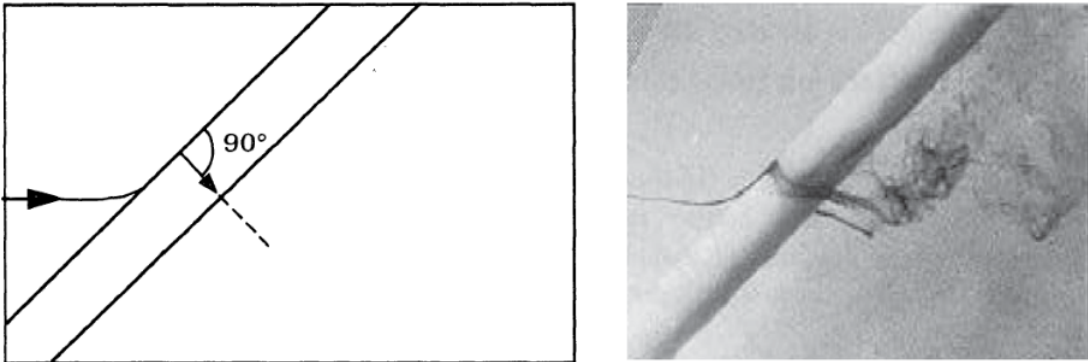
Figure 2.8: Depiction of a streamline (left) and visualization of the flow close to the cylinder (right) at $\theta = 45^{\circ}$. Reprinted with permission from Kozakiewicz *et al.* [27].
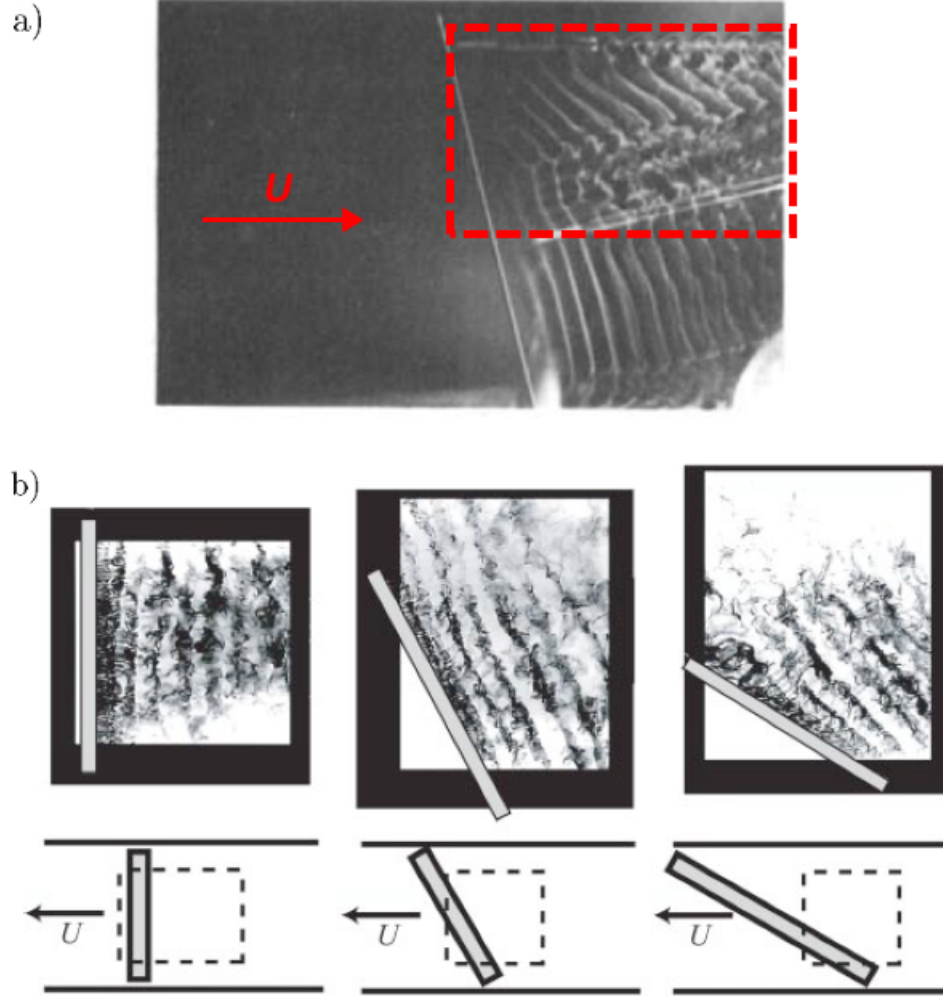
Figure 2.9:   Orientation of wake vortices behind a static yawed cylinder a) Ramberg [8] (static cylinder in a wind tunnel with the flow from right to left) b) Thakur *et al.* at $\theta = 0^o$, 30°, 60° (from left to right) [35] (the cylinder was being towed to the left in a towing tank). Reprinted with permission.

are aligned at approximately the same yaw angle as the cylinder. Contrary to the results of Ramberg, Thakur *et al.* [35] observed that the vortices near the upstream end to have a lesser yaw angle than the cylinder (see Figure 2.9 (b)). They attributed this discrepancy to the effect of the experimental setup and wall velocity relative to the wake vortices. When a cylinder is towed relative to a fixed wall, the downstream tank wall velocity relative to

the cylinder is slightly greater than the mean vortex advection speed within the central part of the channel. The wake vortices, which end on the side walls, consequently appear to be dragged forward by the relative wall motion, giving rise to an apparent decreased yaw angle near the upstream end of the cylinder. Snarski [37] characterized three distinct flow regimes downstream of free ended yawed cylinders depending on the yaw angle; i) classical vortex shedding pattern occurs from a non-yawed cylinder at $\theta = 0^o$ to a cylinder at a yaw angle of $\theta = 37^o$, ii) a system of steady, attached trailing vortices replace the classical vortex shedding in the range of $37^o < \theta < 67^o$ in agreement with the flow visualizations of Thomson and Morrison [38] and Ramberg [8], and iii) an axial boundary layer develops along the length of the cylinder for yaw angles greater than 68°.

For wall-bounded yawed cylinders, Hogan and Hall [39] performed wall pressure measurements to examine the spanwise characteristics of the vortex shedding for yaw angles from $\theta = 0^o$ to 30° and for Reynolds numbers from 2.81×10^4 to 5.61×10^4. They found that the vortex shedding becomes increasingly disorganized as the yaw angle is increased. At large yaw angles, spanwise coherent structures originating from the upstream end of the wall-bounded yawed cylinder disrupt the spanwise coherence of the wake and lead to disorganized vortex shedding. Najafi *et al.* [40] also conducted an experimental study on wall-ended yawed cylinders at a Reynolds number of 5×10^3 in the range of yaw angles of $\theta = 0^o$ to 45°. They identified the presence of two distinct flow patterns and bistable flow situations where these two patterns transition. They attributed the breakdown of the validity of IP to this flow transition. They indicated that by increasing yaw angle the counter-rotating vortices downstream the cylinder detached, moved downstream, and disappeared, respectively, due to the increase in the streamwise velocity. The increase in the streamwise velocity led to a decrease in the velocity difference in the regions inside and outside the shear layers. Thus, the magnitude of the normalized time-averaged spanwise vorticity was reduced as well as the drag coefficient.

In the case of static yawed cylinders with endplates, experimental study of Shirakashi *et al.* [42] for $\theta = 0^o$ to 45° at Re $= 2.5 \times 10^4$ revealed that the secondary (axial) flow in
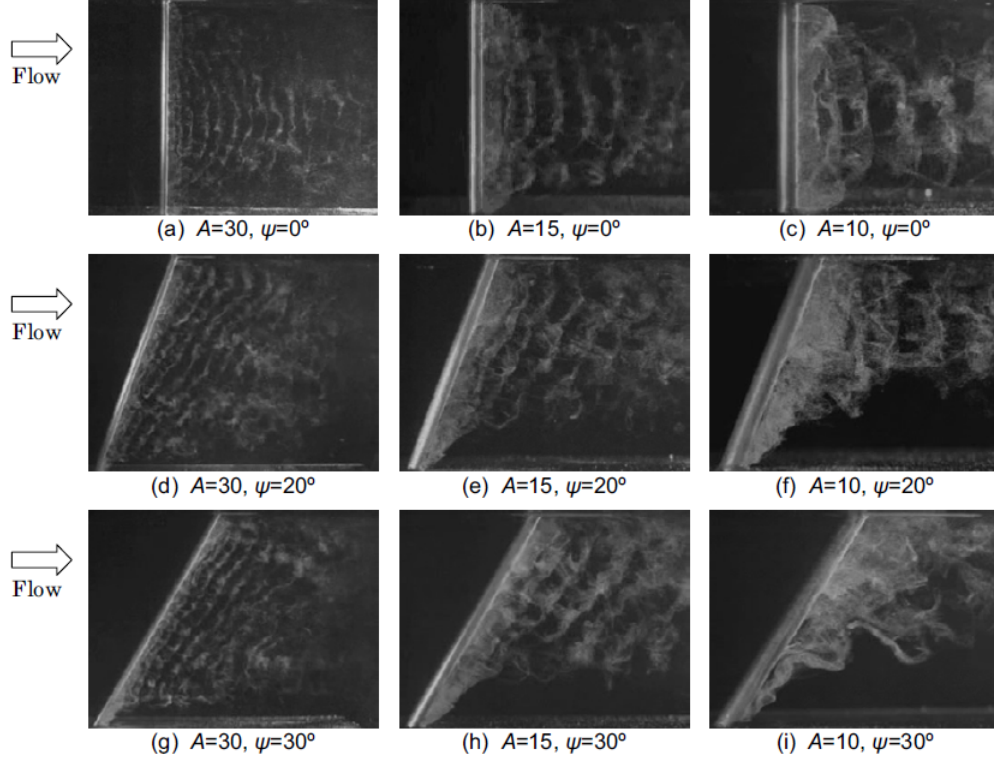
Figure 2.10:   Snapshots of the wake behind the circular cylinder obtained from the flow visualization using the hydrogen bubble method (Re = 450). The aspect ratio and the yaw angle are denoted by A and ψ, respectively. Reprinted with permission from Matsuzaki *et al.* [41].

the wake immediately behind the cylinder damages the regularity of vortex shedding and reduces its frequency. Using endplates downstream of the cylinder, they showed that the vortex shedding becomes further organized and its frequency increases. Shirakashi *et al.* [42] indicated that when the distance between the cylinder is less than $0.6D$, the regularizing effect of the plates is remarkable, however, the increase in the frequency of shedding still occurs when the distance of the endplates is around $1D$ to $1.6D$. Matsuzaki *et al.* [41] investigation on an endplate-bounded static cylinder yawed to $\theta = 0°$, $20°$, and $30°$ with three aspect ratios of $L/D = 10$, 15, and 30 at Reynolds number of Re $= 450$, confirmed that the strong upward flow due to interference of Karman's vortex with the bottom endplate influences the spanwise structure and indicated the impact of the aspect ratio of the cylinder.

They indicated that at $\theta = 30^o$ for $L/D = 15$ and 30 the vortex shedding along the span of the cylinder is not broken down by this interference, however, the significant suppression of vortex shedding occurs for $L/D = 10$. They concluded that the breakdown of the spanwise structure of the regular vortex becomes more remarkable as the aspect ratio is smaller and the inclined angle is larger. Kawaruma and Hayashi [43], simulated the flow over infinite and endplate-bounded yawed cylinder at $\theta = 30^o$ and Reynolds number of Re $= 2 \times 10^3$. Their results supported the existence of a weak axial flow along the span of an infinite cylinder and a strong axial flow downstream the cylinder bounded with endplates. For the latter case, for the range of studied aspect ratio $(5 < L/D < 15)$, they showed how the interaction of flow on the endplates and near the upstream end of the cylinder affects the location of the separation points on the cylinder and the behavior of the axial flow in that region. They also revealed that increasing the aspect ratio leads to a more uniform spanwise pressure distribution at the base of the cylinder. In another study, Hayashi and Kawaruma [44] conducted experiments on stationary cylinder bounded by endplates at $\theta = 30^o$, 45°, and 60° at Reynolds number of Re $= 1.5 \times 10^4$. The pressure measurement along the span of the cylinder with $L/D = 20$ showed that the base pressure of the cylinder and the separation points near both ends of the cylinder, particularly the upstream end, is substantially different from the mid-span region and cannot be predicted by IP. Moreover, Hayashi and Kawaruma showed that IP is only valid for a small section near the mid-span of the cylinder.

2.2.3   Oscillating Yawed Cylinders

Studies carried out on yawed cylinders have also included the effects of vortex-induced vibration (VIV) or forced oscillations. Ramberg [8] showed that for yawed cylinders that are forced to oscillate transversely, the IP remained valid up to $\theta = 60^o$ (the highest angle considered) at the Reynolds number range of Re $= 160$ to 460, while failing for the comparable stationary case. He observed that except for regions close to both ends of the cylinder, the vortex shedding is parallel to the axis of the cylinder. The feature that can be directly linked to the validity of IP. Numerical simulations of Lucor and Karniadakis [33] for the free

vibrating yawed cylinder at yaw angles of $\theta = -60^{\text{o}}$ and -70°, demonstrated the parallel vortex shedding. It should be noted that similar to the results of Ramberg, the parallel vortex shedding did not occur for stationary yawed cylinder at the same yaw angles, as depicted in Figure 2.11. Jain and Modarres-Sadeghi [45] demonstrated that parallel vortex shedding occurs for cylinder under the effect of VIV at yaw angle range of $\theta = 0^{\text{o}}$ to -75° for Reynolds number up to 4×10^3. Franzini *et al.* [46] studied the VIV of a yawed cylinder mounted on a base with one and two degrees of freedom at Reynolds number range of Re $= 3 \times 10^3$ to 1.5×10^4. They indicated that wake characteristics of the oscillating cylinder at yaw angle of $\theta = 45^{\text{o}}$ vary from the oscillating non-yawed cylinder due to the presence of axial flow interfering with the interaction between the free shear layers.

Another group of studies involves harmonically oscillating flow past fixed yawed cylinders such as those conducted by Cotter and Chakrabarti [9] and Sarpkaya and Isaacson [47]. These investigations were mainly devoted to the variation of the hydrodynamic coefficients
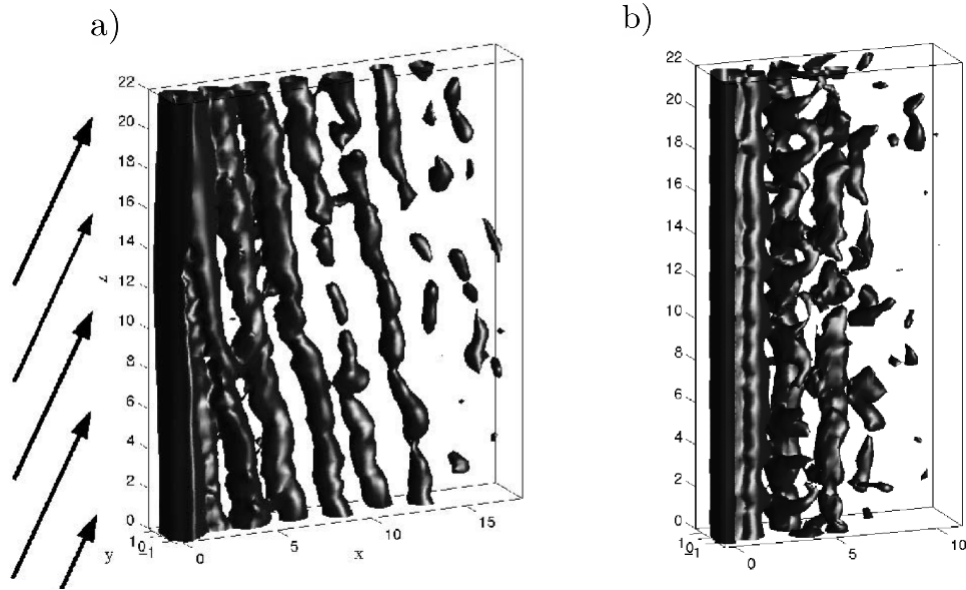
Figure 2.11:   a) Stationary yawed cylinder b) Freely vibrating yawed cylinder ($\theta = -70^{\text{o}}$) at Re $= 1000$. Pressure iso-contour at the value of -0.025. View almost perpendicular to the plane of the inflow. The arrows represent the inflow coming from left to right. Reprinted with permission from Lucor and Karniadakis [33].

.
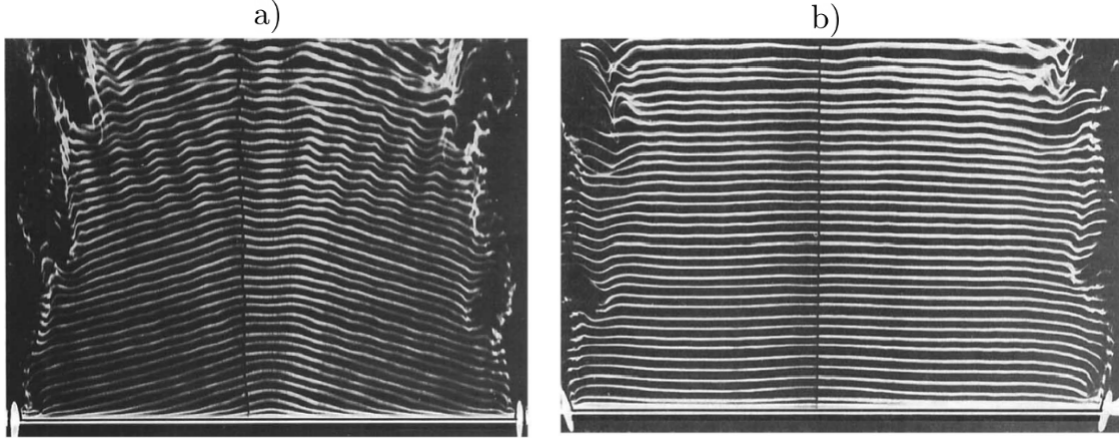
Figure 2.12: a) Oblique vortex shedding downstream a cylinder without endplates at Re = 90 b) Parallel vortex shedding promoted by employing endplates at Re = 110. Reprinted with permission from Williamson [48].

with Keulegan-Carpenter (KC) number and Reynolds number. In wave flows, the validity of IP is not observed except for flows with high KC numbers.

2.3 Effect of End Condition

2.3.1 Non-Yawed Cylinders

In an idealized case, the cylindrical bodies are considered infinite cylinders, which means that they have a large aspect ratio and are free of end effects. For infinite cylinders, the wakes and vortices are independent of the end boundaries. However, in experiments and various practical applications, cylinders have a finite length and inevitably experience the effect of end conditions in some way.

Early studies were mainly devoted to the impact of end conditions on flow past non-yawed cylinders at low Reynolds numbers. For example, Williamson [49] showed a discontinuity in the Reynolds number-Strouhal number relation at Re = 64 as the onset of three-dimensionality in vortex shedding. Williamson proposed the transition to oblique shedding at this critical Reynolds number, where the vortex filaments start to shed with an angle relative to the axis

of the cylinder. Oblique shedding can be associated with the higher base pressure at the mid-span of the cylinder compared to both ends. Williamson [48] altered the end conditions by placing two slanted endplates at both ends of the cylinder to obtain quasi two-dimensional flow at Re $= 90 - 110$, as shown in Figure 2.12.

Eisenlohr and Eckelmann [50] also investigated oblique shedding associated with a jump in the Strouhal number along the span of the cylinder, which leads to a phenomenon called vortex dislocation. By putting two co-axial cylinders with different diameters above and below the test cylinder, they showed that the dislocations occur at a beat frequency between cylinders with different diameters. Hammache and Gharib [51] proposed a novel method to obtain parallel shedding by putting two cylinders upstream near the top and bottom end of the test cylinder that can affect the base pressure at both ends. By placing these orthogonal cylinders, the base pressure gradient along the span was eliminated in the range of Re $= 72 - 158$. Miller and Williamson [52] applied two suction tubes on top and bottom end downstream of the cylinder to achieve the two-dimensional flow at Re $= 140 - 190$. Using suction tubes, more transient or impulsive control is obtainable, which is not possible by putting endplates.

The above literature is predominantly related to low Reynolds numbers while several investigations have been done on the effect of end conditions at the subcritical Reynolds number range. These studies can be categorized by the type of end conditions employed on the cylinder.

One of the most common end conditions used for finite cylinders to promote the two-dimensional flow in the wake region is using endplates. Stansby [53] laid the groundwork for the endplate approach in the subcritical regime. Using base pressure measurement, Stansby determined that the endplates should be mounted outside the tunnel wall boundary layer and recommended that the cylinder should be placed on the endplate far upstream in order to reduce the effect of horseshoe vortices. Szepessy [54] indicated that the trailing edge distance should be longer than the vortex formation region to ensure a uniform base pressure along the cylinder. Szepessy further indicated that for proper endplate use, there is a minimal

pressure gradient two diameters downstream of the cylinder in the spanwise direction. Stagger and Eckelmann [55] also studied the proper size of effective endplates based on the vortex shedding characteristics along the span. They showed that the cell shedding frequency near the end sections is lower than the middle part of the span in $300 < \text{Re} < 8 \times 10^3$. They showed that by increasing the Reynolds number, the size of the low-frequency cell decreases and it is approximately negligible around $\text{Re} = 4.8 \times 10^3$. Thus, they proposed that the ratio of endplate length scale to the cylinder diameter must increase with the increase in the Reynolds number to reduce the length of the affected region. In contrast, Fox and West [56] pointed out that even at high Reynolds numbers around 10^5, the end effect is obvious at the spanwise distance up to $3.5D$ from the endplate.

Finding the importance of cylinder aspect ratio, Szepessy and Bearman [57] investigated the effect of the aspect ratio of the cylinder on the performance of endplates. The results indicated that at $\text{Re} = 10^3$, the change in the aspect ratio from 1 to 10 has no influence on the mid-span flow. In another study, Norberg [58] determined that an infinite cylinder can be represented at the mid-span when the aspect ratio is at least 60 for $400 < \text{Re} < 10^3$. He also found that for $10^3 < \text{Re} < 4 \times 10^4$, the aspect ratio of 25 is required.

A free end is another type of end condition that has been investigated in the literature. A comprehensive review of flow over the free end of the cylinder and another end bounded with the tunnel wall can be found in Sumner [59]. Studies indicate that the Karman vortex shedding is highly impacted by the tip vortices generated near the free end. This impact leads to a lower vortex shedding frequency and Strouhal number near the free end [60, 61]. It is also shown that the cylinder aspect ratio plays a prominent role while the vertically mounted cylinder has a free end condition. Kawaruma [62] showed that for a cylinder with small aspect ratios, an organized vortex shedding does not exist. For the onset of the vortex shedding process, different values of aspect ratios have been reported in the literature [56, 60]. Moreover, the results showed that the drag coefficient of the cylinder decreases as the aspect ratio is reduced.

Another type of end condition is the cylinder piercing the free surface. For the cylinder
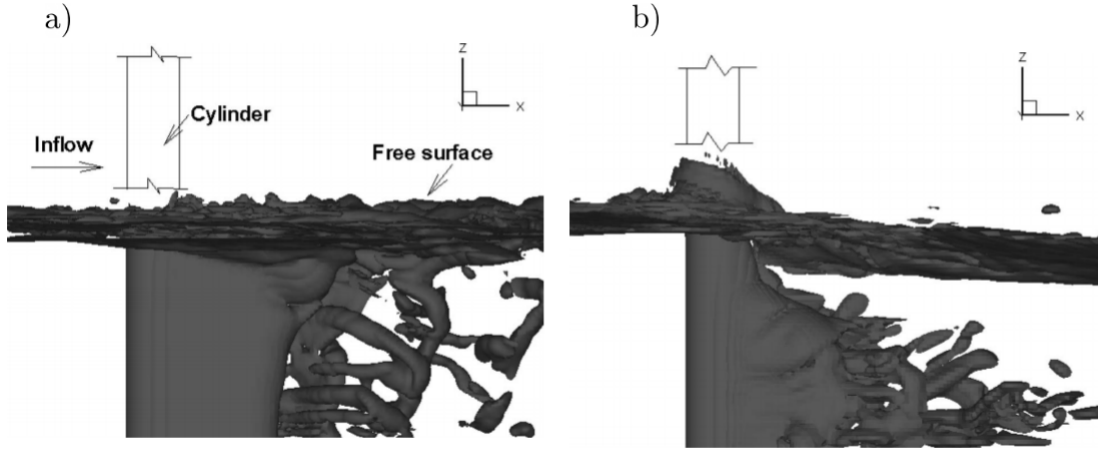
Figure 2.13:   Instantaneous vortex structure in the near wake for a cylinder with free-surface piercing end at a) Re $= 2.7 \times 10^5$ and Fr $= 0.8$ b) Re $= 2.7 \times 10^5$ and Fr $= 2$. The view is taken on the plane cross the cylinder center in the freestream direction. Reprinted with permission from Yu *et al.* [63].

.

mounted on the wall, it is shown that the vortex shedding suppression may occur in the vicinity of the free surface [64, 63, 62]. Results for drag coefficient variation indicated that the total drag coefficient is reduced for such cylinder compared to the value of 1.2, which is suggested for fully submerged cylinders [64, 63, 62, 65]. Moreover, results for the near wake of free-surface piercing cylinders are shown to depend on the Froude number. Froude number is defined as the following indicates the ratio of the inertia force on an element of fluid to the weight of the fluid element:

$$\text{Fr} = \frac{U_\infty}{\sqrt{gD}}, \tag{2.3}$$

where, U_∞ is the freestream velocity, D is the cylinder diameter, and g is the gravitational acceleration. Yu *et al.* [63] showed that at Reynolds number in the range of Re $= 2.7 \times 10^5$ to 1×10^5, for a Froude number of 0.8, the flow in the deep wake has two-dimensional vortex structures while a strong three-dimensional structure is seen near the free surface. At Fr $= 2.0$, the influence of the free surface is felt along the entire span of the cylinder and no regular vortex shedding is observed (see Figure 2.13). Vortices with less intensity dominate

23
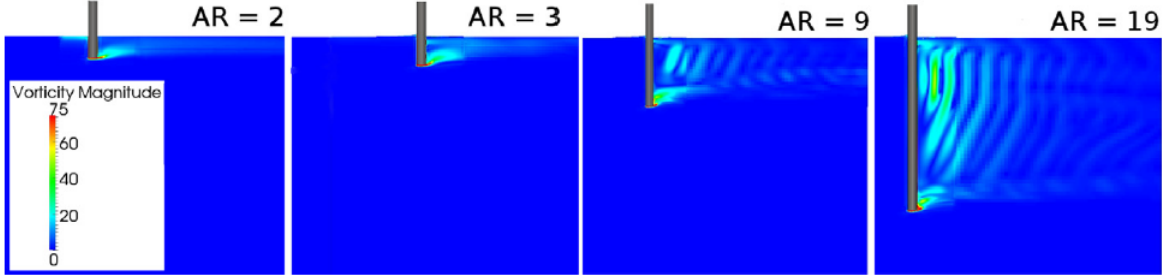
Figure 2.14:   Vertical slices through the numerical domain illustrating the vorticity fields around cylinders of aspect ratios $AR = 2, 3, 9$, and 19 with a top free-surface piercing end and a free bottom end. Freestream direction is from left to right. Reprtinted with permission from Benitz *et al.* [67].

.

the region below the free surface. Yu *et al.* [63] also showed that increasing Reynolds number damp the free surface effect on the vortex structures in the near wake. The experiments of Vlachos and Telionis [66] on cylinders in the crossflow with free surface on one end and tunnel wall on the other showed the existence of a vortex shedding process that is weakened near the free surface end of the cylinder for the subcritical Froude numbers that they studied (namely, Fr = 0.3 and 0.65). They, however, provided evidence that vortex shedding can cease completely close to the free surface for a higher Froude number (Fr = 1.06).

The combination of the free bottom end and top free surface end conditions show three different vortex shedding frequency ranges along the span that varies depending on the aspect ratio and Froude number [67, 68]. Benitz *et al.* [67] showed, at Re = 2900 for a cylinder aspect ratio range of $L/D = 1$ to 19, that vortex shedding is suppressed altogether near the free-surface-piercing end of the cylinder for all cylinder aspect ratios investigated in their study. They also revealed that the flow near the bottom free end is influenced by the tip vortices. This effect is manifested in angled vortex sheets towards the bottom-middle section, while the top-middle section shows perfectly vertical vortex sheets, as shown in Figure 2.14.

2.3.2   Yawed Cylinders

For yawed cylinders, Hayashi *et al.* [69] showed the impact of endplates in decreasing the base pressure and the pressure gradient along the span of the cylinder by increasing yaw angle. They also revealed a significant decrease in the pressure behind the cylinder by moving towards the upstream endplate. In another study on the effect of endplates on the yawed cylinders, Ramberg [8] indicated that endplates with a certain proper inclination with respect to the incoming flow can promote vortex shedding parallel to the cylinder axis.

Through a series of experiments spanning a Reynolds number range of $\mathrm{Re} = 160$ to 1100 and aspect ratio range of $L/D = 20 - 100$, Ramberg [8] showed that the wake of a free-ended yawed cylinder divides along the cylinder span into two shedding modes distinguished by different shedding angles. In the case of a yawed cylinder with one end piercing the free surface and the other bounded by the tunnel wall, Vlachos and Telionis [66] revealed that the effect of the free surface on vortex shedding depends on the orientation of the cylinder. When the free surface piercing end of the yawed cylinder is in the downstream (*i.e.*, positive θ), the strength of vortex shedding enhances towards the free surface end. On the contrary, when the free surface piercing end is in the upstream (*i.e.*, negative θ), the strength of vortex shedding drastically reduces towards the free surface, which may turn into a complete suppression of vortex shedding near the free surface for higher Froude numbers that involve the formation of a free surface depression, as depicted in Figure 2.15.
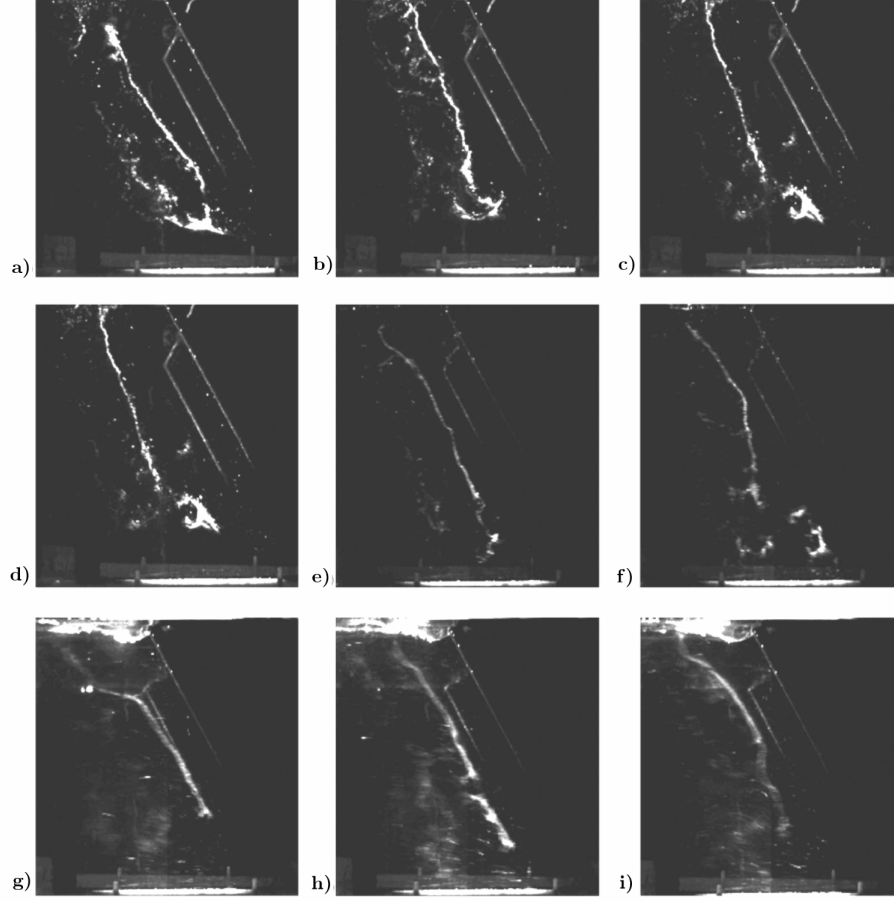
Figure 2.15: Hydrogen bubbles images for cylinder yawed to $\theta = 30^{\circ}$ with free-surface piercing end. a to c) Fr = 0.3 d to f) Fr = 0.65 g to i) Fr = 1.06. The freestream direction is from right to left. Reprinted with permission from Vlachos and Telionis [66]

.

Chapter 3

Experimental Methodologies

3.1 Experimental Setup

3.1.1 Water Tunnel Facility and the Yaw Oscillation System

The experiments were carried out in a recirculating water tunnel located at the University of Toronto Institute for Aerospace Studies (UTIAS), as shown in Figure 3.1. The test section of the tunnel is 610 mm wide, 700 mm high, and 5 m long.

This water tunnel has freestream turbulence of less than 0.5% and flow uniformity of approximately 0.3% for the flow velocities considered in this study. The water depth in the test section was 690 mm for all experiments. Tests were conducted at three Reynolds numbers of 5×10^3, 1×10^4, and 1.5×10^4, based on the cylinder diameter. The temperature of the water could not be controlled and varied with the ambient temperature in the laboratory. In order to maintain the Reynolds number for different tests, the freestream velocity was adjusted after measuring the fluid temperature, using a thermocouple-based sensor with the accuracy of ± 0.1 ^{o}C, and recalculating the kinematic viscosity (ν). The motor running the propeller of the tunnel was controlled by a frequency inverter with a resolution of 0.1 Hz, which leads to the freestream velocity adjustment uncertainty of 1.25 mm/s. The values of Reynolds number (Re), Froude number (Fr), freestream velocity (U_∞), water temperature

Figure 3.1: Image of the water tunnel located at the University of Toronto Institute for Aerospace Studies, prior to the installation of the cylinder yawing system that was used in the present research.

(T), cylinder diameter (D), and submerged length of the non-yawed cylinder (L) for the experiments considered in the present research are summarized in Table 3.1.

The system used to mount the circular test cylinder in the test section, to vary the static yaw angle, and to provide the yaw oscillations is shown in Figure 3.2 (a). It is shown that the system is comprised of five primary parts:

- StepSERVO motor

- Linear belt-driven carriage

- Connecting rod

- Rotating frame

- Circular cylinder

The active yaw system was designed, built, and tested by the author at York University before being transferred to UTIAS. When the setup was installed on the water tunnel, the frame assembly was rigidly mounted to the test section and only the test cylinder was located in

Table 3.1: Details of the flow and geometry related parameters considered in the present experiments.

Re	D (mm)	L (mm)	L/D	T (ºC)	U_∞ (mm/s)	Fr
1.5×10^4	50.8	635	13	25±0.1	300 ±1.25	0.4
1×10^4	50.8	635	13	25±0.1	182 ±1.25	0.25
1×10^4	31.75	635	20	25±0.1	292 ±1.25	0.52
5×10^3	50.8	635	13	25±0.1	98 ±1.25	0.14
5×10^3	31.75	635	20	25±0.1	147 ±1.25	0.26

the water. The linear motion of the belt-driven traverse was transferred to the rotating frame by means of a connecting rod. The traverse was driven by an Applied Motion TSM-34Q StepSERVO motor, which was programmed to prescribe the yaw oscillation parameters, or was held stationary for the static yawed cases. The cylinder was made out of stainless steel tube with sealed ends and a 3.175 mm wall thickness.

3.1.2   The Cylinder Model

Schematics of the experimental configuration are shown in Figure 3.3. Cylinders with two diameters of 50.8 mm and 31.75 mm were used, corresponding to the aspect ratios of $L/D = 13$ and 20. The length (L) of the cylinder is not the physical length, but it is the portion of the cylinder that is immersed when $\theta = 0^\text{o}$. The cylinder was located at an equal distance from the side walls of the tunnel. The top end of the cylinder (downstream end for yawed cases) was bounded by the free water surface, while the bottom end (upstream end for yawed cases) was located above the boundary layer forming over the bottom wall of the water tunnel test section (at a height of 0.03 m) to eliminate any possible end-effect. The thickness of the boundary layer at the location of the cylinder was previously measured for the same tunnel to be around 13 mm [70]. The center of rotation of the cylinder was fixed and located midway between the free end of the cylinder and the water surface, as depicted in Figure 3.2 (b).
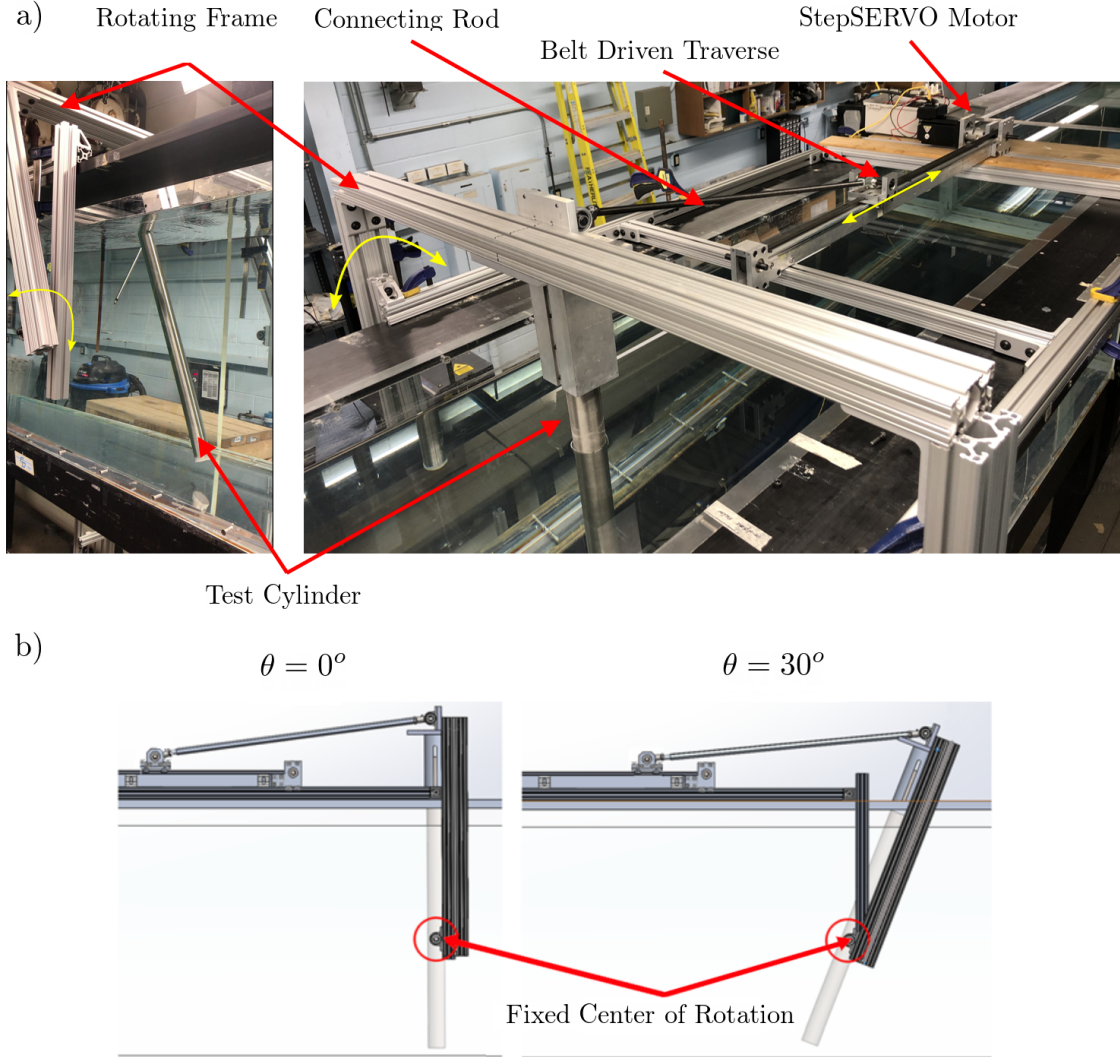
Figure 3.2: a) The experimental setup installed on top of the water tunnel from two different views indicating the main components of the system. Yellow arrows show the rotation of the frame and the linear motion of the carriage. b) CAD drawing depicting the side view of the experimental setup and the fixed center of rotation when the cylinder is at $\theta = 0^o$ and 30°.
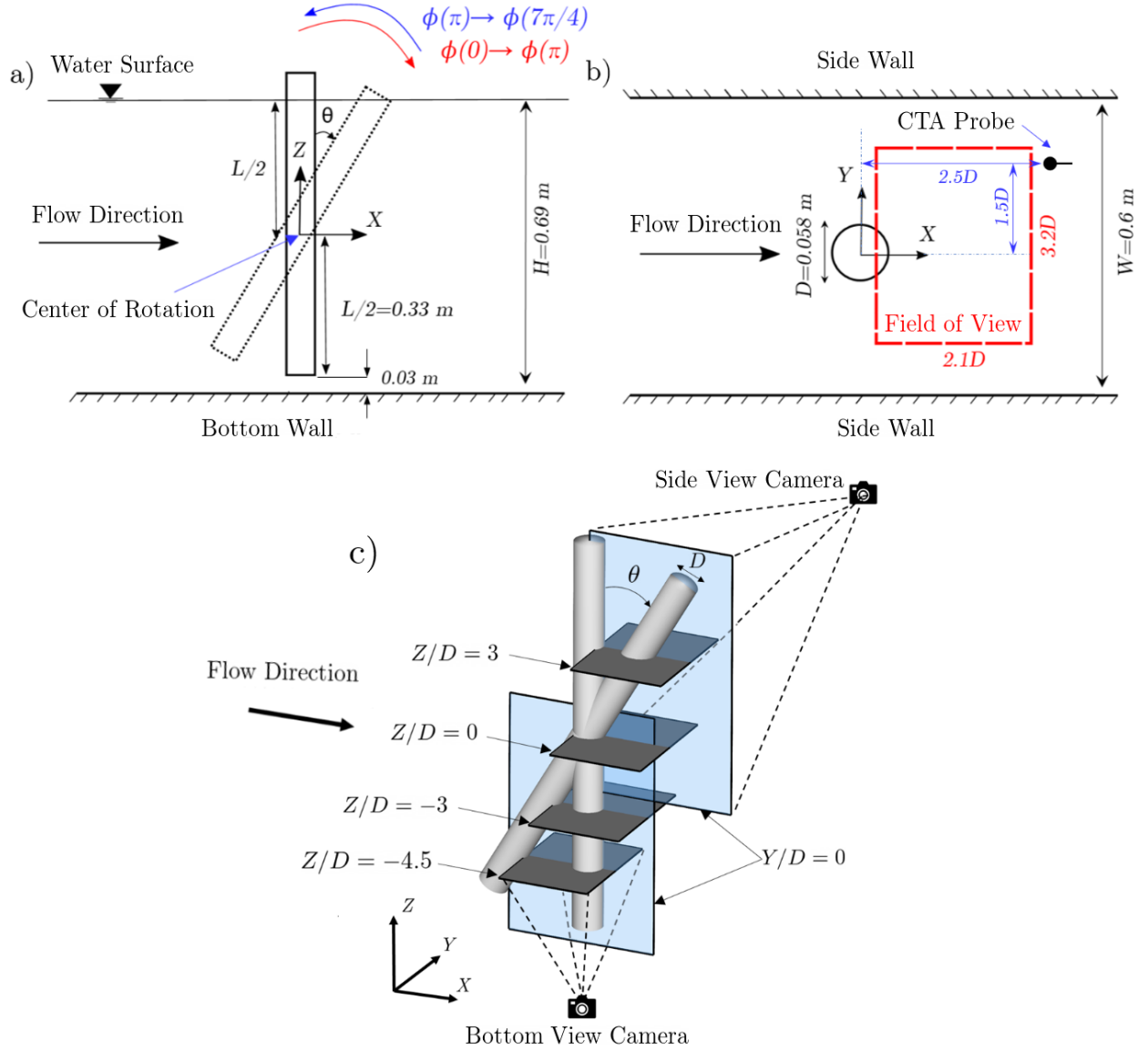
Figure 3.3: Schematic of cylinder yaw motion and PIV measurement planes. a) The side view of the test model showing the direction of oscillation at each phase and the end conditions of the cylinder. b) The bottom view of the test model depicting the PIV measurement plane, which is the plane that passes from the mid-span of the cylinder at $\theta = 0^o$ and the location of the CTA probe. c) The schematic depicting the PIV measurement planes for $L/D = 13$; four (X,Y) planes located at $Z/D = 3$, 0, -3, and -4.5 ($Z/D = 4.5$, 0, -4.5, -7.5 for $L/D = 20$) of the cylinder at $\theta = 0^o$. Two symmetry (X,Z) planes are located at $Y/D = 0$.

About this location the yaw angle varies between $\theta = 0^{\circ}$ and 30°. The origin of the Cartesian coordinate system used in the present experiments passes from the center of rotation and the axis of the cylinder. The X-axis was in the direction of the freestream flow, the Z-axis in the direction normal to the floor of the test section, and the Y-axis was normal to the span of the cylinder and was directed in accord with the right-hand rule, as shown in Figures 3.3 (a) and 3.3 (c).

3.2 Yaw Oscillation Parameters

The yaw oscillation parameters are achieved using a StepSERVO motor that was programmed to provide sinusoidal yaw oscillations to the cylinder at prescribed frequencies (f_c). During a complete cycle of yaw oscillation, the cylinder was yawed from the cross-flow position ($\theta = 0^{\circ}$) to $\theta = 30^{\circ}$ and then returned to $\theta = 0^{\circ}$. The yaw angle (θ) of the cylinder is plotted in Figure 3.4 (a) against the phase (ϕ) of one complete yaw oscillation. The rotation system was programmed to provide a sinusoidal variation in the angular velocity (ω) of the cylinder as shown in Figure 3.4 (b). In this study, the flow past the static and yaw-oscillating cylinders
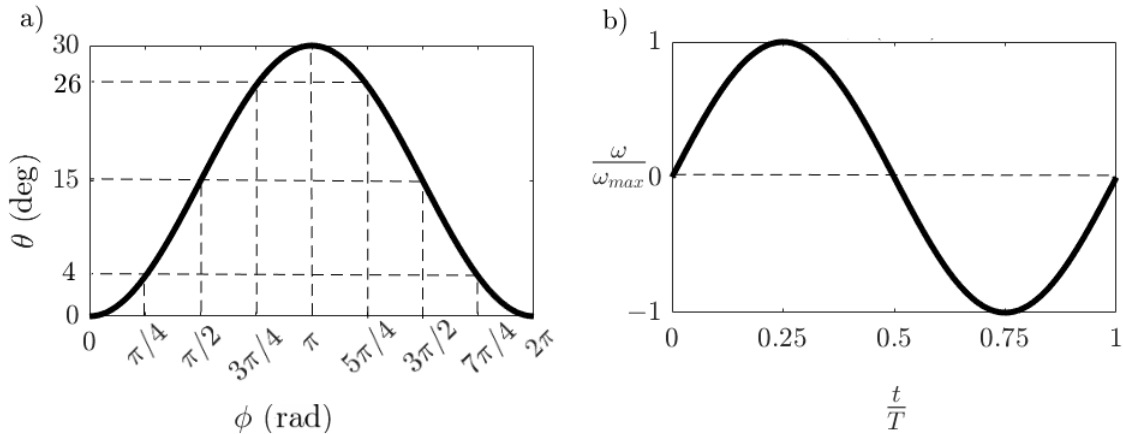
Figure 3.4: a) Variation of the cylinder yaw angle over one complete oscillation cycle. Dashed lines mark the yaw angles and the corresponding phases examined in the present work. b) Angular velocity (ω) of the cylinder normalized by its peak value with respect to time over one period ($T = 1/f_c$).

is compared at eight discrete phases. As marked in Figure 3.4 (a), these eight phases are given by $\phi = 0$, $\pi/4$, $\pi/2$, $3\pi/4$, π, $5\pi/4$, $3\pi/2$, $7\pi/4$. These eight phases correspond to the cylinder yaw angles of $\theta =$ 0º, 4º, 15º, 26º, 30º, 26º, 15º, 4º, respectively. The phase pairs of $\pi/4$ and $7\pi/4$, $\pi/2$ and $3\pi/2$, $3\pi/4$ and $5\pi/4$ correspond to the same yaw angle. However, for the first phase in each pair the yaw angle is increasing whereas for the second phase the yaw angle is decreasing.

The yaw oscillation frequency (f_c) was purposely chosen so that the ratio of the tip speed of the cylinder to the freestream velocity falls between 0 and approximately 2. To relate this value to a reference parameter, the oscillation frequency is chosen to be an integer fraction of the vortex shedding frequency (f_s) of the non-yawed cylinder at the corresponding Reynolds number [71]. The oscillation frequency can be expressed non-dimensionally in terms of the reduced frequency (K) [72]. Using the half-length of the cylinder ($L/2$) as the characteristic length, the reduced frequency for the present case can be defined as:

$$K = \frac{\pi f_c L}{2 U_\infty},$$
(3.1)

The reduced frequencies and the corresponding yaw oscillation frequency for all the test cases in the present study are summarized in Table 3.2. For Re $= 1.5 \times 10^4$ and $L/D = 13$, achieving higher values of K greater than 1.3 was not possible due to the onset of vibrations. However, for Re $= 5 \times 10^3$, higher reduced frequencies of $K = 4$ and 2 were studied, given the lower freestream velocity. For a cylinder with $L/D = 20$, cases with $K = 1.3$ and $K = 2$ at Re $= 5 \times 10^3$ were chosen to examine the influence of the aspect ratio on the near wake.

3.3 PIV Measurements

Particle Image Velocimetry (PIV) is a non-intrusive, optical flow diagnosis technique. The basic principle of Particle Image Velocimetry (PIV) is based on measuring the displacement of the small tracer particle with the flow over a short time interval. The position of the tracer particle is determined when they are illuminated by the thin laser sheet generated by the

double-headed pulsed laser system. The particles are small in size and neutrally buoyant so that they can move with the local flow velocity. A laser light sheet illuminates the region of interest in the flow twice and the scattered light is recorded onto two subsequent image frames. The images are mainly recorded by means of a Charge-Coupled Device (CCD) camera. In the planar PIV, which is used in the present experiment, a single CCD camera is used that yields two velocity components within the measurement plane. To process the images, each image is first divided into smaller regions called interrogation windows. The particle displacements are obtained by performing cross-correlation analysis for corresponding interrogation windows between the two subsequent images. The local fluid velocity is calculated by dividing the particle displacements over the image magnification and the time difference between the laser pulses. The velocity vectors are a projection of the local flow velocity in the center of the interrogation windows. Further details on the working principle of the PIV technique can be found in Westerweel [73].

A TSI planar PIV system was used to measure both the time-averaged and phase-averaged flow fields in the near wake of the static yawed and yaw-oscillating cylinder. The water was seeded with neutrally buoyant, hollow glass particles with a nominal diameter of 10 μm. The flow illumination was provided by a double cavity Nd:YAG laser with a maximum energy output of 200 mJ/pulse at a wavelength of 532 nm. Particles images were taken using a CCD camera with a resolution of 1920 $\times$ 1080 pixels, which was located beneath the transparent

Table 3.2: Summary of the values of yaw oscillation frequency to for the reduced frequency for experiments with different Reynolds numbers and aspect ratios.

Re, L/D	$K = 0.5$	$K = 1$	$K = 1.3$	$K = 2$	$K = 4$
1.5×10^4, $L/D = 13$	$f_s/8$	$f_s/4$	$f_s/3$	-	-
1×10^4, $L/D = 13$	$-$	$f_s/4$	$f_s/3$	-	-
1×10^4, $L/D = 20$	$-$	$f_s/7$	$f_s/5$	-	-
5×10^3, $L/D = 13$	-	-	$f_s/3$	$f_s/2$	f_s
5×10^3, $L/D = 20$	-	-	$f_s/5$	$f_s/3$	-
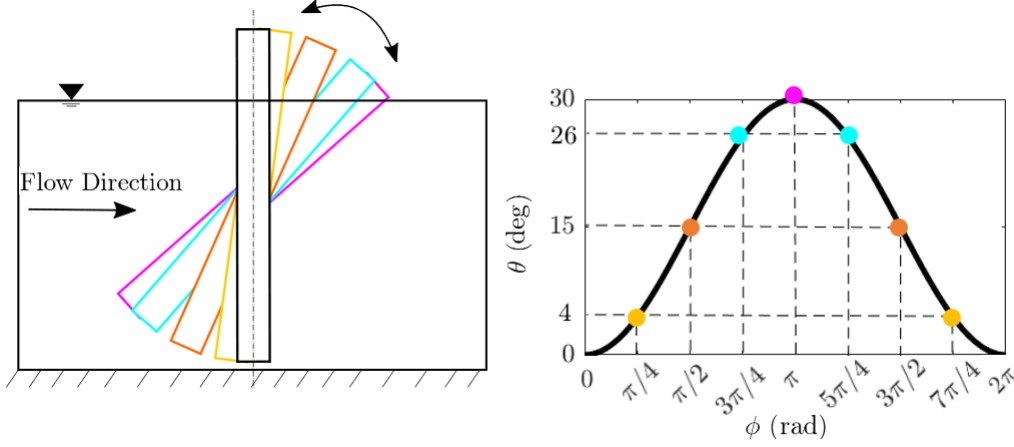
Figure 3.5: Phase-averaged PIV measurements. Image pairs were taken at eight select phases corresponding to yaw angles of $\theta = 0^o$, 4°, 15°, 26°, and 30°, as marked with different colors.

bottom wall and outside of the side wall of the tunnel for bottom view and side view analysis, respectively.

PIV measurements were performed in four (X, Y) planes, namely located at $Z/L = 0.23$, 0, -0.23, and -0.34 of the cylinder at $\theta = 0^o$ (field of view dimensions of $2.5D \times 3.5D$ in streamwise and transverse direction, respectively) and two (X, Z) symmetry planes located at $Y/D = 0$ (field of view dimensions of $4D \times 7D$ in streamwise and spanwise direction, respectively), as shown in Figure 3.3 (b) and (c). Note that the (X, Y) planes were located at $Z/D = 3$, 0, -3, and -4.5 for cylinder with $L/D = 13$ and $Z/D = 4.5$, 0, -4.5, and -7.5 for cylinder with $L/D = 20$ so that the distance from the center of rotation is maintained. Since the out-of-plane component of the velocity could be significant, particularly for (X, Z) planes, the time interval between the two successive images and laser sheet thickness were determined to be in the acceptable range [73]. The desired thickness of the light sheet was produced using a combination of a spherical lens (1000 mm focal length) and a cylindrical lens (50 mm focal length).

Two types of PIV analysis were performed in the current study; time-averaged and phase-averaged analysis. To construct the time-averaged velocimetry results, a total of 4,000 image pairs were captured from the flow field for every static and yaw-oscillating case investigated in this study. This approach was mainly used to obtain the time-averaged results for the

35

stationary yawed cylinder and yaw-averaged results for the yaw-oscillating cylinder. The laser repetition rate for these measurements was 14.5 Hz, which was the maximum repetition rate obtainable by the laser. A set of 400 image pairs were used to construct the phase-averaged velocity fields for yaw-oscillating cases. In the phase-averaged analysis of the yaw-oscillating cylinder cases, the PIV system was synchronized with the cylinder motion to obtain data at specific phases during the cylinder oscillation, as shown in Figure 3.5.

In PIV processing by MATLAB-based PIVlab program [74], interrogation windows of 32×32 pixels were used with 50% overlap in both directions, producing 92×42 and 95×75 in-plane velocity vectors for the (X, Z) and (X, Y) planes, respectively. The uncertainty of the instantaneous velocity vectors is estimated to be approximately $0.021 U_\infty$ and $0.033 U_\infty$ for the (X, Y) and (X, Z) planes, respectively. This uncertainty was determined using standard methods of the PIV measurements [75] and uncertainty propagation [76] for possible sources of error including the pixel displacements, time duration of a laser pulse, calibration, magnification, and grid spacing. Details of the uncertainty analysis can be found in Appendix.

3.4 Constant Temperature Anemometery

Constant temperature anemometry is widely used to measure varying velocities with high spatial and time resolution, little interference with the flow, high-frequency response, and high sensitivity at low velocities [77]. The sampling rate in CTA measurements is remarkably higher than the PIV measurements, however, the data is collected at a specific point as opposed to the global information obtained by PIV. The working principle of CTA is associated with a transducer that senses the variations in the heat transfer from a small electrically heated sensor due to the fluid motion. The output signal of the sensor is a voltage signal and needs to be converted to velocity. The conversion is done by means of a calibration procedure associated with a relation between the output voltage (E) of the sensor and the flow velocity (U_∞) after exposing the probe to known flow velocities controlled by the frequency inverter of the impeller of the water tunnel. The power law (King's law) curve fitting was used in the

present experiment:

$$E^2 = A + B(U_\infty)^m; m = 0.45 \tag{3.2}$$

where A to B are the calibration coefficients. In order to avoid calibration drift due to the temperature effects, the water temperature was monitored using a thermocouple-based sensor and a temperature correction factor was applied using the recommendation by Jorgensen [78].

The CTA system used in the present project included a probe support, an anemometer, and a data acquisition system. The hot-film sensor used was a Dantec Dynamics 55R11 type with an overheat ratio of 1.1, sensor resistance of 7.19 Ω, sensor lead resistance of 0.5 Ω, and a sensor temperature coefficient of resistance (TCR) of 0.39. The sensor had a length of 1.25 mm and a diameter of 70 μm, and had a sputtered quartz coating of 2 μm. This sensor was connected to a single channel Dantec mini-CTA anemometer. The data acquisition system consisted of a NI BNC 2110 terminal and a NI PCI 6251 data acquisition card connected to a computer.

Details of the CTA data acquisition parameters are summarized in Table 3.3. For static yawed cylinders, the probe was located at three spanwise locations to evaluate the flow variation along the span of the cylinder. The streamwise and lateral distance from the cylinder was chosen so that the probe was located outside the wake and the frequency of the vortex shedding can be easily captured. The total sampling time for the static yawed cylinder was chosen to be large enough to span at least 1000 complete cycles of vortex shedding (assuming St = 0.2). For the yaw-oscillating cylinders, the probe was located at the mid-span plane in order to have nearly a constant distance from the surface of the cylinder during the oscillation cycle. To evaluate the sensitivity of the results to the spanwise locations near the mid-span, the data was also collected at $Z/D = \pm 1$ and the similarity of the results with those obtained at the mid-span location was confirmed. The sampling frequency (f_{sa}) was 1500 Hz with the total sampling time (t_{sa}) of 1.5 hours that covers a range of 400 to 1200 complete cycles of oscillation (n_c) depending on the reduced frequency. The uncertainty of the signal power spectrum estimation was calculated to be less than 6% [79].

Table 3.3: CTA measurement parameters for the static and yawed cylinders and the location of the probe downstream the cylinder. X' is the streamwise distance from the base of the cylinder along the wake centerline.

Experiments	X'/D	Y/D	Z/D	$f_{sa}(Hz)$	$t_{sa}(s)$	n_c
Static Cylinder	2.0	1.5	$-3,0,3$	1500	900	-
Yaw-Oscillating Cylinder	2.0	1.5	0	1500	4800	400-1200

3.5 Data Analysis Procedures and Determination of Flow Quantities

Prior to presenting the results in the following chapters, it is imperative to understand the approaches taken in the current work to study the flow behavior. Williamson [1] indicated that in case of the vortex shedding from the circular cylinder, such as the flow behavior in the subcritical regime, if one averages the flow field for a long time, a region called the mean recirculation region is obtained in the wake. For a non-yawed two-dimensional cylinder, he reported that this region is closed and contains symmetric counter-rotating vortices, as shown in Figure 3.6 (b). The features of the mean recirculation region can be directly related to the base pressure and therefore, the drag coefficient of the cylinder in different regimes.

In the qualitative analysis of the current work, using the time-averaged or phase-averaged flow fields obtained by the PIV measurements, the existence or the elimination of the mean recirculation region was investigated for various cases. This could be done by means of seeking the presence or the absence of the saddle points on the wake centerline (in the (X, Y) planes) or backflow (reverse flow) immediately behind the cylinder (in the (X, Z) planes). The saddle point defines the region between the mean recirculation region and the outer region on the wake centerline. The backflow occurs in the near wake of the cylinder when the mean flow, due to the presence of the counter-rotating vortices, possesses negative streamwise velocity, as depicted in Figure 3.6 (a).

In the quantitative analysis of the PIV results, three characteristics of the mean recirculation region, namely, the wake closure length (L_c), half wake width ($Y_{1/2}/D$), and backflow angle (β) were measured in the present study. The wake closure length is defined as the distance from the base of the cylinder to the point on the wake centerline where the sign of the mean streamwise velocity changes from negative to positive. This parameter is often used to measure the length of the mean recirculation region [80, 81] (see Figure 3.6 (b)). A parameter that frequently appears in characterizations of the near wake regions is the so-called formation length. The formation length has different definitions that are all mutually compatible [82]. As Norberg [83] showed, the wake closure length can be used as a measure for the vortex formation length. Other widely employed definitions of formation length determined it, for example, as the streamwise distance from the base of the cylinder on the wake centerline to the point where the level of velocity fluctuation reaches its maximum [1] or as the streamwise distance from the base of the cylinder to the position of the initial fully formed vortex [8]. As to the second wake parameter characterized in this study, the half wake width ($Y_{1/2}$), it is measured outside the recirculation region at $X/D = 2$ using streamwise velocity deficit values ($\langle U_d \rangle = U_\infty - \langle U(x,y) \rangle$) and the approach proposed by Wygnanski *et al.* [84], as shown in Figure 3.6 (c). The wake width for the static yawed cylinder and yaw-oscillating cases is only reported at the mid-span plane. Reverse flow angle (β) is defined as the angle between the freestream direction and the line that coincides with the middle straight part of the phase-averaged streamlines between the rear surface of the cylinder and the wake closure point, as marked in Figure 3.6 (d). Notice that for the locations with the suppressed mean recirculation bubble (*i.e.*, no reverse flow), the angle is measured between the freestream direction and the direction of the streamline at a distance of $0.5D$ from the rear surface of the cylinder.

The time-resolved data obtained in the CTA measurements were predominantly used to evaluate the variation in the vortex shedding frequency by comparing the streamwise velocity power spectra for different cases, as depicted in Figure 3.7. The power spectral density (PSD) from the streamwise velocity signal was calculated using the Welch averaging method (details

can be found in [85]). Figure 3.7 represents a sample of the streamwise velocity signal and the corresponding power spectra for a non-yawed static cylinder. The peak frequency in the velocity spectra is recognized as the vortex shedding frequency.
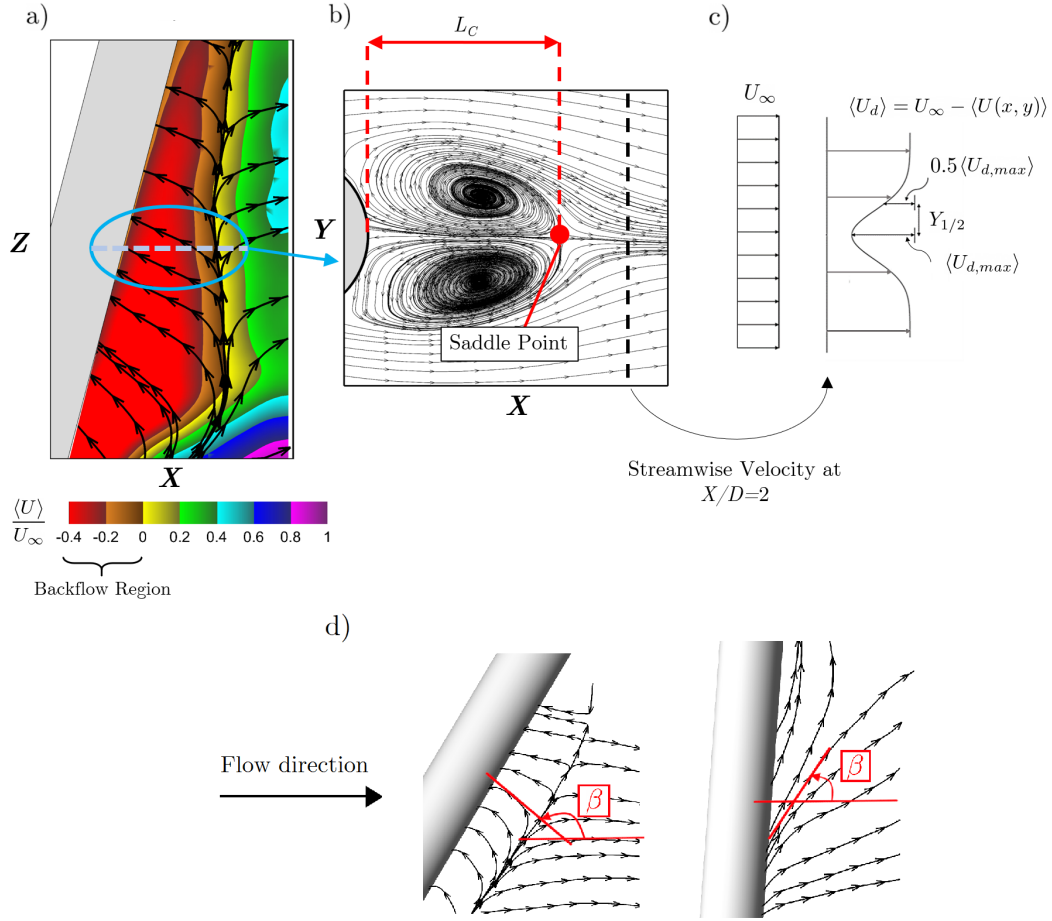
Figure 3.6: a) Contours of mean normalized streamwise velocity ($\langle U \rangle / U_\infty$) overlaid by the mean streamline topology ($\langle \psi \rangle$) indicating the backflow region behind the cylinder in the (X, Z) plane. b) The (X, Y) plane view of the marked location in the (X, Z) plane, depicting the mean recirculation region, the location of the saddle point, and the definition of the wake closure length. c) The measurement of the wake width on $X/D = 2$ using the variation of the velocity deficit $\langle U_d \rangle$ as proposed by Wygnanski *et al.* [84]. d) The schematics show how the reverse flow angle is measured in the presence (right) or the absence (left) of the mean recirculation region.
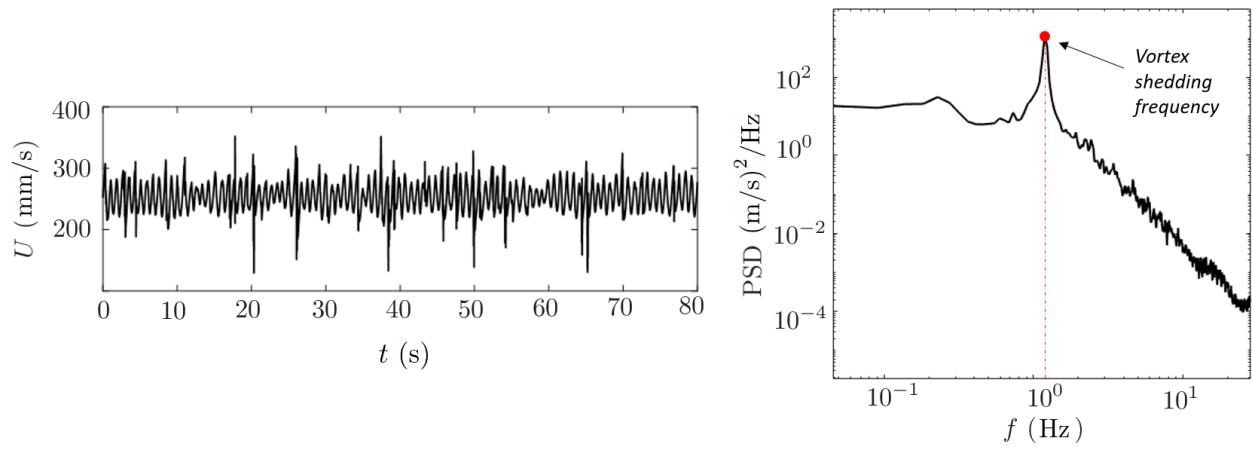
Figure 3.7: Sample of the velocity signal (left) and the power spectra of the streamwise velocity (right). The highest peak is corresponding to the vortex shedding frequency as marked in the plot.

Chapter 4

Results: Static Yawed Cylinders

The near wake of the static cylinder with $L/D = 13$ yawed to different angles in the range of $\theta = 0^\text{o}$ to 30° at $\text{Re} = 1.5 \times 10^4$ is studied to evaluate the influence of cylinder inclination on the flow behavior. More importantly, the results will create a baseline reference for the investigation of the impact of the yaw-oscillation on the near wake of the cylinder with a similar aspect ratio and at the same Reynolds number in Chapter 5. Studies on the effect of Reynolds number and aspect ratio on the flow past static yawed and yaw-oscillating cylinders will be conducted in Chapters 6 and 7, respectively.

4.1 Mean Near Wake Flow Topology

4.1.1 Flow Structure in the (X, Z) Symmetry Plane

Measurements of the flow past the static yawed cylinder are a baseline for the yaw-oscillating counterpart. The ensemble average of velocity components in the X and Y directions ($\langle U \rangle$ and $\langle V \rangle$, respectively) are obtained from 4,000 snapshots of velocity fields for each yaw angle. Figure 4.1 shows the mean streamline topology ($\langle \psi \rangle$) and contours of normalized mean streamwise velocity ($\langle U \rangle / U_\infty$) for static yawed cylinder at yaw angles of $\theta = 0^\text{o}$, 4°, 15°, 26° and 30° in the symmetry plane. These yaw angles correspond to the eight evenly spaced
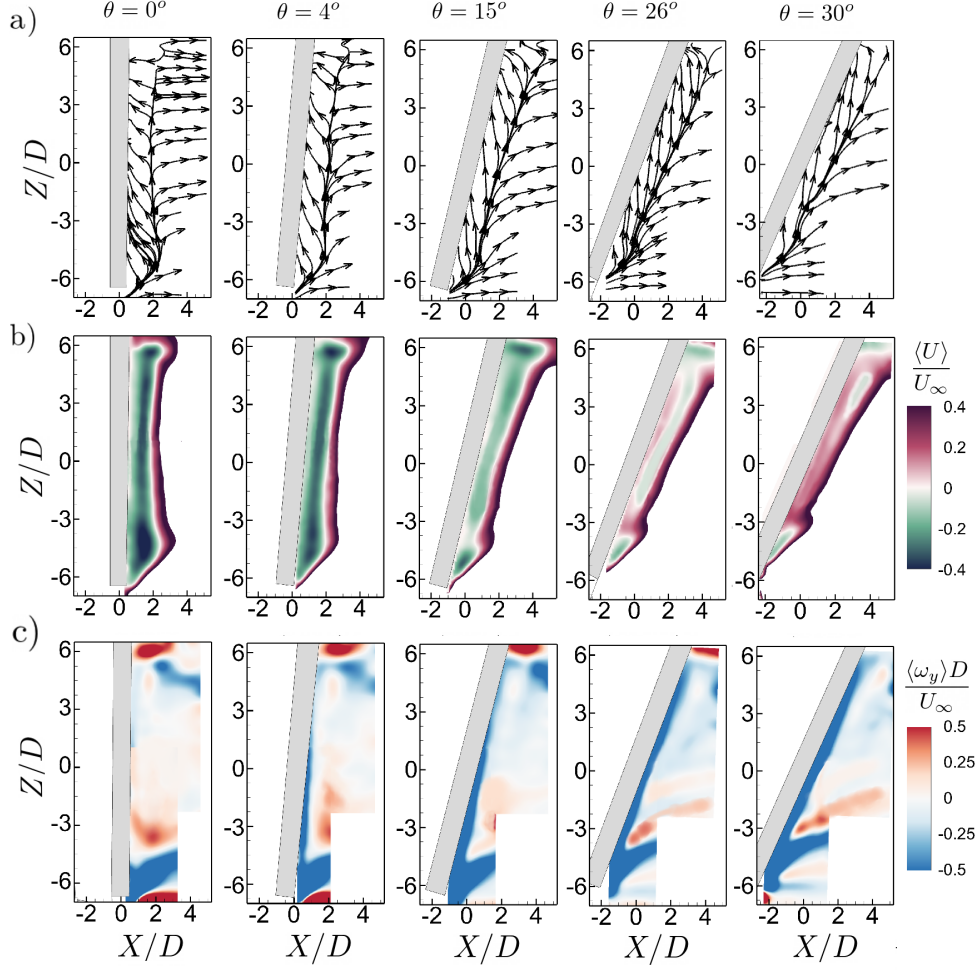
Figure 4.1: a) Mean streamline topology ($\langle\psi\rangle$) b) Contours of mean normalized streamwise velocity ($\langle U\rangle/U_\infty$) c) Contours of mean normalized vorticity ($\langle\omega_y\rangle D/U_\infty$) for the static cylinder at yaw angles of $\theta = 0^o$, 4°, 15°, 26°, and 30°. Results are shown in the symmetry plane at $Y/D = 0$.

phases taken over one complete oscillation, which was previously explained in Section 3.2.

Figure 4.1 (a) shows that the streamline patterns of the static yawed cylinder at yaw angles of $\theta = 0^o$ to 26° contain a reverse flow region, indicating the existence of a mean recirculation region, behind the majority of the cylinder span except for the regions near the bottom end of the cylinder. It can also be seen that the streamlines within the mean recirculation region change their orientation as the yaw angle is altered, getting, in general, progressively closer to a direction parallel to the cylinder span as the yaw angle increases.

In support of these observations, Figure 4.1 (b) also depicts that the negative direction streamwise velocity persists in the wake of the cylinder over a large section of the span for this yaw angle range. However, the spatial extent of the reverse flow velocity is decreased along with the magnitude of the negative velocity with increasing yaw angle. For $\theta = 30^{\circ}$, the $\langle \psi \rangle$ patterns show that the streamlines immediately behind the cylinder are highly directed in the spanwise direction, and the contours of $\langle U \rangle / U_{\infty}$ reveal that the positive streamwise velocity occupies the major part of the near wake, indicating a significant suppression in the mean recirculation region at this high yaw angle. The observed general trend of decreasing streamwise velocity and eventual replacement of the reverse flow with positive streamwise velocity along larger sections of the cylinder span as the yaw angle increases is a result of the development of large magnitude spanwise flow with increasing yaw angle (as apparent from the general reorientation of the streamlines more and more in the spanwse direction for larger yaw angles). Notice from Figure 5.2 that for the static yawed cylinder, near its upstream end (around the location of $Z/D = -4$ to - 5.5), a reverse flow region is observable for all yaw angles. The velocity magnitude and streamwise extent of this region decrease with increasing yaw angle. This flow behavior appears to result from the interaction of the free end trailing vortices shedding from the free end of the cylinder with the regular Karman vortices [67, 60]. Near the free-surface piercing end of the static cylinder, the streamlines are generally oriented perpendicular to the axis of the cylinder, and there is a local region of increased reverse flow velocity, which is presumably related to the turbulent wake at the air-water interface. It should be noted that the effect of the free surface on the near wake becomes less pronounced with increasing yaw angle, as apparent from the reduction in the extent of the negative velocity near the downstream end of the cylinder (in Figure 4.1 (b)).

Figure 4.1 (c) shows the contours of time-averaged normalized vorticity ($\langle \omega_y \rangle D/U_{\infty}$) for static yawed cylinder. From Figure 4.1 (c), it is apparent that for the static yawed cylinder, at all yaw angles considered, negative (counter-clockwise) vorticity is generated near the bottom free end, and it is associated with the separation of the incoming flow from the free end of the cylinder, as previously shown in Figures 4.1 (a) and (b). It is apparent that the

interaction of the free end trailing vortices with the Karman vortices [67] generates a positive (clockwise) vorticity region above this negative vorticity. As the yaw angle increases, this positive vorticity region is inclined in the spanwise direction and extends further downstream, immediately above and parallel to the negative vorticity region. This observation is aligned with the flow visualization results of Ramberg [8], which showed that, with the increase of the yaw angle, the vortex filaments near the free end form wavy lines that stream out behind the cylinder.

It has been previously shown that spanwise or axial flow plays a prominent role in the near-wake flow characteristics of a static yawed cylinder [44, 34, 42]. In this section, to investigate the spanwise (axial) flow behavior behind the static and yaw-oscillating cylinders, the X-direction (streamwise) velocity $\langle U \rangle$ and the (Z-direction) wall-normal velocity $\langle W \rangle$ components are projected on the spanwise direction of the cylinder at each yaw angle to obtain the axial velocity field ($\langle V_A \rangle = \langle W \rangle \cos\theta + \langle U \rangle \sin\theta$).

Figure 4.2 illustrates the contours of time-averaged normalized axial velocity ($\langle V_A \rangle / U_\infty$) for the static yawed cylinder. When the cylinder has no yaw ($\theta = 0^{\text{o}}$), a concentrated region of very high-amplitude, positive axial flow (with a direction towards the top end of the cylinder) is detectable at and in the vicinity of the free end of the cylinder. With increasing yaw, this high-amplitude axial velocity that originates from the free end of the cylinder gradually spreads in the wake along the span of the cylinder, approaching the free-surface piercing end of the cylinder. For instance, for $\theta = 30^{\text{o}}$, the magnitude of the axial velocity near the base of the cylinder ranges between $0.4U_\infty$ to $0.9U_\infty$ over nearly 90% of the span, which can be noticed immediately from the contour plots of Figure 4.2, where a dotted line highlights the contour levels of $\langle V_A \rangle / U_\infty = 0.4$. Additionally, in this symmetry plane, it can be seen that also a low-amplitude, opposite-direction axial flow develops behind a small portion of the cylinder in the vicinity of the free surface as a result of the downward flow that forms behind the cylinder due to the free surface effects [63]. Previous studies have shown the role of the axial flow immediately behind the cylinder in the breakdown and suppression of the Karman vortex shedding for the static yawed cylinders [44, 42, 40]. Comparing Figures 4.2 and 4.1
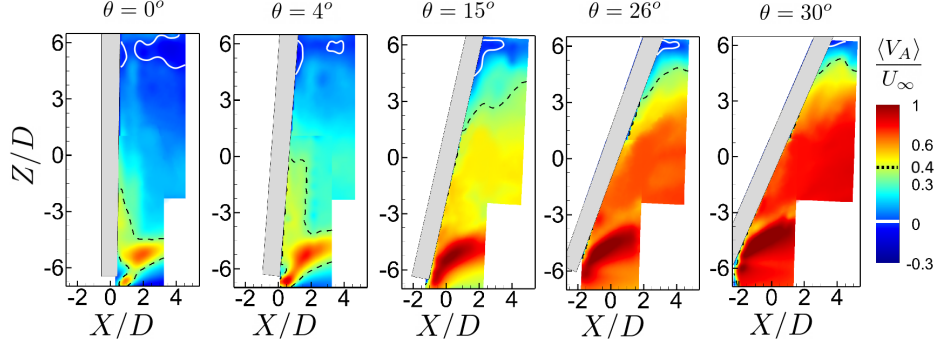
Figure 4.2: Contours of mean normalized axial velocity ($\langle V_A \rangle / U_\infty$) for the static cylinder at yaw angles of $\theta = 0^o$, 4°, 15°, 26°, and 30° at $\mathrm{Re} = 1.5 \times 10^4$ in symmetry plane at $Y/D = 0$. The contour levels of $\langle V_A \rangle / U_\infty = 0$ and 0.4 are shown by solid white and black dashed line, respectively.

(b) shows that, for the static cylinder, the gradual increase in the axial flow velocity and its spatial extent with increasing yaw angle comes together with a weaker and weaker reverse flow in the streamwise direction immediately behind the cylinder, which eventually leads to the complete elimination of the mean recirculation region over the majority of the span at $\theta = 30^o$.

4.1.2   Flow Structure in the (X,Y) Planes

The spanwise variation of the near wake flow topology for the static yawed cylinder can be examined by comparing the flow topology in different (X,Y) planes located along the span of the cylinder. In the present study, results are provided for three planes located at $Z/D = -3, 0$ (the mid-span plane), and 3 for the same yaw angles and Reynolds number as previously discussed. First, the flow behavior is shown for the mid-span plane and the results are then compared to the planes biased towards each end of the cylinder.

4.1.2.1   The Mid-Span Plane

Figure 4.3 shows the mean streamline topology ($\langle \psi \rangle$), normalized mean streamwise velocity ($\langle U \rangle / U_\infty$), and the normalized mean vorticity ($\langle \omega_z \rangle D/U_\infty$) in the near wake of the static
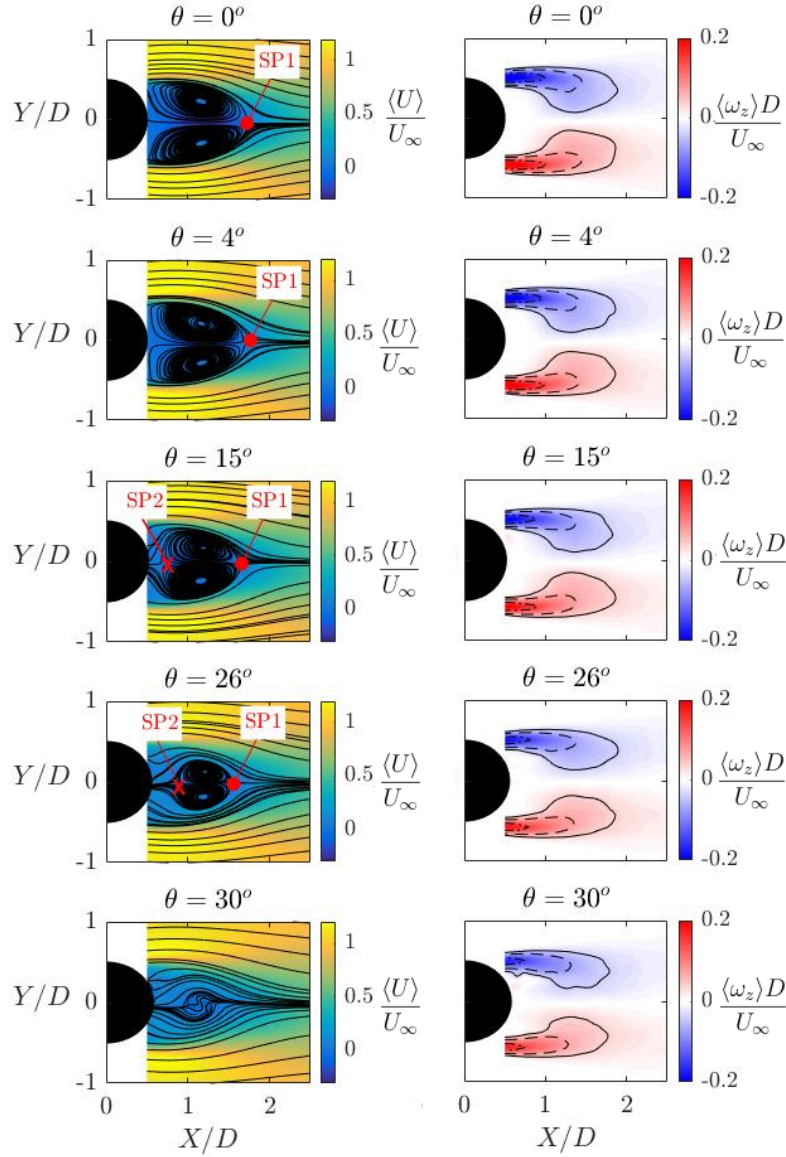
Figure 4.3: Mean flow streamline ($\langle\psi\rangle$) topology superimposed over contours of normalized mean streamwise velocity ($\langle U\rangle/U_\infty$) and the contours of the mean normalized vorticity ($\langle\omega_z\rangle D/U_\infty$) for static yawed cylinder at different yaw angles at Re $= 1.5 \times 10^4$. For the contours of $\langle\omega_z\rangle D/U_\infty$ given in the second column, the contour levels for the solid, dashed, and dash dot lines are ±0.025, ±0.05, ±0.1, respectively. In the patterns of $\langle\psi\rangle$, SP1 marks the saddle point formed at the closure of the mean recirculation region, while SP2 marks the saddle point formed between the base of the cylinder and the mean recirculation region.

cylinder. The first column of Figure 4.3 shows the mean streamline patterns superimposed over the color contours of the normalized mean streamwise velocity for the static cylinder at each yaw angle considered. The mean streamline topology for $\theta = 0^o$ depicts a pair of symmetric counter-rotating swirl patterns and a saddle point (SP1), which bounds the patterns of swirl streamlines. The observation appears similar to that reported earlier for the cylinder in cross-flow position [40, 34]. For small yaw angles, such as for $\theta = 4^o$, the streamline topology appears to be similar to that of the non-yawed case albeit the saddle point (SP1) is positioned nearer to the cylinder. For $\theta = 15^o$ an additional saddle point (SP2) is formed between the cylinder and the core of the recirculation region in the wake. The additional saddle point (SP2) indicates the presence of an axial flow [40] along the longitudinal axis of the cylinder, which is known to occur from the upstream to downstream end of yawed cylinders [86, 32, 40, 27], as previously shown in Figure 4.2. For $\theta = 26^o$, SP1 occurs further upstream while SP2 moves downstream such that the streamwise extent of the swirl area is reduced. For $\theta = 30^o$, the mean recirculation region appears to be suppressed significantly, which suggests a weakening of the vortex shedding. Notably, the wake appears more streamlined at high yaw. Axial flow, as shown in Figure 4.2, is known to decrease suction at the cylinder base, which leads to reduced drag in yawed cylinders [87, 34].

Variations in the shear layers on each side of the yawed cylinder are shown in the second column of Figure 4.3, using the normalized mean vorticity color contours overlaid by three contour lines at $\langle \omega_z \rangle D/U_\infty = \pm 0.025, \pm 0.05, \pm 0.1$ shown by solid, dash, and dash-dot lines, respectively. The length of the shear layers can be compared using the contour lines at ± 0.025. The length of the shear layers are almost similar for yaw angles from $\theta = 0^o$ to 26° and slightly decreased for $\theta = 30^o$. However, the tip of the contour lines of ± 0.025 are less curved toward the wake centerline and becomes thinner as the cylinder yaw angle becomes greater. Comparing contour lines of ± 0.1 indicates that as the cylinder is yawed, the region of high vorticity within the shear layers extends less downstream.

4.1.2.2 $Z/D = \pm 3$ Planes

Figure 4.4, for the non-yawed cylinder and the cylinder yawed to angles of $\theta = 15^{\text{o}}$ and 30°, illustrates the variation in the mean flow streamlines ($\langle \psi \rangle$) along with the contours of normalized mean streamwise velocity ($\langle U \rangle / U_\infty$) on three planes along the span of the cylinder, namely at $Z/D = -3$, 0, and 3. These planes are marked in Figure 3.3 (a). It is observed that the streamwise length of the mean recirculation region decreases as the free surface end of the cylinder is approached for $\theta = 0^{\text{o}}$ and 15°. For $\theta = 15^{\text{o}}$, the location of the additional saddle point (SP2) moves further downstream on planes near the upstream end. A similar discussion can be proposed for $\theta = 30^{\text{o}}$, where the suppressed mean recirculation region on $Z/D = -3$ and mid-span plane is recovered for $Z/D = 3$, which is nearer the downstream end. Najafi *et al.* [40] attributed such flow behavior to the onset of fluid movement in the streamwise direction (see Figure 4.2) in the vicinity of cylinder rear surface and the flow along the span from bottom free end to the top free surface-piercing end of the cylinder.

Figure 4.5 represents an average of the $Z/D = 3$ and $Z/D = -3$ planes shown previously in Figure 4.4. These results are remarkably similar to those obtained for $Z/D = 0$ (mid-span plane) in Figure 4.4. The contribution of each end condition on the wake structure of the mid-span plane is therefore approximately equal. However, at higher yaw angles, the averaged value of the wake appears to be biased toward the influence of the upstream end, which is supported by earlier published results [35, 39, 8], however, employing different end conditions. This result is further discussed in Chapter 5 concerning the effect of yaw oscillation.

4.1.3   Effect of End Conditions

The time-averaged wake closure points along the span of the cylinder yield a line, generally referred to as the demarcation line [81], which is shown in Figure 4.6 for the static yawed cylinder in the present study. The demarcation line represents the border of positive and negative mean streamwise velocity levels downstream of the cylinder. Analysis of the angle of inclination of the demarcation line is an appropriate technique to assess the uniformity
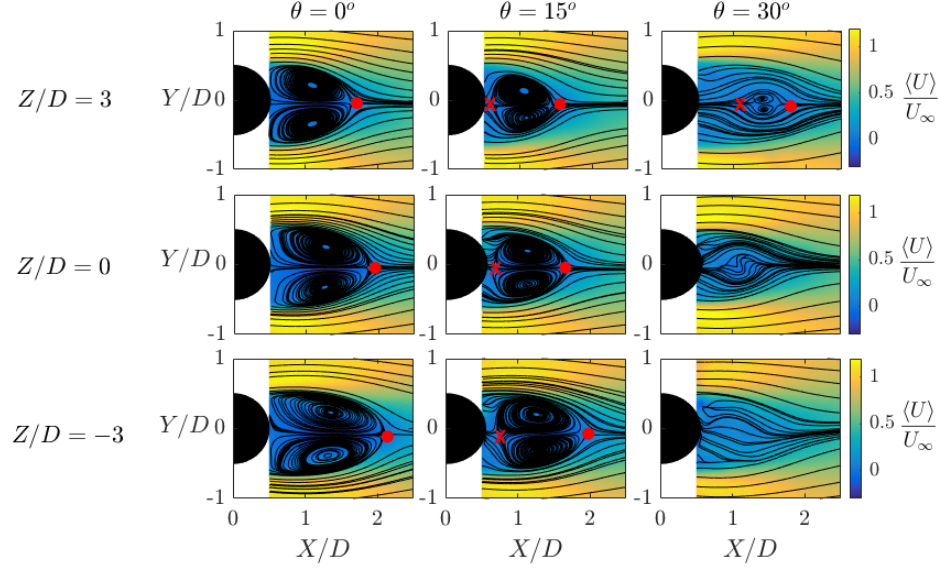
Figure 4.4: Mean flow streamline topology ($\langle\psi\rangle$) superimposed over contours of normalized mean streamwise velocity ($\langle U\rangle/U_\infty$) for three planes parallel to the bottom wall of the tunnel along the span of the static cylinder located at $Z/D = -3$, 0, 3 for yaw angles of $\theta = 0^o$, 15°, and 30° at $\mathrm{Re} = 1.5 \times 10^4$. The symbols represent saddle points as previously described in Figure 4.3.
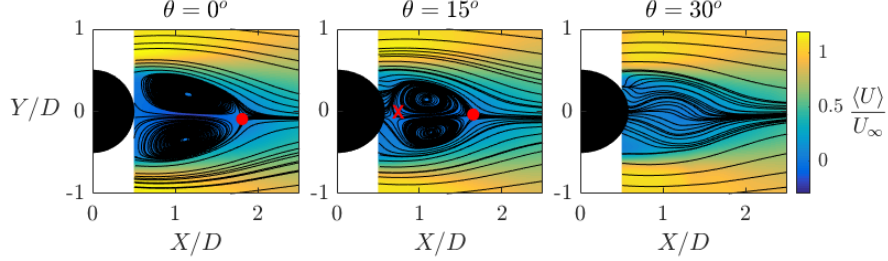
Figure 4.5: Average of streamwise flow for $Z/D = 3$ and $Z/D = -3$ planes, shown in Figure 4.4, for the static cylinder at $\theta = 0^o$, 15°, and 30°. The symbols represent saddle points as previously described in Figure 4.3.

of the flow along the span for time-averaged flow field results. Other methods exist for instantaneous data, such as based on streaklines detected using flow visualization (see for example Williamson [88]). For a two-dimensional wake, the demarcation line or the vortex filaments should be parallel to the longitudinal axis of the cylinder [32, 40, 89]. For the
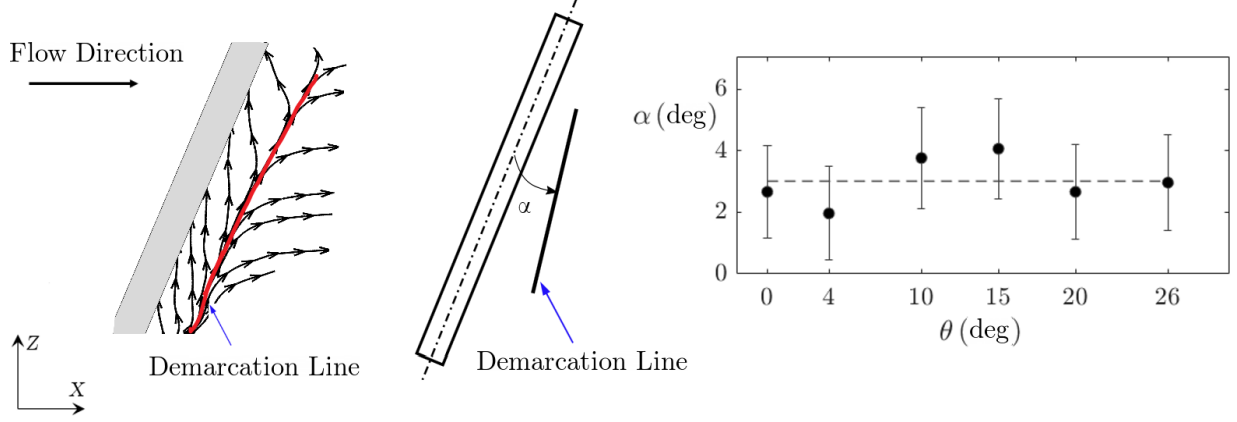
Figure 4.6: Schematic of the bifurcation line and corresponding measurements of α for the various yaw angles considered. The mean value of $\alpha = 3.8^{\rm o}$ is shown by the dashed line.

present study, a straight line was fitted to the wake closure points calculated from the planes at $Z/D = 3$, 0, and 3, and was used to determine the angle of inclination with respect to the cylinder. Figure 4.6 shows the calculated values of the demarcation line angle α (as defined by the schematic given in the same figure) with respect to the yaw angle and the uncertainty of this measurement (which was primarily related to the small number of points used for the assumed linear fit). The yaw-averaged value of the demarcation line angle (α) is approximately $3.2^{\rm o}$, as shown by the dashed line in Figure 4.6. For the range of yaw angles considered, the values of α remain approximately constant, (as seen in Figure 4.6) and the spanwise variation in the wake structure towards the free-surface piercing end offsets the variation towards the free immersed end of the cylinder at the mid-span (as seen in Figure 4.5), therefore, the competing influence of the end conditions may be assumed to be constant at the mid-span of the cylinder as it is yawed within the range considered.

4.2   Mean Wake Parameters

To quantitatively study the spanwise variation of the near wake flow of the static yawed cylinder, the streamwise velocity profiles on the wake centerline and across the wake are

compared for the three (X, Y) planes considered. For the mid-span plane, the wake parameters including the wake closure length and the wake width and the correlation between the two are compared in detail for different yaw angles. The variation of the wake closure length along the whole span of the cylinder is also provided for the static yawed cylinder.

4.2.1   Velocity Profiles

4.2.1.1   The Mid-Span Plane

The normalized mean streamwise velocity along the centerline of the wake for the case with $\theta = 0^{\text{o}}$ is plotted in Figure 4.7 in comparison to similar data found in the literature [83, 90]. These velocity profiles are plotted against X', which is the streamwise distance measured from the base of the cylinder along the wake centerline (that is, $X' = X - a/2$, where a is the semi-major axis of the cylinder cross-section at the visualization plane). While the results of the present study at $\text{Re} = 1.5 \times 10^4$ are in good agreement with those of McKillop and Durst [90] obtained at $\text{Re} = 1.4 \times 10^4$, the current results at $\text{Re} = 5 \times 10^3$ differ from those of Norberg [83] at the same Reynolds number. This disparity between the present results and those reported in Norberg presumably originates due to the differences in the following experimental parameters: i) length to diameter ratio of the cylinder (Norberg's cylinder had a length to diameter ratio of $L/D = 65$, whereas this ratio in the present study is $L/D = 13$), ii) the blockage ratio (Norbeg's study had a blockage ratio of 1.5%, while this value for the present study is 8%), and iii) cylinder end condition (Norberg's study used endplates, while the cylinder in the present work has free ends). On the other hand, these conditions in McKillop and Durst's study with a blockage ratio of 10% and aspect ratio of $L/D = 10$ are more similar to the conditions of the present work.

Figure 4.8 shows the evolution of the normalized mean streamwise velocity along the wake centerline for the static cylinder for the yaw angles of $\theta = 0^{\text{o}}$ to 30°. The maximum backflow velocity in the wake of the cylinder decreases with increasing yaw angle. Moreover, at the yaw angle of $\theta = 30^{\text{o}}$, the backflow is eliminated owing to the suppressed mean recirculation region,

apparent from the corresponding streamline patterns found in Figure 4.3. The wake closure length (L_c) normalized by the cylinder diameter (D) are $L_c/D = 1.18, 1.14, 1.07, 0.98$ for yaw angles of $\theta = 0^o, 4^o, 15^o$, and 26°, respectively. These results show a 20% decrease in the wake closure length from the non-yawed cylinder to the yaw angle of 26°.

The effect of yaw angle on the wake width can be seen in Figure 4.9, where the cross-stream profiles of the normalized mean streamwise velocity at two streamwise locations downstream of the cylinder are depicted for the yaw angles of $\theta = 0^o$ to 30°. For the top plot in Figure 4.9, $X/D = 1.5$ is located near the vicinity of wake closure whereas for the bottom plot $X/D = 2$ is downstream of the mean recirculation region. The characteristic features of these profiles are given in Table 4.1. At $X/D = 1.5$, the maximum velocity deficit ($\langle U_{d,max} \rangle$) decreases as the yaw angle increases. This indicates that the mean streamwise velocity increases in the near wake of the cylinder with yaw. The trend is consistent with the results shown in Section 4.1, where the increase in the mean streamwise velocity with increasing yaw angle was attributed to the increasing contribution of the axial flow to the velocity in the streamwise direction. As listed in Table 4.1, the minimum value of the mean streamwise velocity ($\langle U_{min} \rangle$) varies from $0.17U_\infty$ in the backflow direction for the non-yawed cylinder to streamwise velocity $0.08U_\infty$ in the inflow direction for $\theta = 30^o$. The maximum value of the mean streamwise velocity, $\langle U_{max} \rangle$ for most cases at $X/D = 1.5$ are around $1.1U_\infty$. $\langle U_{max} \rangle$ occurs at $Y/D = 0.65$, which is in
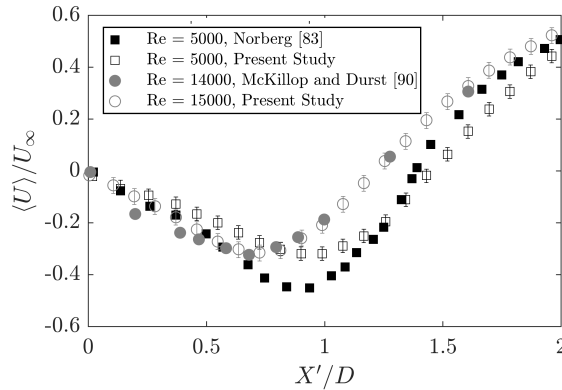
Figure 4.7: Comparison of the normalized mean streamwise velocity ($\langle U \rangle / U_\infty$) along the wake centerline for a cylinder with its longitudinal axis normal to the freestream (*i.e.*, $\theta = 0^o$).
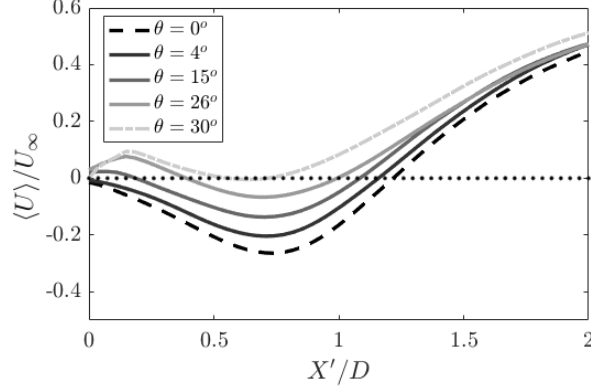
Figure 4.8: Normalized mean streamwise velocity ($\langle U \rangle / U_\infty$) along wake centerline for the static cylinder at yaw angles of $\theta = 0^\text{o}$, 4°, 15°, 26°, and 30°.

agreement with previously published data [83, 40].

Streamline patterns for all yaw angles (see Figure 4.3) show that $X/D = 2$ is located downstream of the wake closure point. Therefore, a local maximum value in the mean streamwise velocity previously identified in the similar plots at $X/D = 1.5$ does not occur. Comparing $\langle U_{max} \rangle$ values at $X/D = 2$ in Table 4.1 indicates that the maximum value of the mean streamwise velocity is 1% of the freestream velocity for all θ, while values higher than freestream velocity are shown at $X/D = 1.5$ at the same lateral position. As reported in Table 4.1, the highest velocity deficit still occurs for the non-yawed cylinder while the minimum velocity deficit occurs for a yaw angle of 30°. Comparing the half wake width values, the wake width at $X/D = 2$ is increasing with the yaw angle. The maximum value of half wake width occurs for $\theta = 30^\text{o}$ where it is approximately 8% higher than the non-yawed cylinder.

4.2.1.2 $Z/D = \pm 3$ Planes

Figure 4.10 shows the profiles of the mean normalized velocity ($\langle U \rangle / U_\infty$) for the static yawed cylinder for $\theta = 0^\text{o}$, 4°, 15°, 26° and 30° at Re $= 1.5 \times 10^4$. Results are shown on two spanwise locations along the span of the cylinder, namely at $Z/D = 3$ plane (top row) and $Z/D = -3$ plane (bottom row).

From the top row of Figure 4.10, it is apparent that in the $Z/D = 3$ plane, by increasing
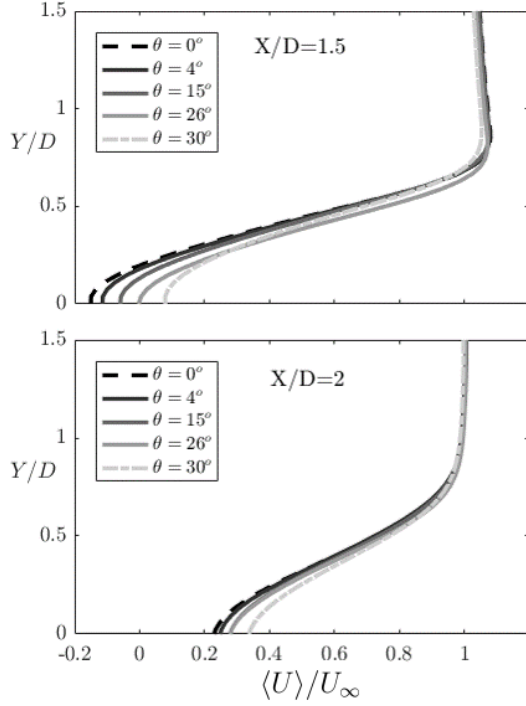
Figure 4.9: Normalized mean streamwise velocity ($\langle U \rangle / U_\infty$) at $X/D = 1.5$ (top) and $X/D = 2$ (bottom).

Table 4.1: The minimum and maximum values of the normalized mean streamwise velocity, and the maximum streamwise velocity deficit ($\langle U_{d,max} \rangle = U_\infty - \langle U(x,y) \rangle$) for static yawed cylinder at two different streamwise locations downstream of the cylinder.

| θ° | $X/D = 1.5$ | | | $X/D = 2$ | | | |
	$\dfrac{\langle U_{min} \rangle}{U_\infty}$	$\dfrac{\langle U_{max} \rangle}{U_\infty}$	$\dfrac{\langle U_{d,max} \rangle}{U_\infty}$	$\dfrac{\langle U_{min} \rangle}{U_\infty}$	$\dfrac{\langle U_{max} \rangle}{U_\infty}$	$\dfrac{\langle U_{d,max} \rangle}{U_\infty}$	$\dfrac{y_{1/2}}{D}$
0	-0.17	1.09	1.17	0.22	1.01	0.79	0.47
4	-0.13	1.08	1.13	0.24	1.01	0.76	0.49
15	-0.05	1.08	1.05	0.28	1.01	0.72	0.50
26	0.00	1.07	0.99	0.28	1.01	0.72	0.51
30	0.08	1.05	0.92	0.33	1.01	0.66	0.52

the yaw angle from $\theta = 0^o$ to 15°, the extent of the reverse flow region and the wake closure length decreases. Beyond $\theta = 26^o$, at $Z/D = 3$, it can be observed that a region of positive streamwise velocity occurs immediately behind the rear surface of the cylinder and the wake closure length increases. The highest positive streamwise velocity occurs at $\theta = 30^o$ while the reverse flow velocity on the wake centerline decreases to almost zero. In the $Z/D = -3$ plane, there is a similar trend of reduction in the extent of reverse flow region with increasing yaw angle, as shown in the bottom row of Figure 4.10. For yaw angles of $\theta = 26^o$ and 30°, the flow at the rear side of the cylinder experiences a no-reverse flow situation.
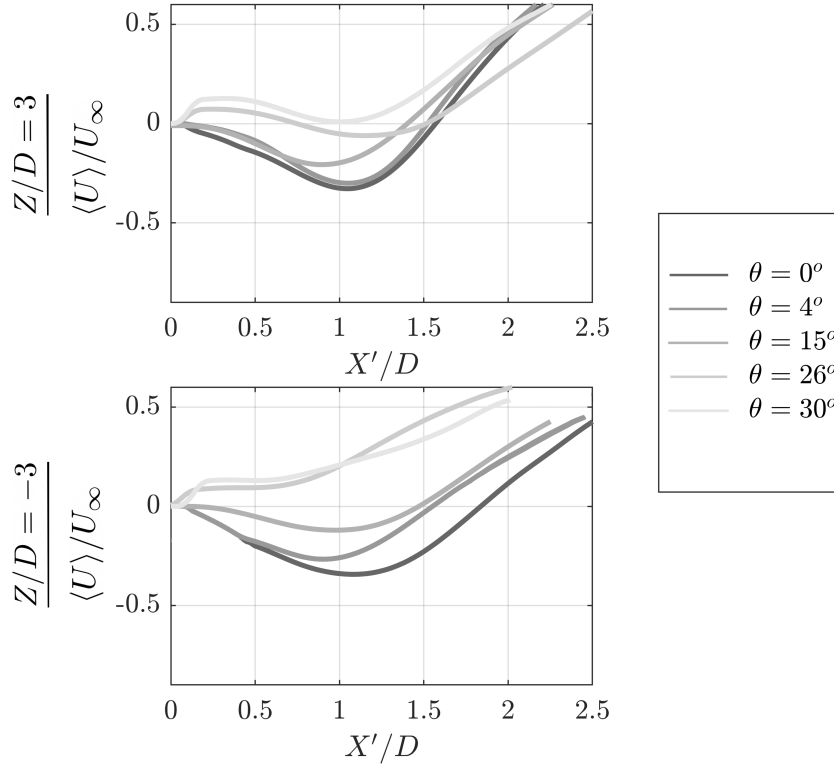
Figure 4.10: Profiles of mean normalized streamiwse velocity ($\langle U \rangle / U_\infty$) for the static yawed cylinder in $Z/D = 3$ plane (top) and $Z/D = -3$ plane (bottom) for yaw angles of $\theta = 0^o$, 4°, 15°, 26°, and 30° at Re $= 1.5 \times 10^4$.
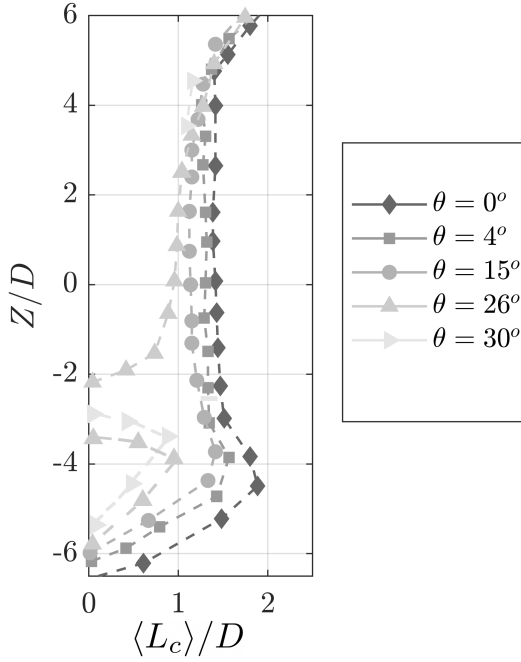
Figure 4.11: Spanwise variation of the mean wake closure length for static yawed cylinder ($\langle L_c \rangle / D$) for yaw angles of $\theta = 0^o$, 4°, 15°, 26°, and 30° at Re $= 1.5 \times 10^4$.

4.2.2 Spanwise Variation of Wake Closure Length

Figure 4.11 depicts the spanwise variation the time-averaged wake closure length ($\langle L_c \rangle$) for the static yawed cylinder at yaw angles of $\theta = 0^o$, 4°, 15°, 26°, and 30°. From profiles of Figure 4.11, it is evident that the wake closure length is almost constant along the majority of the span of the cylinder for the yaw angles of $\theta = 0^o$ to $\theta = 15^o$. For $\theta = 26^o$ and 30°, the wake closure length along the span of the cylinder is reported for two separated regions. The mean recirculation region between the two is shown to be suppressed. The extension of mean recirculation region suppression along the top half of the cylinder is remarkable at $\theta = 30^o$, where it only exists for regions between $Z/D = 3.5$ to 4.5. For all yaw angles, the wake closure length significantly decreases near the bottom end due to the interaction of the cylinder free end trailing vortices and the regular vortex shedding. Near the free surface-piercing end, the recirculation region is elongated downstream presumably under the impact of the free surface end condition. Figure 4.11 also reveals that the wake closure length along the span of the cylinder progressively decreases with increasing yaw angle for the static yawed cylinder. The results are consistent with the flow topology presented in Figure 4.1.

57

4.3   Vortex Shedding

4.3.1   The Mid-Span Plane

The vortex shedding is determined by obtaining the frequencies on the power spectral density function. The frequency of vortex shedding in the present work is presented in terms of the Strouhal number. Figure 4.12 (a) shows the velocity spectra at $X'/D = 2.0$ and $Y/D = 1.5$ for the static cylinder at different yaw angles. X', which is the streamwise distance from the base of the cylinder, is used to locate the probe at the same distance from the surface of the cylinder at all yaw angles. It is apparent that for all yaw angles there is a peak on the energy spectra that corresponds to the Strouhal number of vortex shedding. The value of St for each yaw angle is presented in Figure 4.12 (b). By increasing the yaw angle, the Strouhal number of vortex shedding decreases from around St $= 0.197$ for $\theta = 0^\text{o}$ to around St $= 0.175$ for $\theta = 30^\text{o}$. Similar trend in the vortex shedding frequency of the static yawed cylinders are can be seen in the literature [8, 32, 40, 91]. Moreover, Figure 4.12 (a) reveals that the height of the peak on the energy spectra is significantly reduced by increasing the yaw angle indicating the reduction in the vortex shedding intensity. At higher yaw angles, especially beyond $\theta = 15^\text{o}$, the width of the region centered about the peak on the spectra broadens with the yaw angle, which can be associated with the decorrelation or breakdown of the large organized structures [36, 32]. The disorganized vortex shedding is depicted by the instantaneous vorticity downstream the cylinder for $\theta = 0^\text{o}$ and 30° at the mid-span in Figure 4.13. The broadening of the peak and reduction in its magnitude is consistent with the variation of flow structure that was shown for the related PIV results previously presented in Figures 4.2 and 4.3, where increasing yaw angle led to suppression of swirl patterns due to the increase in the magnitude of positive axial velocity.

Applicability of the independence principle for the static yawed cylinder in the current study is examined from the ratio of St_N/St_o at each yaw angle and is shown in Figure 4.14. The Strouhal number of vortex shedding based on the normal component of the freestream is

given by St_N and St_o is the Strouhal number of vortex shedding at $\theta = 0º$, which is calculated to be around 0.203 in the current study at $\text{Re} = 1.5 \times 10^4$. In Figure 4.14, the results are compared to the literature for both static downstream (DY) and upstream (UY) yawed cylinders at subcritical flow. In case of validity of IP, the St_N/St_o should be equal to 1 at all yaw angles. For the present study, the St_N/St_o ratio is close to 1 up to $\theta = 20º$. For $\theta = 25º$ and $30º$, the results deviate from those predicted by the IP, which aligns with the other experimental results for finite cylinders obtained by Ramberg [8] and Zhou *et al.* [91]. This can be related to the change in the flow patterns at high yaw angles previously shown in Figure 4.3, namely an increase in the positive streamwise flow behind the cylinder and the reduction and eventually suppression of the swirl patterns. Interestingly, for an infinite yawed cylinder, the numerical flow simulation of Zhao *et al.* [32] are observed to indicate $\text{St}_N/\text{St}_o = 1$ even at the high yaw angles. The differences between the results shown in Figure 4.14 are presumably attributed to differences in the end conditions, blockage ratio, and the aspect ratio of the cylinder considered in each study. The impact of Reynolds number and aspect ratio on the vortex shedding of the static yawed cylinder will be examined later in Chapters 6 and 7, respectively.
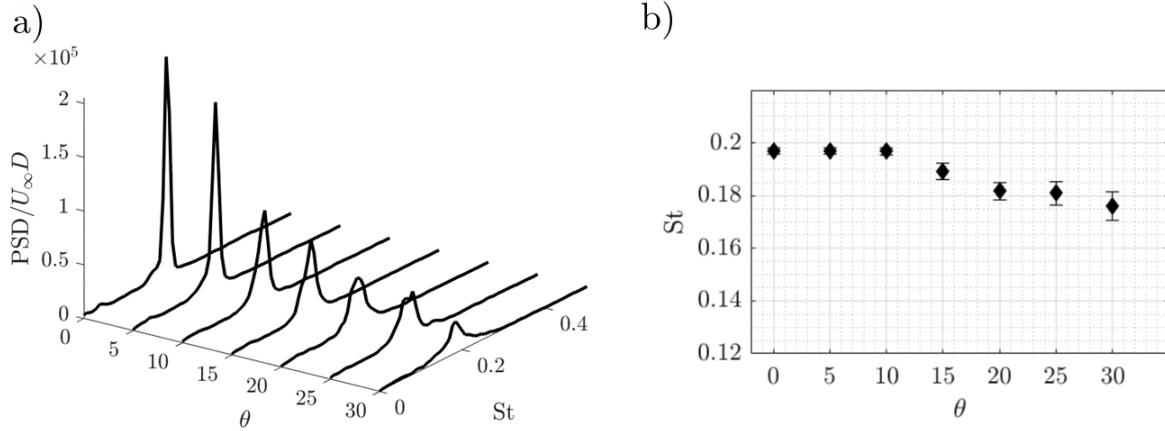
Figure 4.12:   a) Normalized power spectral density of the streamwise velocity for $X'/D = 2$ and $Y/D = 1.5$ for the static cylinder at different yaw angles. b) Variation of Strouhal number of vortex shedding with yaw angle at $\text{Re} = 1.5 \times 10^4$.
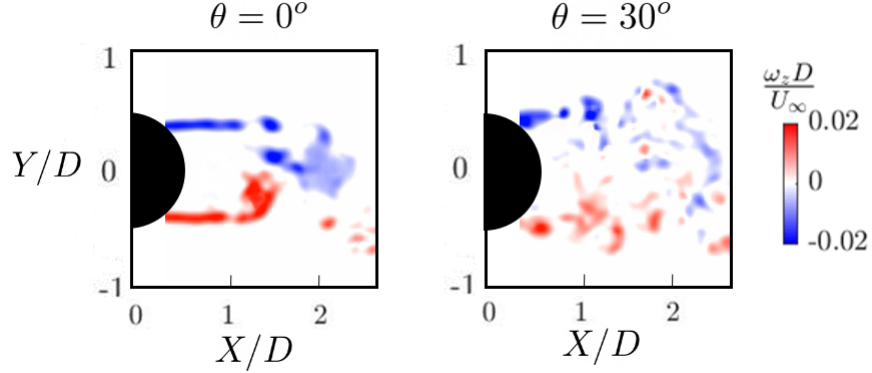
Figure 4.13: Instantaneous vorticty ($\omega_z D/U_\infty$) at the mid-span for the static cylinder at $\theta = 0^o$ and 30°.
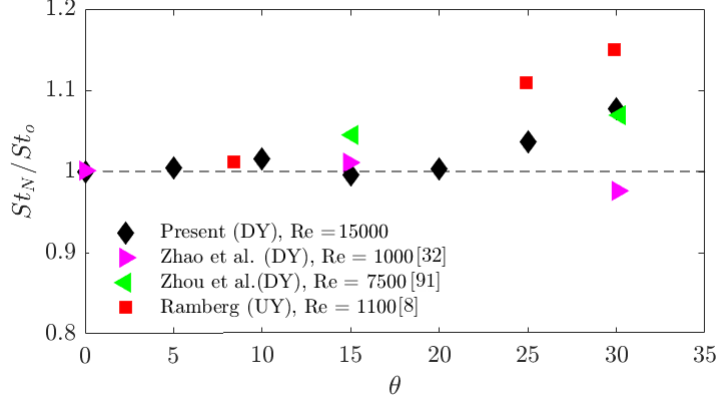
Figure 4.14: Variation of St_N/St_o with the yaw angle for the present work and other experimental and numerical studies. DY indicates the cases with the static cylinder inclined in the downstream direction and UY denotes the case with upstream yawed cylinder.

4.3.2 Spanwise Variation

In order to assess the variation of the vortex shedding frequency along the span of the static yawed cylinder, the probe was located at $X'/D = 2$ and $Y/D = 1.5$ and three spanwise locations of $Z/D = 3$, 0, -3. The spanwise variation of the streamwise velocity spectra at for the static cylinder at $\theta = 0^o$, 15°, and 30° are shown in Figure 4.15. It is apparent that the height of the peak region associated with vortex shedding decreases and it becomes further broadband towards the bottom free end. This is attributed to the effect of high-

magnitude positive axial flow generated from the upstream end that interferes and suppresses the organized vortex shedding, as previously demonstrated in Figures 4.4 and 4.2). The reduction in the energy of the peak and the enlargement in the width of the peak region at $Z/D = -3$ is more pronounced at the yaw angle of $\theta = 30^o$, which indicates the significant mitigation of the vortex shedding near this region. However, it is apparent that even for $\theta = 30^o$, the vortex shedding is recovered downstream the top half of the cylinder at $Z/D = 3$. This is consistent with the PIV results previously shown in Figure 4.1 and 4.11 in which the mean recirculation region is suppressed significantly along the bottom half of the span up to around $Z/D = 3$ and is recovered up to around $Z/D = 4.5$. Figure 4.15 also indicates that the Strouhal number of vortex shedding decreases for the plane closer the bottom free end. The values Strouhal number of vortex shedding along the span of the cylinder for yaw angle of $\theta = 15^o$ are presented in this figure as an example. It is shown that the Strouhal number decreases from St $= 0.197$ at $Z/D = 3$ to St $= 0.184$ at $Z/D = -3$. The reduction in the Strouhal number closer to the free end of the static cylinder is in agreement with the trend provided in the literature [39, 60].
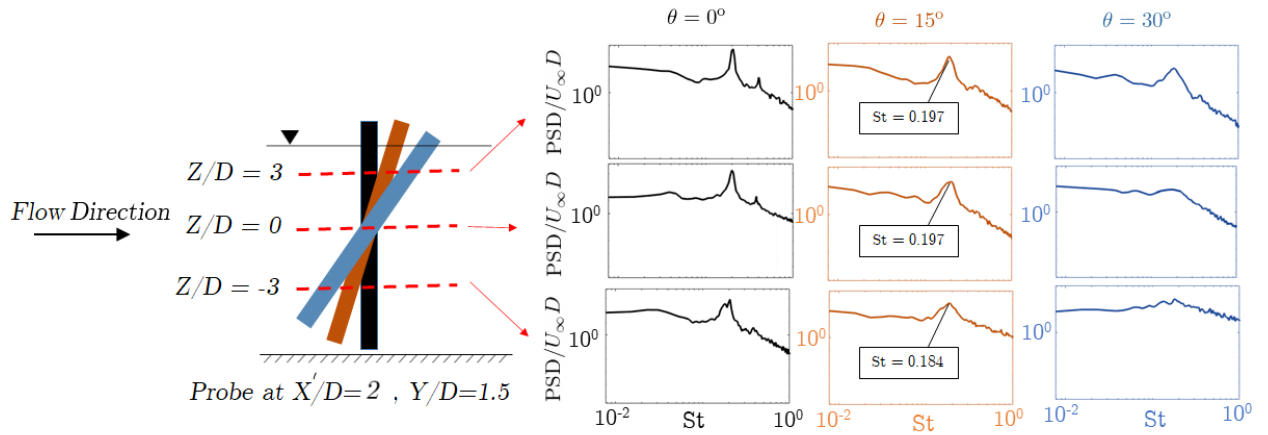
Figure 4.15: Spanwise variation of the streamwise velocity spectra for the static cylinder at $\theta = 0^o$, 15°, and 30°.

4.4   Chapter Summary

In this chapter, the near wake of the static yawed cylinder at Reynolds number of 1.5×10^5 with $L/D = 13$ were studied. The range of yaw angle varied between $\theta = 0^\text{o}$ to 30°. It was shown that by increasing the yaw angle, the streamline patterns downstream the cylinder becomes further parallel to the axis of the cylinder, except for the regions in the vicinity of both ends that are under the impact of the free-surface near the top and the free-end trailing vortices at the bottom. Results revealed that the magnitude of the reverse flow velocity within the mean recirculation region decreases with yaw angle and at high yaw angle of $\theta = 30^\text{o}$, the suppression of the mean recirculation region was observed along the majority of the span that could result in lower drag. Studying the variation of axial velocity, it was observed that the increase in the magnitude of axial flow generated from the bottom free end of the cylinder is the dominant factor that led to the spanwise variations in the near wake of a yawed cylinder.

Evaluation of the vortex shedding behavior showed that the high-magnitude axial flow reduces the mixing between the separating shear layers and leads to a less periodic vortex shedding at lower frequencies for high yaw angles. Investigation of the validity of the IP for the static cylinder indicated that it did not apply beyond $\theta = 20^\text{o}$.

Chapter 5

Results: Effect of Reduced Frequency

The near wake of the cylinder undergoing yaw oscillation over a range of reduced frequencies is examined for the cylinder with $L/D = 13$ at $\mathrm{Re} = 1.5 \times 10^4$. A comparison is made between the near wake flow characteristics of a yaw-oscillating cylinder and the baseline stationary counterpart at corresponding yaw angles previously discussed in Chapter 4. First, the effect of yaw oscillation on the flow characteristics is studied from the phase-averaged perspective in the (X, Z) planes at specific yaw angles. Next, the phase-averaged and yaw-averaged data are used to evaluate the influence of reduced frequency on flow topology and the wake parameters in the (X, Y) planes. Finally, the time-resolved results are used to assess the variation of vortex shedding frequency with the yaw oscillation of the cylinder.

5.1   Flow Structure in the (X, Z) Symmetry Plane

Phase-averaged streamline topology ($\langle \psi_\phi \rangle$) and contours of normalized streamwise velocity ($\langle U_\phi \rangle / U_\infty$) for the yaw-oscillating cylinder at different oscillation frequencies ranging from $K = 0.5$ to 1.3 in the (X, Z) plane are shown in Figures 5.1 and 5.2, respectively. The time-averaged results for the static cylinder at yaw angles corresponding to each phase are given in the first row of Figures 5.1 and 5.2.

    Figure 5.1 indicates that when the cylinder undergoes yaw-oscillations, the flow patterns
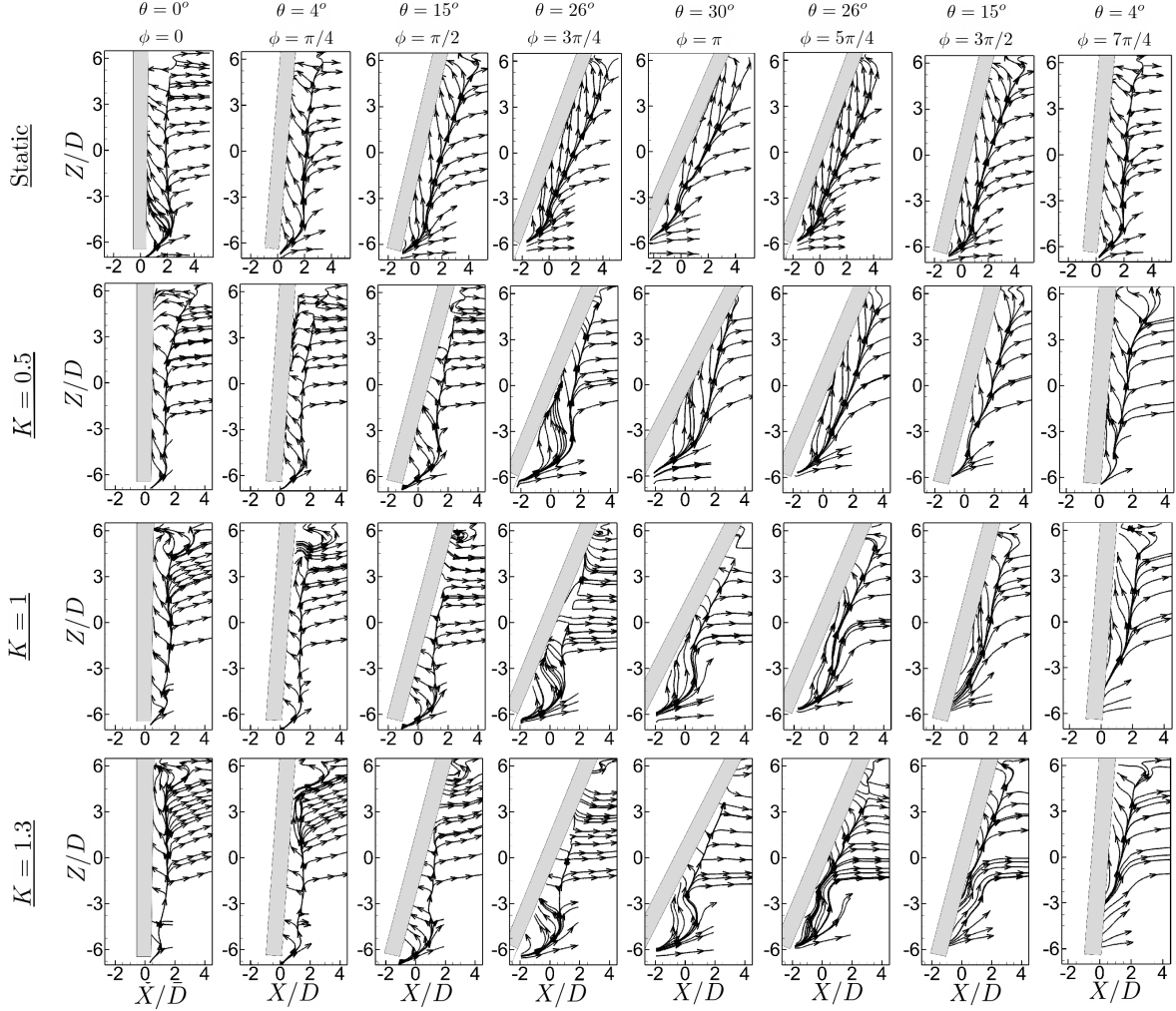
Figure 5.1: Phase-averaged streamline topology ($\langle\psi_\phi\rangle$) for the static yawed cylinder and the yaw-oscillating cylinder at various reduced frequencies with $K = 0.5$, 1, and 1.3 in the $Y/D = 0$ symmetry plane for eight discrete phases over a complete oscillation cycle at Re $= 1.5 \times 10^4$. The time-averaged results for the static yawed cylinder at corresponding yaw angles are given in the first row.

deviate from the corresponding flow patterns of the static cylinder, and this discrepancy becomes even more substantial with increasing reduced frequency. During the first half of an oscillation cycle (from $\phi = 0$ to $\phi = \pi$), the $\langle\psi\rangle$ patterns in Figure 5.1 show that as the yaw angle increases, the near-wake region around the top-middle section of the yaw-oscillating cylinders (centered about $Z/D = 3$) shows a reduction in the streamwise extent of the mean recirculation region, which generally becomes suppressed by increasing the reduced frequency.

The mean recirculation region in this region elongates gradually back in the second half of the cycle (from $\phi = \pi$ to $7\pi/4$) as the cylinder returns to the non-yawed position. On the other hand, flow patterns near the bottom half of the yaw-oscillating cylinders exhibit the opposite trend. That is, the reverse flow region elongates in the streamwise direction in the first half of the oscillation cycle, whereas it shrinks or becomes eliminated in the return cycle. Additionally, at the phase of $\phi = 3\pi/4$, the streamlines within the mean recirculation region on the lower half of the cylinder (centered around $Z/D = -4.5$) start getting further directed towards the downstream end for all reduced frequencies. This tendency in the near-wake streamlines extends to a larger section of the cylinder span for the following phases up to $\phi = 3\pi/2$. This observation in streamline patterns is associated with the presence of a large-magnitude axial flow around the same region, which will be discussed later.

In Figure 5.2, contours of phase-averaged streamwise velocity for the yaw-oscillating cylinder with a reduced frequency of $K = 0.5$ show that the negative streamwise velocity in the upper half of the cylinder (centered about $Z/D = 3$) gradually decreases in magnitude in the first half of the oscillation cycle from $\phi = 0$ to π. This result may be attributed to the positive streamwise thrust added to the fluid behind the cylinder by the same direction movement of the cylinder's top half. For higher reduced frequencies of $K = 1$ and 1.3 and at $\phi = \pi/4$, the significant increase in the streamwise thrust of the fluid, induced by the positive-direction motion of the cylinder combined with the large acceleration in the cylinder's top half, leads to suppression in the mean recirculation region near the top of the cylinder (around $Z/D = 5$). At this phase, the increase in the spanwise extent of this suppression when the reduced frequency is increased from $K = 1$ to 1.3 is presumably a result of the increase in the acceleration of the cylinder motion with increasing oscillation frequency. This suppression spreads to a larger spanwise region in the top half of the cylinder (centered around $Z/D = 3$) when the cylinder reaches $\phi = \pi/2$ for both $K = 1$ and 1.3. Although for the low reduced frequency of $K = 0.5$, the magnitude of reverse velocity keeps decreasing gradually near the top half of the cylinder continues to move in the positive X-direction as the oscillation phase of the cylinder passes from $\phi = 3\pi/4$ and reaches $\phi = \pi$, for the higher reduced frequencies of
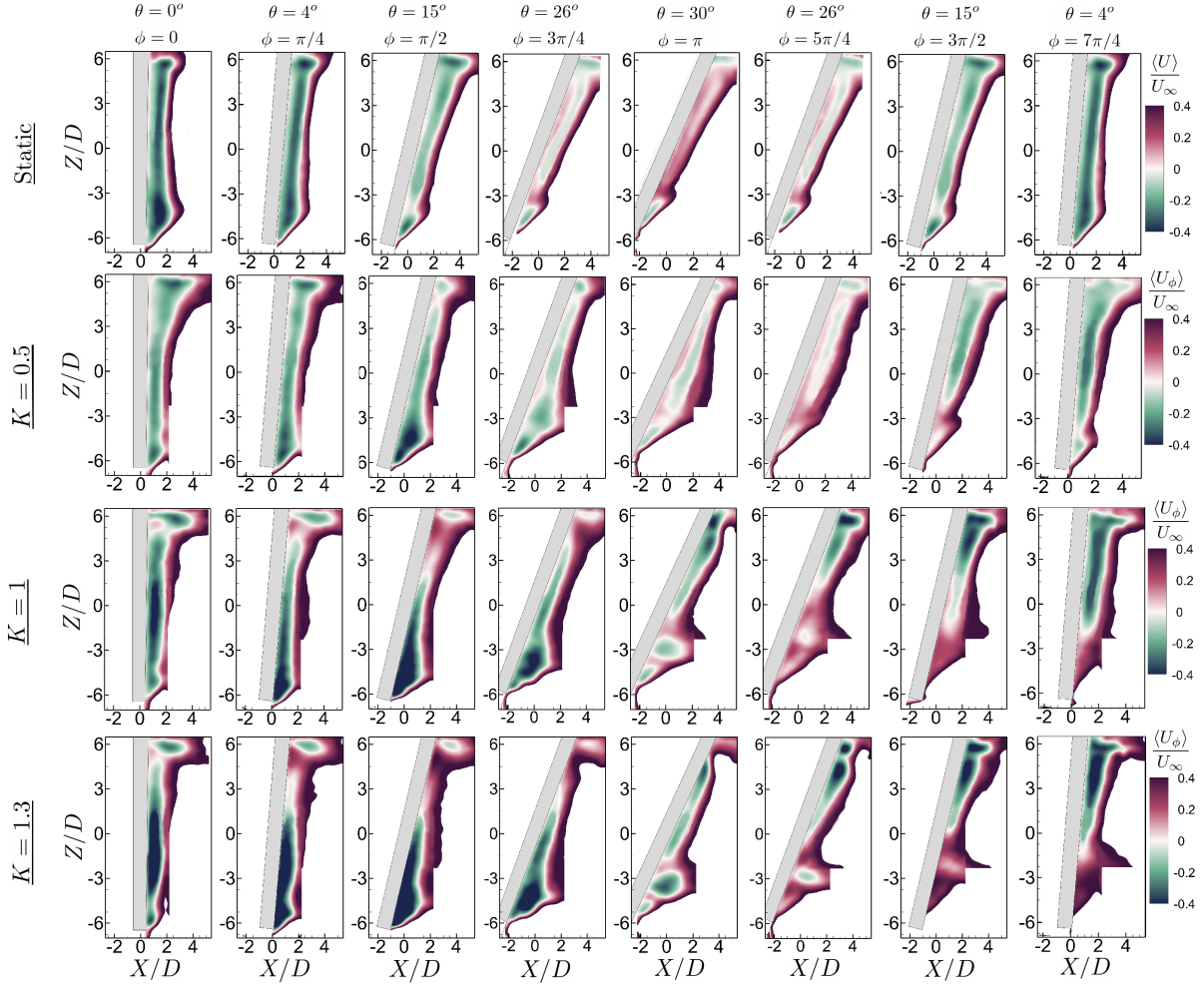
Figure 5.2: Contours of normalized phase-averaged streamwise velocity ($\langle U_\phi \rangle / U_\infty$) for the static yawed and the yaw-oscillating cylinder at various reduced frequencies of $K = 0.5$, 1, and 1.3 in the $Y/D = 0$ symmetry plane for eight discrete phases over a complete oscillation cycle at $\mathrm{Re} = 1.5 \times 10^4$. The time-averaged results for the static yawed cylinder at corresponding yaw angles are given in the first row.

$K = 1$ and 1.3, the cylinder deceleration at these phases leads to a recovery in the negative streamwise velocity and a local resurgence of the mean recirculation region in the wake of the upper half of the cylinder for the same phases. From these trends, it appears that the acceleration or deceleration of the cylinder during its yaw oscillation influences the near wake in the top half span notably only at moderate reduced frequencies ($K = 1$ and 1.3). In the return cycle, as the top half of the cylinder moves against the freestream direction,

the magnitude and the streamwise extent of the reverse flow region gradually increase for all the reduced frequencies. However, the start of this increase in the magnitude of the negative streamwise velocity is delayed to $\phi = 3\pi/2$ for $K = 0.5$ due to the development of a very high-magnitude positive axial flow in the top half of the cylinder at earlier phases of the return cycle, which will be shown in Figure 5.4. Note that the increase in the negative streamwise velocity in the direct vicinity of the cylinder top end at each phase is related to the effect of the free surface, which becomes more pronounced with increasing reduced frequency.

Contours of $\langle U_\phi \rangle / U_\infty$ in Figure 5.2 reveal that for all the yaw-oscillating cylinders during the movement of the bottom half of the cylinder against the inflow direction, the peak magnitude of the reverse flow behind the bottom half of the cylinder (near $Z/D = -3$) first gradually increases from $\phi = 0$ to $\pi/2$, and then breaks up and gradually decreases from $\phi = \pi/2$ to π. This reduction in the reverse flow velocity from $\phi = \pi/2$ to π is presumably related to the increase in the spanwise flow near the lower half of the cylinder (discernable from the $\langle \psi \rangle$ patterns given earlier in Figure 5.1 and from the axial velocity distributions to be discussed later in Figure 5.4. The deceleration in the cylinder motion as it moves from $\phi = \pi/2$ to π might also contribute to this trend. In the return cycle of the yaw-oscillating cylinders, as the movement of the bottom half of the cylinder is reversed so that it moves in the inflow direction, the induced positive-direction streamwise thrust on the fluid by the bottom half of the moving cylinder and the increase in the spanwise flow leads to the gradual decrease or even local disappearance of the reverse velocity from $\phi = \pi$ to $5\pi/4$ around the lower half of the cylinder for all reduced frequencies. In the return cycle from $\phi = 3\pi/2$ to $7\pi/4$, although the increase in the magnitude and extent of the reverse flow seen in the top half gradually spreads to almost the entire lower half of the cylinder for the lower reduced frequency of $K = 0.5$, for higher reduced frequencies, with the deceleration of the cylinder, the resurgence of the reverse flow in the lower half mainly occurs near the top end of the lower half.

Figure 5.3 shows the contours of phase-averaged normalized vorticity ($\langle \omega_{y,\phi} \rangle D/U_\infty$) for
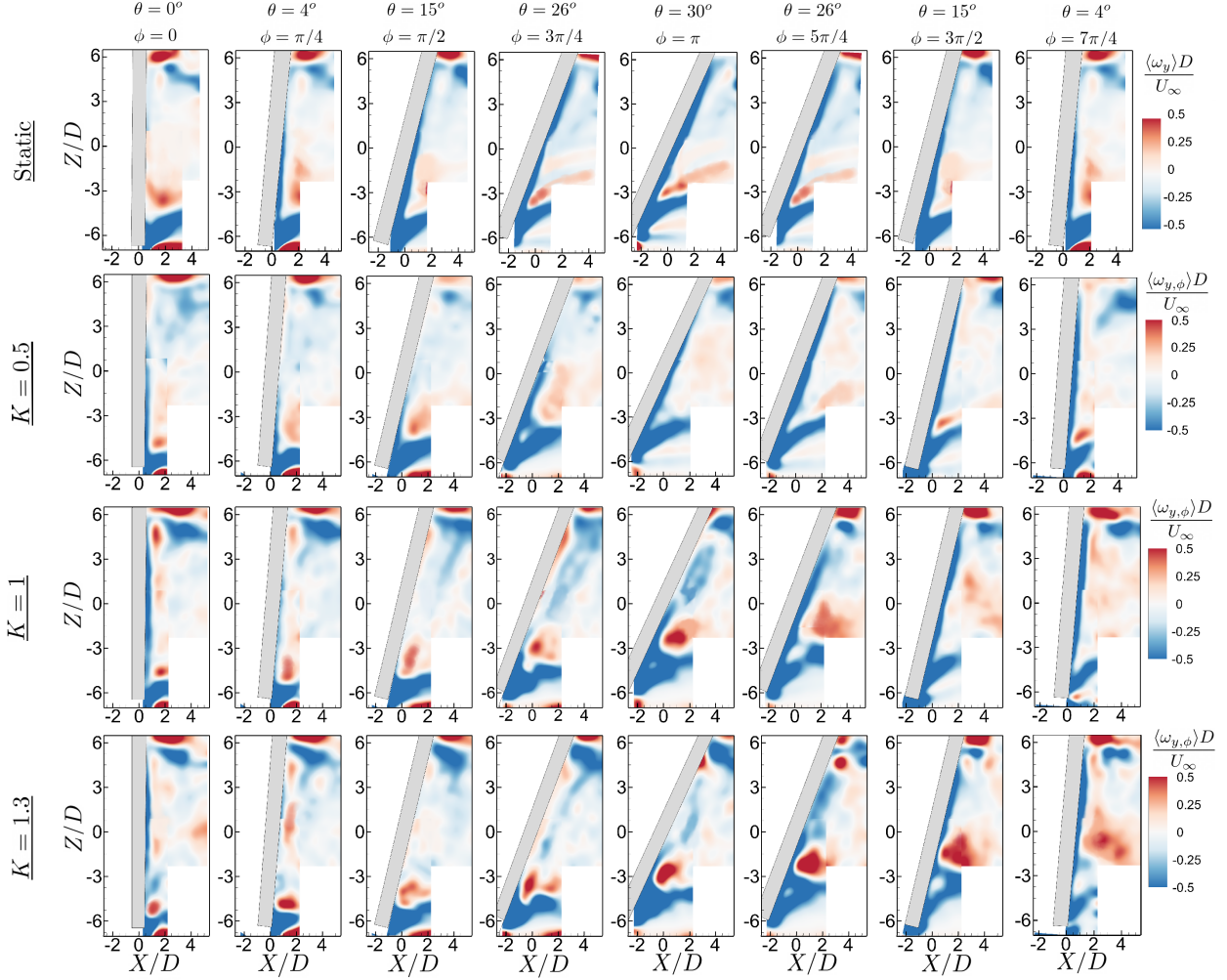
Figure 5.3: Contours of normalized phase-averaged vorticity ($\langle\omega_{y,\phi}\rangle D/U_\infty$) for the static yawed and the yaw-oscillating cylinder at various reduced frequencies of $K = 0.5$, 1, and 1.3 in the $Y/D = 0$ symmetry plane for eight discrete phases over a complete oscillation cycle at $\mathrm{Re} = 1.5 \times 10^4$. The time-averaged results for the static yawed cylinder at corresponding yaw angles are given in the first row.

the yaw oscillations at various reduced frequencies. Time-averaged results ($\langle\omega_y\rangle D/U_\infty$) for the static yawed cylinder are also shown as a reference for comparison. Figure 5.3 reveals that the flow in the near-wake is strongly three-dimensional. Similar to the observation made for the static cylinder, the negative vorticity still occurs near the bottom free end of the yaw-oscillating cylinders all along their oscillation period. However, contrary to the results of the statically yawed cylinder, the positive vorticity is not always located near the

bottom end of the oscillating cylinder, but rather it is spread both in the spanwise and the streamwise directions depending on the phase of the oscillation. As the reduced frequency of oscillations increases, the peak magnitude of positive vorticity increases for a given phase, and its ascend towards the mid-span section in the return cycle is delayed. In the return cycle, the positive vorticity dissipates while it ascends towards the middle section of the cylinder. This dissipation in the peak clockwise vorticity initiates starting from $\phi = 5\pi/4$ for $K = 1$, whereas it is delayed until $\phi = 3\pi/2$ for $K = 1.3$.

Figure 5.4 illustrates the contours of time-averaged normalized axial velocity ($\langle V_A \rangle / U_\infty$) for the static yawed cylinder and contours of phase-averaged normalized axial velocity ($\langle V_{A,\phi}/U_\infty \rangle$) for the yaw-oscillating cylinder at three reduced frequencies of $K = 0.5$, 1, and 1.3 obtained in the symmetry plane. A general inspection of Figure 5.4 for the yaw-oscillating cylinders demonstrates a substantial spanwise variation for the axial flow, which is strongly dependent on the oscillation phase and the frequency of oscillations. For $K = 0.5$, the moderate levels of positive axial flow, detected near the vicinity of the bottom end of the cylinder at $\phi = 0$, increases progressively both in magnitude and extent, spreading towards the upper sections of the wake, with increasing yaw angle during the first half of the oscillation cycle from $\phi = 0$ to π. The extent of the axial flow reaches its maximum at $\phi = 5\pi/4$ and $3\pi/2$. At $\phi = 7\pi/4$, which is when the cylinder is about to return to its non-yawed position, this upward axial flow in the near-wake and along the span of the cylinder decreases significantly. On the other hand, a weak negative axial flow (oriented from the top to the bottom end of the cylinder) emerges at $\phi = 0$ to $\pi/2$ locally behind the upper half of the cylinder (within $Z/D > 0$), as can be distinguished through the solid white line marking the $\langle V_{A,\phi} \rangle / U_\infty = 0$ level in the contour patterns (*i.e.*, the border between the negative and positive contour levels). This weak negative axial flow eventually recedes at $\phi = 3\pi/4$, becoming constrained to a very small spanwise region near the free surface before completely disappearing in the following phases of oscillation.

For moderate reduced frequencies of $K = 1$ and 1.3, in the first half of the oscillation cycle, with increasing yaw angle from $\phi = 0$ to $3\pi/4$, the low-magnitude, negative axial velocity
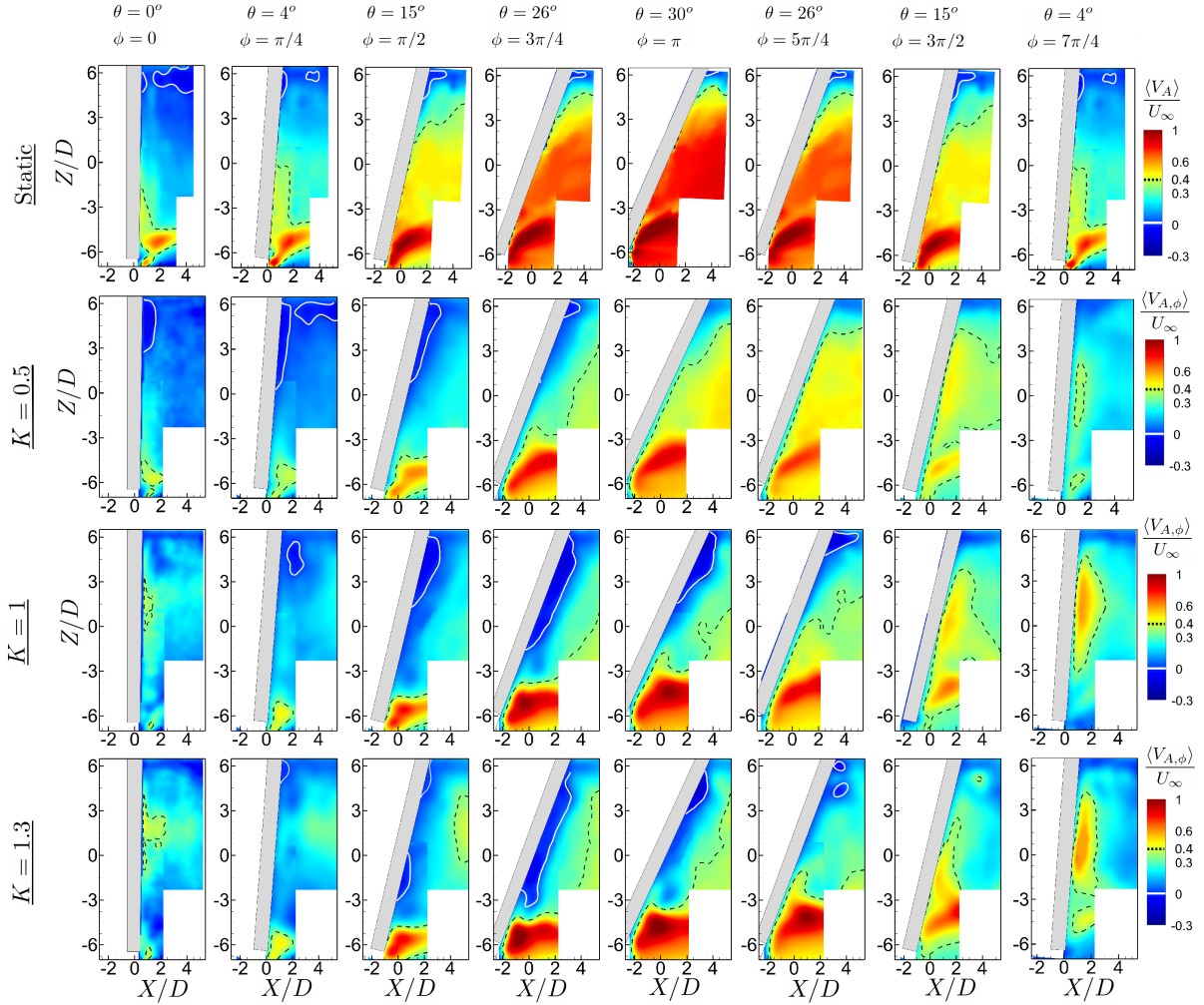
Figure 5.4:   Contours of normalized phase-averaged axial velocity ($\langle V_{A,\phi} \rangle / U_\infty$) for the static yawed cylinder and the yaw-oscillating cylinder at various reduced frequencies of $K = 0.5$, 1, and 1.3 in the $Y/D = 0$ symmetry plane for eight discrete phases over a complete oscillation cycle at $\mathrm{Re} = 1.5 \times 10^4$. The time-averaged results for the static yawed cylinder at corresponding yaw angles are given in the first row. The contour levels of $\langle V_{A,\phi} \rangle / U_\infty = 0$ and 0.4 are shown by white solid line and black dashed line, respectively.

region prevalent near the top end of the cylinder at the early oscillation stage of $\phi = \pi/4$, extends toward the lower sections of the span with increasing yaw angle until the phase of $\phi = 3\pi/4$. The negative axial velocity levels reach up to $Z/D = -1.5$ and -2 in the lower half of the cylinder wake when the cylinder is at $\phi = 3\pi/4$ for $K = 1$ and 1.3, respectively. Notice that this trend of increasing extent in the low-amplitude downward-oriented flow toward the lower sections of the span with increasing yaw angle is the direct opposite of what was

observed at the lower reduced velocity of $K = 0.5$ and may be attributed to the dominance of the downward motion of the flow near the upper half of the span under the effect of the cylinder's downstream movement (see Figure 5.1). This low-amplitude downward axial flow clashes with the opposite-direction axial flow that originates from the free lower end of the cylinder and prevents the upward axial flow from being expanded over the entire span. Near the lower end of the cylinder, the upward oriented axial flow is generated at moderate levels starting from $\phi = 0$. This positive axial flow becomes stronger and stronger in magnitude as the phase of oscillation advances in the first half of the oscillation cycle up until $\phi = \pi$. In the first half of oscillations, the positive (upward-oriented) axial velocity near the bottom free end of the cylinder for $K = 1$ and 1.3 appears to be higher in magnitude than those seen for $K = 0.5$. The spread of the positive axial flow over the span of the cylinder becomes notable for $K = 1$ and 1.3 in the return cycle from $\phi = \pi$ to $7\pi/4$. In the last quarter cycle of oscillations, from $\phi = 3\pi/2$ to 0, both the spanwise extent and the magnitude of the positive axial flow undergoes a reduction. The remnants of the strong positive axial flow can still be observed around the middle section of the cylinder at $\phi = 0$. Comparing the results of the yaw-oscillating cases in Figure 5.4, where contour levels of $\langle V_{A,\phi} \rangle / U_\infty = 0.4$ are highlighted by a dotted line, it can be noticed that with increasing reduced frequency, the development of a strong positive axial flow over the span of the cylinder is delayed. For instance, the positive axial velocity of around $0.4U_\infty$ and higher occurs behind the mid-span of the cylinder for the first time at $\phi = \pi$ for $K = 0.5$, whereas it is delayed to $\phi = 5\pi/4$ and $3\pi/2$ for $K = 1.0$ and 1.3, respectively.

5.2   Flow Structure in the (X,Y) Planes

The near-wake flow in the (X,Y) planes, namely at the mid-span and the $Z/D = \pm 3$ planes is studied in this section. First, the results at the mid-span are evaluated from the time-averaged perspective and then the phase-averaged technique is used to study the flow at discrete phases at the mid-span and $Z/D = \pm 3$ planes.

5.2.1 Yaw-Averaged Near Wake Flow Topology in the Mid-Span Plane

For the yaw-oscillating cylinders, the yaw-averaged near-wake results at a given oscillation frequency are determined from the average of the velocity field over 4000 consecutive snapshots, which covers at least 40 complete cycles of yaw oscillation. In contrast, for the static cylinder, the yaw-averaged results are determined by averaging the time-averaged velocity data of 12 discrete yaw angles from $\theta = 0^{\mathrm{o}}$ to 30°. Note that, hereafter, the symbols signifying the quantities corresponding to the yaw-averaged data are given a subscript of θ to denote the applied averaging procedure. The left column of Figure 5.5 depicts the yaw-averaged streamline topology ($\langle \psi_\theta \rangle$) superimposed over the contours of the normalized yaw-averaged streamwise velocity ($\langle U_\theta \rangle / U_\infty$) for both the stationary yawed cylinder and the cylinder undergoing yaw oscillations at various oscillation frequencies ranging from $K = 0.25$ to 1.3 at $\mathrm{Re} = 1.5 \times 10^4$. From these plots, it is apparent that the counter-rotating swirl patterns remain visible for each of the cases. However, with increasing reduced frequency, the core of these swirl patterns gradually approaches the base of the cylinder, and the streamwise extent of the swirls decreases. This effect is further shown by the upstream relocation of saddle points SP1 and SP2 with reduced frequency. For higher reduced velocities of $K = 1$ and 1.3, SP2 is not detectable. As indicated earlier in Section 4.1.2.1, the existence of SP2, which is the saddle point between the base of the cylinder and the mean recirculation region, is related to the presence of an axial flow along the longitudinal axis of the cylinder. The observed disappearance of this saddle point at high-frequency yaw oscillations (*i.e.*, $K = 1$ and 1.3) may be related to the weakening of the axial flow in the spanwise direction.

The corresponding contours of normalized yaw-averaged vorticity ($\langle \omega_{z,\theta} \rangle D / U_\infty$) are presented in the right column of Figure 5.5. In these plots, the contour levels of $\langle \omega_{z,\theta} \rangle D / U_\infty = \pm 0.025$, ± 0.05, ± 0.01 are specified by the solid, dash, and dash-dot lines, respectively. Note that the lowest of these three highlighted vorticity levels ($\langle \omega_{z,\theta} \rangle D / U_\infty = \pm 0.025$) is approximately 10% of the maximum vorticity in the field of view. A comparison of the
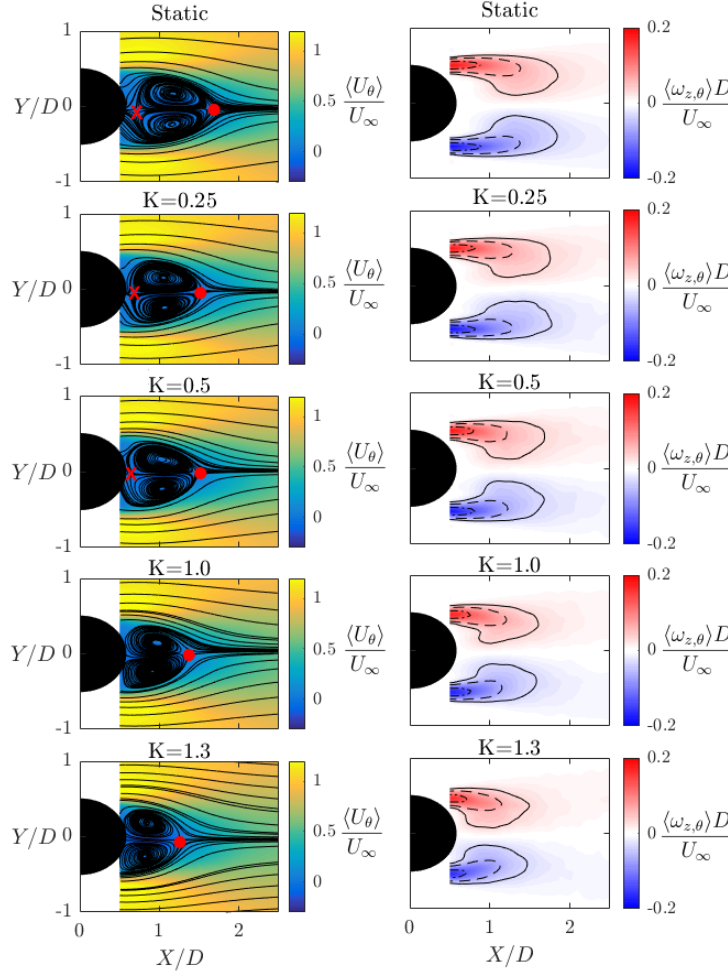
Figure 5.5: Yaw-averaged streamline ($\langle\psi_\theta\rangle$) topology superimposed over the normalized yaw-averaged streamwise velocity ($\langle U_\theta\rangle/U_\infty$) and the contours of the yaw-averaged normalized vorticity ($\langle\omega_{z,\theta}\rangle D/U_\infty$) for static yawed and yaw-oscillating cylinder at reduced frequencies of $K = 0.25$, 0.5, 1, and 1.3 at Re $= 1.5 \times 10^4$. For the contours of $\langle\omega_{z,\theta}\rangle D/U_\infty$ given in the second column, the levels for the solid, dashed, and dash dot lines are ± 0.025, ± 0.05, ± 0.1, respectively. Symbols represent saddle points as described in Figure 4.3.

downstream extend of the contour lines with $\langle\omega_{z,\theta}\rangle D/U_\infty = \pm 0.025$ shows that the length of the shear layers reduces with increasing oscillation frequency. The observed reduction in the streamwise extend of the shear layers with increasing oscillation frequency is consistent with the observed decrease in the streamwise extend of the mean recirculation region with increasing K, shown in the left column of Figure 5.5. Furthermore, from the downstream ends of the solid contour lines of the $\langle\omega_{z,\theta}\rangle D/U_\infty = \pm 0.025$ level, it can be seen that the

yaw-averaged shear layers become more curved towards the wake centerline at higher reduced frequencies. For comparison, Figure 4.3 showed that for the static cylinder, the shape of the mean shear layers was less curved with a greater yaw angle, which suggested that the shear layer would become more stable resulting in the mitigation of vortex shedding as was shown by Wang *et al.* [34]. Therefore, increasing reduced frequency leads to a reduction in the stability of the yaw-averaged shear layers.

The effect of the yaw oscillation on the drag can be speculated based on the near-wake flow topology information (albeit for only the central mid-span region). It was previously shown that an increase in the time-averaged streamwise velocity near the rear surface of a yawed cylinder and/or an increase in the streamwise length of the mean recirculation region reduces the momentum deficit and leads to a reduction in the base suction pressure [34, 32, 40]. This is consistent with the modified Kirchhoff's free streamline theory proposed by Roshko [92]. In the present results, since the streamwise extent of the mean recirculation region reduces in the mid-span for the higher reduced frequencies of oscillation at $K = 1$ and 1.3, it can be inferred that there is an increase in the base suction pressure and therefore an increase in the mean drag coefficient. Again, this is only relevant to the mid-span and the total drag over the entire span of the cylinder could not be so simply speculated on.

5.2.2   Phase-Averaged Flow Topology in the Mid-Span Plane

The near-wake flow topology at the mid-span of the cylinder using phase-averaged data at eight discrete phases of yaw oscillation, which were marked earlier in Figure 3.4 (a). At each phase, a set of 400 independent velocity fields were acquired and ensemble-averaged to determine the corresponding streamline topology ($\langle \psi_\phi \rangle$), streamwise velocity ($\langle U_\phi \rangle$), and vorticity ($\langle \omega_{z,\phi} \rangle$). The phases (corresponding yaw angles) considered for the yaw-oscillating cylinder in this section exactly correspond to the yaw angles of the static yawed cylinder examined so far. Thereby, the phase-averaged flow topology of the yaw-oscillating cylinder is also compared in this section against the time-averaged topology of the static yawed cylinder at corresponding yaw angles.
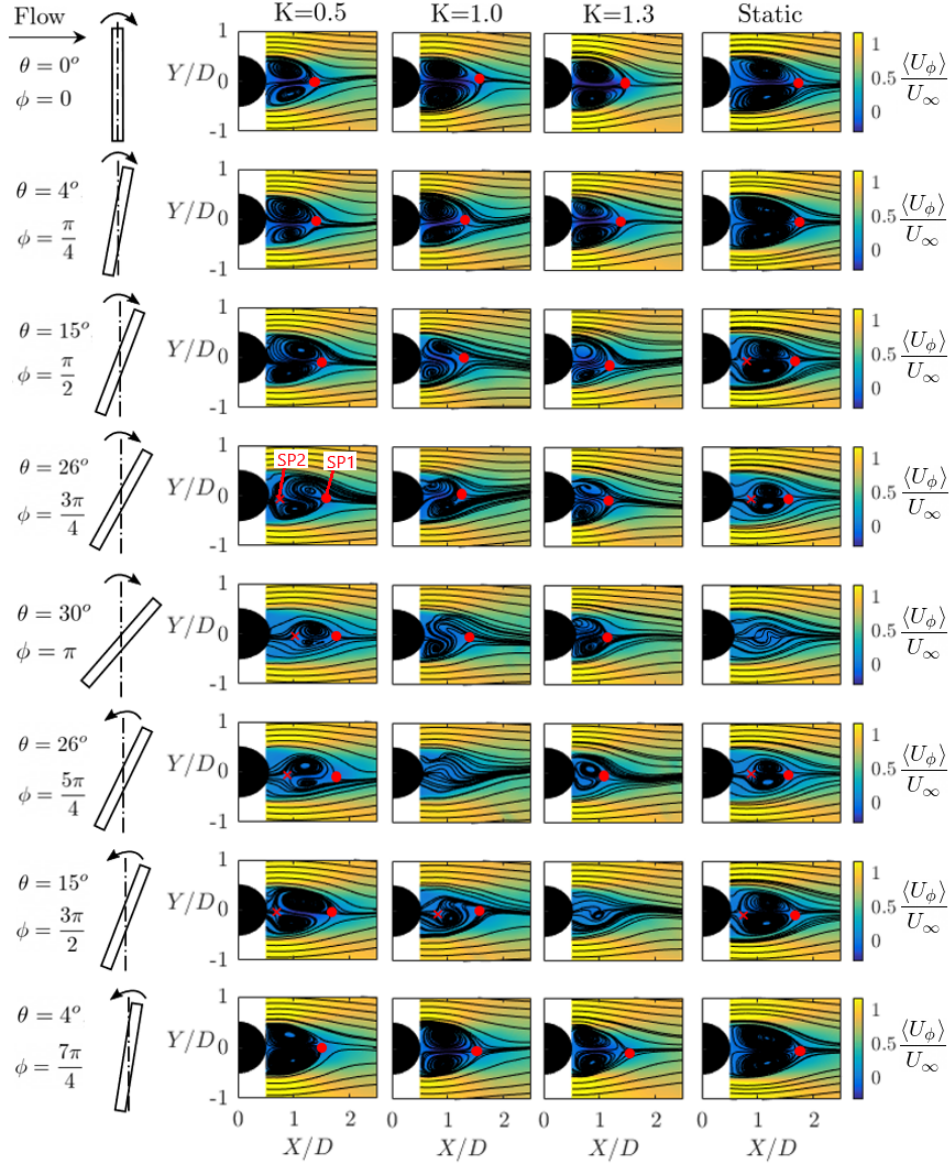
Figure 5.6: Phase-averaged flow streamline topology ($\langle\psi_\phi\rangle$) superimposed over the contours of phase-averaged normalized streamwise velocity ($\langle U_\phi\rangle/U_\infty$) for eight select phases of yaw oscillations cylinder for $K = 0.5$, $K = 1$, and $K = 1.3$ (in the first, second, and third column of images, respectively). For the static yawed cylinder, time-averaged streamline topology ($\langle\psi\rangle$) superimposed over the contours of time-averaged normalized streamwise velocity ($\langle U\rangle/U_\infty$) at yaw angles corresponding to the phases of the yaw-oscillating cylinder (in the fourth column of images). The Reynolds number is $\text{Re} = 1.5 \times 10^4$. The symbols SP1 and SP2 represent saddle points. Schematics on the far left depict the phase, its corresponding yaw angle, and the direction of motion of the cylinder with respect to the freestream.
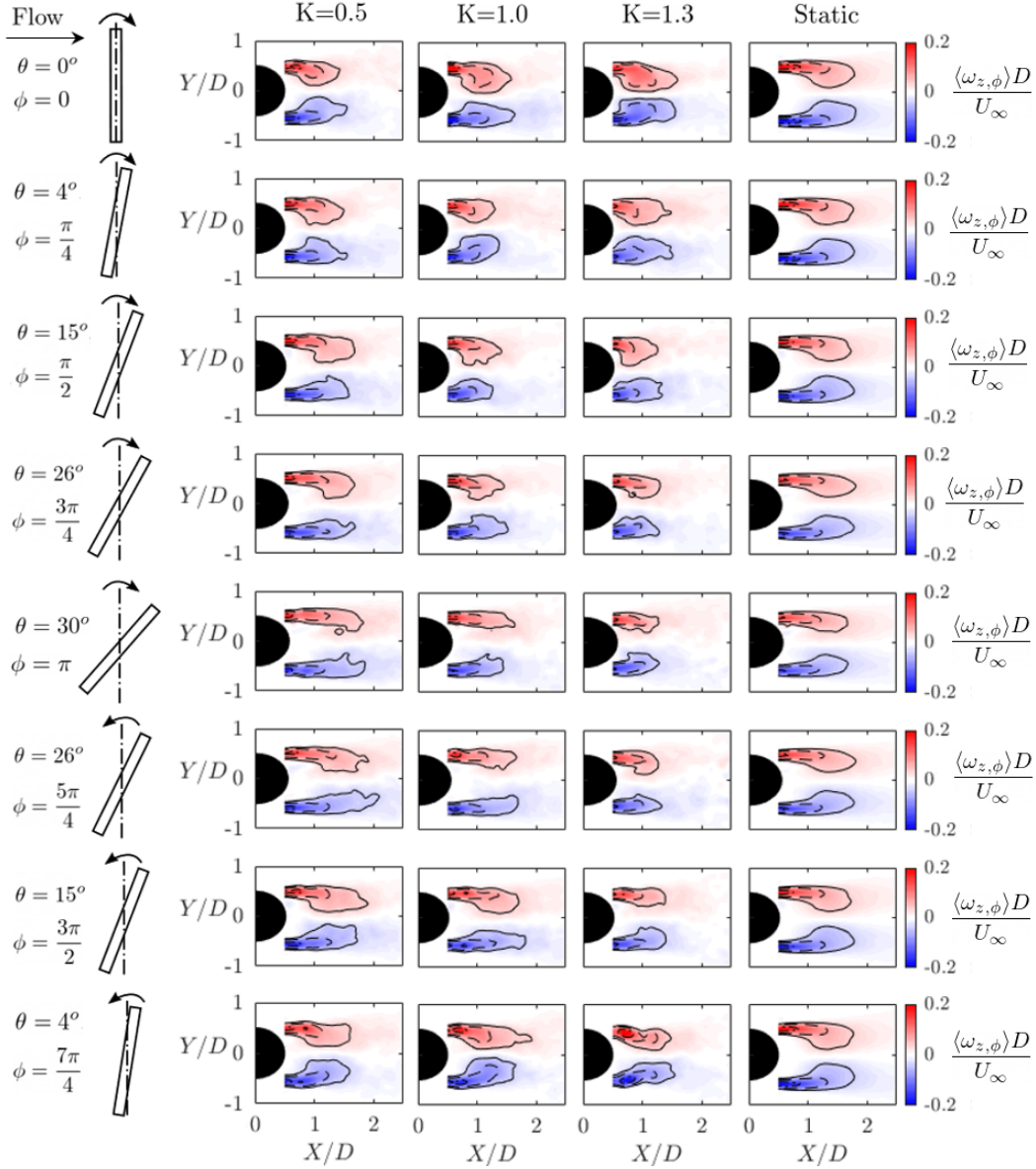
Figure 5.7: Contour plots of the phase-averaged normalized vorticity ($\langle\omega_{z,\phi}\rangle D/U_\infty$) for eight select phases of yaw-oscillations with reduced frequencies of $K = 0.5$, $K = 1$, and $K = 1.3$ at $\mathrm{Re} = 1.5 \times 10^4$ (in the first, second, and third column of images, respectively). For the static yawed cylinder, contour plots of the time-averaged normalized vorticity ($\langle\omega_z\rangle D/U_\infty$) at yaw angles corresponding to the phases of the yaw-oscillating cylinder (in the fourth column of images). The solid, dashed, and dash dot lines correspond to the contour levels of ± 0.025, ± 0.05, ± 0.1, respectively. Schematics on the far left depict the phases of oscillation, its corresponding yaw angle, and the direction of motion of the cylinder with respect to the freestream.

Figures 5.6 shows the phase-averaged streamline ($\langle\psi_\phi\rangle$) patterns overlaid on the contours of the normalized phase-averaged streamwise velocity and Figure 5.7 shows the contours of normalized phase-averaged vorticity $\langle\omega_{z,\phi}\rangle D/U_\infty$. Results of the yaw-oscillating cylinder are shown in these figures at eight phases and three reduced frequencies ($K = 0.5$, 1, and 1.3). In addition, the time-averaged results for the static yawed cylinder at yaw angles corresponding to each phase are included in the far-right column of these figures. Inspecting Figure 5.6 for $K = 0.5$ shows that a pair of counter-rotating swirl patterns is visible at every phase of yaw oscillation. The streamwise extent of these swirl patterns depends not only on the yaw angle but also on the phase of oscillation. For example, for the yaw angles of $\theta = 15^\text{o}$ and $\theta = 26^\text{o}$, comparing the results at $\phi = \pi/2$ and $3\pi/4$ in the first half-cycle of oscillation with the phases $\phi = 3\pi/2$ and $5\pi/4$ in the second half respectively, it is evident that for the same yaw angle, SP1 is further downstream in the return cycle compared to the first half cycle. Aligned with this observation, Figure 5.7 also shows for $K = 0.5$ that the shear layers are further elongated downstream for the phases on the second half-cycle compared to those with the same yaw angle but on the first half-cycle. Also, the assessment of $\langle\psi_\phi\rangle$ patterns over all phases of the yaw-oscillating cylinder case at $K = 0.5$ shows that once the cylinder passes the yaw angle of $\theta = 4^\text{o}$ (corresponding to $\phi = \pi/4$), SP1 gradually moves downstream, reaching the farthest downstream location at $\theta = 26^\text{o}$ in the return cycle ($\phi = 5\pi/4$). This is unlike the static case where, as the yaw angle increases beyond $\theta = 4^\text{o}$, SP1 gradually moves upstream with increasing yaw angle (as seen in the far right column in Figure 5.6). Also, during the return cycle for $K = 0.5$, from $\theta = 26^\text{o}$, as the yaw angle reduces with the advancement of the phase, SP1 moves gradually upstream. Another interesting trend for the yaw-oscillating cylinder at the reduced frequency of $K = 0.5$ is related to the cores of the swirl patterns. Beyond $\theta = 4^\text{o}$, the cores of the swirl patterns move gradually upstream with increasing yaw in the first-half cycle and move back in the return cycle as the yaw angle changes from $\theta = 30^\text{o}$ to 0°. Furthermore, the swirls are asymmetric around the wake centerline for $\theta > 4^\text{o}$, with the core of the upper swirl generally being located more downstream. However, the situation for the static yawed cylinder at the corresponding yaw angles is quite different. The location of

the cores of the swirl patterns in the static case remains unchanged and symmetric for all yaw angles.

At higher reduced frequencies of $K = 1$ and 1.3, the discrepancy in the streamwise extent of the swirl patterns exists between the opposite directions of cylinder motion over the cycle. For $K = 1$, the mean recirculation region is either weak or absent for the yaw angles of $\theta = 30^\circ$, $\theta = 26^\circ$, and $\theta = 15^\circ$ in the return cycle, which correspond to the oscillation phases of $\phi = \pi$, $\phi = 5\pi/4$ and $\phi = 3\pi/2$, respectively. At these particular phases, Figure 5.7 also shows that the shear layers are relatively longer and flat, suggesting suppression in vortex shedding [34] compared to other phases. For $K = 1.3$, at $\theta = 15^\circ$ in the return cycle (corresponding to a phase of $\phi = 3\pi/2$), the mean recirculation region is significantly suppressed in Figure 5.6 and the shear layers of that phase appear less curved in Figure 5.7, suggesting the suppression in vortex shedding.

The overall inspection of the phase-averaged flow topology of the yaw-oscillating cases in the mid-span of the cylinder reveals that with increasing oscillation frequency, the suppression of the vortex shedding at the mid-span of the cylinder occurs at increasingly later phases of oscillation in the return cycle. For instance, the less curved and elongated shear layers and suppressed mean recirculation region occur at the phase of $\phi = \pi$ for the reduced frequency of $K = 0.5$, while it is delayed to $\phi = 5\pi/4$ and $\phi = 3\pi/2$ for $K = 1$ and 1.3, respectively. This delay in the suppression of the mean recirculation region is associated with the delay in the development of high magnitude axial flow, as discussed in Section 5.1. It should also be noted here that the substantial distinctions observed in the mid-span flow topology between the same yaw angles of the static yawed cylinder (which is in a state of zero acceleration at all times) and the yaw-oscillating cases, as well as between the same yaw angle of a yaw-oscillating cylinder at different oscillation phases indicates that the acceleration of the cylinder may be one of the important parameters influencing the flow. For instance, according to Figure 3.4 (a), the cylinder at phase $\phi = 3\pi/4$ is decelerating at $\theta = 26^\circ$ while it is accelerating at $\theta = 26^\circ$ at the phase of $\phi = 5\pi/4$.

5.2.3 Phase-Averaged Flow Topology in $Z/D = \pm 3$ Planes

In this section, the spanwise variation of the near-wake of the yaw-oscillating cylinder is studied by comparing the phase-averaged results obtained on two (X,Y) planes, namely at $Z/D = 3$ and -3. In order to have a better understating of the impact of spanwise flow in these planes, flow patterns on the (X,Z) planes are also provided.

5.2.3.1 $Z/D = 3$ Plane

Figure 5.8 depicts the phase-averaged streamline patterns ($\langle \psi_\phi \rangle$) overlaid on contours of the phase-averaged normalized streamwise velocity ($\langle U_\phi \rangle U_\infty$) and Figure 5.9 shows the contours of normalized vorticity ($\langle \omega_{z,\phi} \rangle D/U_\infty$) at the same eight phases as previously considered for each of the yaw-oscillating cases in the $Z/D = 3$ plane. Moreover, the phase-averaged streamline patterns ($\langle \psi_\phi \rangle$) and contours of normalized Y-direction vorticity ($\langle \omega_{y,\phi} \rangle D/U_\infty$) in the $Y/D = 0$ symmetry plane are included in Figures 5.8 and 5.9, respectively.

Inspecting Figure 5.8 demonstrates that the mean recirculation region deforms, becomes entirely suppressed or contains strong counter-rotating swirls in the $Z/D = 3$ plane at different phases of oscillation depending on the frequency of oscillations. For $K = 0.5$, when the phase of oscillation is $\phi = 0$, the counter-rotating swirl patterns forming behind the cylinder in the $Z/D = 3$ plane appear highly deformed and asymmetric, which may be related to the change in the direction of the cylinder motion at the end of a complete oscillation cycle. As the phase of oscillation advances from $\phi = \pi/4$ to $3\pi/4$, the asymmetry in the swirl patterns continues to exist while the negative streamwise velocity in this Z/D plane gradually reduces under the impact of the positive-direction motion of the cylinders' top half (as also detected for these phases in Figure 5.2 at this Z/D level). When the phase of oscillation reaches $\phi = \pi$ and $\phi = 5\pi/4$, the mean recirculation bubble is suppressed at this Z/D plane, where no swirl patterns are detectable anymore behind the rear surface of the cylinder. This is presumably a result of the strong upward axial flow, which originates from the lower free end of the cylinder and spreads over the span as the phase of oscillation increases, reaching

this $Z/D = 3$ level at these two oscillation phases (as seen earlier in the phase-averaged axial velocity contours given in Figure 5.4). This suppression in the recirculation bubble is also in accord with the observed significant reduction in the reverse flow velocity at $\phi = \pi$ and $5\pi/4$ at this Z/D plane (as seen in the corresponding contours of streamwise velocity given in the present Figure 5.8 and the previously-shown Figure 5.2). Moreover, for $K = 0.5$, the contours of Z-direction vorticity in Figure 5.9 also depict that at $\phi = \pi$ and $5\pi/4$, the shear layers in the $Z/D = 3$ plane are less curved towards the wake centerline compared to other phases. This implies a reduction in the flapping of the separating shear layers (*i.e.*, an increase in the stability of the shear layers) due to the mitigation of the Karman vortex shedding [34]. From a further inspection of the $\langle \psi_\phi \rangle$ patterns in Figures 5.8 and $\langle \omega_{z,\phi} \rangle D/U_\infty$ patterns in Figure 5.9 for $K = 0.5$, it is apparent that at $\phi = 3\pi/2$ and $7\pi/4$, the swirl patterns accompanied by an intense reverse flow velocity re-appear in the near wake of the cylinder and the vorticity in the separating shear layers becomes more curved towards the wake centerline in the $Z/D = 3$ plane, suggesting increased strength in Karman vortex shedding at this Z/D plane.

As depicted in Figure 5.8, the wake flow behavior in the $Z/D = 3$ plane for the yaw-oscillating cylinders with reduced frequencies of $K = 1$ and 1.3 is almost similar. For both cases, the swirl patterns, seen at $\phi = 0$, become substantially suppressed when the cylinder reaches the oscillation phases of $\phi = \pi/4$ and $\pi/2$. In accord with this observation, Figure 5.9 shows that the curving of the shear layers towards the wake centerline becomes lesser for those phases and the shear layers depict a large lateral distance from each other, suggesting a suppression in regular vortex shedding. Notice that the suppression of the mean recirculation bubble at $\phi = \pi/4$ and $\pi/2$ must be linked to the significant amount of positive streamwise thrust conveyed on the fluid behind the top half of the cylinder (including the $Z/D = 3$ plane in question here) as a result of the positive X-direction movement of the cylinder's top half combined with the cylinder's large acceleration at these phases, as indicated earlier while discussing Figure 5.2. Here, as mentioned before, unlike the lower reduced frequency of $K = 0.5$, the influence of the cylinder's acceleration becomes an essential factor leading to this outcome at the higher reduced frequencies of $K = 1$ and 1.3. The substantial increase
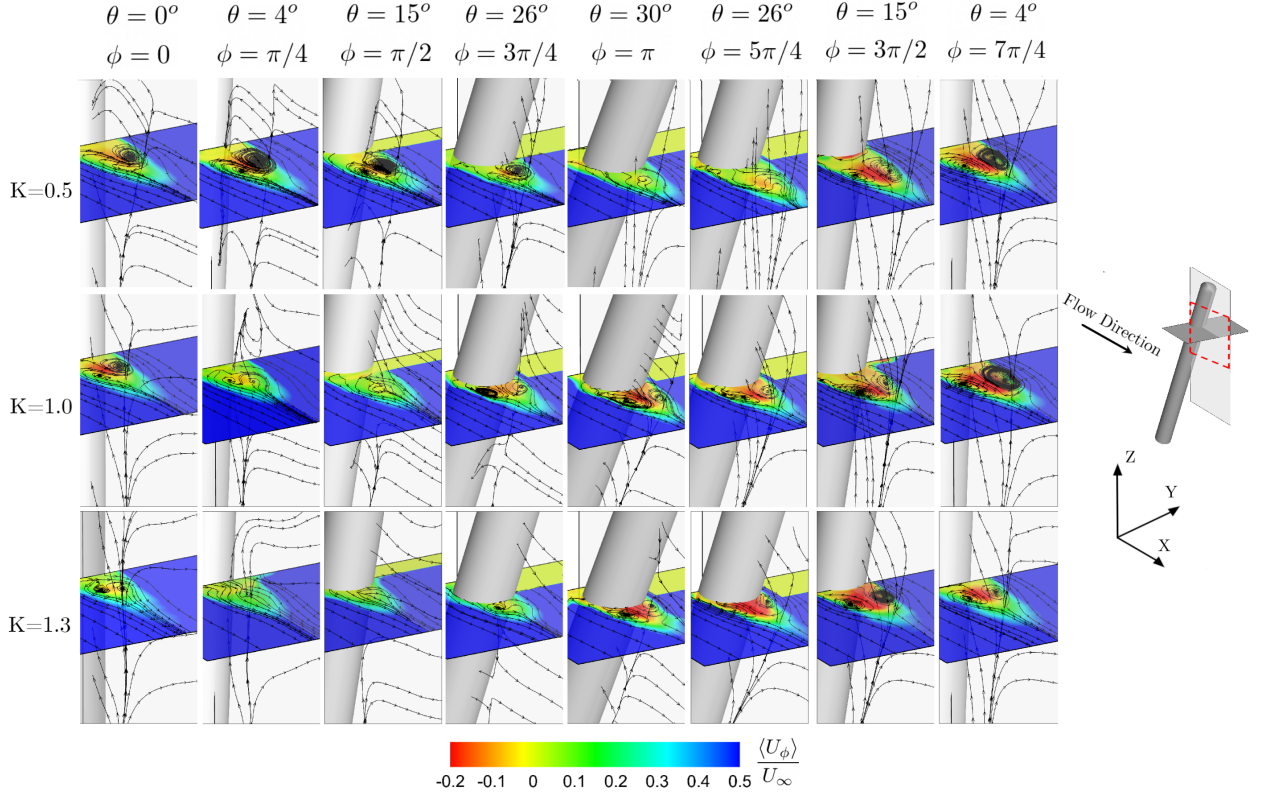
Figure 5.8: Phase-averaged streamline topology ($\langle \psi_\phi \rangle$) in the $Y/D = 0$ and $Z/D = 3$ planes and contours of phase-averaged streamwise velocity ($\langle U_\phi \rangle / U_\infty$) on $Z/D = 3$ plane for eight select phases of yaw-oscillating cylinder with reduced frequencies of $K = 0.5$, 1, and 1.3 at $\mathrm{Re} = 1.5 \times 10^4$. The coordinate system, the flow direction, and the PIV field of visualization (with the red dashed lines marking the boundaries of the field of view in the $Y/D = 0$ plane) are depicted on the far right.

in the positive streamwise velocity at the base of the cylinder would obstruct the mixing

of the shear layers, thereby suppressing the regular Karman vortex shedding. Furthermore,

remember from Figure 5.2 that unlike the lower K value of 0.5, at $\phi = 3\pi/4$ and π, the

significant deceleration in the positive X motion of the cylinder's top half for the higher

oscillation frequencies of $K = 1$ and 1.3 leads to a recovery in the reverse flow velocity, which

gradually spreads to upper sections in the wake of the cylinder's top half as the phase of

oscillation progresses in the second quarter of its oscillation cycle (*i.e.*, when the forward

movement of the cylinder's top is decelerating). With the recovery of the reverse flow comes
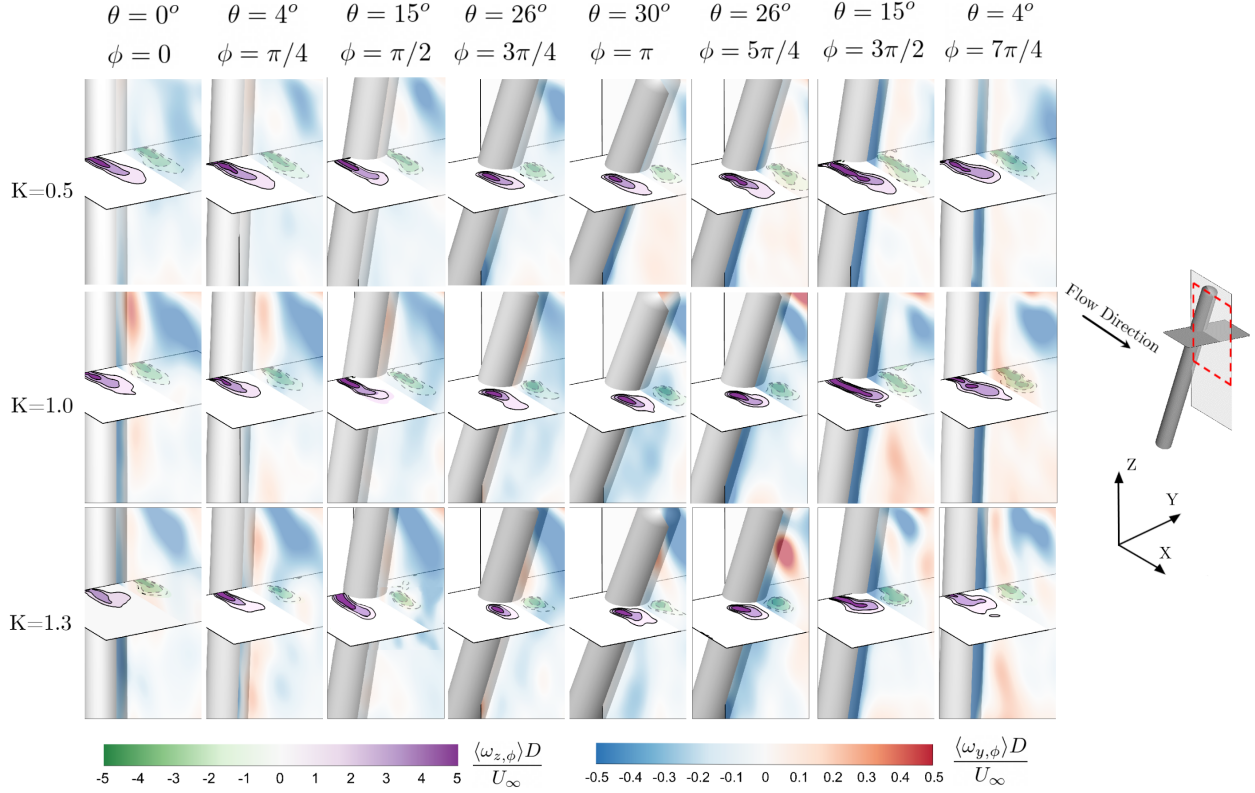
Figure 5.9: Contours of phase-averaged normalized Y-direction vorticity ($\langle\omega_{y,\phi}\rangle D/U_\infty$) in $Y/D = 0$ and phase-averaged normalized Z-direction vorticity ($\langle\omega_{z,\phi}\rangle D/U_\infty$) in $Z/D = 3$ plane for eight select phases of yaw-oscillating cylinder with reduced frequencies of $K = 0.5$, 1, and 1.3 at $\mathrm{Re} = 1.5 \times 10^4$. The coordinate system, the flow direction, and the PIV field of visualization (with the red dashed lines marking the boundaries of the field of view in the $Y/D = 0$ plane) are depicted on the far right.

the resurgence of the swirl patterns. As a result, the revival in the mean recirculation bubble with counter-rotating swirls occurs at $\phi = 3\pi/4$ and π in the $Z/D = 3$ plane for $K = 1$, in agreement with the inwardly curved shear layers depicted in the corresponding contours of Z-direction vorticity in Figure 5.3. Note that, for $K = 1.3$, because the recovery in the negative streamwise velocity has yet to reach the $Z/D = 3$ plane at $\phi = 3\pi/4$ (as apparent from Figure 5.2), a complete resurgence of the mean recirculation bubble does not occur at this phase at $Z/D = 3$. In the return cycle, at $\phi = \pi$ and $5\pi/4$, unlike $K = 0.5$, no suppression is observed in the mean recirculation bubble for $K = 1$ and 1.3. This is associated with the low magnitudes in the axial flow around the $Z/D = 3$ plane for the cases with higher

K, as shown in Figure 5.4. Instead, under the effect of negative X-direction motion of the cylinder's top along with large acceleration, as the phase changes from $\phi = \pi$ to $3\pi/2$, the negative streamwise velocity gradually recovers and the swirl patterns become stronger. From $\phi = 3\pi/2$ to $7\pi/4$, as the cylinder's top half moves against the freestream direction, the reverse flow velocity increases and the swirl patterns in the $Z/D = 3$ plane become stronger. Notice that at $\phi = 3\pi/2$ and $7\pi/4$ for the reduced frequencies of $K = 1$ and 1.3, the effect of the axial flow near the $Z/D = 3$ plane subsides due to the rapid decrease in its strength for the phases near the end of the return cycle, and as a result, the reverse flow velocity revives in the wake and no suppression is observed in the mean recirculation bubble. Also, Figure 5.9 demonstrates that for $K = 1$ and 1.3 at $\phi = 3\pi/2$ and $7\pi/4$, the shear layers appear to be more curved toward each other, suggesting amplification in the Karman vortex shedding. It is also evident that when the positive Y-direction vorticity in the $Y/D = 0$ plane ascends and reaches the $Z/D = 3$ plane at the oscillation phase of $\phi = 7\pi/4$ in the return cycle, the magnitude of the Z-direction vorticity within the shear layers decreases significantly as the cylinder moves to this phase. As the remnants of the positive vorticity in the $Y/D = 0$ plane continue to exist at $\phi = 0$, the Z-direction vorticity also continues to have low magnitudes at this phase in the $Z/D = 3$ plane.

5.2.3.2 $Z/D = -3$ Plane

Figures 5.10 and 5.11 show the similar results as Figure 5.8 and 5.9 but in the $Z/D = -3$ plane. General inspection of Figure 5.10 demonstrates that for all three reduced frequencies, from $\phi = 0$ to $3\pi/4$ in the first half of the yaw oscillation cycle, when the bottom half of the cylinder moves against the incoming flow, a pair of well-defined counter-rotating swirls forms behind the cylinder in accord with the strong reverse velocity developing at the lower half of the cylinder (as apparent from the $\langle U_\phi \rangle / U_\infty$ contours in the present Figure 5.10 as well as the previously-given Figure 5.2 for this Z/D level at these phases). The streamwise extent of these swirls increases with increasing yaw angle.

In the second half of the yaw oscillation cycle, as a common feature for all K values in
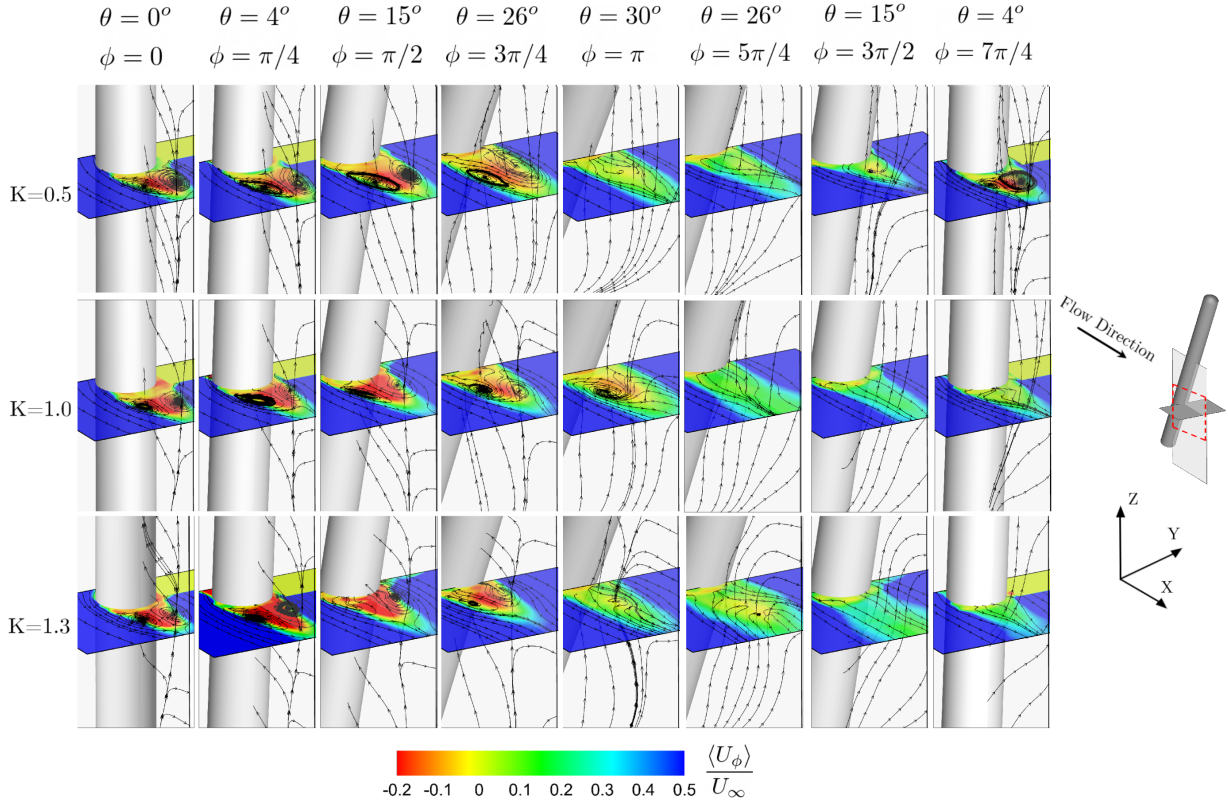
Figure 5.10: Phase-averaged streamline topology ($\langle\psi_\phi\rangle$) in $Y/D = 0$ and $Z/D = -3$ planes and contours of phase-averaged streamwise velocity ($\langle U_\phi\rangle/U_\infty$) in $Z/D = -3$ plane for eight select phases of yaw-oscillating cylinder with reduced frequencies of $K = 0.5$, 1, and 1.3 at $\text{Re} = 1.5 \times 10^4$. The coordinate system, the flow direction, and the PIV field of visualization (with the red dashed lines marking the boundaries of the field of view in the $Y/D = 0$ plane) are depicted on the far right.

question, the patterns of swirls become significantly suppressed or totally eliminated at the $Z/D = -3$ plane for the oscillation phases of $\pi \leqslant \phi \leqslant 3\pi/2$, which is associated with the impact of the strong axial flow passing through the $Z/D = -3$ plane (as detected earlier in Figure 5.4 at this Z/D level) as well as the positive streamwise flow conveyed on the wake fluid by the movement of the lower middle section of the cylinder in the inflow direction (as discernible from Figure 5.2 at this Z/D level). For $K = 0.5$, the reverse flow velocity increases and a pair of swirl patterns re-appears again at $\phi = 7\pi/4$ at the $Z/D = -3$ plane. On the other hand, for higher reduced frequencies of $K = 1$ and 1.3, unlike $K = 0.5$, the suppression

84

of the mean recirculation bubble extends to $\phi = 7\pi/4$ in the return cycle. This is presumably due to cylinder's large deceleration at higher oscillation frequencies. As mentioned earlier during the discussion of the corresponding $\langle U_\phi \rangle / U_\infty$ results for $K = 0.5$ in Figure 5.2, as the cylinder's top half moves opposite to the inflow direction in its return cycle, the negative streamwise velocity in the wake behind the top half grows and spreads toward the lower spanwise regions as the yaw angle decreases (reaching the $Z/D = -3$ plane discussed here at $\phi = 7\pi/4$). However, for higher yaw oscillation frequencies of $K = 1$ and 1.3, with the deceleration effects being significant, the reverse flow presumably cannot make it to the $Z/D = -3$ plane at $\phi = 7\pi/4$ (right before returning to the unyawed position), which explains the suppressed mean recirculation bubbles detected at this phase for $K = 1$ and 1.3 at the Z/D level in question. The significant suppression of the mean recirculation bubble observed at $\pi \leqslant \phi \leqslant 3\pi/2$ for $K = 0.5$ and $\pi \leqslant \phi \leqslant 7\pi/4$ for $K = 1$ and 1.3 in Figure 5.10 is also aligned with the drastic divergence of the shear layers from the wake centerline for these phases in Figure 5.11. That is, for the phases of $\phi = \pi$, $5\pi/4$ and $3\pi/2$, the shear layers for all K are generally less curved towards each other, suggesting the mitigation of the vortex shedding. Furthermore, at $\phi = 7\pi/4$, this is continued to be the case for the higher frequencies of $K = 1$ and 1.3, but for $K = 0.5$, aligned with the observed resurgence of the swirl patterns at this phase, the shear layers are inclined toward the wake centerline again, suggesting the recovery of the vortex shedding. Another observation that surfaces from an inspection of Figure 5.11 is that when the strong positive Y-direction vorticity in the $Y/D = 0$ plane passes through the $Z/D = -3$ plane, which happens at $\phi = \pi$ for the yaw-oscillating case of $K = 1$ and at $\phi = \pi$ and $5\pi/4$ for $K = 1.3$, the magnitude of the Z-direction vorticity within the shear layers substantially decreases.
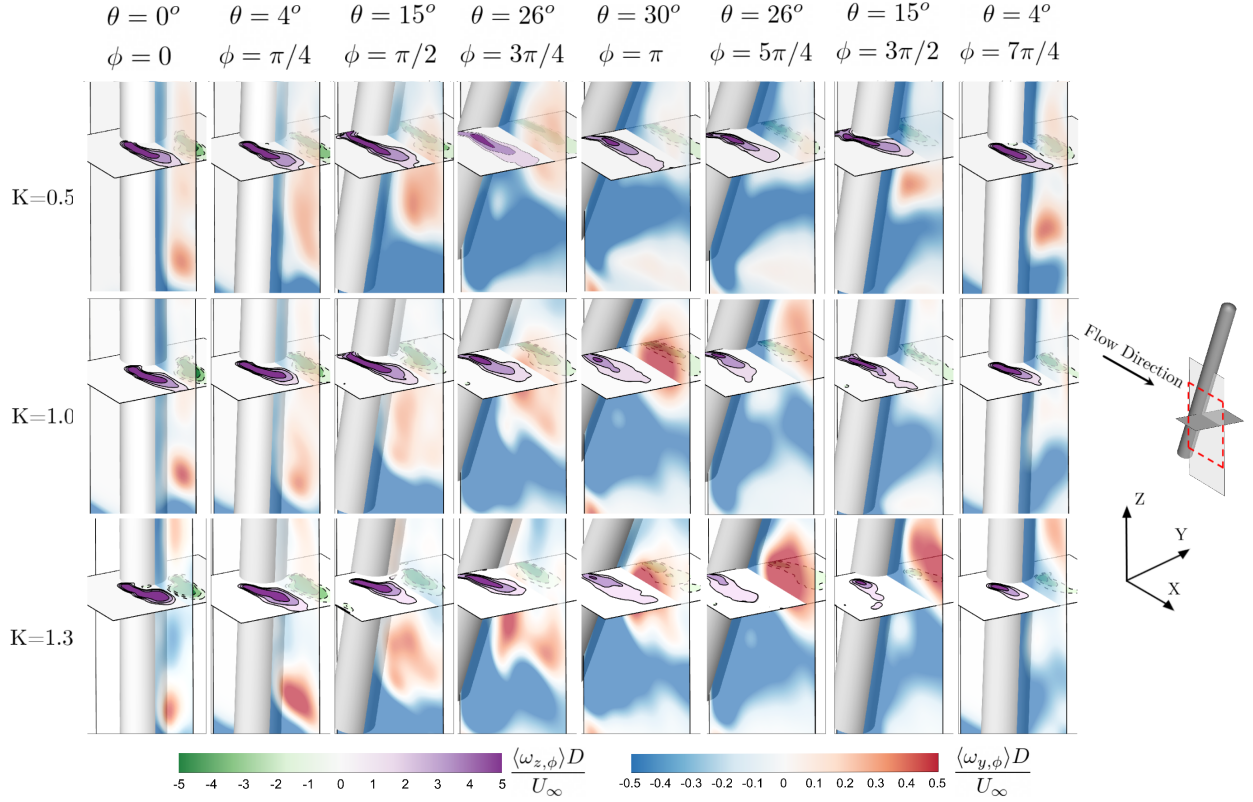
Figure 5.11: Contours of phase-averaged normalized Y-direction vorticity ($\langle\omega_{y,\phi}\rangle D/U_\infty$) in $Y/D = 0$ and phase-averaged normalized Z-direction vorticity ($\langle\omega_{z,\phi}\rangle D/U_\infty$) in $Z/D = -3$ plane for eight select phases of yaw-oscillating cylinder with reduced frequencies of $K = 0.5$, 1, and 1.3 at $\mathrm{Re} = 1.5 \times 10^4$. The coordinate system, the flow direction, and the PIV field of visualization (with the red dashed lines marking the boundaries of the field of view in the $Y/D = 0$ plane) are depicted on the far right.

5.3   Wake Parameters

5.3.1   Yaw-Averaged Wake Parameters

In order to evaluate the effect of yaw-oscillation on the wake closure length, profiles of the normalized yaw-averaged streamwise velocity on the wake centerline are plotted against X', which is the streamwise distance measured from the base of the cylinder, for the static cylinder and oscillating cases at reduced frequencies of $K = 0.25$, 0.5, 1, and 1.3 in Figure 5.12. The calculated wake closure lengths are shown in the inset of Figure 5.12. As apparent
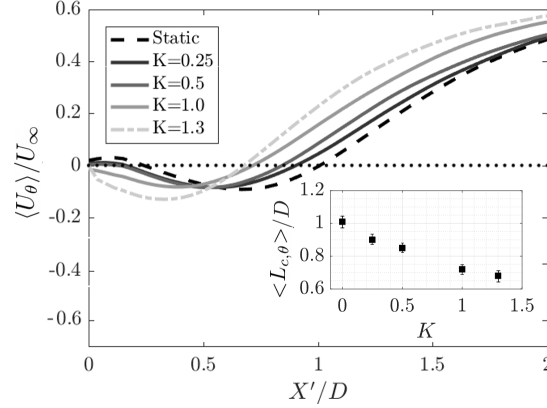
Figure 5.12:   Normalized yaw-averaged streamwise velocity ($\langle U_\theta \rangle / U_\infty$) along the wake centerline for static yawed cylinder and yaw-oscillating cylinder at different reduced frequencies. Inset shows the variation of yaw-averaged wake closure length ($\langle L_{c,\theta} \rangle$) with reduced frequency (K).

from the profiles in Figure 5.12, the maximum backflow velocity occurs at $K = 1.3$. The streamwise velocity in the inflow direction is observed near the base of the cylinder for the static and yaw-oscillating cases at $K = 0.25$ and 0.5 and changes to the backflow direction at $K = 1$ and 1.3 exhibiting the streamwise flow behavior shown in Figure 5.5. In regions beyond $X/D = 0.5$, an increase in the mean streamwise velocity with the oscillation frequency is observed, which can be related to a shortening of the wake closure length. The decrease in the wake closure length with increasing the reduced frequency is inline with the observations in the flow topology shown in Figure 5.5. The inset of Figure 5.12 reveals that from the static cylinder to the oscillating cylinder at $K = 1.3$ (the highest reduced frequency), $\langle L_{c,\theta} \rangle$ is reduced by 30%.

Figure 5.13 shows the cross-stream profiles of the normalized yaw-averaged streamwise velocity for the static and four yaw-oscillating cases at two locations downstream. As shown in the top plot in Figure 5.13 and from the summarized wake parameters given in Table 5.1, the maximum velocity deficit ($\langle U_{d,max} \rangle$) decreases as K increases for $X/D = 1.5$. The decrease corresponds with the reduction in the wake closure length for the yaw-oscillating cases. The profiles for $X/D = 2$ follow the same trend as those shown previously. From the values of half wake width at $X/D = 2$ given in Table 5.1, it is found that the wake width
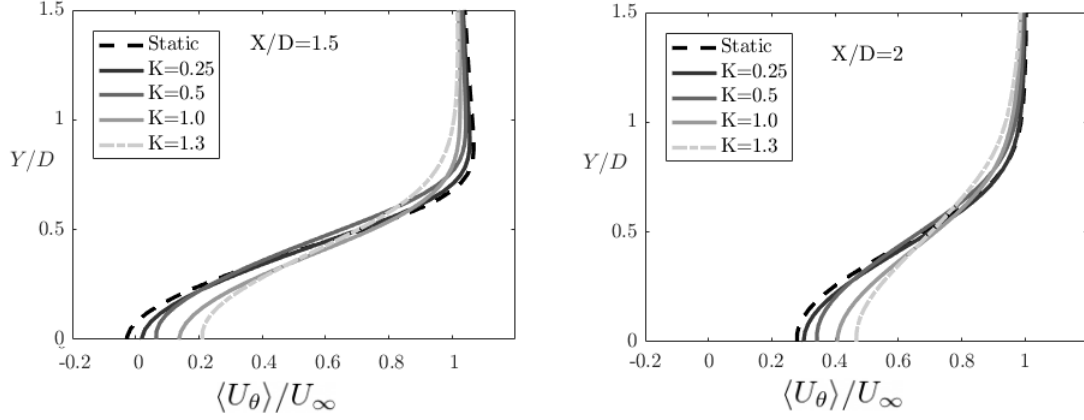
Figure 5.13: Normalized yaw-averaged streamwise velocity ($\langle U_\theta \rangle / U_\infty$) across the wake at $X/D = 1.5$ (top) and $X/D = 2$ (bottom) for the static yawed cylinder and yaw-oscillating cylinder at different reduced frequencies.

Table 5.1: The minimum and maximum values of the normalized yaw-averaged streamwise velocity, and the maximum streamwise velocity deficit ($\langle U_{d,max} \rangle = U_\infty - \langle U(x,y) \rangle$) for static yawed cylinder and oscillating yawed cylinder at different reduced frequencies at two different streamwise locations downstream of the cylinder.

		$X/D = 1.5$			$X/D = 2$		
K	$\dfrac{\langle U_{min} \rangle}{U_\infty}$	$\dfrac{\langle U_{max} \rangle}{U_\infty}$	$\dfrac{\langle U_{d,max} \rangle}{U_\infty}$	$\dfrac{\langle U_{min} \rangle}{U_\infty}$	$\dfrac{\langle U_{max} \rangle}{U_\infty}$	$\dfrac{\langle U_{d,max} \rangle}{U_\infty}$	$\dfrac{y_{1/2}}{D}$
Static	-0.04	1.07	1.04	0.27	1.0	0.73	0.45
0.25	0.01	1.06	0.99	0.29	0.99	0.71	0.47
0.5	0.06	1.04	0.94	0.34	0.99	0.66	0.51
1.0	0.13	1.03	0.87	0.40	0.99	0.60	0.56
1.3	0.20	1.02	0.80	0.46	0.99	0.54	0.64

increases with the reduced frequency. For instance, the wake width increased by 42% for the highest reduced frequency in comparison to the static case.

5.3.2   Phase-Averaged Wake Parameters

5.3.2.1   Velocity Profiles in the Mid-Span Plane

Figure 5.14 shows the profiles of normalized phase-averaged streamwise velocity ($\langle U_\phi \rangle / U_\infty$) along the wake centerline at eight select phases of yaw oscillation for the reduced frequencies of

$K = 0.5$, 1, and 1.3 (from the top plot to the bottom, respectively). The profile of normalized time-averaged streamwise velocity ($\langle U \rangle / U_\infty$) for the stationary yawed cylinder at $\theta = 0^o$ is also included in these plots as a reference for comparison. Note again that, in these plots, the horizontal axis is X'.

From Figure 5.14, it is evident that, compared to the cases with $K = 1$ and 1.3, the maximum phase-averaged backflow velocity for each phase of the yaw-oscillating cylinder at $K = 0.5$ appears much closer to the maximum backflow velocity of the stationary cylinder at corresponding yaw angles (see Figure 4.8 for the streamwise velocity profiles of the stationary yawed cylinder at corresponding yaw angles). This implies that with increasing frequency of yaw oscillations, the near-wake deviates more and more from the near-wake structure of the stationary yawed case. For a given reduced frequency, the location where the maximum backflow velocity is reached at the mid-span depends on the phase of yaw oscillation. Furthermore, for all reduced frequencies, the maximum phase-averaged backflow velocity consistently occurs at the phase of $\phi = 0$ (corresponding to $\theta = 0^o$). For $K = 0.5$, although the value of this maximum backflow velocity at $\theta = 0^o$ is almost the same as that of the stationary cylinder case with $\theta = 0^o$ (*i.e.*, no yaw), it increases progressively with increasing the reduced frequency. For $K = 0.5$, the maximum backflow velocity gradually reduces as the oscillation phase changes from $\phi = 0$ to $\phi = \pi$ in the first half of the cycle. It then increases gradually from $\phi = \pi$ to $\phi = 0$ in the return cycle. For $K = 1$, the maximum phase-averaged backflow velocity gradually reduces from $\phi = 0$ to $\phi = \pi$, reaching the no-backflow situation at $\phi = 5\pi/4$, which indicates a suppressed mean recirculation region at the corresponding yaw angle of $\theta = 26^o$ in the return cycle, as observed earlier in Figure 5.6. It then gradually increases with increasing ϕ from $\phi = 3\pi/2$ to $\phi = 0$ in the return cycle. For $K = 1.3$, with increasing ϕ, there is a similar trend of gradual reduction followed by a gradual increase in the phase-averaged maximum backflow velocity, with the no-backflow scenario occurring at $\phi = 3\pi/2$ (corresponding to a yaw angle of $\theta = 15^o$ in the return cycle). Once again, zero backflow encountered at $\theta = 15^o$ in the return cycle is in accord with the inferences drawn from the corresponding plots, given in Figures 5.6 and 5.7, where suppression recirculation
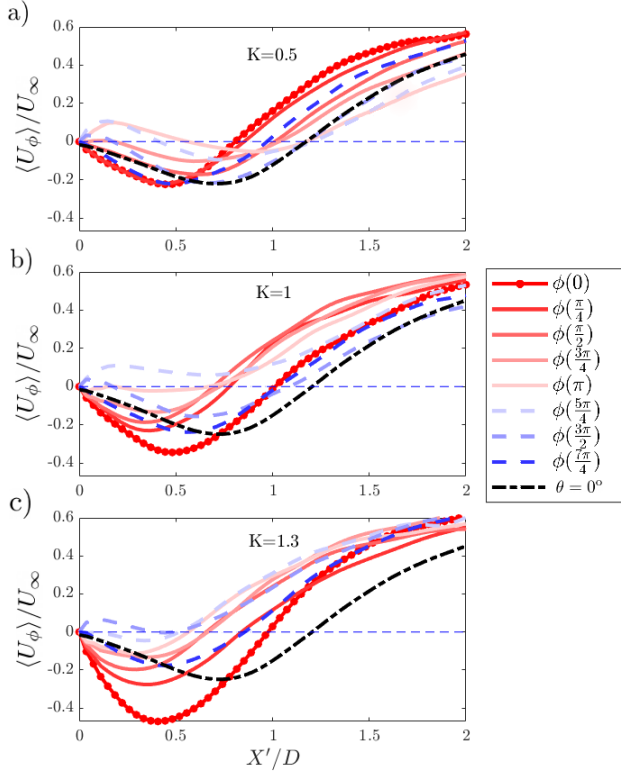
Figure 5.14: Phase-averaged normalized streamwise velocity ($\langle U_\phi \rangle / U_\infty$) along the wake centerline for the yaw-oscillating cylinder at a) $K = 0.5$ b) $K = 1$ c) $K = 1.3$ at eight select phases. Also, $\langle U_{0^o} \rangle / U_\infty$ shows the stationary case with $\theta = 0^o$.

region and vortex shedding was reported.

Figure 5.15 shows the cross-stream profiles of normalized phase-averaged streamwise velocity ($\langle U_\phi \rangle / U_\infty$) for the yaw-oscillating cylinder at different phases of its oscillation for three reduced frequencies. Profiles are provided for the streamwise locations of $X/D = 1.5$ (in the top row) and $X/D = 2$ (in the bottom row). For $K = 0.5$, at the streamwise station of $X/D = 1.5$, the minimum phase-averaged streamwise velocity (which is reached at the wake centerline) changes from being in the inflow direction at the first two phases studied ($\phi = 0$ and $\pi/4$) to being in the backflow direction for the rest of the oscillation phases (Figure 5.15 (a)). This observation is a result of the fact that once the yaw-oscillating cylinder passes the phase of $\phi = \pi/4$ (or in other words, the yaw angle of $\theta = 4^o$), the closure in the near-wake region occurs downstream of the $X/D = 1.5$ at the mid-span of the cylinder (in accord with the streamwise extends of the recirculation region seen Figure 5.6). At $X/D = 2$, on the other hand, for all phases of yaw oscillation at $K = 0.5$, the flow at the wake centerline

90
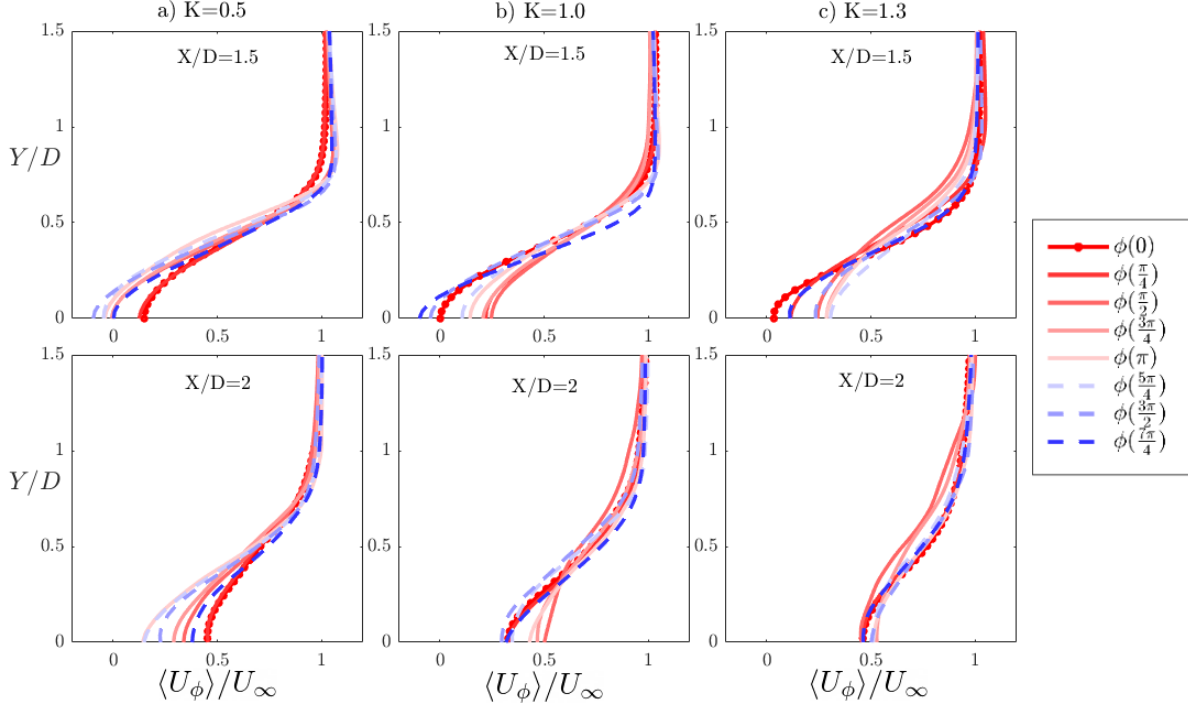
Figure 5.15: Phase-averaged normalized streamwise velocity ($\langle U_\phi \rangle / U_\infty$) across the wake at two downstream locations of $X/D = 1.5$ and $X/D = 2$ for yaw-oscillating cylinder at each phase a) $K = 0.5$, b) $K = 1$, and c) $K = 1.3$.

is in the freestream direction, indicating the wake closure upstream of that station. For $K = 1.0$, the flow at the wake centerline in the mid-span of the cylinder is in the backflow direction only between the phases of $\phi = 3\pi/2$ to $\phi = 7\pi/4$ in the return cycle at $X/D = 1.5$, in accord with elongated wake regions seen in Figure 5.6 at these phases. The minimum phase-averaged velocity at the wake centerline turns out to be in the freestream direction at all phases for $X/D = 2$, indicating closure of the mean recirculation region upstream of this streamwise station for all phases of oscillation. For $K = 1.3$, there is no backflow for either of the X/D locations. Notice that, overall inspection of Figure 5.15 shows that the velocity deficit at the wake centerline varies depending on the phase of oscillation, the frequency of oscillation, and the X/D station considered. However, for $K = 1.3$, unlike others, the maximum phase-averaged velocity deficit does not vary significantly with the phase of oscillation at $X/D = 2$.

Figure 5.16 (a) and (b) depict the variations in the phase-averaged wake closure length ($\langle L_{c,\phi} \rangle$) and the phase-averaged half wake width ($\langle Y_{1/2,\phi} \rangle$) at the $X/D = 2$ station, respectively, at different phases of oscillation for the three reduced frequency under consideration. The results for the static yawed cylinder at corresponding yaw angles are also included for comparison purposes. Figure 5.16 (a), shows that for $K = 0.5$, the wake closure length gradually increases with the yaw angle in the first half of the oscillation cycle, and in the return cycle, it continues to increase until $\phi = 5\pi/4$, after which it decreases, as visually seen earlier in Figure 5.6. This trend is also in line with the inferences made above from Figure 5.15 (a). Figure 5.16 (b) indicates that for $K = 0.5$, the wake width at $X/D = 2$ decreases as the cylinder is yawed to higher angles in the first half-cycle and then starts increasing in the second half as the cylinder returns to the cross flow position. For $K = 0.5$, comparison of a given yaw angle in the first-half cycle with the same yaw angle in the return cycle shows that the wake is wider and the wake closure length is lower in the first half-cycle.

Figure 5.16 (a) demonstrates that for $K = 1$, the wake closure length decreases with increasing the yaw angle in the first half of the oscillation cycle. After the suppression of the mean recirculation region at $\phi = 5\pi/4$, the wake closure length increases as the cylinder returns to the cross-flow position in the second half of the cycle. Discrepancy in the wake closure length is significant between phases corresponding to the same yaw angle in the
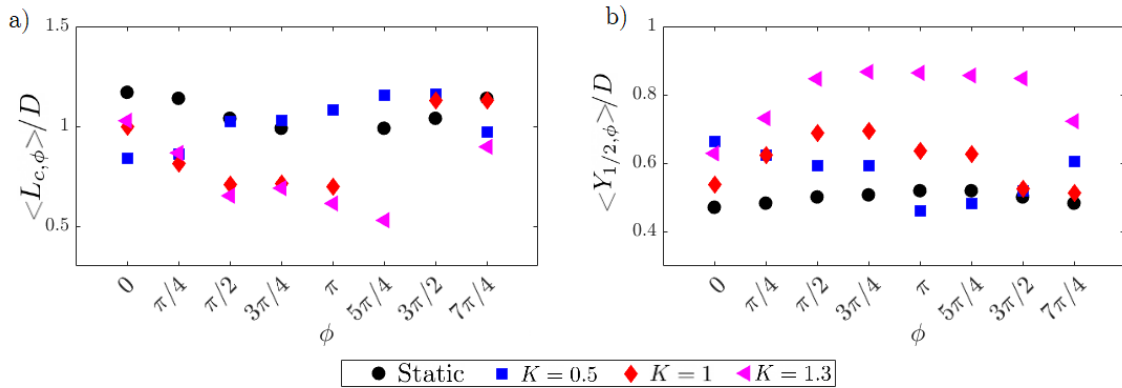
Figure 5.16:   Phase-averaged wake parameters of all the static and yaw-oscillating cylinder cases at Re $= 1.5 \times 10^4$. a) Wake closure length ($\langle L_{c,\phi} \rangle/D$) and b) Half wake width ($\langle Y_{1/2,\phi} \rangle/D$) at $X/D = 2$.

first and second half of the oscillation cycle. For instance, the mean recirculation region extends in the streamwise direction by 60% from $\phi = \pi/2$ to $\phi = 3\pi/2$ and by 48% from $\phi = \pi/4$ to $\phi = 7\pi/4$. Results for $K = 1$ in Figure 5.16 (b) indicate that the wake width increases in the first half cycle of oscillation from the phase of $\phi = 0$ to $\phi = 3\pi/4$, and starts decreasing for the rest of the oscillation cycle. For $K = 1.3$, the wake closure length in the first half-cycle follows similar trend to that of the previous case, that is, it decreases gradually with increasing yaw angle. In the second half, the wake closure length continues to decrease until the suppression of the mean recirculation region occurs at $\phi = 3\pi/2$. Then, it increases back again. From Figure 5.16 (b), it can be inferred that the wake width for almost all phases at $K = 1.3$ is higher than other yaw-oscillating cases. From an overall inspection of the trends in Figure 5.16 (a) and (b), one can conclude that the lower the mean recirculation region length, the wider the wake width outside the mean recirculation region and vice versa (*i.e.*, at the $X/D = 2$ location), which is in agreement with the trend shown by Norberg [83].

5.3.2.2   Velocity Profiles in $Z/D = \pm 3$ Planes

Figure 5.17 shows the profiles of the mean normalized velocity ($\langle U \rangle / U_\infty$) and the phase-averaged normalized velocity ($\langle U_\phi \rangle / U_\infty$) along the wake centerline for the static yawed cylinder and the yaw-oscillating cases, respectively. Results are shown at two locations along the span of the cylinder, namely at the $Z/D = 3$ plane (top row) and the $Z/D = -3$ plane (bottom row).

In the $Z/D = -3$ plane, Figure 5.17 for the yaw-oscillating cylinder shows that in the first half cycle of oscillation, when the cylinder is accelerating from $\phi = 0$ to $\pi/2$, the streamwise velocity increases. For $K = 1$ and 1.3, this increase in the streamwise velocity is significant enough to eliminate the reverse flow at $\phi = \pi/4$ and $\pi/2$ aligned with the observation previously made in Figure 5.18. While for $K = 0.5$ the streamwise velocity still increases behind the cylinder at $\phi = 3\pi/4$, the impact of cylinder deceleration of the cylinder at this phase leads to a reduction in the streamwise velocity for $K = 1$ and 1.3. The trend for all the reduced frequencies in the return cycle is identical and the reverse flow increases as the
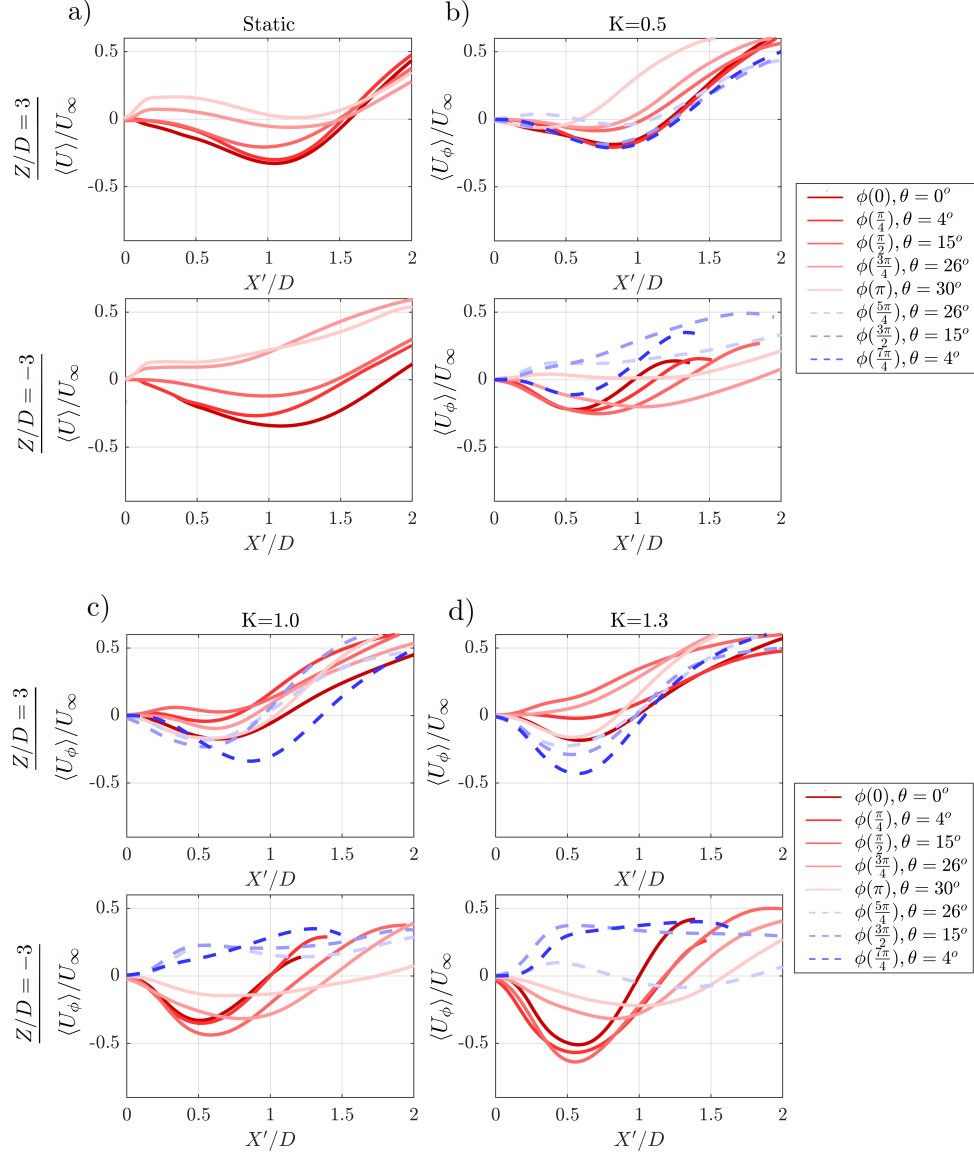
Figure 5.17:   Profiles of a) Mean normalized streamwise velocity ($\langle U \rangle / U_\infty$) on the wake centerline for the static yawed cylinder and b-d) Phase-averaged normalized streamwise velocity ($\langle U_\phi \rangle / U_\infty$) on the wake centerline for eight select phases of yaw-oscillations with reduced frequencies of $K = 0.5$, 1, and 1.3 in $Z/D = 3$ and -3 planes at Re $= 1.5 \times 10^4$.

cylinder return to the non-yawed position.

Figures 5.17 reveals that in the $Z/D = -3$ plane for all the yaw-oscillating cases, the reverse flow velocity increases from $\phi = 0$ and reaches its maximum at $\phi = \pi/2$ in association with the acceleration and direction of motion of the cylinder bottom half. Deceleration of the

cylinder and the increase in the axial flow around the $Z/D = -3$ plane leads to an increase in the streamwise velocity at $\phi = 3\pi/4$. In the return cycle, the strong axial flow (see Figure 4.2) and the induced positive streamwise velocity under the influence of the cylinder motion contribute to the increase in the streamwise velocity on the wake centerline at all the reduced frequencies. For $K = 0.5$, there is no reverse flow occurs behind the cylinder at $\phi = \pi$, $5\pi/4$, and $3\pi/2$. It is only for $\phi = 7\pi/4$ in the return cycle where negative streamwise velocity can be seen on the wake centerline. For $K = 1$, negative streamwise velocity never appears behind the cylinder. However, for $K = 1.3$, reverse flow can be only observed at $\phi = 5\pi/4$ in the return cycle that can be related to the counter-rotating swirls ascending from near the upstream end towards the mid-span.

5.3.2.3   Spanwise Variation of Wake Closure Length

Figure 5.18 depicts the spanwise variation of phase-averaged wake closure length ($\langle L_{c,\phi} \rangle$) for different yaw-oscillating cases at eight select phases of oscillation. The time-averaged wake
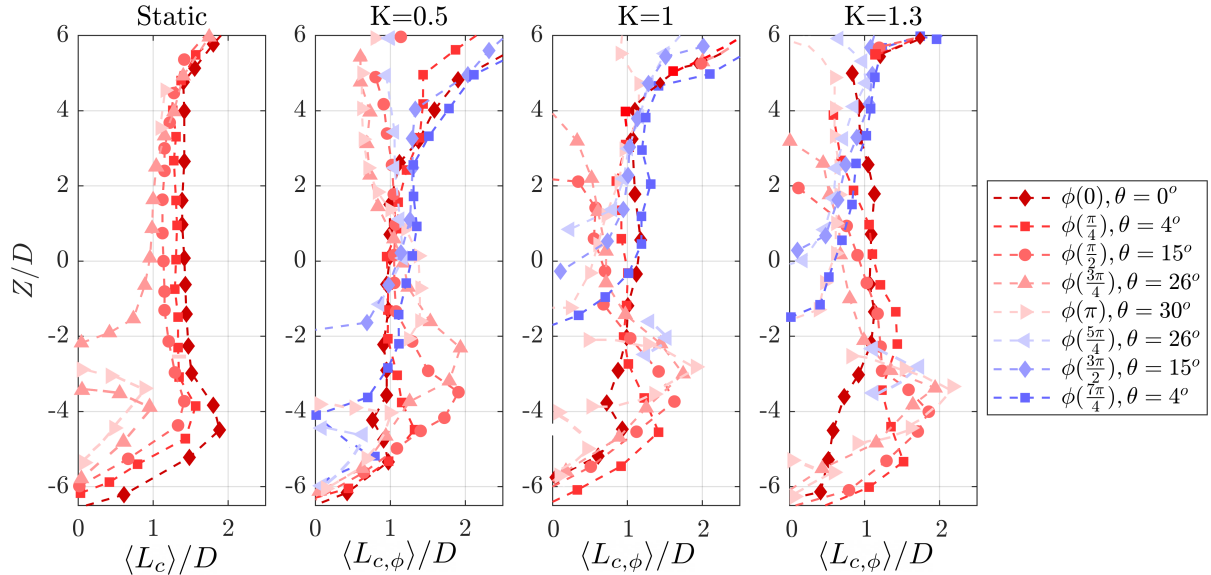
Figure 5.18:   The spanwise variation of phase-averaged wake closure length ($\langle L_{c,\phi} \rangle/D$) at eight select phases for the yaw-oscillating cylinder with various reduced frequencies at Re $= 1.5 \times 10^4$. The mean wake closure length ($\langle L_c \rangle/D$) for the static yawed cylinder are shown at corresponding yaw angles.

closure ($\langle L_c \rangle$) for the static yawed cylinder for corresponding yaw angles are also included in Figure 5.18 as reference values.

Results for the yaw-oscillating cases in Figure 5.18 show that unlike the static yawed cylinder, the wake closure length substantially varies along the span of the cylinder for all yaw-oscillating cases over their entire oscillation period. For $K = 0.5$, it can be observed that in the first half cycle, the wake closure length on the top half of the cylinder generally decreases with increasing yaw angle. For the higher reduced frequencies of $K = 1$ and 1.3, $\langle L_{c,\phi} \rangle / D$ on the top half of the cylinder also generally shows a decrease from $\phi = 0$ to $\pi/2$, with the mean recirculation bubble being partially suppressed near the top half of the cylinder below the free-surface affected region where the recirculation bubble is locally enlarged. This suppressed region for the mean recirculation bubble in the top half extends at most from $Z/D = 5.5$ to around $Z/D = 2$ for both $K = 1$ and 1.3 at $\phi = \pi/2$, which may be attributed to a high acceleration rate in cylinder's top half motion in the freestream direction. For $K = 1$ and 1.3 from $\phi = 3\pi/4$ to π, the large deceleration in the motion of cylinder causes the mean recirculation bubble on the top half to appear again (as also seen in Figure 5.2), and the wake closure length gradually increases. On the bottom half of the cylinder, in the first half of the oscillation cycle, the trend in Figure 5.18 is almost similar for all the reduced frequencies. That is, near the bottom half of the cylinder (particularly from the bottom end up to around $Z/D = -2$), the maximum wake closure length generally increases from $\phi = 0$ to $3\pi/4$, and at these phases, the location of the maximum $\langle L_{c,\phi} \rangle / D$ approaches more and more toward the middle section of the cylinder with increasing yaw angle. This trend seems to be related to the spread of the tip vortices to upper spanwise regions with increasing yaw angle as a result of the increase in the spanwise flow (which is apparent from a combined inspection of Figures 5.2 to 5.4). In the first half of the return cycle, as the cylinder moves from $\phi = \pi$ to $5\pi/4$, the phase-averaged recirculation bubble becomes suppressed over a large spanwise extent within the lower half of the span for $K = 0.5$ due to the positive streamwise thrust exerted on the fluid by the movement of the bottom half of the cylinder and the large axial flow (which was noted in Figure 5.4). This suppression covers the entire lower half of

the cylinder for larger reduced oscillation frequencies of $K = 1$ and 1.3, presumably due to the additional effect of large cylinder acceleration. In the second half of the return cycle, as the cylinder moves from $\phi = 5\pi/4$ to its upright location at $\phi = 0$, the spanwise region having zero wake closure length behind the lower half of the cylinder gradually lessens for all K, with $K = 1$ and 1.3 still showing most of the lower half span suppressed before returning to the upright position at $\phi = 7\pi/4$.

5.3.2.4 Backflow Angle

In another approach to quantitatively investigate the spanwise variation of near-wake flow patterns, the direction of the reverse flow streamlines has been explored in the current study as defined in Section 3.5. Figures 5.19 (b) to 5.19 (d) depict the variation of β on three spanwise locations in the $Y/D = 0$ plane, namely at $Z/D = 3$, 0, and -3, for the yaw-oscillating cylinder at eight select phases of oscillation with various reduced frequencies. Results for the static yawed cylinder at yaw angles corresponding to the phases of oscillation are presented in Figure 5.19 (a). The dashed line in Figure 5.19 represents the reverse flow angle of $\beta = 90^{\circ}$. Below this angle, the flow in the near wake possesses no negative streamwise velocity component, hence, no mean recirculation region exists.

For the static yawed cylinder in Figure 5.19 (a) show that from the crossflow position ($\theta = 0^{\circ}$) to $\theta = 26^{\circ}$, the reverse flow angle near the upper-middle section of the cylinder is higher than the one obtained near the lower-middle section, however, this difference gradually decreases by increasing the yaw angle. The reverse flow angle is almost identical on the three locations for $\theta = 30^{\circ}$. This implies that with increasing yaw angle, the flow patterns become more uniform along the span of the cylinder. The decrease in the reverse flow angle by increasing yaw angle can be attributed to the increase in the extent of axial flow in the near-wake of the cylinder that directs the streamlines further orthogonal to the freestream direction.

For $K = 0.5$, similar to the static case, the spanwise uniformity of the reverse flow angle increases with increasing yaw angle from $\phi = 0$ to $\phi = \pi$. However, when the cylinder is
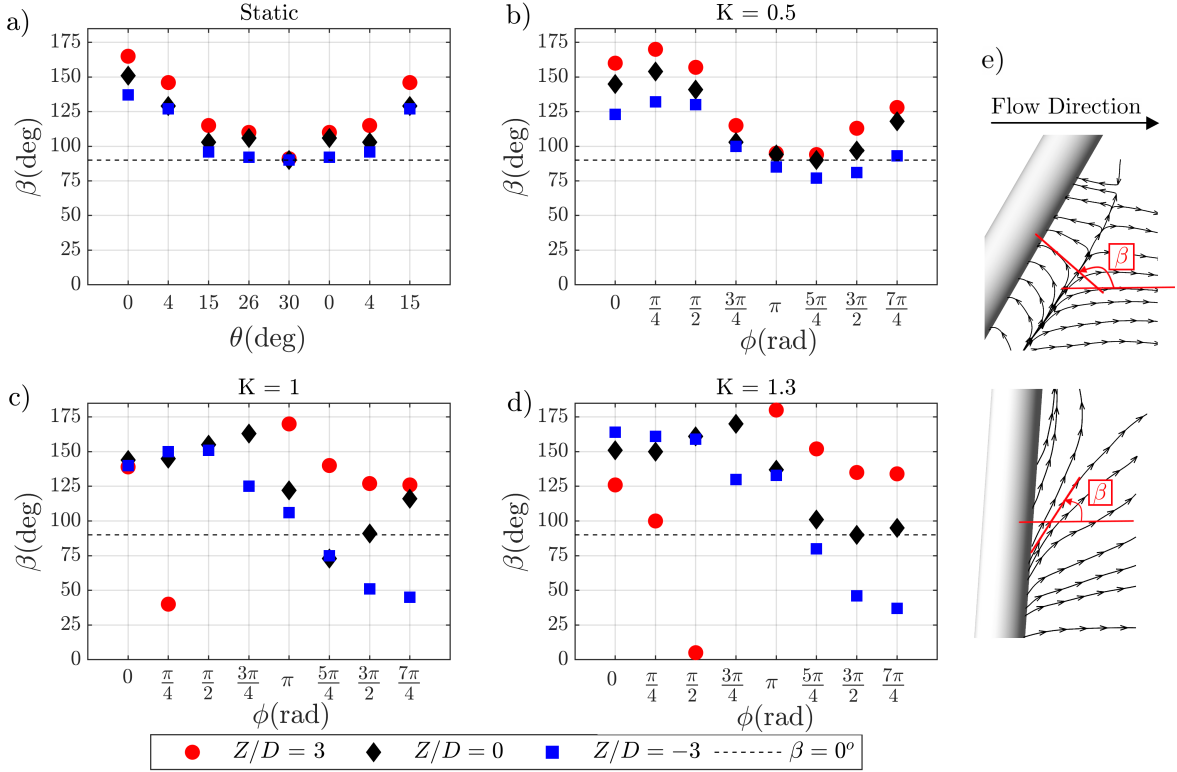
Figure 5.19:   Variation of the reverse flow angle (β) at three spanwise locations of $Z/D = 3$, 0, and -3 for a) The static yawed cylinder at different yaw angles corresponding to the phases of oscillation and b-d) The yaw-oscillating cylinder at eight select phases of yaw oscillations with reduced frequencies of $K = 0.5$, 1, and 1.3 at Re $= 1.5 \times 10^4$. e) The schematics show how the reverse flow angle is measured in the presence (top) or the absence (bottom) of the mean recirculation region.

yawed from the crossflow position ($\phi = 0$) to $\phi = \pi/4$, the reverse flow angle increases on all three locations. At $Z/D = 3$, this trend is presumably the influence of the downward flow occurring on the rear surface of the cylinder (near the top end) whereas for $Z/D = -3$, it can be attributed to the increase in the strength of the reverse flow near the upstream end of the cylinder. At $\phi = \pi$, the reverse flow angle of around $\beta = 90º$ occurs at $Z/D = 3$ and the first acute reverse flow angle is observed at $Z/D = -3$. Notice that when the acute reverse flow angle is obtained at each location, the mean recirculation region is shown to be suppressed at the vicinity of that region (see Figure 5.18). The suppression at $Z/D = -3$ occurs due to a strong axial flow around that location, which is in agreement with the axial velocity contours previously shown in Figure 4.2. The development of the axial flow along the majority of the

span is seen at $\phi = 5\pi/4$ with the measured reverse flow angles being close and even below 90°. From $\phi = 3\pi/2$ to $\phi = 7\pi/4$, the increase in β at the mid-span and $Z/D = 3$ indicates the increase in the reverse flow around these locations while the effect of axial flow is still discernible at $Z/D = -3$.

Increasing the reduced frequency to $K = 1$ and $K = 1.3$ leads to a substantial spanwise variation of β. In the first half of the oscillation cycle, at $Z/D = 3$, as the cylinder is yawed from the non-yawed position, the reverse flow angle drops from obtuse to acute angle at $\phi = \pi/4$. Negative values of β are obtained at $\phi = \pi/2$ and $3\pi/4$ (not shown in Figures 5.19 (c) and (d)). This flow pattern is aligned with the previous observation made in Figure 5.1, where the flow behind the upper half of the cylinder is in the downward direction under the influence of the rapid cylinder motion. From $\phi = \pi$ to $7\pi/4$, the obtuse angle is obtained at $Z/D = 3$ indicating the existence of the reverse flow region and progressively decreases as the cylinder is returning to crossflow position due to the development of axial flow on the span of the cylinder around this location. At $Z/D = 0$, it is evident that the axial flow becomes effective from $\phi = 3\pi/4$ where β starts decreasing from around $\beta = 180^o$. This trend continues until the acute angle is first obtained at $\phi = 5\pi/4$ and $3\pi/2$ for $K = 1$ and 1.3, respectively. Beyond these phases, the reverse flow angle increases in the return cycle. On the lower-middle section of the cylinder, at $Z/D = -3$, the decrease in the reverse flow angle starts from $\phi = 3\pi/4$, similar to the trend discussed for the mid-span location. However, at $Z/D = -3$, β consistently decreases from $\phi = 3\pi/4$ until $\phi = 7\pi/4$ from around 100° and 125° to around 50° and 30° for $K = 1$ and $K = 1.3$, respectively.

5.4 Vortex Shedding

5.4.1 Yaw-Averaged Analysis

In this section, the frequency analysis is performed on the continuous streamwise velocity signal obtained during 1200 oscillation cycles. Figure 5.20 shows the velocity spectra for the yaw-oscillating cylinder with a reduced frequency that varies from 0.25 to 1.3 at Re
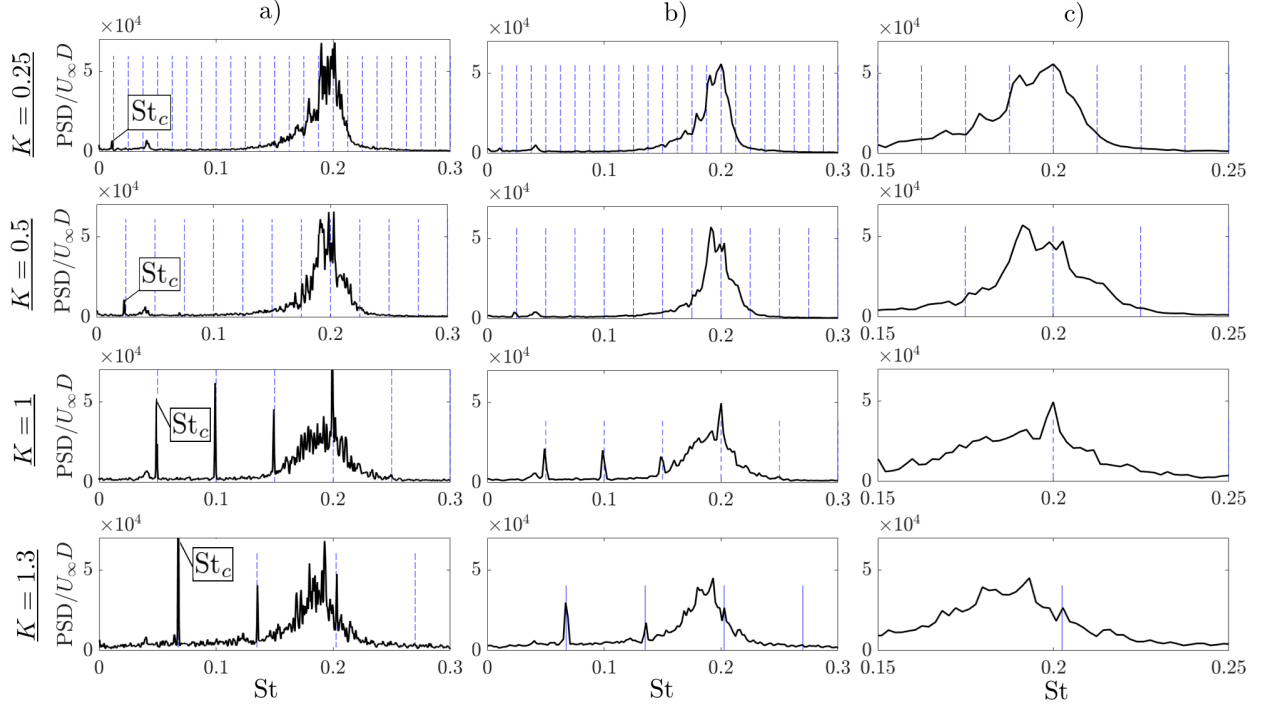
Figure 5.20: The velocity spectra for the yaw-averaged streamwise velocity signal of the yaw-oscillating cylinder at various reduced frequencies. a) The PSD obtained at the frequency resolution of 0.012 Hz ($\mathrm{St}_{res} = 0.0019$) b) The PSD obtained at the frequency resolution of 0.006 Hz ($\mathrm{St}_{res} = 0.00095$) c) The velocity spectra in the in the range of $0.15 < \mathrm{St} < 0.25$. The Strouhal number of fundamental oscillation frequency (St_c) and its harmonics are marked with blue dashed lines.

$= 1.5 \times 10^4$. The power spectral density (PSD) estimation is provided for two different window sizes used in the Welch method, which results in different frequency resolutions (f_{res}) in the fast Fourier transform (FFT). Note that 50% overlap is used in Welch method for all the cases. Figure 5.20 (a) and (b) represent the velocity spectra for FFT frequency resolutions of 0.012 Hz ($\mathrm{St}_{res} = 0.0019$) and 0.006 Hz ($\mathrm{St}_{res} = 0.00095$), respectively. The variation of velocity spectra in Figure 5.20 (b) that is limited to the range of Strouhal numbers associated with the vortex shedding frequencies are shown in Figure 5.20 (c). The dashed lines in each plot mark the Strouhal number of frequency of oscillation and its harmonics. The Strouhal numbers corresponding to the fundamental frequency of oscillations ($\mathrm{St}_c = f_c D / U_\infty$) are 0.0125, 0.025, 0.05, and 0.065 for $K = 0.25$, 0.5, 1, and 1.3, respectively. Figures 5.20 (a) and
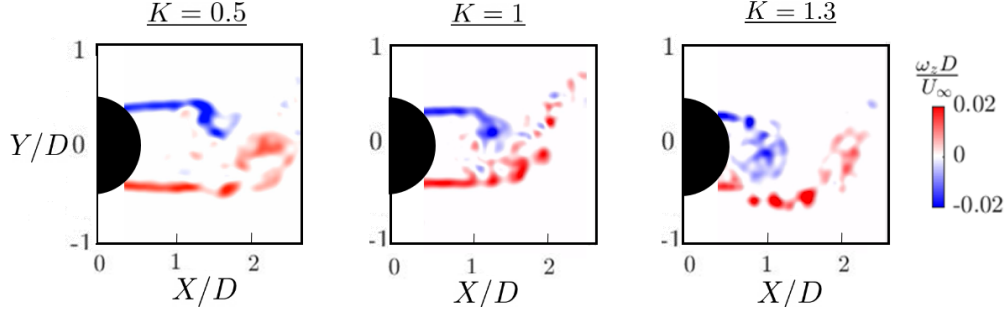
Figure 5.21: Instantaneous vorticity ($\omega_z D/U_\infty$) at the mid-span for the yaw-oscillating cylinder with $K = 0.5$, 1, and 1.3 at $\phi = \pi/2$.

(b) reveal the narrow-band peaks in the range of low Strouhal numbers from 0 to around 0.15. These peaks are associated with the frequency of oscillation (St_c) and its harmonics at each reduced frequency. It is shown that the energy of these peaks is substantially higher at higher reduced frequencies of $K = 1$ and 1.3, which is more pronounced when the lower frequency resolution is used in the FFT process in Figure 5.20 (a). Additionally, it is apparent that for reduced frequencies of $K = 1$ and 1.3, the high energy peaks in the velocity spectra, which are related to the harmonics of the oscillation frequency, occur in the range of frequencies associated with the frequency of vortex shedding that is around $\text{St} = 0.2$.

Inspecting Figures 5.20 (b) and (c) for the range of $0.15 < \text{St} < 0.25$ demonstrates that by increasing the reduced frequency, the peak frequencies corresponding to the vortex shedding become more broadband while the peak region is drawn towards lower frequencies. In other words, by increasing the reduced frequency, the vortex shedding becomes further disorganized accompanied by the breakdown of the large-scale structures and consists of lower frequencies. Moreover, Figures 5.20 (b) and (c) indicate the reduction in the height and energy of the peaks in the range of $0.15 < \text{St} < 0.25$ by increasing the reduced frequency, which can be associated with the lower intensity of the vortex shedding. Figure 5.21 depicts the instantaneous vorticity field at $\phi = \pi/2$ for the yaw-oscillating cases with $K = 0.5$, 1, and 1.3 at the mid-span. The figure demonstrates that the vortices shed closer to the surface of the cylinder and become more disorganized by increasing the yaw angle.

5.4.2   Phase-Averaged Analysis and Validity of IP

In this section, the variation of the vortex shedding frequency with the phase of oscillation for the yaw-oscillating cylinder at various reduced frequencies is investigated. In the phase-averaged analysis, the frequency analysis is performed using the peak finding method. In the first step, as the focus is only on the range of vortex shedding frequency, low frequencies associated with the oscillation frequency and its harmonics, as well as very high frequencies, are required to be filtered from the signal. Therefore, a bandpass filter is applied to the streamwise velocity signal to filter out frequencies below 0.75 Hz and above 1.75 Hz. Note that the harmonics of the oscillation frequency are also removed using a narrow bandpass filter. Figure 5.22 shows the velocity spectra of the raw and filtered streamwise velocity signal for the yaw-oscillating cylinder with the reduced frequencies of $K = 0.5$ and 1.0.

In the next step, for each yaw-oscillating cylinder case, as shown in Figure 5.23 (a) for $K = 0.5$ as an example, the minimum and the maximum peaks in the streamwise velocity
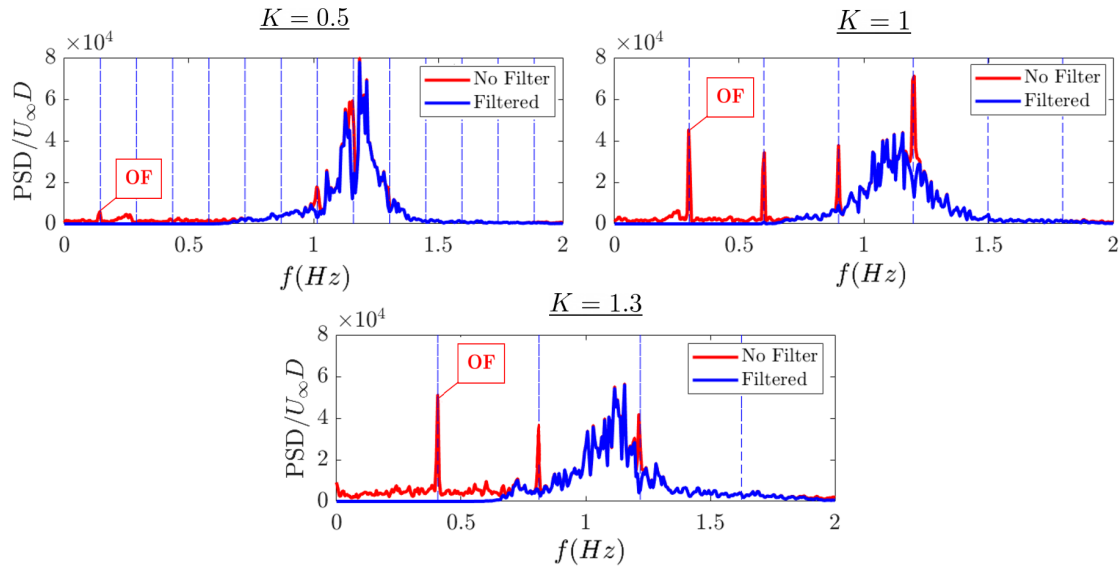
Figure 5.22: The velocity spectra for the streamwise velocity signal of the yaw-oscillating cylinder for two reduced frequencies of $K = 0.5$, 1, and 1.3. The red line indicates the velocity spectra without any filtering against the velocity spectra of the signal with bandpass filter of $f > 0.75$ and $f < 1.75$ applied represented by blue line. For the blue line, the yaw oscillation frequency and its harmonics are also filtered out.
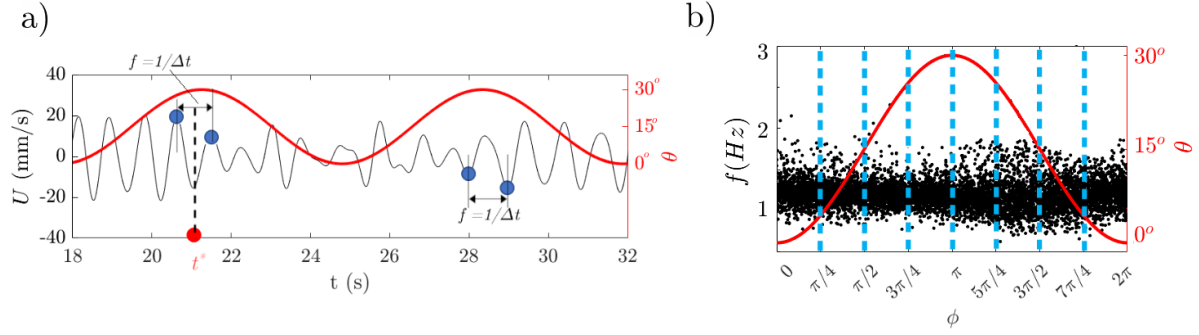
Figure 5.23: a) The variation of the streamwise velocity signal with time and the phase of oscillation (marked by red color). The time difference between each maximum and minimum peaks are calculated and converted to frequency ($f = 1/\Delta t$). Time (t^*) is allocated to each set of successive peaks. b) Distribution of all the calculated peak frequencies along a complete phase of oscillation. To measure the variation of vortex shedding with the phase of oscillation, the values of f are averaged over eight equal periods marked by blue dashed lines.

signal is founded. Then, the time difference (Δt) between the successive maximum peaks and successive minimum peaks in the velocity signal is calculated. This time difference is inverted to be represented as a frequency and is obtained for all the peaks within the whole duration of the signal. In order to relate the occurrence of the peaks to the phase of oscillation, a specific time (t^*) is allocated to each set of successive peaks, which is the average of their actual time in the signal. This time can be directly related to the corresponding phase of oscillation and yaw angle of the cylinder, marked by the red curves in Figure 5.23 (a). Finally, the frequencies (f) and their respective time (t^*) in each yaw oscillation cycle are obtained and for around 1200 cycles are distributed along a complete yaw oscillation cycle as shown in Figure 5.23 (b).

In order to estimate the variation of the frequency of vortex shedding with the phase of oscillation, the peak frequency values are averaged over eight equal periods with the length of $\pi/4$ throughout the oscillation, as marked in Figure 5.23 (b). The analysis on different yaw-oscillating cases indicated that by increasing the reduced frequency, the peak frequencies tend to be distributed along a wider range of values, hence, the averaging over each period would be inevitably biased and would lower the accuracy of the phase-averaged vortex shedding frequencies at each phase. Therefore, in the present study, the phase-averaged analysis for

the peak frequencies is only implemented on the low reduced frequencies of $K = 0.25$ and 0.5.

Figure 5.24 (a) indicates the variation of the averaged values of peak frequencies at eight different phases for reduced frequencies of $K = 0.25$ and 0.5. It is shown that for $K = 0.25$, the frequencies for the same yaw angle but at different half cycles of oscillation are almost similar and the frequency of shedding decreases with yaw angle at each half cycle. In other words, the results for $K = 0.25$ are almost independent of the direction of motion of the cylinder and similar to the static cylinder, the frequency of shedding only changes with the yaw angle. It can be deduced that the yaw-oscillating cylinder at very low K values represents the quasi-steady state case. However, for $K = 0.5$, it is observed that the frequency of shedding at the same yaw angle depends on the direction of motion of the cylinder. In the first half of oscillation, increasing yaw angle leads to a decrease in the frequency of shedding. This decrease in the frequency continues to around $\phi = 3\pi/2$ in the second half of oscillation and then starts increasing up to $\phi = 7\pi/4$. The decrease in the vortex shedding frequency is in agreement with the increase in the length and the lateral distance of the shear layers at the
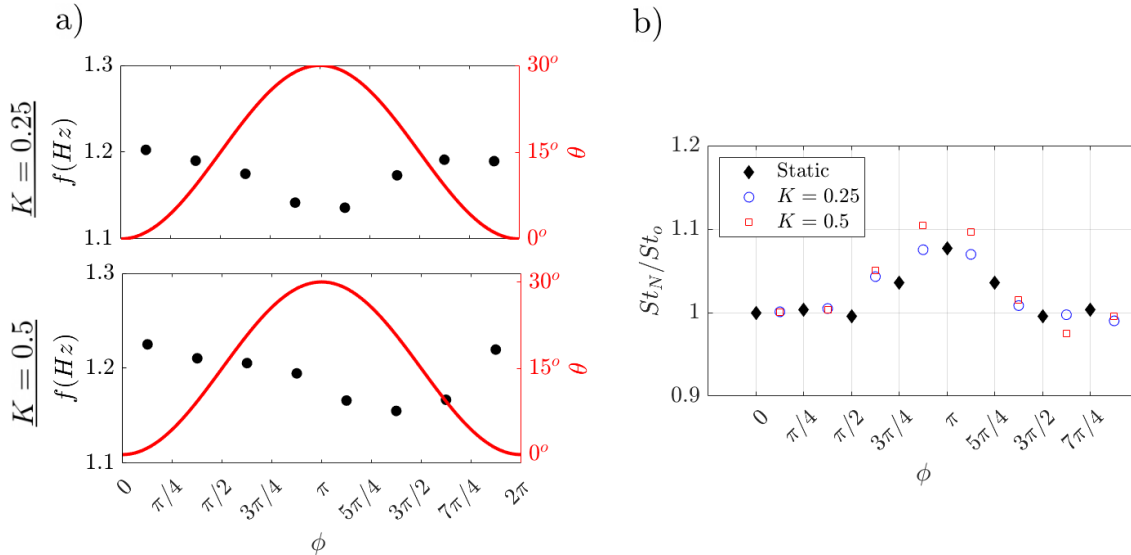
Figure 5.24: a) Phase-averaged vortex shedding frequency at various phases for the yaw-oscillating cylinders with reduced frequencies of $K = 0.25$ and 0.5. b) Variation of St_o/St_N with the phase of oscillation for the yaw-oscillating cylinders. Results for the static yawed cylinders are also provided as reference values.

corresponding phases, as previously shown in the phase-averaged vorticity field in Figure 5.7.

The validity of IP for the yaw-oscillating cases using the results obtained in Figure 5.24 is evaluated in Figure 5.24 (b). Results of the static yawed cylinders discussed in Section 4.3 are also provided to ease the comparison. Figure 5.24 (b) reveals that similar to the static yawed cylinder, the IP fails for the yaw-oscillating cases beyond $\phi = \pi/2$ ($\theta = 15^\text{o}$) up to around $\phi = 7\pi/4$ ($\theta = 4^\text{o}$) in the return cycle. It can also be seen that increasing the reduced frequency leads to further deviation of the vortex shedding frequency from the IP prediction.

5.5   Chapter Summary

In this chapter, the effect of the reduced frequency on the near wake of a yaw-oscillating cylinder with $L/D = 13$ at $\text{Re} = 1.5 \times 10^4$ was evaluated and compared with the static basline. The reduced frequency varied from low ($K = 0.25$, 0.5) to moderate ($K = 1$ and 1.3) values.

For the yaw-oscillating cylinder, the phase-averaged results showed that unlike the static cylinder, the near wake is highly three-dimensional. The spanwise variation in the near wake increased with the increase in the reduced frequency from low to moderate values. The cylinder's direction of motion, its acceleration/deceleration, and the axial flow generated from the bottom end impacted the near-wake flow behavior. For low reduced frequencies, the cylinder's direction of motion played the most prominent role in the topology of the near wake until large yaw angles. When half of the cylinder's span moved in the freestream direction, this movement added a positive thrust to the flow, leading to a shorter wake closure length and a weaker mean recirculation region behind that section. In contrast, the movement of the cylinder's half against the freestream direction increased the reverse flow behind that section of the cylinder, making the mean recirculation region stronger. At large yaw angles, high-magnitude axial flow developed along the span, becoming the most influential parameter controlling the flow topology in addition to the cylinder's direction of motion effect. The development of strong axial flow resulted in lower reverse flow velocity in the wake and eventually led to the suppression of the mean recirculation region. For moderate values

of reduced frequencies, the acceleration/deceleration of the cylinder became another factor influencing the flow behavior. For the phases with the accelerating cylinder, the effect of the cylinder's direction of motion was intensified whereas it was weakened for the phases with the decelerating cylinder.

Evaluating the vortex shedding behavior at the mid-span of the yaw-oscillating cylinder revealed that increasing the reduced frequency results in a more disorganized vortex shedding at a relatively lower range of shedding frequencies. Moreover, for the yaw-oscillating cylinder, the failure of the independence principle at high yaw angles was found, similar to the trend observed for the static cylinder.

Chapter 6

Results: Effect of Reynolds Number

The influence of Reynolds number on the near wake of the stationary yawed and the yaw-oscillating cylinder is assessed by considering two additional lower Reynolds numbers of 1×10^4 and 5×10^3. The flow topology, wake parameters, and vortex shedding for the lower Reynolds numbers are compared to the results for $\mathrm{Re} = 1.5 \times 10^4$ discussed in Chapters 4 and 5.

6.1 Flow Structure in the (X, Z) Symmetry Plane

6.1.1 Static Yawed Cylinder

Figure 6.1 and 6.2 depict the mean streamline topology ($\langle \psi \rangle$) and contours of normalized mean streamwise velocity ($\langle U \rangle / U_\infty$) in the near wake of the static yawed cylinder at three Reynolds numbers for yaw angles of $\theta = 0^\text{o}$, 4°, 15°, 26°, and 30°. In these figures, it is shown that in the near wake of the cylinder at $\mathrm{Re} = 1.5 \times 10^4$ and 1×10^4, the topology of the streamlines is almost identical whereas the streamwise extent of the reverse flow region is slightly greater for the lower Reynolds number. The elongation of the mean recirculation region with decreasing Reynolds number is consistent with the results shown in the literature for the non-yawed static cylinder in the subcritical flow regime [1]. Figure 6.1 depicts that

107
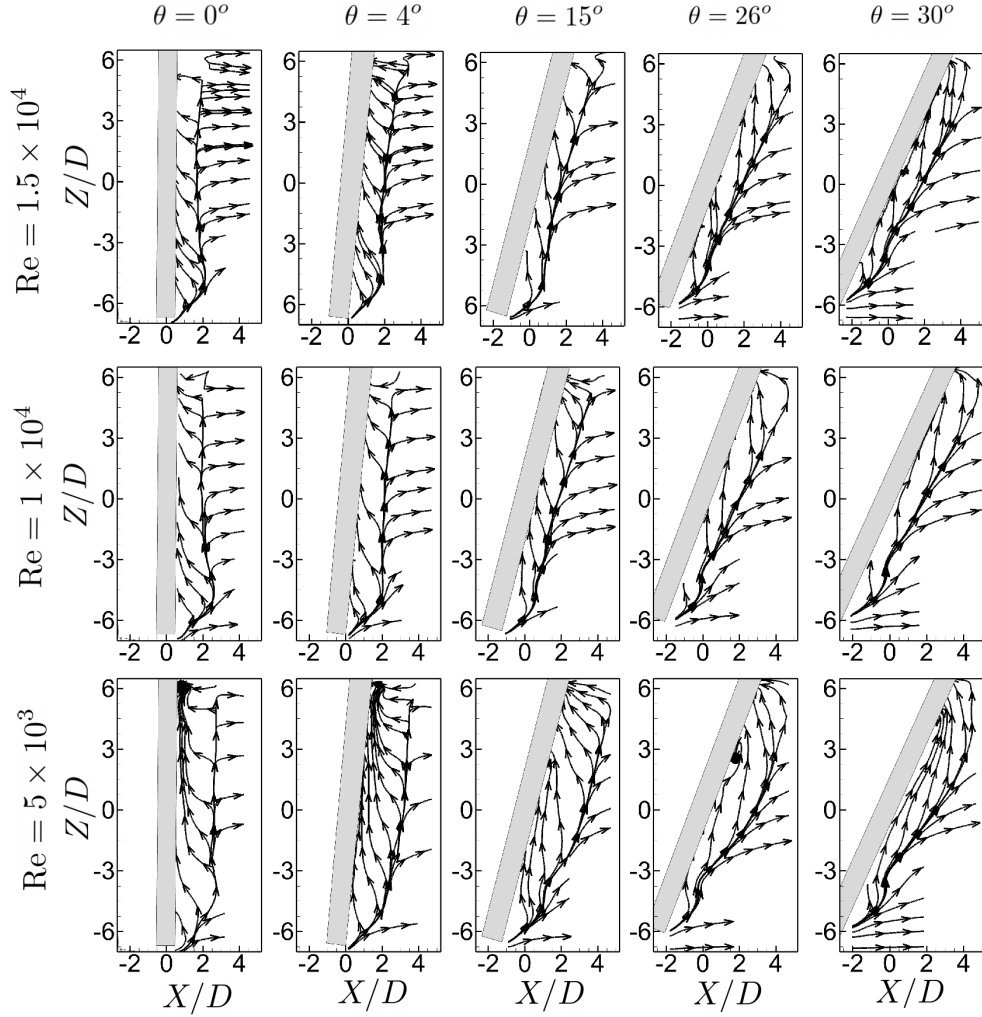
Figure 6.1: Mean streamline topology ($\langle \psi \rangle$) for the static cylinder at yaw angles of $\theta = 0^o$, 4°, 15°, 26°, and 30° at Re $= 1.5 \times 10^4$, 1×10^4, and 5×10^3 in the symmetry plane at $Y/D = 0$.

for Re $= 5 \times 10^3$ at $\theta = 0^o$ and $\theta = 5^o$, the flow immediately downstream the cylinder is more inclined in the spanwise direction compared to higher Reynolds number cases. Moreover, it can be seen that for Re $= 5 \times 10^3$, at $\theta = 15^o$ the streamlines near the mid-span tend to move in the downward direction and at $\theta = 26^o$ the flow separates on the downstream surface of the cylinder and then reattaches around $Z/D = 3$. The same flow behavior is seen closer to the top free surface-piercing end of the cylinder (around $Z/D = 5$) at $\theta = 30^o$. As shown
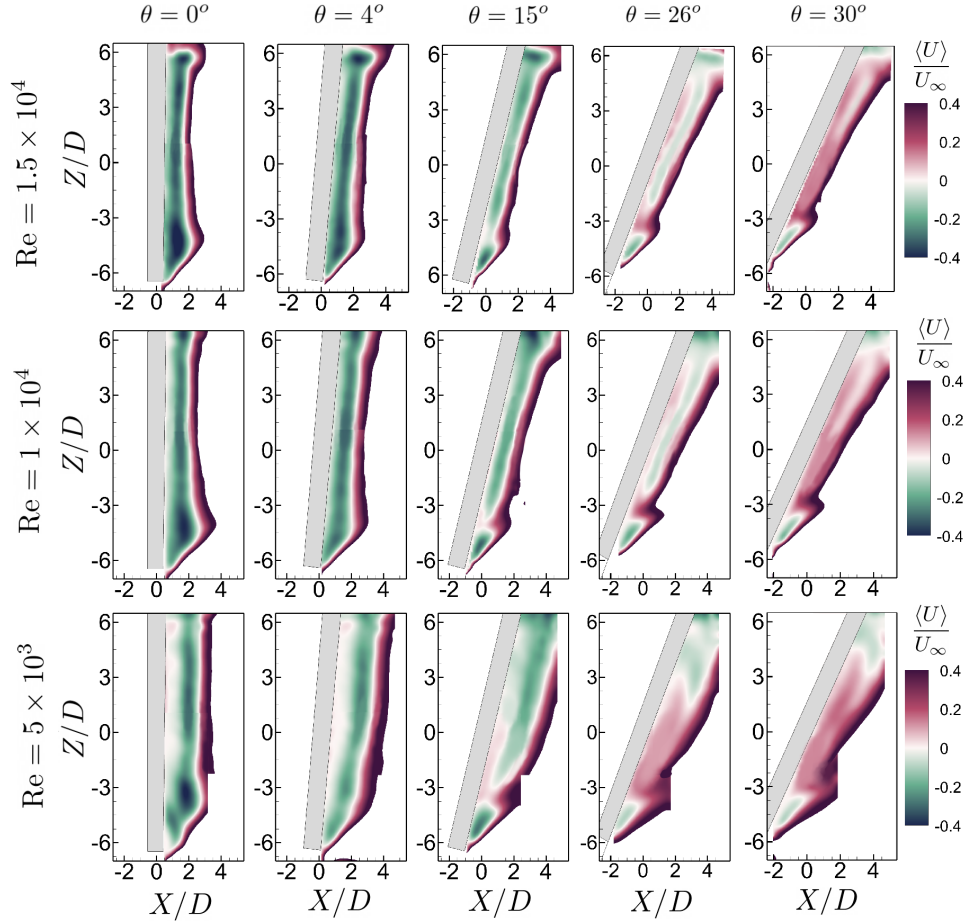
Figure 6.2: Contours of mean normalized streamwise velocity ($\langle U \rangle / U_\infty$) for static cylinder at yaw angles of $\theta = 0^o$, 4°, 15°, 26°, and 30° at Re $= 1.5 \times 10^4$, 1×10^4, and 5×10^3 in the symmetry plane at $Y/D = 0$.

in Figure 6.2, from $\theta = 15^o$ to 30°, the magnitude of the streamwise velocity near the lower half of the cylinder at Re $= 5 \times 10^3$ is greater than for other cases. Overall inspection of $\langle \psi \rangle$ and $\langle U \rangle / U_\infty$ shows that by decreasing the Reynolds number the mean recirculation region is further elongated downstream by moving towards the top surface-piercing end.

Figure 6.3 shows the mean normalized vorticity ($\langle \omega_y \rangle D / U_\infty$) for the static yawed cylinder at the three Reynolds numbers. The general trend in the variation of the negative and positive vorticity is similar for all the Reynolds numbers, particularly for regions close to
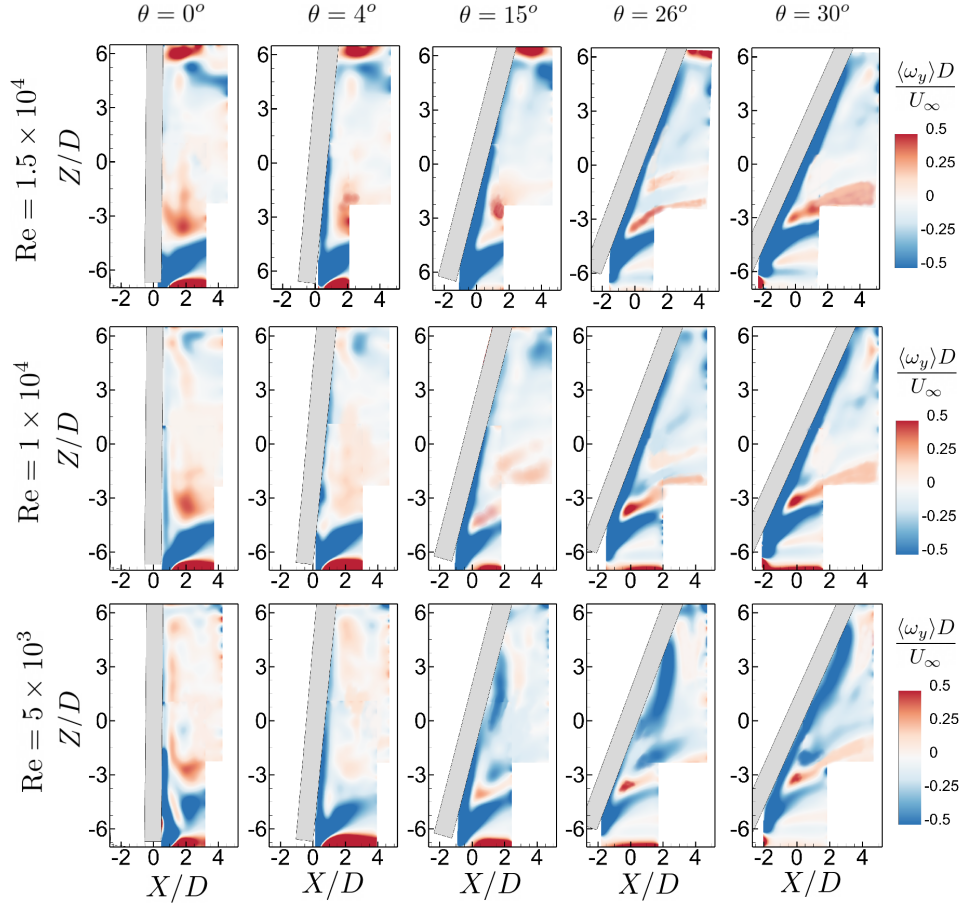
Figure 6.3: Contours of mean normalized vorticity $(\langle\omega_y\rangle D/U_\infty)$ for the static cylinder at yaw angles of $\theta = 0^o$, 4°, 15°, 26°, and 30° at Re $= 1.5 \times 10^4$, 1×10^4, and 5×10^3 in the symmetry plane at $Y/D = 0$.

the upstream free end. Near the surface-piercing end of the cylinder, for all yaw angles, the region and magnitude of the positive vorticity decrease with the Reynolds number, which occurs due to lower impact of free surface on the near wake of the cylinder at lower Reynolds numbers. For $\theta = 0^o$ and 4°, it is evident that the negative vorticity develops further in the spanwise direction for lower Reynolds numbers. For Re $= 5 \times 10^3$, beyond $\theta = 15^o$, an increase in the negative vorticity is observed near the downstream surface of the cylinder in the range of $Z/D = 0$ to $Z/D = 3$. The strong negative vorticity around $Z/D = 3$ at $\theta = 26^o$ and 30° is aligned with the separation and reattachment of the flow on the downstream surface of cylinder, as shown in Figure 6.1.
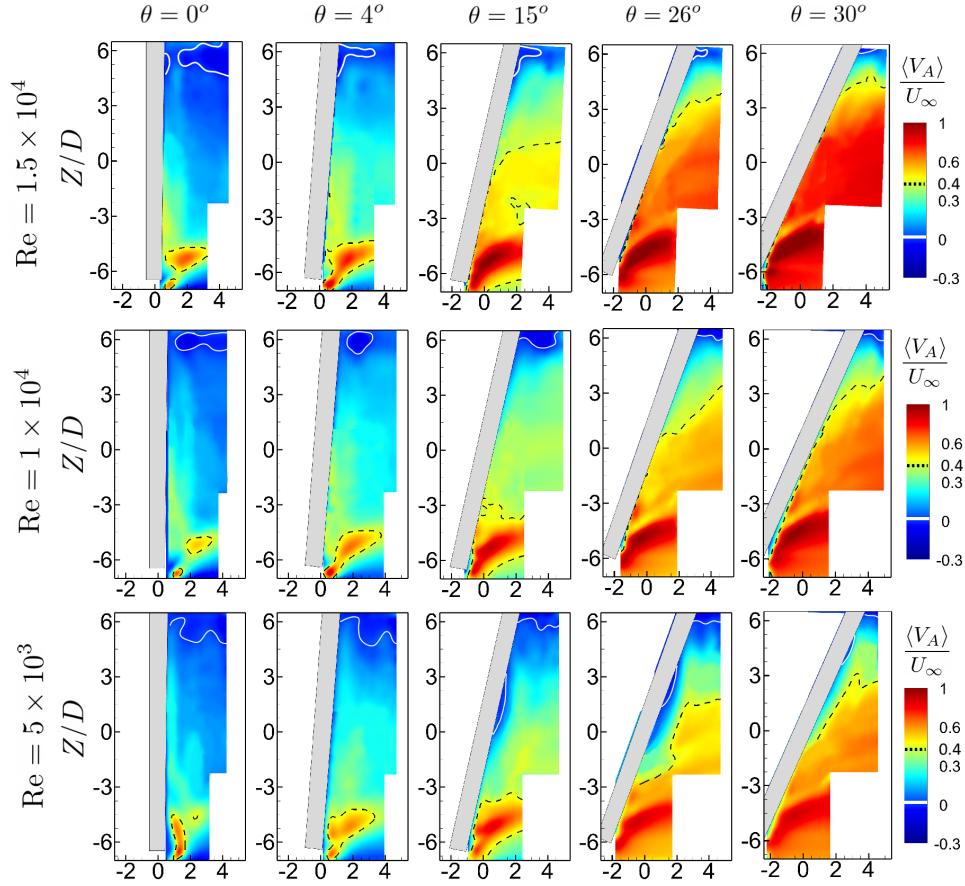
Figure 6.4: Contours of mean normalized axial velocity ($\langle V_A \rangle / U_\infty$) for static cylinder at yaw angles of $\theta = 0^o$, 4°, 15°, 26°, and 30° at Re $= 1.5 \times 10^4$, 1×10^4, and 5×10^3 in the symmetry plane at $Y/D = 0$. Contour levels of $\langle V_A \rangle / U_\infty = 0$ and 0.5 are marked by while solid line and black dashed line, respectively.

Contours of mean axial velocity ($\langle V_A \rangle / U_\infty$) for the static yawed cylinder at the three Reynolds numbers are depicted in Figure 6.4. As previously explained in Section 4.1 for Re $= 1.5 \times 10^4$, the extent of axial velocity in the spanwise direction increases with yaw angle and the trend is similar for all Reynolds numbers. From Figure 6.4 it can be inferred that in the range of the subcritical regime, the magnitude of positive axial velocity behind the cylinder increases with Reynolds number at all yaw angles. This variation is more pronounced at higher yaw angles of $\theta = 26^o$ and 30°. For instance, at Re $=1.5 \times 10^4$, the axial velocity

of around $0.8U_\infty$ occurs downstream the lower half of the span, while the maximum axial velocity of $0.5U_\infty$ is seen from the bottom free end up to $Z/D = -3$ at Re $= 5 \times 10^3$. For Re $= 5 \times 10^3$, beyond $\theta = 15^o$, the separation of flow on the downstream surface of the cylinder, which was explained earlier in this section, is shown by a decrease in the magnitude of axial velocity between the mid-span and $Z/D = 3$.

6.1.2 Yaw-Oscillating Cylinder

In this section, the effect of Reynolds number is investigated on the flow behavior in the near wake of a yaw-oscillating cylinder. Results in Chapter 5 for the cylinder undergoing yaw oscillation at Reynolds number of 1.5×10^4 are compared with the lower Reynolds numbers of 1×10^4 and 5×10^3. For the analysis done in this section, only the yaw-oscillating case with $K = 1.3$ is considered as the case with significant near-wake flow variations along the span. Figure 6.5 shows the phase-averaged streamline patterns ($\langle \psi_\phi \rangle$) for the eight phases of oscillation with $K = 1.3$ at the three Reynolds numbers considered. Contours of phase-averaged normalized streamwise velocity ($\langle U_\phi \rangle / U_\infty$) for the aforementioned cases are depicted in Figure 6.6.

Discussions on the spanwise flow structure downstream the yaw-oscillating cylinder at $K = 1.3$ and Re $= 1.5 \times 10^4$ can be found in Section 5.1. Comparing the results over the entire cycle indicates that the flow topology for $K = 1.3$ is generally similar at all the Reynolds numbers considered and only subtle differences are observed. For instance, near the free surface-piercing end of the cylinder, particularly in the first half of the oscillation cycle, the region of negative streamwise velocity is diminished owing to the lower impact of the free surface. Moreover, similar to the observation made for the static yawed cylinder, when the mean recirculation region exists in the wake, the streamwise extent of this region increases with decreasing Reynolds number. In the first half cycle, near the bottom half of the cylinder, it can be seen from Figure 6.6 that the magnitude of backflow velocity decreases with decreasing Reynolds number at the same phase of oscillation. In the return cycle and near the top half of the span, the negative streamwise velocity is shown to be slightly higher for
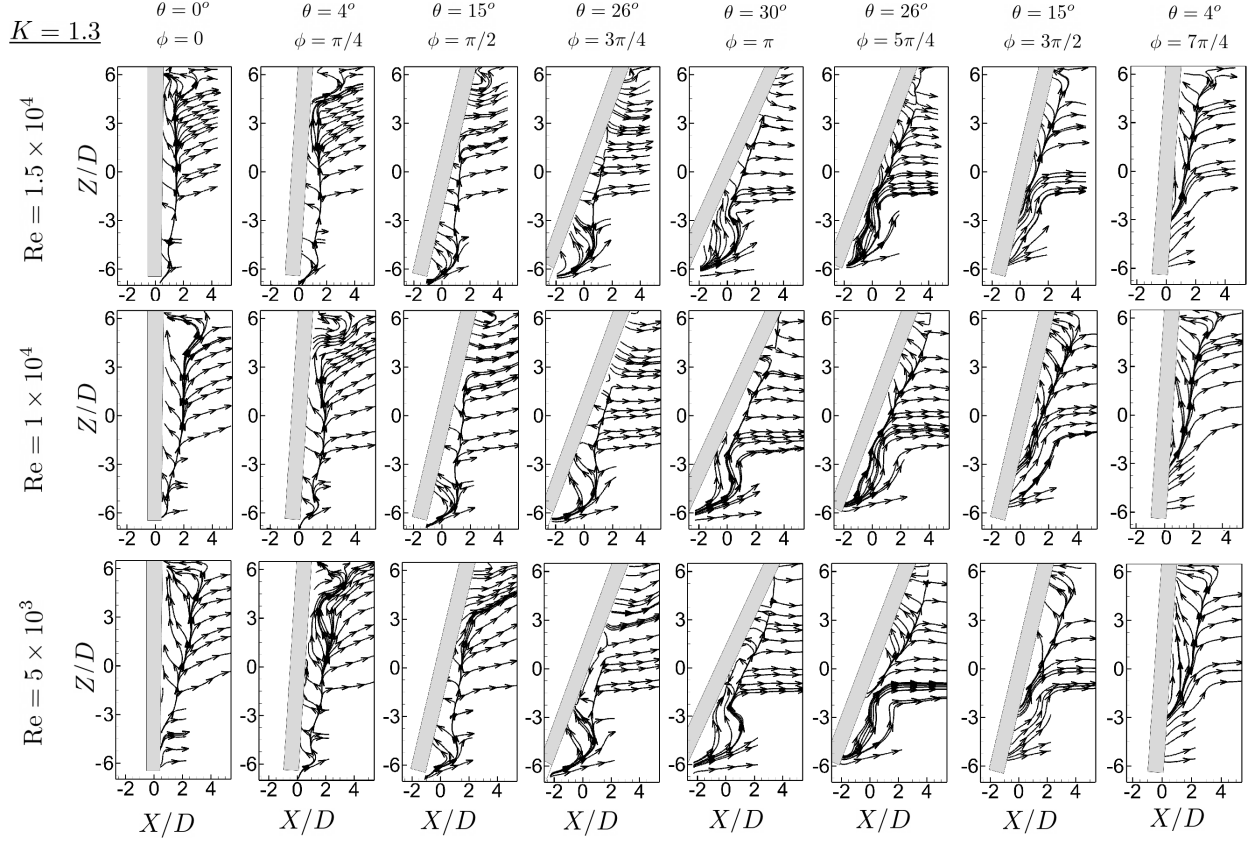
Figure 6.5: Phase-averaged streamline topology ($\langle \psi_\phi \rangle$) for the yaw-oscillating cylinder with reduced frequency of $K = 1.3$ at Re $= 1.5 \times 10^4$, 1×10^4, and 5×10^3 in the symmetry plane at $Y/D = 0$.

Re $= 5 \times 10^3$. From the similarity of the flow structure for the yaw-oscillating cylinder with $K = 1.3$ at all Reynolds numbers shown in Figures 6.5 and Figure 6.6, it can be inferred that flow past yaw-oscillating cylinder is almost independent of Reynolds number in the range of subcritical flow.

6.1.3   High Reduced Frequencies

The range of reduced frequency was extended to greater values within the mechanical limitations of the system. By reducing the freestream velocity for the lower Reynolds number, the reduced frequency can be increased while remaining below the maximum value
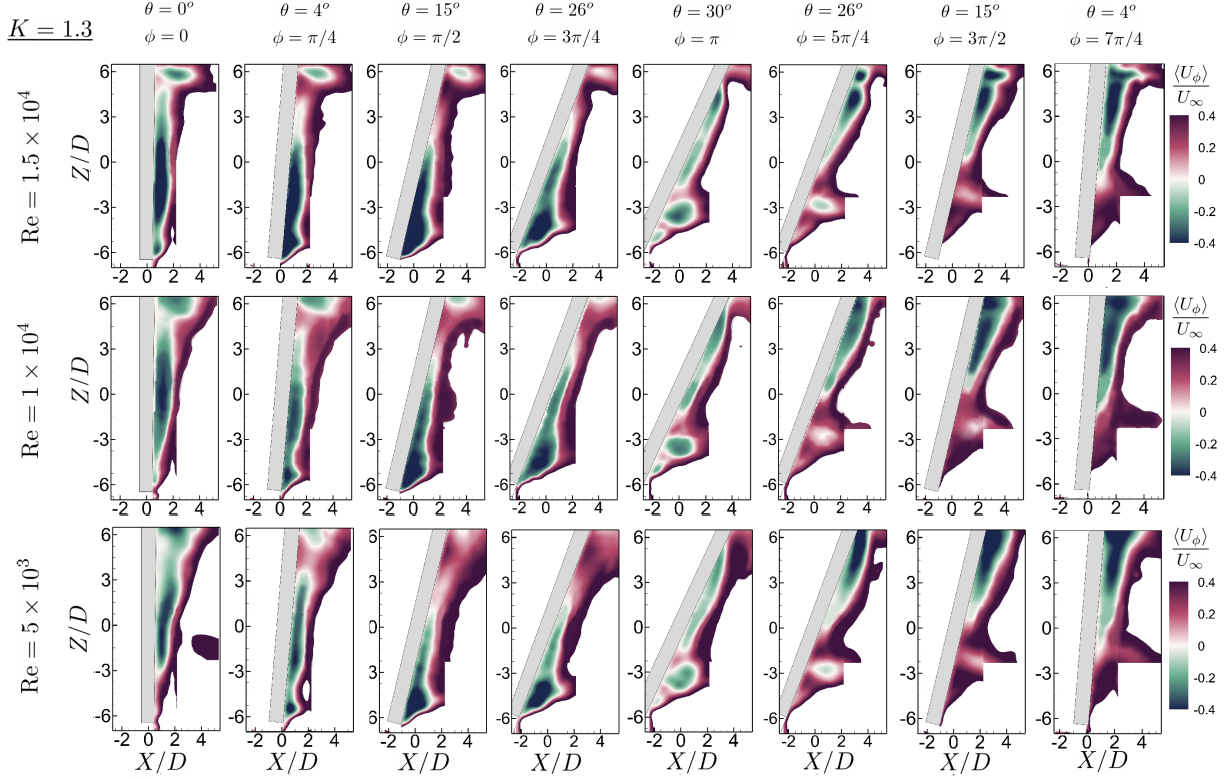
Figure 6.6:   Contours of phase-averaged streamwise velocity ($\langle U_\phi \rangle / U_\infty$) for the yaw-oscillating cylinder with reduced frequency of $K = 1.3$ at Re $= 1.5 \times 10^4$, 1×10^4, and 5×10^3 in the symmetry plane at $Y/D = 0$.

of vortex shedding frequency that was limited by the yaw-oscillation mechanism. For Re $= 5 \times 10^3$, reduced frequencies of $K = 2$ and 4 were achieved. From the previous section, it was shown that the spanwise variation of the near-wake at a specific reduced frequency is almost independent of the Reynolds number. Therefore, it is anticipated that the following discussions on the influence of higher reduced frequencies of $K = 2$ and 4 on the near wake of the cylinder at Re $= 5 \times 10^3$ apply to the range of Reynolds numbers considered.

Figures 6.7 and 6.8 show the phase-averaged streamline patterns ($\langle \psi_\phi \rangle$) and contours of phase-averaged normalized streamwise velocity ($\langle U_\phi \rangle / U_\infty$) for the yaw-oscillating cylinder with $K = 2$ and 4 at Re $= 5 \times 10^3$. Comparing the wake flow patterns at $K = 2$ to those at the previously-discussed, moderately high reduced frequency values of $K = 1$ and 1.3 reveals a general similarity in wake flow patterns at corresponding oscillation phases, although

increasing the reduced frequency to $K = 2$ leads to the suppression of the mean recirculation bubble in the first half of oscillation over a much larger spanwise extent in the wake of the cylinder's top half, as discernible from the existence of a larger spanwise region where the positive streamwise velocity prevails at the base of the cylinder and the streamlines point in the inflow direction. However, for $K = 2$, Figure 6.7 depicts a distinct local wake flow pattern at $\phi = \pi/2$ to $5\pi/4$; that is, the streamline patterns demonstrate a swirl being generated in the vicinity of the mid-span region. This observation can presumably be ascribed to the interaction of the strong positive streamwise velocity forming behind the top half of the span and the high-magnitude reverse flow developing behind the bottom half of the cylinder at $\pi/2 \leqslant \phi \leqslant 3\pi/4$, which is reversed at $\pi \leqslant \phi \leqslant 5\pi/4$ to having strong reverse flow above the mid-span region and high-magnitude positive streamwise flow below owing to the switch in the direction of motion of the cylinder. Although the reverse flow velocity grows to even larger magnitudes behind the top half of the cylinder beyond $\phi = 5\pi/4$, a swirl development in the mid-span region is not observable at other phases. This may be related to the existence of a positive axial flow around the mid-span region at other phases of oscillation, as seen in the contour plots of phase-averaged normalized axial flow velocity given in Figure 6.10. Also, it should be noted here that, similar to the previously discussed yaw-oscillating cases with moderately high reduced frequencies of $K = 1$ and 1.3, as the cylinder's lower half moves against the inflow direction, the reverse flow velocity behind the lower half of the cylinder gradually grows in magnitude as the cylinder accelerates from $\phi = 0$ to $\pi/2$ and decreases during its deceleration from $\phi = \pi/2$ to $\pi/2$. However, compared to $K = 1$ and 1.3, this variation in reverse velocity magnitude is minute, and hence, the effect of cylinder acceleration/deceleration on the near-wake flow appears to be less pronounced for $K = 2$.

For $K = 4$, Figures 6.7 and 6.8 show that the near wake flow field is highly affected by the rapid motion of the cylinder. That is, in the first half cycle, significant positive X-direction thrust is imparted onto the flow behind the top half of the cylinder from the cylinder's top half that moves in the inflow direction with a high velocity, directing the streamlines behind the upper half of the cylinder in the inflow direction and eliminating the reverse flow, which
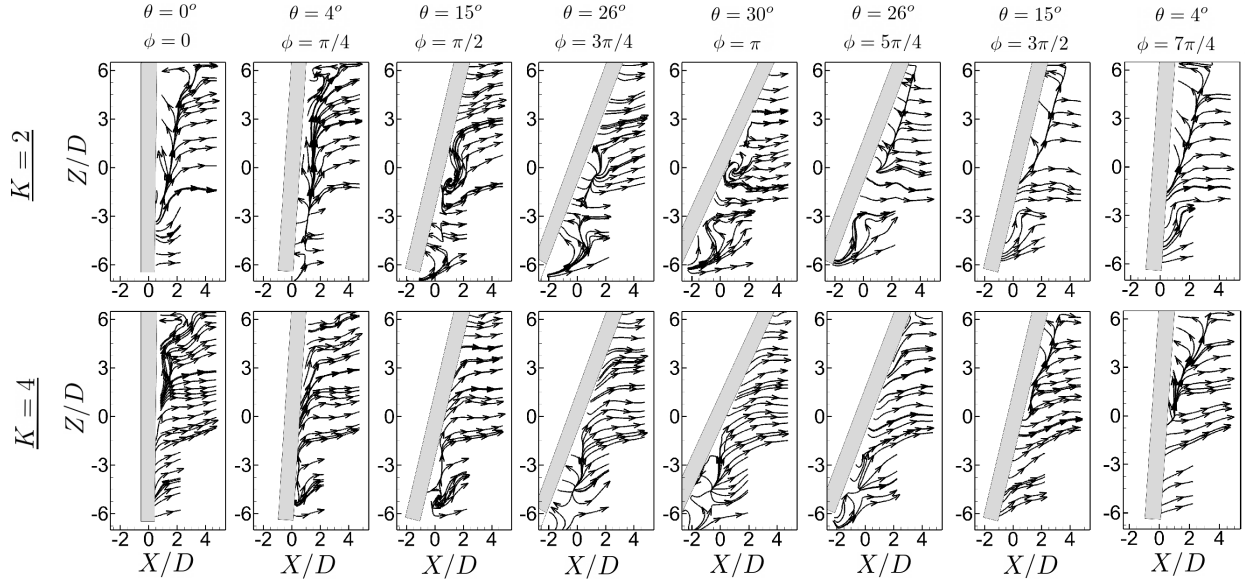
Figure 6.7:   Phase-averaged streamline topology ($\langle\psi_\phi\rangle$) for eight select phases of yaw-oscillating cylinder with reduced frequencies of $K = 2$ and 4 at $\mathrm{Re} = 5 \times 10^3$ in the $Y/D = 0$ symmetry plane.
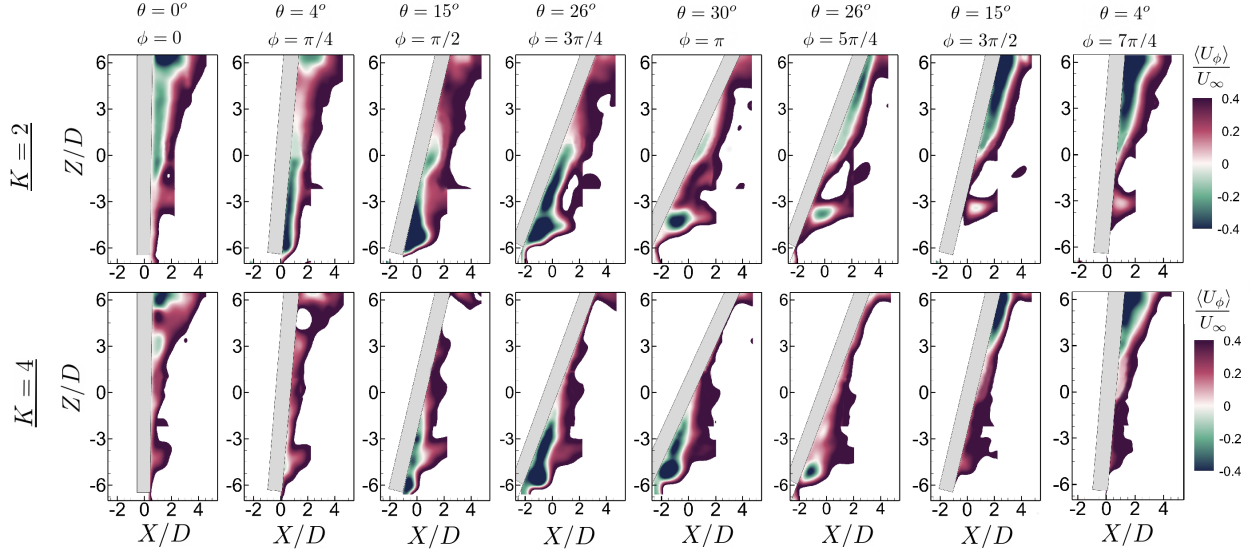
Figure 6.8: Phase-averaged normalized streamwise velocity ($\langle U_\phi\rangle/U_\infty$) for eight select phases of yaw-oscillating cylinder with reduced frequencies of $K = 2$ and 4 at $\mathrm{Re} = 5 \times 10^3$ in the $Y/D = 0$ symmetry plane.

implies complete elimination of the recirculation bubble behind the top half of the cylinder. This nonexistence of a recirculation region pattern behind the top half of the cylinder is extended to the return cycle up to $\phi = 5\pi/4$. Similarly, in the return cycle, the rapid motion of the cylinder's bottom half in the freestream direction suppresses the mean recirculation bubble behind this section of the cylinder starting from $\phi = 5\pi/4$, and this impact continues to be effective even when the cylinder's movement reverses until $\phi = \pi/4$ in the first half-cycle. Moreover, unlike the previously discussed cases of yaw-oscillating cylinders with K = 1 and 1.3, the recovery of the mean recirculation region near the top half of the cylinder is delayed; it occurs later in the return cycle at $\phi = 3\pi/2$ for $K = 4$. All these delayed changes in the flow behavior at the highest considered reduced frequency value of $K = 4$ imply that there is a phase lag between the response of the flow and the cylinder oscillations. This phase-lag results from the lower response rate of the flow to the fast oscillatory motion of the cylinder. Also, the impact of the cylinder acceleration/deceleration is not evident for $K = 4$, as, for example, contrary to the cases of $K = 1$ and 1.3, the maximum reverse flow velocity, which appears near the bottom end of the cylinder, continually increases as the phase of oscillation advances in the first half cycle.

Corresponding contours of phase-averaged axial flow velocity ($\langle V_{A,\phi} \rangle / U_\infty$) for $K = 2$ and 4 are given in Figure 6.10. From the contour levels of $\langle V_{A,\phi} \rangle / U_\infty = 0.4$, which are marked using a dashed line in the plots, it can be seen that increasing the reduced frequency to $K = 2$ leads to a further delay in the spread of high-magnitude positive axial flow that originates from the bottom end of the cylinder along the span of the cylinder in the return cycle, following the same trend previously discussed in Figure 5.4 for the moderate reduced frequencies of $K = 1$ and 1.3. For $K = 2$, the spanwise spread of the large-magnitude positive axial flow in the return cycle is blocked until $\phi = 5\pi/4$ by the negative axial flow region developing immediately behind the cylinder around the mid-span and the second negative axial flow zone forming downstream of this region (detached from the cylinder surface) as a result of the swirl pattern. For $K = 4$, as a result of the delay of the flow response to cylinder oscillations, the first appearance of a high-amplitude positive axial flow near the bottom end of the cylinder occurs

at $\phi = \pi/2$. Distinct from other reduced frequencies, an interesting feature observed only for $K = 4$ is that from $\phi = \pi/2$ to $5\pi/4$, although moderate levels of negative axial flow dominate immediately downstream of the cylinder over a significant spanwise portion of the bottom half of the cylinder (distinguishable from the pocket of negative axial velocity contours bounded by the solid white line depicting the $\langle V_{A,\phi} \rangle / U_\infty = 0$ level), the high-magnitude positive axial flow originating from the free lower end of the cylinder still spreads in the spanwise direction, wrapping around that negative axial flow region, and impacts directly downstream of the cylinder near the top half of the cylinder (about $Z/D = 3$). Also, unlike other cases, due to the high angular velocity of the cylinder motion, the remnants of this strong axial flow near the top half of the cylinder remain attached to the surface of the cylinder at $\phi = 0$ and $\pi/2$ in the first half cycle.

Figure 6.9 depicts the contours of vorticity for the yaw-oscillating cylinder with reduced frequencies of $K = 2$ and 4. Results for $K = 2$ indicate that unlike the moderate reduced frequencies ($K = 1$ and 1.3), very close to the bottom free end of the cylinder, the negative vorticity region is not present for all the phases. For the phases where a negative vorticity region exists near the upstream end, the streamwise extent is remarkably lower than those observed for the moderate reduced frequencies. Another notable distinction can be seen in the positive vorticity regions along the span of the cylinder. For $K = 2$, positive vorticity is generated close to the surface of the cylinder from mid-span down to around $Z/D = -5$ at $\phi = \pi/2$. This is presumably related to the significant velocity gradient near the mid-span caused by the opposite direction streamwise velocities near the top and bottom half of the span. At $\phi = 3\pi/4$, the bottom section of this vorticity region splits into two parts. The part that is located further downstream, moves away from the surface of the cylinder in the freestream direction from $\phi = \pi$ to $7\pi/4$. On the other hand, from $\phi = \pi$ to $7\pi/4$, the split part of the positive vorticity that is closer to the surface of the cylinder is kept attached to the surface of the cylinder and ascends in the spanwise direction towards the mid-span. This positive vorticity detaches from the surface of the cylinder at $\phi = 0$ and dissipates in the following phases. The upper part of the positive vorticity region (from the mid-span to
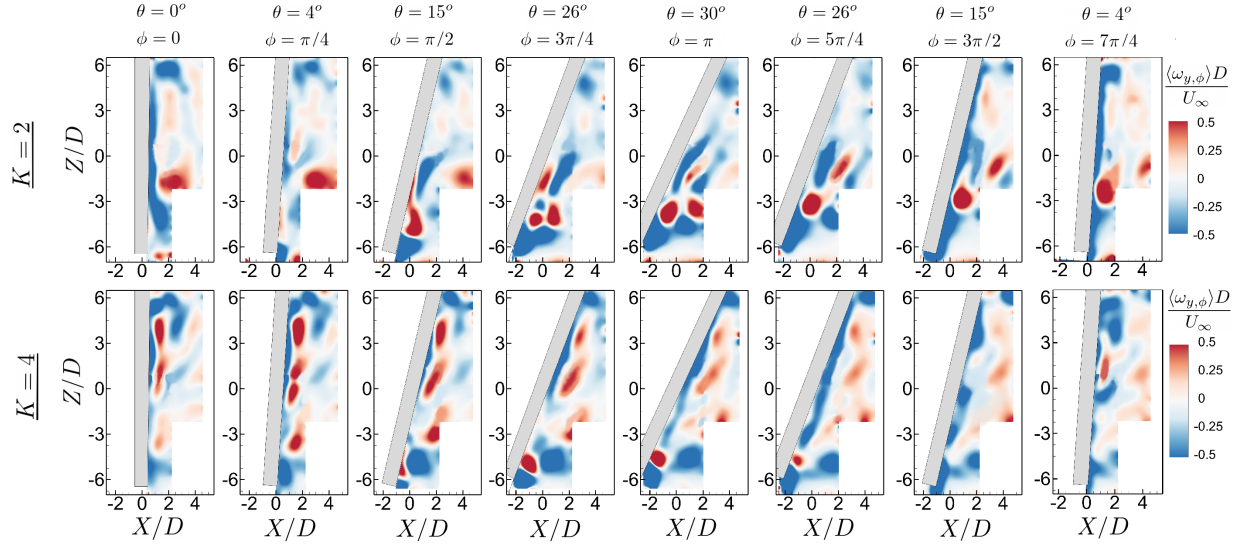
Figure 6.9: Phase-averaged vorticity ($\langle\omega_{y,\phi}\rangle D/U_\infty$) for eight select phases of yaw-oscillating cylinder with reduced frequencies of $K = 2$ and 4 at $\mathrm{Re} = 5 \times 10^3$ in the $Y/D = 0$ symmetry plane.
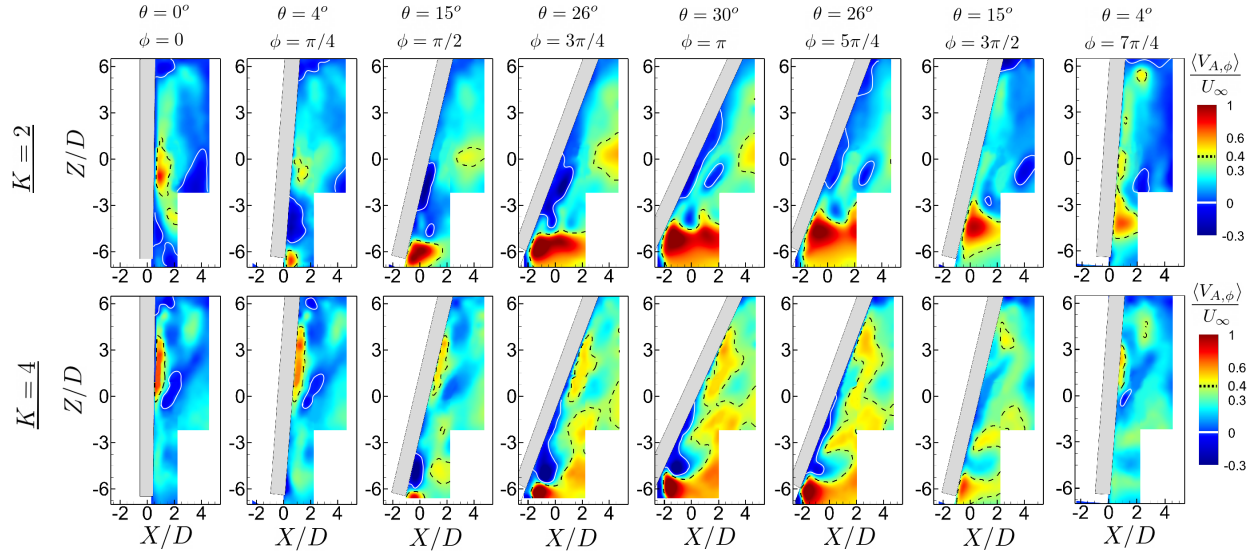
Figure 6.10: Phase-averaged normalized axial velocity ($\langle V_{A_\phi}\rangle/U_\infty$) for eight select phases of yaw-oscillating cylinder with reduced frequencies of $K = 2$ and 4 at $\mathrm{Re} = 5 \times 10^3$ in the $Y/D = 0$ symmetry plane. Contour levels of $\langle V_{A_\phi}\rangle/U_\infty = 0$ and 0.4 are marked with white solid line and black dashed line, respectively.

119

around $Z/D = -2$), detaches from the surface of the cylinder beyond $\phi = \pi$ and progressively moves downstream until phase $\phi = 7\pi/4$.

From Figure 6.9, for $K = 4$, it is apparent that the flow structure along the span of the cylinder is not influenced by the vorticity generated near the upstream end, in contrast to the observation made for the moderate reduced frequencies. Instead, it can be seen that the positive vorticity is generated along the span of the cylinder from $\phi = 0$ by the change in the direction of motion of the cylinder and dissipates downstream over the oscillation cycle. A large section of the positive vorticity is generated in the first half cycle associated with significant thrust added to the flow immediately behind the cylinder and then dissipates in the return cycle. This implies that the remarkably rapid motion of the cylinder is the parameter that dominates the flow structure along the span of the cylinder.

6.2   Flow Structure in the (X,Y) Planes

6.2.1   The Mid-Span Plane

In this section, the effect of the Reynolds number on the flow topology at the mid-span of the stationary and yaw-oscillating cylinder is considered. The left column of Figure 6.11 shows the yaw-averaged streamline patterns ($\langle \psi_\theta \rangle$) superimposed over contours of normalized yaw-averaged streamwise velocity ($\langle U_\theta \rangle / U_\infty$), and the right column gives the contours of normalized yaw-averaged vorticity ($\langle \omega_{z,\theta} \rangle D / U_\infty$) for both the static yawed cylinder and yaw-oscillating cylinder cases at $K = 0.5$, 1.3, and 4 for Re $= 5 \times 10^3$. Similar to the previous results of Figure 5.5 with Re $= 1.5 \times 10^4$, as the frequency of oscillation increases, the streamwise length of the mean recirculation region gradually reduces, and the core of counter-rotating swirls moves towards the cylinder until they are suppressed at the case with $K = 4$. The vorticity contours in the second column indicate a sharp reduction in the streamwise extent of shear layers with increasing reduced frequency. The increasingly shorter mean recirculation region and shorter length of shear layers as K increases suggest that vortices shed gradually closer to the cylinder base, until they are suppressed at $K = 4$. Similar
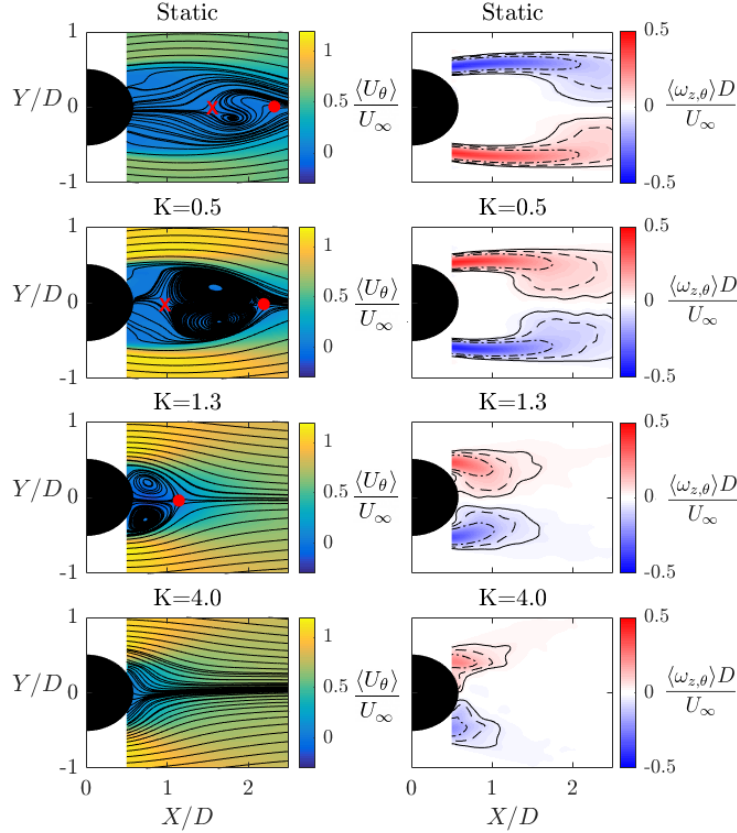
Figure 6.11:   Yaw-averaged streamline ($\langle\psi_\theta\rangle$) topology superimposed over the normalized mean streamwise velocity ($\langle U_\theta\rangle/U_\infty$) and the contours of the mean normalized Z-direction vorticity ($\langle\omega_{z,\theta}\rangle D/U_\infty$) for the static yawed cylinder and yaw-oscillating cylinder at reduced frequencies of $K = 0.5$, 1, and 4 at $\mathrm{Re} = 5 \times 10^3$. For the contours of $\langle\omega_{z,\theta}\rangle D/U_\infty$ given in the second column, the contour levels for the solid, dashed, and dash dot lines are ± 0.0625, ± 0.125, ± 0.25, respectively. Symbols represent saddle points as described in Figure 4.3.

to the high Reynolds number counterparts at $\mathrm{Re} = 1.5 \times 10^4$, the mean drag coefficient in the mid-span of the cylinder at this lower Reynolds number of $\mathrm{Re} = 5 \times 10^3$ may be speculated to increase from the stationary case to the oscillating case with $K = 1.3$ due to gradual reduction in the streamwise length of the mean recirculation region suggesting an increase in suction at the base of the cylinder in the mid-span. Nevertheless, this inference is only rational for the mid-span of the cylinder.

Figure 6.12 shows the contours of normalized phase-averaged streamwise velocity ($\langle U_\phi\rangle/U_\infty$) overlaid by the phase-averaged streamline ($\langle\psi_\phi\rangle$) patterns for the stationary yawed cylinder and the two yaw-oscillating cases of $K = 1.3$ and 4 at $\mathrm{Re} = 5 \times 10^3$. Streamlines for the case
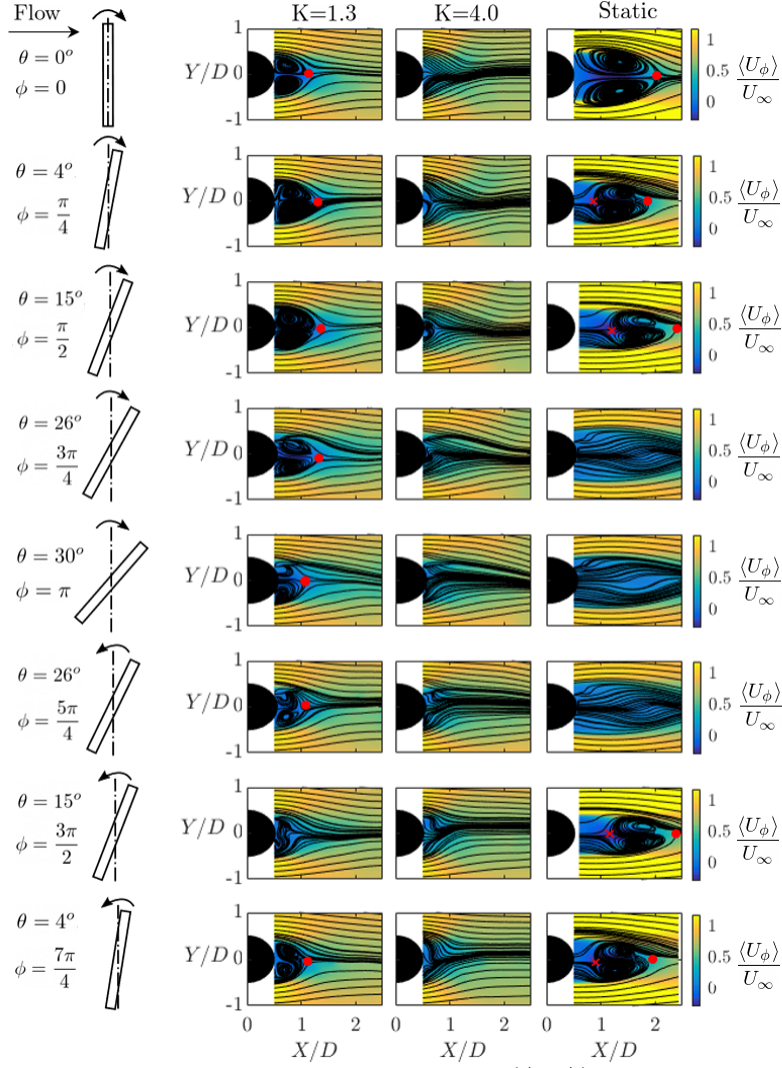
Figure 6.12: Phase-averaged flow streamline topology ($\langle\psi_\phi\rangle$) superimposed over the contours of mean normalized streamwise velocity ($\langle U_\phi\rangle/U_\infty$) for the yaw-oscillating cylinder at reduced frequencies of $K = 1.3$ and $K = 4$ (The first and second column, respectively) at eight select phases and the static yawed cylinder (last column) at $\mathrm{Re} = 5 \times 10^3$. The symbols represent saddle points as previously described in Figure 4.3. Schematics on the far-left indicate the phase and its corresponding yaw angle as well as the direction of motion of the cylinder with respect to the freestream.

of the stationary yawed cylinder show that at $\theta = 4^o$ and 15° in both the first-half and return cycles, the streamwise flow develops at the base of the cylinder, pushing the swirl patterns downstream. The mean recirculation region is eliminated at higher yaw angles of $\theta = 26^o$ and 30° in agreement with the flow visualization shown by Najafi *et al.* [40].

For the yaw-oscillating cylinder at $K = 1.3$, the streamline patterns at different phases resemble those obtained for higher Reynolds number of $\mathrm{Re} = 1.5 \times 10^4$ at the same reduced frequency. The mean recirculation region exists all along the oscillation period, except for the $\phi = 3\pi/2$ phase in the return cycle, where the swirl patterns are significantly suppressed. Results for $K = 4$ point out an interesting flow behavior. It can be seen that with the oscillation frequency being substantially high at $K = 4$, the patterns of swirl are nearly suppressed at all yaw angles.

6.2.2 $Z/D = \pm 3$ **Planes**

In this section, the flow topology on $Z/D = \pm 3$ planes is compared for static cylinder and yaw-oscillating cylinder at two Reynolds numbers of 1.5×10^4 and 5×10^3. Results for the static cylinder are presented first and then compared with the yaw-oscillating cylinder with a reduced frequency of $K = 1.3$.

Figure 6.13 illustrates the mean streamline topology ($\langle \psi_\phi \rangle$) overlaid on contours of mean normalized streamwise velocity ($\langle U \rangle / U_\infty$) for the static cylinder in the $Z/D = 3$ plane at three yaw angles of $\theta = 0^o$, 15°, and 30°. Results are shown for $\mathrm{Re} = 5 \times 10^3$ and 1.5×10^4. From Figure 6.13, it can be observed that for $\theta = 0^o$ and 15°, a pair of swirl patterns exists behind the cylinder whereas they are completely suppressed at $\theta = 30^o$ for both Reynolds numbers. The general difference between the two cases lies in the streamwise extent of the mean recirculation region, which is further elongated downstream for the lower Reynolds number case. At the yaw angle of $\theta = 15^o$ an additional region of swirl appears immediately behind the cylinder for the lower Reynolds number case. This swirl is presumably related to the flow separation on the rear surface of the cylinder at $\mathrm{Re} = 5 \times 10^3$ around $Z/D = 3$, which is aligned with the observation made near this location in Figures 6.1 and 6.3.
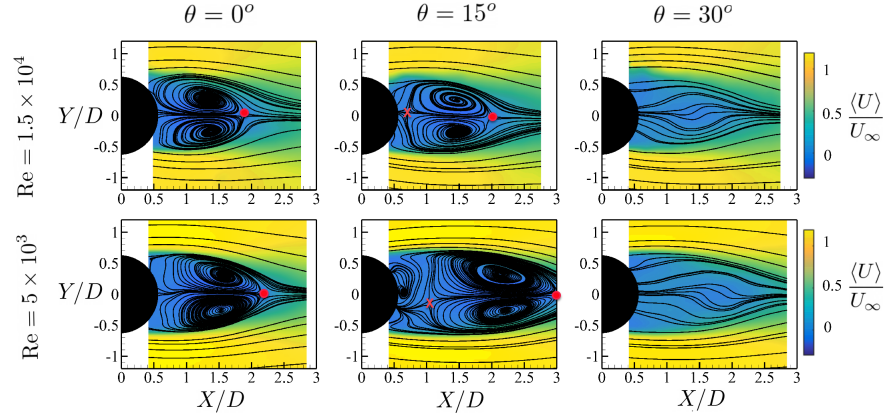
Figure 6.13:   Mean streamline topology ($\langle\psi\rangle$) superimposed over the contours of mean normalized streamwise velocity ($\langle U \rangle/U_\infty$) in the $Z/D = 3$ plane for the static yawed cylinder at yaw angles of $\theta = 0^o$, 15°, and 30°. Reynolds numbers considered are 5×10^3 and 1.5×10^4. Symbols represent the saddle points.

Figure 6.14 shows the results for the static yawed cylinder in the $Z/D = -3$ plane. Similar to the observation made for the plane on the top half of the cylinder, at $\theta = 0^o$, the streamwise extent of swirl patterns are remarkably higher for the lower Reynolds number. For Re $= 1.5 \times 10^4$, at $\theta = 15^o$, the streamwise flow can be seen between the swirls and the surface of the cylinder. On the other hand, for the same yaw angle and at Re $= 5 \times 10^3$, the mean recirculation region is significantly suppressed. This implies that at lower Reynolds, the regular vortex shedding is highly impacted by the axial flow generated from the upstream end. Note that in Figure 6.4, it was shown that the magnitude of positive axial flow for Re $= 5 \times 10^3$ is less around the location of the $Z/D = -3$ plane at $\theta = 15^o$, however, it is shown to be more influential compared to higher Reynolds number case. At $\theta = 30^o$, for both Reynolds numbers, results show the complete suppression of the recirculation region and therefore vortex shedding.

To evaluate the impact of Reynolds number in $Z/D = \pm 3$ planes for the yaw-oscillating cylinder, the flow topology on these planes along with the $Y/D = 0$ symmetry planes are illustrated in Figures 6.15 and 6.16 for $K = 1.3$ at Re $= 5 \times 10^3$ and 1.5×10^4. Overall inspection of Figure 6.15 shows a resemblance in the general flow behavior in the near wake
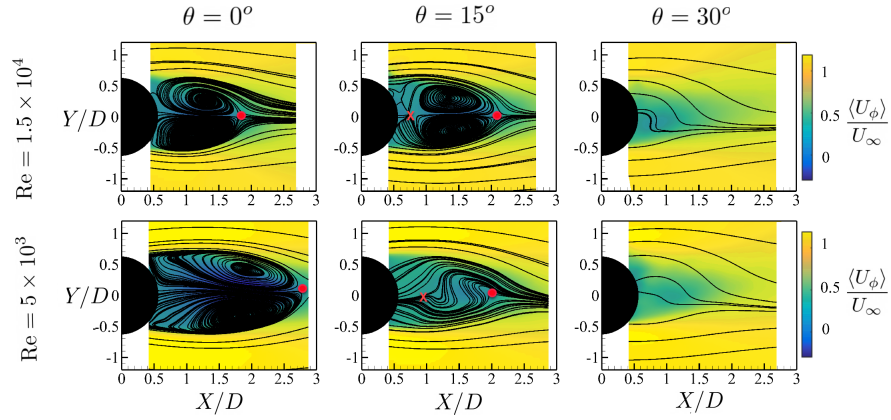
Figure 6.14: Mean streamline topology ($\langle\psi\rangle$) superimposed over the contours of mean normalized streamwise velocity ($\langle U\rangle/U_\infty$) in the $Z/D = -3$ plane for the static yawed cylinder at yaw angles of $\theta = 0^o$, 15°, and 30°. Reynolds numbers considered are 5×10^3 and 1.5×10^4. Symbols represent the saddle points.

of the cylinder in each half of oscillation for both Reynolds numbers. However, for $\phi = 0$, the backflow and the pair of swirls are stronger for the lower Reynolds number. As previously mentioned, in the first half of oscillation cycle for Re $= 1.5 \times 10^4$, when the cylinder accelerates in the inflow direction at $\phi = \pi/4$, the mean recirculation region is suppressed and this effect continues further until $\phi = 3\pi/4$ where the swirl patterns are recovered. However, for Re $= 5 \times 10^3$, the suppression of the mean recirculation region is delayed until $\phi = \pi/2$.

As for the $Z/D = -3$ plane, flow patterns are generally similar for each Reynolds number. For both cases, from $\phi = 0$ to $\phi = \pi/2$, the backflow velocity and the streamwise extent of the swirl patterns increase with the yaw angle. At $\phi = 3\pi/4$, increase in the spanwise flow decreases the backflow velocity and the separated backflow region from the upstream end reaches the $Z/D = -3$ plane at $\phi = \pi$ and $\phi = 5\pi/4$. The only discrepancy is apparent in the magnitude of the backflow velocity, which is higher for the higher Reynolds number.
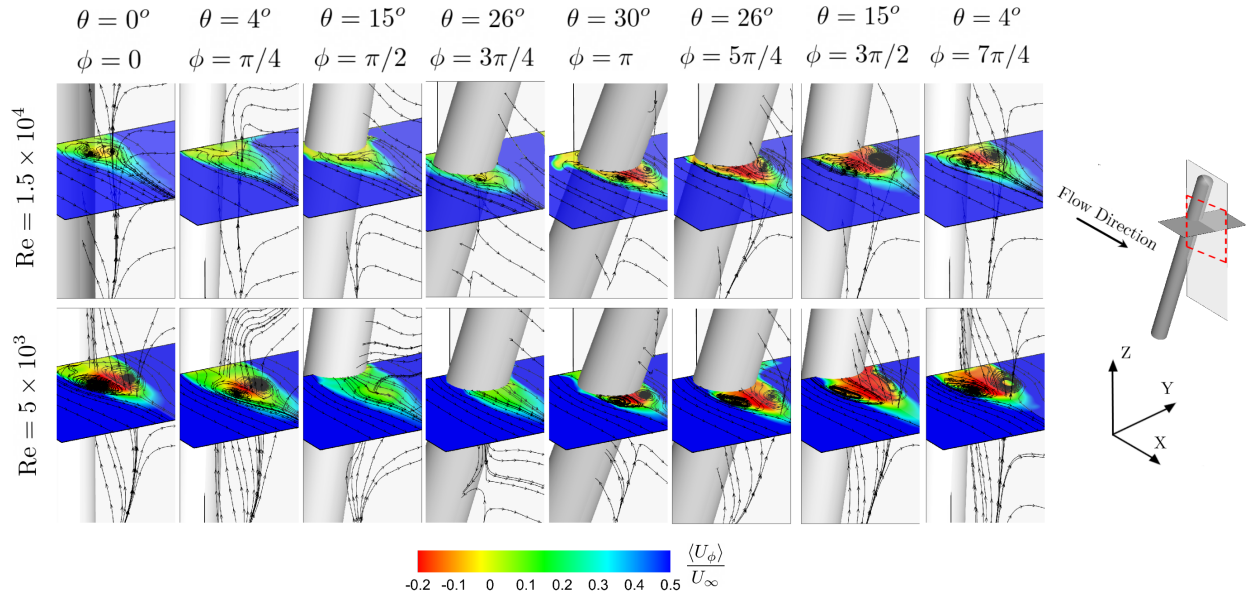
Figure 6.15: Phase-averaged streamline topology ($\langle\psi_\phi\rangle$) superimposed over the contours of phase-averaged normalized streamwise velocity ($\langle U_\phi\rangle/U_\infty$) in the $Z/D = 3$ plane at eight select phases of yaw-oscillating cylinder with $K = 1.3$. Reynolds numbers considered are 5×10^3 and 1.5×10^4.
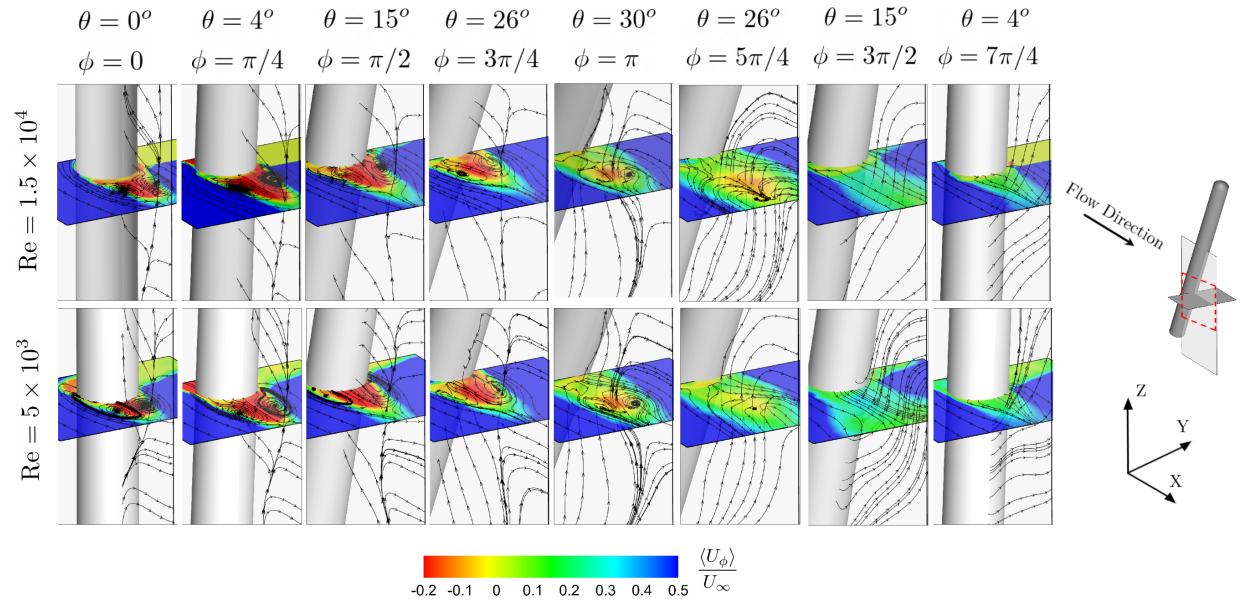
Figure 6.16: Phase-averaged streamline topology ($\langle\psi_\phi\rangle$) superimposed over the contours of phase-averaged normalized streamwise velocity ($\langle U_\phi\rangle/U_\infty$) in the $Z/D = -3$ plane at eight select phases of yaw-oscillating cylinder with $K = 1.3$. Reynolds numbers considered are 5×10^3 and 1.5×10^4.

6.3   Wake Parameters

6.3.1   Wake Width and Closure Length at the Mid-Span Plane

In Figure 6.17, the phase-averaged characteristics of the near wake are plotted to compare the two different Reynolds numbers. From Figure 6.17 (a), it can be seen that for both Reynolds numbers, yaw oscillation at $K = 1.3$ leads to a shorter wake closure length at every phase of oscillation compared to the stationary cylinder. Suppression of the mean recirculation region occurs at $\phi = 3\pi/2$ for both Reynolds numbers. In addition, the wake closure length is shorter for the lower Reynolds number case, relative to the stationary case of the same Reynolds number.

As previously shown in Figure 6.12, increasing the reduced frequency to $K = 4$ at Re $= 5 \times 10^3$ leads to complete suppression of the mean recirculation region throughout the entire oscillation, thus, no wake closure length is reported for this reduced frequency. Figure 6.17 (b) shows that for Re $= 5 \times 10^3$, the wake width at $X/D = 2$ becomes wider for each phase as the oscillation frequency increases, reaching the highest value of the wake width at the fastest yaw-oscillating case that has a reduced frequency of $K = 4$. This latter case also depicts the least variation in the wake width over the cycle.

6.3.2   Backflow Angle

In order to better understand the influence of the Reynolds number on the spanwise flow pattern of the static and yaw-oscillating cylinder at $K = 1.3$, the variation of the backflow angle on three different locations along the span, namely at $Z/D = 3$, 0, and -3, are shown in Figure 6.18. The backflow angles are calculated for the three Reynolds numbers previously studied in Figures 6.1 and 6.5. The top row in Figure 6.18 indicates that for the static cylinder, for each of the Reynolds numbers, increasing yaw angle from $\theta = 0^\circ$ to 30° leads to a decrease in the backflow angle over the entire span. Moreover, it can be observed that the difference between the backflow angles at each yaw angle increases with decreasing Reynolds
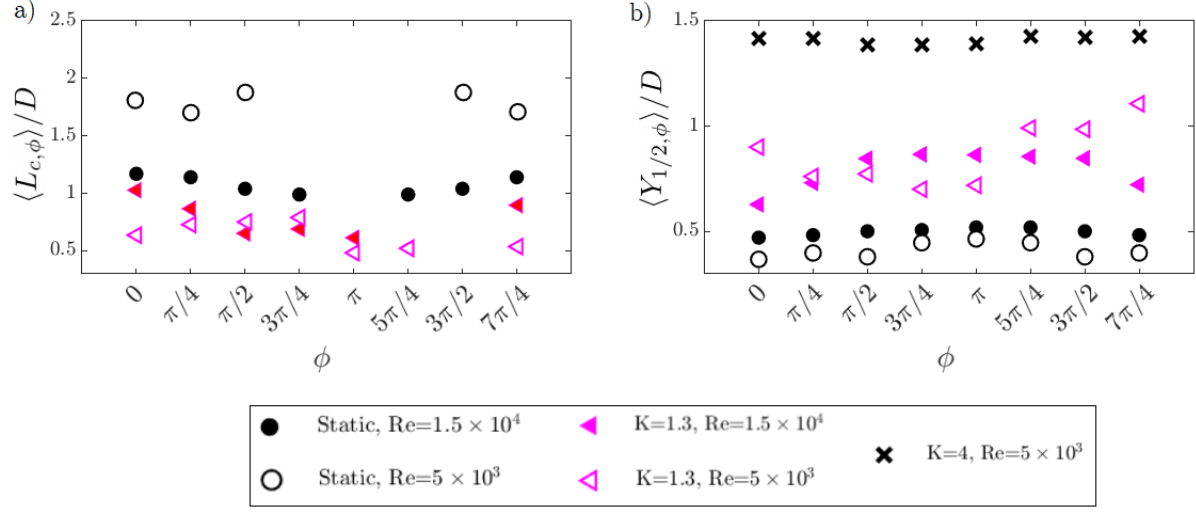
Figure 6.17: Phase-averaged wake parameters of the static and yaw-oscillating cylinder cases at two Reynolds numbers considered. a) Wake closure length ($\langle L_{c,\phi}\rangle/D$) and b) Half wake width ($\langle Y_{1/2,\phi}\rangle/D$) at $X/D = 2$.

number. At $Z/D = -3$ and the mid-span, the lowest backflow angle is obtained for Re = 5×10^3 at all yaw angles. The results for other Reynolds numbers are similar. At $Z/D = 3$, the highest backflow angles at most of the yaw angles (except for $\theta = 0^\text{o}$) occurs for Re = 5×10^3. Comparing the results at different Z/D locations shows that decreasing the Reynolds number causes an increase in the non-uniformity of the flow pattern over the span of the static cylinder.

Results for the yaw-oscillating cylinder with reduced frequency of $K = 1.3$ are shown along the bottom row of Figure 6.18. From the comparison of the values of the backflow angle on various locations along the span, it can be discerned that the flow pattern in the near wake of a yaw-oscillating cylinder, unlike the static yawed cylinder, is remarkably similar for all the Reynolds numbers.
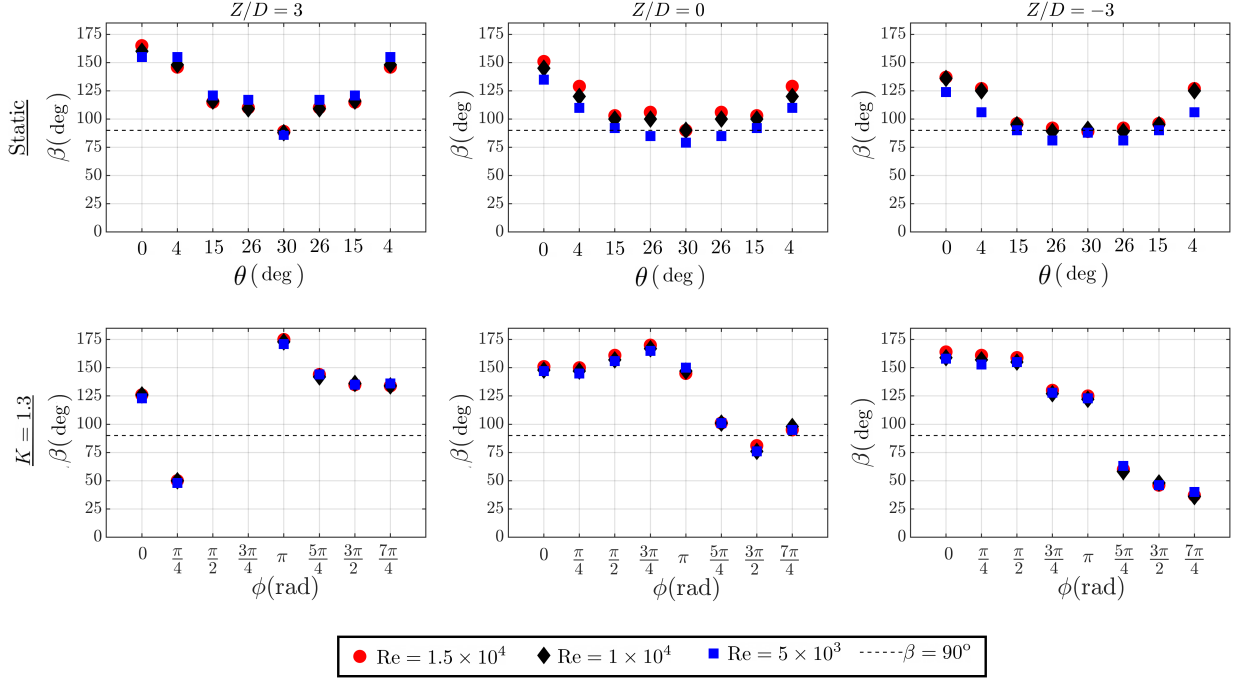
Figure 6.18: Variation of backflow angle on three locations along the span of the cylinder, namely at $Z/D = 3$, 0, and 3 for the static yawed cylinder (top) and yaw-oscillating cylinder at $K = 1.3$ (bottom) at three Reynolds numbers of 1.5×10^4, 1×10^4, and 5×10^3.

6.4 Vortex Shedding

6.4.1 Static Yawed Cylinder

To evaluate the effect of Reynolds number on the vortex shedding frequency of the static yawed cylinder, the velocity spectra and the variation of Strouhal number of vortex shedding with the yaw angle are presented in Figure 6.20 for Re $= 5 \times 10^3$ and 1.5×10^4. Results for Re $= 1 \times 10^4$ are remarkably similar to the Re $= 1.5 \times 10^4$ case and are not presented in this section. The top row of Figure 6.20 reveals that regardless of the Reynolds number, increasing yaw angle leads to a reduction in the height of the frequency peaks accompanied by the enlargement of the width of the peak region. However, it is apparent that the reduction in the height of the peaks by yaw angle is more pronounced at a higher Reynolds number. Moreover,

it can be concluded that even at lower Re in the range of subcritical flow, the vortex shedding becomes further disorganized by yaw angle and is significantly suppressed at high yaw angles. As shown in the bottom row of Figure 6.20, the general trend in the variation of Strouhal number with the yaw angle is similar, which is a decrease in St as the cylinder is further yawed. However, at $\theta = 15^{\text{o}}$ for $\text{Re} = 5 \times 10^3$ where the vortex shedding frequency suddenly increases with yaw angle. This observation is aligned with a corresponding increase in the wake closure length at $\theta = 15^{\text{o}}$ previously shown in Figure 6.12. One possible explanation for this unexpected increase in the wake closure length and the vortex shedding frequency can be associated with the flow separation on the surface of the cylinder near the mid-span region with the regular vortex shedding, as shown in Figure 6.3. Current results are in agreement with the observations of Najafi *et al.* [40] for the yawed cylinder with one side bounded by the wall at the same Reynolds number.

6.4.2   Yaw-Oscillating Cylinder

In this section, the frequency analysis for the yaw-oscillating cases is conducted using the yaw-averaged approach previously discussed in Section 5.4.1. Figure 6.20 shows the velocity spectra for the yaw-oscillating cylinder with various reduced frequencies at Reynolds numbers of 5×10^3, 1×10^4, and 1.5×10^4. The velocity spectra are obtained from the streamwise velocity signal in 1200 oscillation cycles. From Figure 6.20, it is apparent that for all Reynolds numbers, the distinct energy peaks indicating the oscillation frequency and its harmonics occur in the lower range of Strouhal numbers and the peak height increases with the reduced frequency. At all Reynolds numbers, in the range of St corresponding to the vortex shedding frequency, it is indicated that increasing reduced frequency results in a reduction in the height of the peak and an increase in the width of the peak region. As previously mentioned, such behavior is consistent with the reduction in the organization and intensity of vortex shedding. Comparing the results indicates that the drift of the peak region on the spectra towards the lower values by increasing the reduced frequencies is more pronounced at higher Reynolds numbers.

The velocity spectra for $K = 2$ and 4 at $\text{Re} = 5 \times 10^3$ are shown in Figure 6.21. For $K = 2$, two narrowband peaks can be seen on the spectra that correlate with the fundamental oscillation frequency and its harmonics. Moreover, broad-band energy peaks occur in the range of vortex shedding frequency around $0.15 < \text{St} < 0.2$. The low height of the peak region indicates the mitigated vortex shedding. In addition to the regular vortex shedding, the existence of vorticity near the hotwire probe at the mid-span plane could attribute to the broadband peak frequencies in the range of $0.15 < \text{St} < 0.2$. The contour level of $(\langle \omega_{y,\phi} \rangle D/U_\infty = +0.1)$ for $K = 2$ is presented in Figure 6.22. In this Figure, as previously shown in Figure 6.9, a positive Y-direction vorticity region is generated near the mid-span region at $\phi = \pi/2$ and moves downstream in the following phases. For $K = 4$, a narrow-band peak for the oscillation frequency occurs at $\text{St} = 0.18$. Inspecting the velocity spectra for
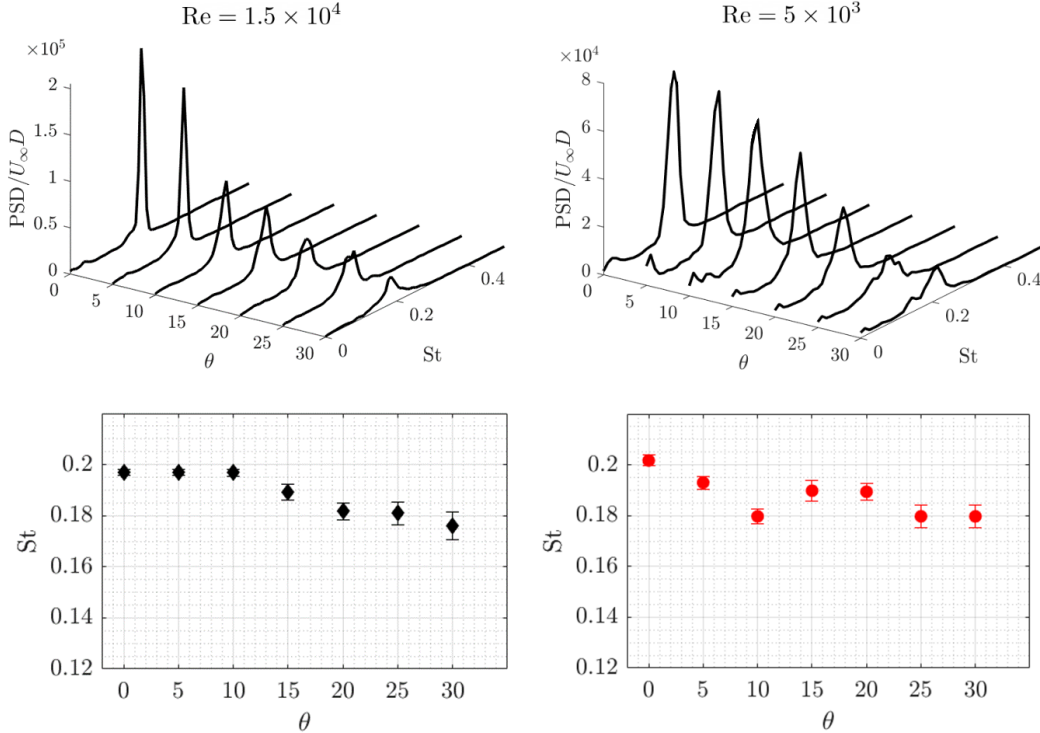
Figure 6.19:   The velocity spectra at different yaw angles (top) and the variation of Strouhal number of vortex shedding with yaw angle (bottom) for the static yawed cylinder at Re $= 5 \times 10^3$ and 1.5×10^4.

$K = 4$ shows that there is no discernible peak around the range of vortex shedding frequency for the previous cases (around $\mathrm{St} = 0.2$) that suggests the suppression of the vortex shedding in agreement with the flow topology presented in Figure 6.11. However, a peak region can be observed in the spectra in the range of $\mathrm{St} = 0.07$ to 0.12. This peak region can be associated with the positive region of vorticity that is generated near the cylinder and moves downstream as marked by $\langle \omega_{y,\phi} \rangle D/U_\infty = +0.1$ contour level in Figure 6.22. Moreover, it should be noted that the peak at 0.09 could also be related to the sub-harmonics of oscillation frequency. Figure 6.23 depicts the instantaneous vorticity for the yaw-oscillating cases with $K = 2$ and 4 at the mid-span for $\phi = \pi/4$. As shown in this figure, for $K = 2$ the vortices shed very close to the surface of the cylinder and for $K = 4$ the shear layers are attached to the surface of the cylinder and detach from the surface of the cylinder almost every half cycle.
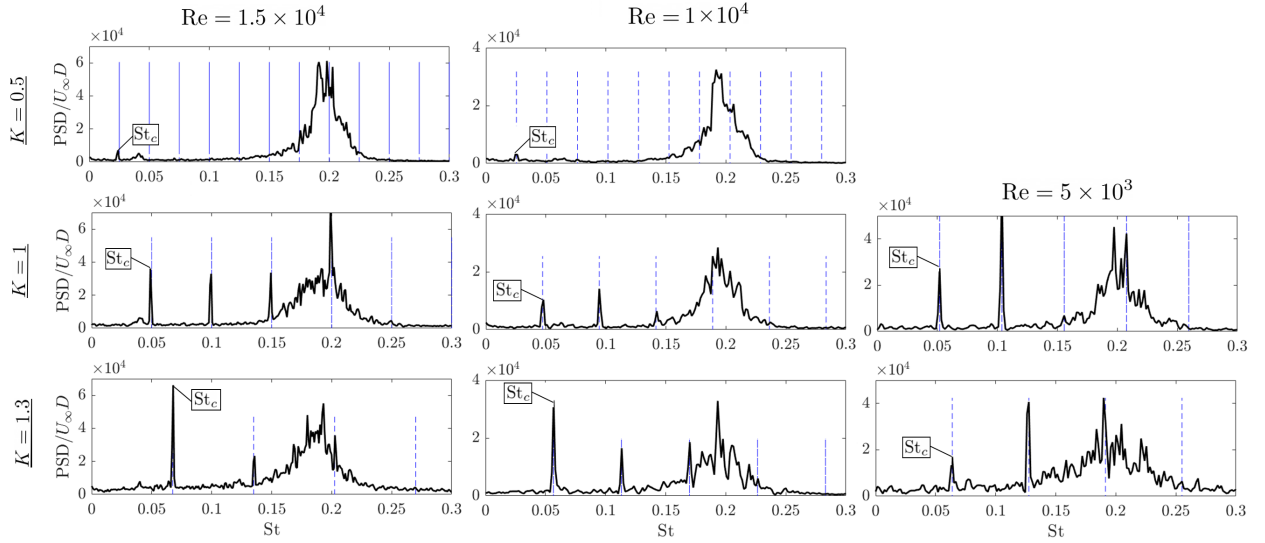
Figure 6.20: The velocity spectra of the streamwise velocity for the yaw-oscillating cylinder with various reduced frequencies at $\mathrm{Re} = 5 \times 10^3$, 1×10^4, and 1.5×10^4. The Strouhal number of fundamental oscillation frequency (St_c) and its harmonics are marked with blue dashed lines.
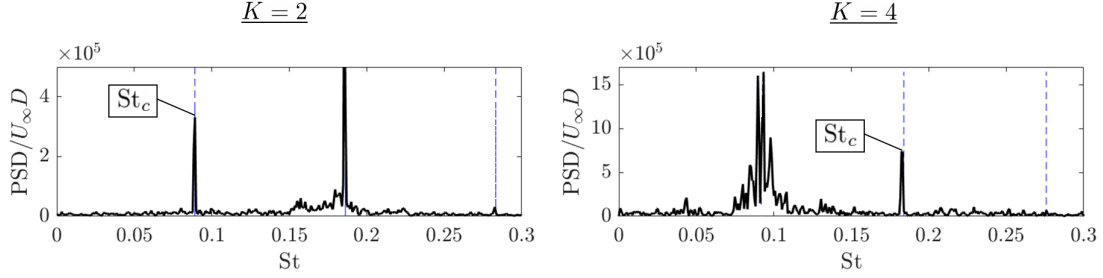
Figure 6.21: The velocity spectra of the streamwise velocity for the yaw-oscillating cylinder with high reduced frequencies of $K = 2$ and 4 at $\mathrm{Re} = 5 \times 10^3$. The Strouhal number of fundamental oscillation frequency (St_c) and its harmonics are marked with blue dashed lines.

6.5   Chapter Summary

In this chapter, the effect of the Reynolds number on the near wake of both static and yaw-oscillating cylinders was studied. Herein, two lower Reynolds numbers cases of 1×10^3 and 5×10^3 were studied and compared to the case of $\mathrm{Re} = 1.5 \times 10^4$ previously discussed in the previous chapters.

For the static yawed cylinder, it was shown that decreasing the Reynolds number leads to an increase in the streamwise extent of the mean recirculation region. The significant suppression of the mean recirculation region along the majority of the span occurred at lower yaw angles for the lowest Reynolds number. An increase in the magnitude of the axial flow along the span of the cylinder with yaw angle occurred at all Reynolds numbers, however, the axial flow had a higher magnitude for higher Reynolds numbers.

For the yaw-oscillating cylinders, the near wake structure was shown to be almost independent of the Reynolds number. However, an increase in the length of the mean recirculation region with decreasing Reynolds number at each yaw angle was observed, similar to the results of the static cylinder.

At the lowest Reynolds number of 5×10^3, higher reduced frequencies of $K = 2$ and 4 were tested. While the wake structure at $K = 2$ was almost similar to the moderate values of $K = 1$ and 1.3, special behavior was observed for the highest reduced frequency of $K = 4$. At this reduced frequency, the near wake became more uniform again and the mean recirculation

region was suppressed over most of the span under the dominant effect of the cylinder's direction of motion. Results showed that at high reduced frequencies, the response of the flow to the fast oscillation motion of the cylinder was delayed leading to the elimination of the effect of acceleration/deceleration of the cylinder.
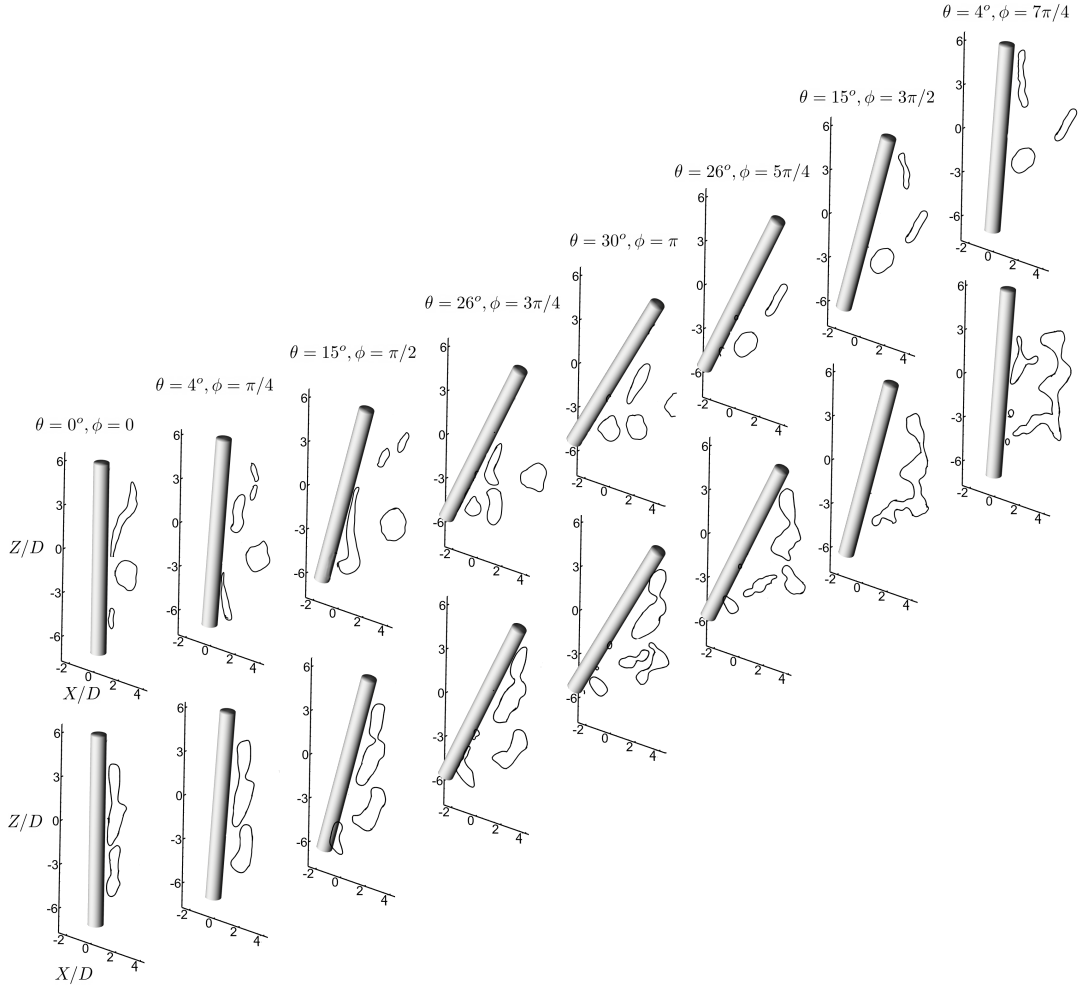
Figure 6.22:   Depiction of $\langle\omega_{y,\phi}\rangle D/U_\infty = +0.1$ contour level at eight different phases of oscillation for yaw-oscillating cylinder at reduced frequencies of $K = 2$ and 4 at $\text{Re} = 5 \times 10^3$.
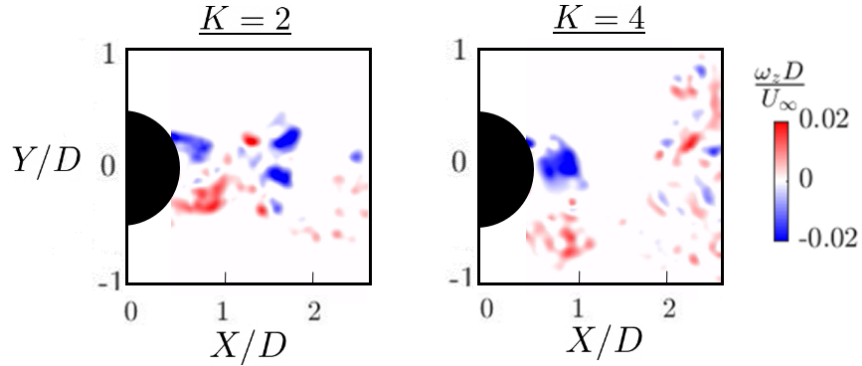
Figure 6.23: Instantaneous vorticity $(\omega_z D/U_\infty)$ for the yaw-oscillating cylinder with $K = 2$ and 4 at the mid-span for $\phi = \pi/4$.

135

Chapter 7

Results: Effect of Aspect Ratio

The influence of the cylinder aspect ratio (L/D) on the near wake of a static yawed cylinder and a cylinder undergoing yaw oscillation is investigated in this chapter. A comparative study is conducted on the flow occurring in the near-wake of cylinders with two aspect ratios of $L/D = 13$ and 20 at Re $= 5 \times 10^3$. For the yaw-oscillating cylinders, two reduced frequencies of $K = 1.3$ and 2 are considered.

7.1 Static Yawed Cylinder

Figure 7.1 shows the mean streamline topology ($\langle\psi\rangle$) and contours of mean normalized streamwise velocity for the static yawed cylinders with aspect ratios of 13 and 20 at Re $= 5 \times 10^3$. Assessment of $\langle\psi\rangle$ indicates that for both cylinders, as previously discussed in Section 4.1, the separated flow from the edge of the bottom free end moves towards the top end in the near wake of the cylinder. Moreover, it is shown that for both cylinders, increasing the yaw angle causes the streamlines to become further parallel to the longitudinal axis of the cylinder. A discrepancy can be observed in the streamline topology of the two cylinders beyond $\theta = 15^\text{o}$. For the cylinder with $L/D = 13$, as previously shown in Section 6.1, the flow separates and then reattaches on the downstream surface of the cylinder around $Z/D = 3$ at $\theta = 15^\text{o}$ and the separation point moves further towards the surface-piercing end
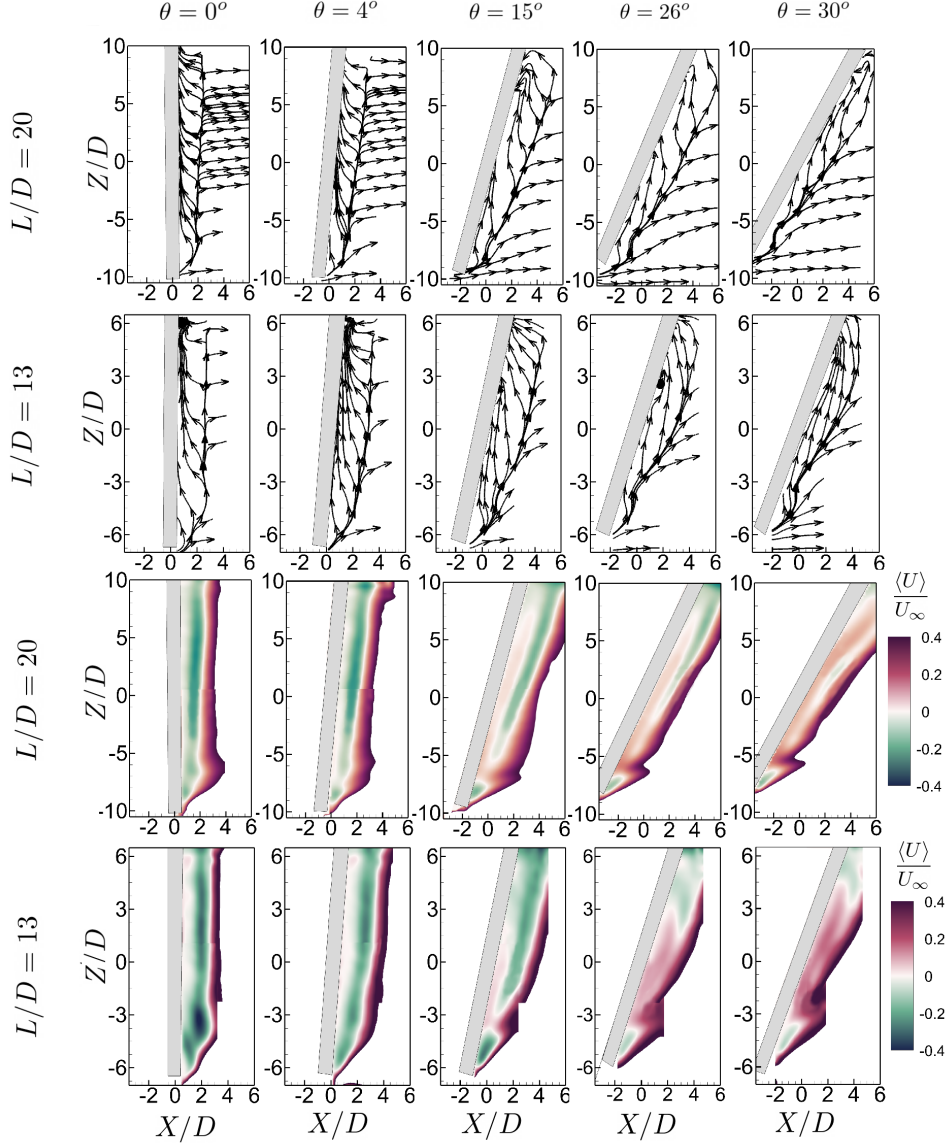
Figure 7.1: Mean streamline topology ($\langle\psi\rangle$) and contours of mean normalized streamwise velocity ($\langle U\rangle/U_\infty$) for the static yawed cylinders with aspect ratios of $L/D = 13$ and 20 at yaw angles of $\theta = 0^o$, 4°, 15°, 26°, and 30° at Re $= 5 \times 10^3$ in $Y/D = 0$ symmetry plane.

for higher yaw angles. For the cylinder with $L/D = 20$, the streamlines are only inclined in the downward direction near the surface-piercing end of the cylinder and no separation can be seen on the downstream surface of the cylinder at any of the yaw angles. Moreover, it is shown that for the cylinder with higher aspect ratio, the mean recirculation region along

137
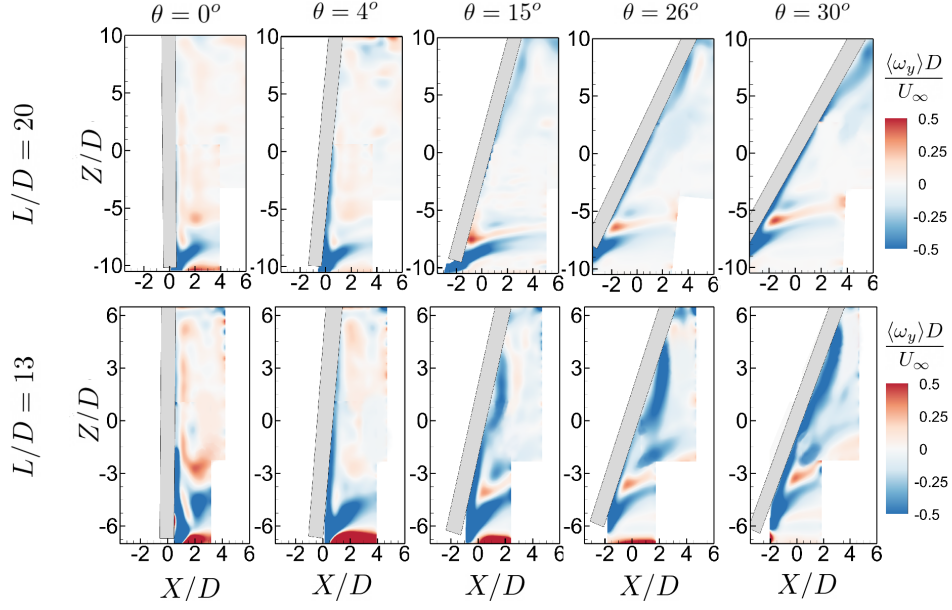
Figure 7.2: Contours of mean normalized vorticity ($\langle\omega_y\rangle D/U_\infty$) for the static yawed cylinders with aspect ratios of $L/D = 13$ and 20 at yaw angles of $\theta = 0^o$, 4°, 15°, 26°, and 30° at Re $= 5 \times 10^3$ in $Y/D = 0$ symmetry plane.

the span of the cylinder is less extended in the streamwise direction. Comparing contours of the normalized streamwise velocity, it is evident that the negative streamwise velocity is generally lower in the near wake of the cylinder with $L/D = 20$ at yaw angles of $\theta = 0^o$, 5°, and 15°. At $\theta = 26^o$ and 30°, the suppression of the mean recirculation region along the span is less significant for the higher aspect ratio cylinder, especially behind the top half of the cylinder. For $L/D = 20$, the mean recirculation region exist from above the mid-span up to the free surface at $\theta = 26^o$ and from above the mid-span to $Z/D = 3$ at $\theta = 30^o$. The discrepancy between the flow behavior of the two cylinders can be associated with the flow separation on the downstream surface of the cylinder at $L/D = 13$ that could contribute to the breakdown of the vortex shedding behind the top half of the cylinder. Figure 7.2 also indicates this discrepancy in the contours of mean normalized vorticity ($\langle\omega_y\rangle D/U_\infty$). For $L/D = 13$ and beyond the yaw angle of $\theta = 15^o$, a strong negative vorticity region is seen above the middle section of the cylinder that extends towards the free-surface piercing end

by increasing yaw angle. However, for the cylinder with $L/D = 20$, there is no such region downstream of the cylinder. Notice that other patterns of the vorticity for both cylinders at different yaw angles are almost identical.

Contours of mean normalized axial velocity ($\langle V_A \rangle / U_\infty$) for the two static cylinder are shown in Figure 7.3. Complete discussions on the variation of the axial velocity with yaw angle for the static cylinder can be found in Section 4.1. As indicated in Figure 7.3, at all yaw angles, higher magnitude axial flow is generated near the bottom free end of the cylinder with $L/D = 13$. However, the development of axial flow along the span of the cylinder varies with the aspect ratio of the cylinder. At $\theta = 15°$ and $26°$, for the cylinder with a lower aspect ratio, low-magnitude positive and negative axial flow is observed around the mid-span whereas for the higher aspect ratio cylinder, the axial velocity of around $0.3 U_\infty$ can be seen in the same region and low positive axial velocity occurs only for near the downstream end of the cylinder.
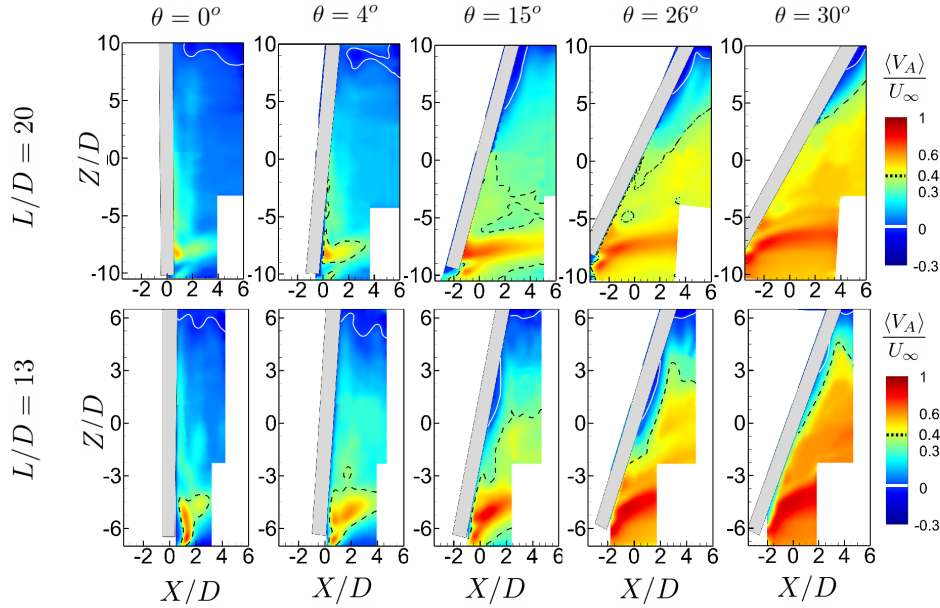
Figure 7.3:   Contours of mean normalized axial velocity ($\langle V_A \rangle / U_\infty$) for the static yawed cylinders with aspect ratios of $L/D = 13$ and 20 at yaw angles of $\theta = 0°$, $4°$, $15°$, $26°$, and $30°$ at Re $= 5 \times 10^3$ in $Y/D = 0$ symmetry plane. Contour levels of $\langle V_{A,\phi} \rangle / U_\infty = 0$ and 0.4 are marked with white solid line and black dashed line, respectively.

At $\theta = 30^\circ$ for $L/D = 13$, the low-magnitude positive axial velocity occurs downstream the cylinder from around $Z/D = 1$ up to the top surface-piercing end of the cylinder while for the cylinder with $L/D = 20$ and at the same yaw angle, a significant reduction in the axial velocity can only be seen at the vicinity of the free surface.

7.2   Yaw-Oscillating Cylinder

7.2.1   Flow Structure in the (X, Z) Symmetry Plane

In this section, the influence of aspect ratio on the near wake of a yaw-oscillating cylinder is investigated. Figure 7.4 illustrates the phase-averaged streamline topology ($\langle \psi_\phi \rangle$) and contours of normalized phase-averaged velocity ($\langle U_\phi \rangle / U_\infty$) for the two yaw-oscillating cylinders considered with the reduced frequency of 1.3. A discernible difference between the two cylinders is the impact of the cylinder's acceleration/deceleration on the near wake in the first half cycle as apparent from the following observations. Contours of $\langle U_\phi \rangle / U_\infty$ reveal that as the cylinder accelerates while moving from $\phi = 0$ to $\pi/2$, both the increase in the positive streamwise velocity in the top half of the span and the increase in the magnitude of the negative streamwise velocity near the bottom of the cylinder are relatively greater for the higher aspect ratio cylinder. Also, comparing the corresponding patterns of $\langle \psi_\phi \rangle$ between these two cylinders during their acceleration from $\phi = \pi/4$ to $\pi/2$ shows that the streamlines very close to the free surface are perpendicular to the surface of the cylinder for the larger aspect ratio cylinder with the effect of acceleration augmenting the streamwise thrust exerted on the flow through the positive X-direction motion of the cylinder's top half. In contrast, the corresponding streamlines look more chaotic for the smaller aspect ratio cylinder under the effect of the free surface. Moreover, when the cylinder decelerates from $\phi = \pi/2$ to π, the mean recirculation bubble is recovered on a relatively larger section of the top half of the cylinder for the larger L/D. For instance, for $L/D = 13$, as the cylinder moves from $\phi = \pi/2$ to π, the reverse flow zone expands from being over the spanwise region below $Z/D = 1.1$ to being below $Z/D = 2$ (implying a recovery of the mean recirculation bubble over a spanwise
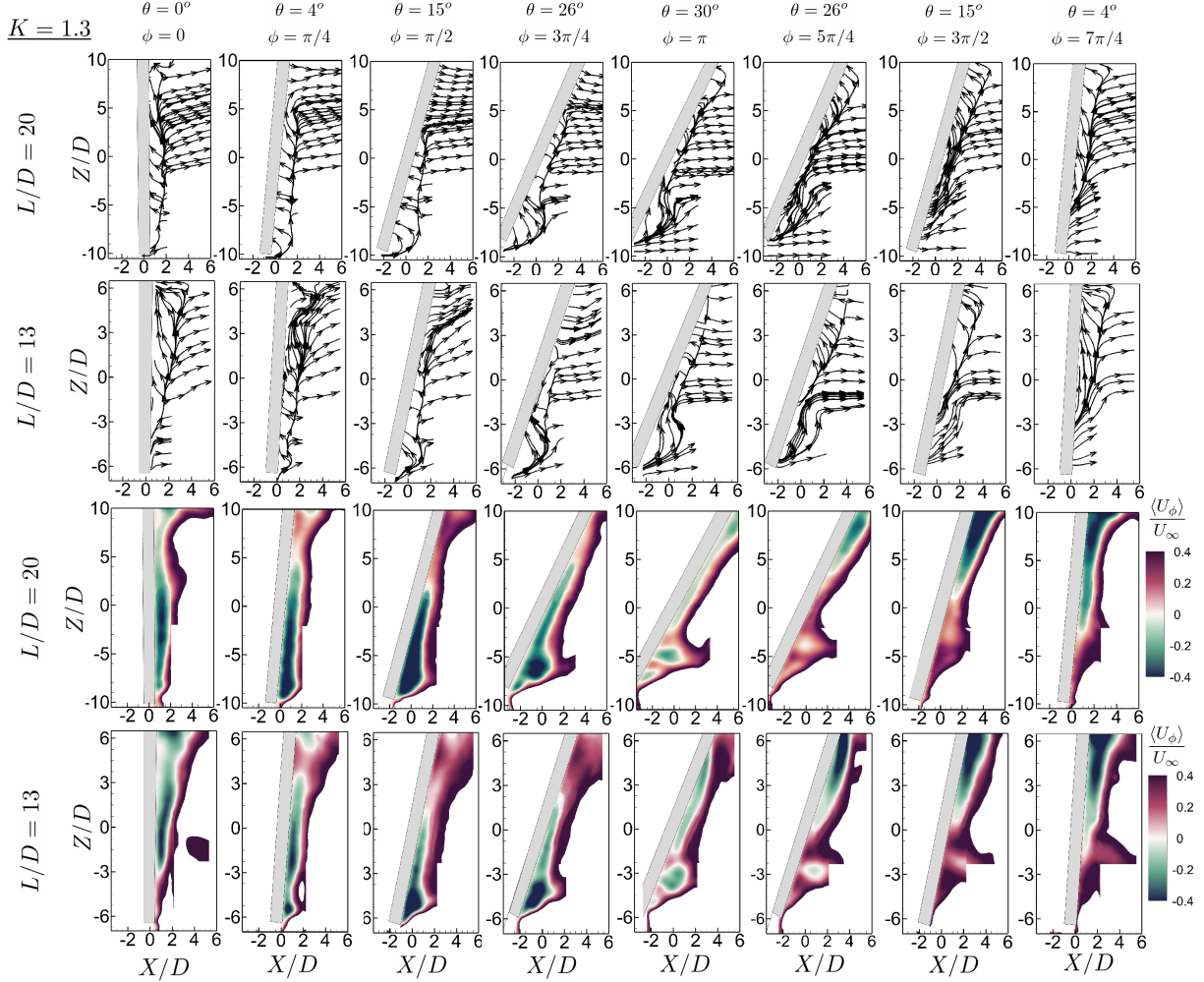
Figure 7.4: Phase-averaged streamline topology ($\langle\psi_\phi\rangle$) and phase-averaged normalized streamwise velocity ($\langle U_\phi\rangle/U_\infty$) for eight select phases of a yaw-oscillation with reduced frequency of $K = 1.3$ and aspect ratios of $L/D = 20$ and 13 at $\mathrm{Re} = 5 \times 10^3$ in $Y/D = 0$ symmetry plane.

length of $0.071L$), whereas for $L/D = 20$, the spanwise extent of the reverse flow grows from being in regions below $Z/D = 2$ to being below $Z/D = 5$ (a recovery over a spanwise length of $0.15L$). All these observations suggest the presence of a more significant influence from the acceleration/deceleration of the cylinder on the near-wake for the larger aspect ratio cylinder.

In order to compare the impact of the aspect ratio on the near wake of yaw-oscillating cylinder at high reduced frequencies, the phase averaged flow patterns $\langle\psi_\phi\rangle$ and contours of phase averaged normalized vorticity $\langle\omega_{y,\phi}\rangle D/U_\infty$ for the yaw oscillation with the reduced
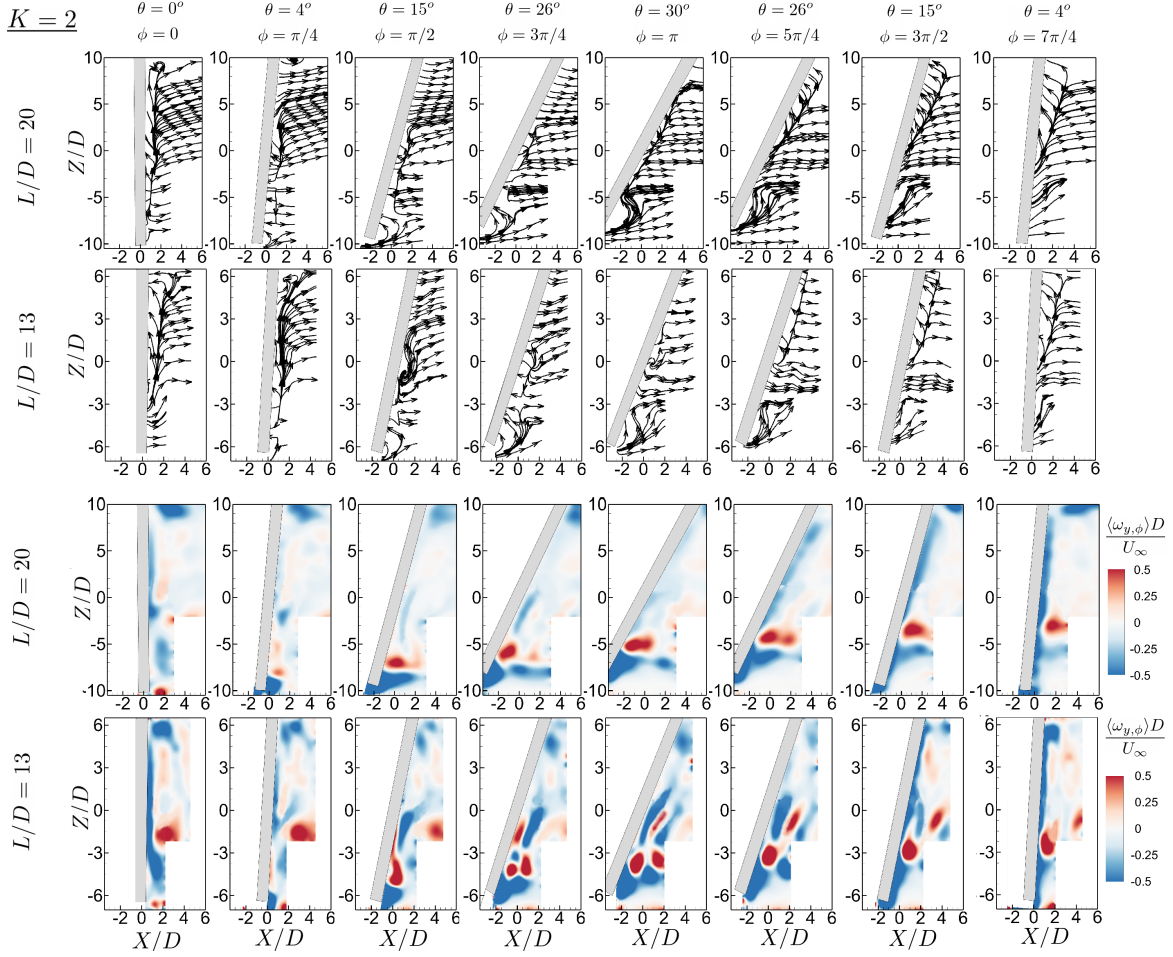
Figure 7.5:   Phase-averaged streamline topology ($\langle\psi_\phi\rangle$) and phase-averaged normalized vorticity ($\langle\omega_{y,\phi}\rangle/U_\infty$) for eight select phases of a yaw-oscillation with reduced frequency of $K=2$ and aspect ratios of $L/D=20$ and 13 at $\mathrm{Re}=5\times10^3$ in $Y/D=0$ symmetry plane.

frequency of $K=2$ is shown in Figure 7.5. Note that the discrepancies in the contours of streamwise velocity for $K=2$ is similar to what was shown for $K=1.3$, hence, the focus here is only on the differences in the flow streamline topology and vorticity fields for the two cylinders. As mentioned in Section 6.1.3, high angular velocity of the cylinder at $K=2$ leads to a specific flow behavior around the mid-span of the cylinder for $L/D=13$. Comparing the streamline topology for the two cylinders demonstrates that the swirl created behind the middle section of the cylinder with $L/D=13$ is not visible for the one with the higher aspect ratio. This is aligned with what is depicted in the contours of vorticity, which show that for
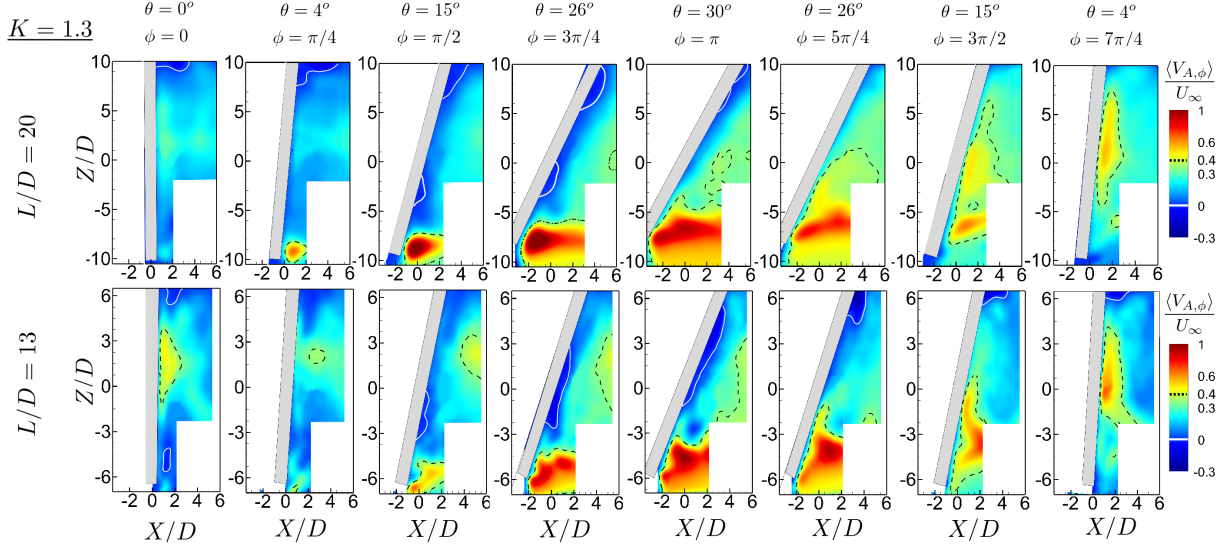
Figure 7.6: Phase-averaged normalized axial velocity ($\langle V_{A,\phi}\rangle/U_\infty$) for eight select phases of a yaw-oscillation with reduced frequency of $K = 1.3$ and aspect ratios of $L/D = 13$ and 20 at $\mathrm{Re} = 5 \times 10^3$ in $Y/D = 0$ symmetry plane. Contour levels of $\langle V_{A,\phi}\rangle/U_\infty = 0$ and 0.4 are marked with white solid line and black dashed line, respectively.

the $L/D = 20$ cylinder, a positive vorticity region is only generated around $Z/D = -7$ at $\phi = \pi/2$ and gradually ascends near the surface of the cylinder up to around $Z/D = -5$ at $\phi = 7\pi/2$. Moreover, it can be seen that this positive vorticity region is seen to be dissipated at the beginning of the next oscillation cycle.

Figure 7.6 shows the contours of phase-averaged normalized axial velocity ($\langle V_{A,\phi}\rangle/U_\infty$) for a yaw oscillation with reduced frequency of $K = 1.3$ for the two cylinders considered. From Figure 7.6, it is apparent that the positive axial flow originating from the free lower end of the cylinder is notably more substantial from $\phi = \pi/4$ to $3\pi/4$ in the first half of the oscillation cycle for the cylinder with the higher length-to-diameter ratio. Furthermore, in the return cycle, from $\phi = \pi$ to $3\pi/2$, this positive axial flow spreads more rapidly along the span of the cylinder for the higher aspect ratio case, possibly, once again, due to the more significant influence of the cylinder's acceleration for the larger L/D. This trend can be identified by noting that, at these phases of $\phi = \pi$ to $3\pi/2$, almost or entirely no negative axial velocity is seen near the top of the cylinder and the contour levels of $\langle V_{A,\phi}\rangle/U_\infty = 0.4$, for example, which are marked by dashed contour lines, appear at locations with a higher

143
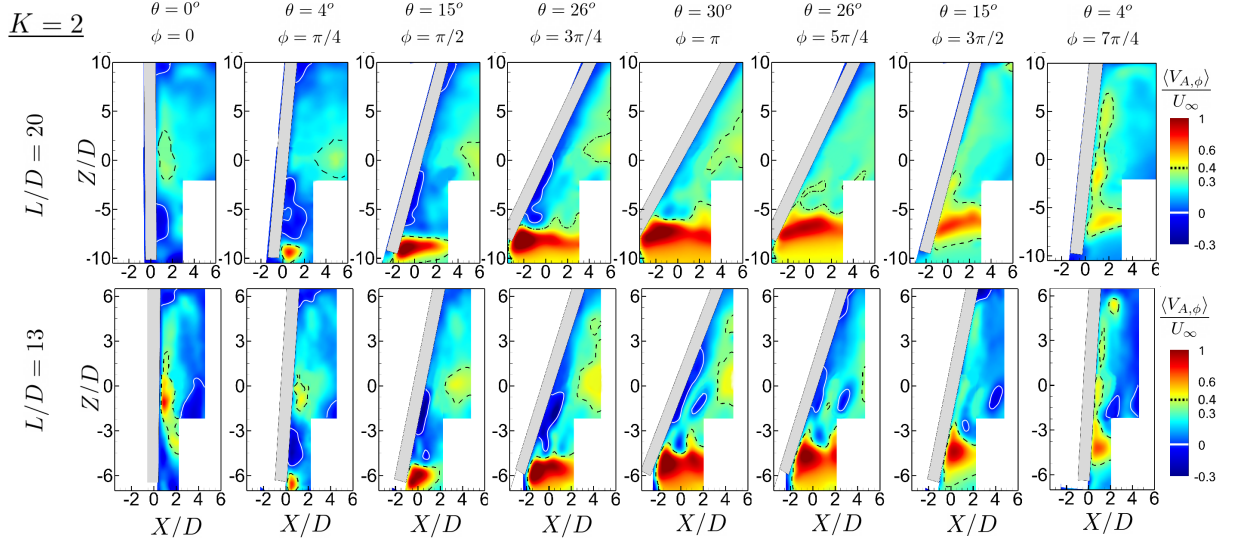
Figure 7.7: Phase-averaged normalized axial velocity ($\langle V_{A,\phi}\rangle/U_\infty$) for eight select phases of a yaw-oscillation with reduced frequency of $K = 2$ and aspect ratios of $L/D = 13$ and 20 at $\mathrm{Re} = 5\times10^3$ in $Y/D = 0$ symmetry plane. Contour levels of $\langle V_{A,\phi}\rangle/U_\infty = 0$ and 0.4 are marked with white solid line and black dashed line, respectively.

Z/D for the larger L/D case.

Figure 7.7 illustrates the variation of the phase-averaged normalized axial velocity ($\langle V_{A,\phi}\rangle/U_\infty$) for the yaw-oscillating cylinders at $K = 2$. it is apparent from Figure 7.7 that for the $L/D = 13$ case, strong negative axial velocity occurs close to the bottom end (centered about $Z/D = -3$) and immediately behind the cylinder at $\phi = \pi/4$ and it ascends towards the middle section at $\phi = \pi/2$ and $3\pi/4$. Moreover, it is shown that high magnitude positive axial velocity generated from the upstream end of the cylinder cannot develop in the near wake of the cylinder in the return cycle (unlike moderate reduced frequencies, see Figure 4.2) as it is hindered by the negative axial flow region generated near below the mid-span. For the cylinder with $L/D = 20$, the low positive and negative axial velocity occurs behind the bottom half of the cylinder (centered about $Z/D = -5$), however, the magnitude of the negative axial velocity is lower than that of the lower aspect ratio cylinder. Contrary to the observation made for the lower aspect ratio cylinder, for the cylinder with $L/D = 20$, the positive axial flow develops significantly along the span and covers nearly an entire near wake of the cylinder beyond $\phi = 5\pi/4$. Furthermore, it can be seen that the low axial velocity

region downstream the lower half of the span is eliminated in the return cycle for the higher aspect ratio cylinder.

7.2.2 Flow Structure in the (X,Y) Planes

7.2.2.1 The Mid-Span Plane

Figure 7.8 depicts the yaw-averaged streamwise velocity ($\langle U_\theta \rangle / U_\infty$) and the yaw-averaged streamline patterns ($\langle \psi_\theta \rangle$) for the yaw-oscillating cylinders with aspect ratios of 13 and 20. As shown in Figure 7.8, for $K = 1.3$, symmetric counter-rotating swirls occur behind the cylinder for both aspect ratios. Notice that the streamwise length of the mean recirculation region is greater for the cylinder with high aspect ratio. For $K = 2$, the yaw-averaged near wake is shown to be remarkably different for each cylinder. It is evident that for $L/D = 13$, asymmetrical counter-rotating swirls occur downstream the cylinder whereas the wake structure is completely symmetrical for $L/D = 20$. Moreover, the size of the swirls appears to be smaller for the cylinder with a lower aspect ratio cylinder. This discrepancy is presumably related to swirls created behind the middle section of the cylinder with $L/D = 13$, as previously shown in Figure 7.5.

The yaw-averaged vorticity field ($\langle \omega_{z,\theta} \rangle D/U_\infty$) for the above-mentioned cases are shown in Figure 7.9. Comparing the vorticity field in the near wake of the yaw-oscillating cylinders with different aspect ratios demonstrates that the high vorticity region within shear layers on both sides of the cylinder with higher aspect ratio are further elongated and straight in the streamwise direction. The variation in the shape of the shear layers is probably associated with the higher magnitude of positive axial velocity near the mid-span for the $L/D = 20$ case, particularly in the return cycle of the oscillation, as indicated in Figures 7.6 and 7.7. Figure 7.9 also indicates the yaw-averaged shear layers for the cylinder with $L/D = 13$ at $K = 1.3$ is asymmetrical owing to the influence of the swirl created behind the middle section of the cylinder during the oscillation cycle, as depicted in Figure 7.5.

Figures 7.10 and 7.11 show the contours of phase-averaged normalized streamwise velocity

Figure 7.8: Contours of yaw-averaged normalized streamwise velocity ($\langle U_\theta \rangle / U_\infty$) overlaid by yaw-averaged streamline topology ($\langle \psi_\theta \rangle$) for yaw-oscillating cylinders with reduced frequencies of $K = 1.3$ and 2 for $L/D = 13$ and 20 at $\mathrm{Re} = 5 \times 10^3$ in the mid-span plane.
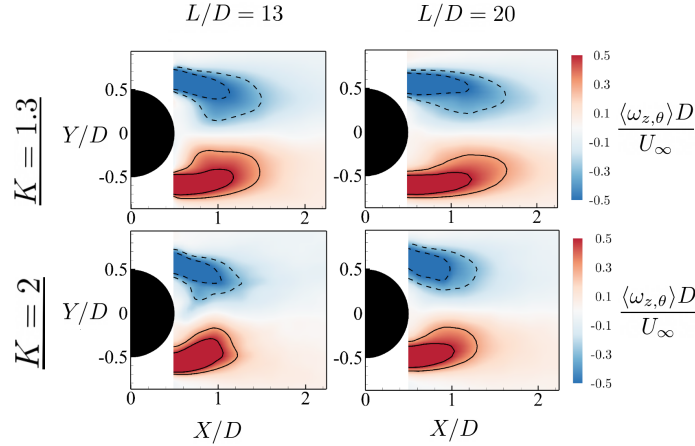
Figure 7.9: Contours of yaw-averaged normalized vorticity ($\langle \omega_{z,\theta} \rangle D / U_\infty$) for yaw-oscillating cylinders with reduced frequencies of $K = 1.3$ and 2 for $L/D = 13$ and 20 at $\mathrm{Re} = 5 \times 10^3$ in the mid-span plane. Contour lines show the vorticity levels of ± 0.5 and ± 0.3 with negative values marked by the dashed lines.

($\langle U_\phi \rangle / U_\infty$) overlaid by phase-averaged streamline topology ($\langle \psi_\phi \rangle$) for the yaw-oscillating cylinders with reduced frequencies of $K = 1.3$ and 2, respectively. As evident in Figure 7.10, for the phases in the first half of oscillation cycle from $\phi = 0$ to $3\pi/4$ for both cylinders, a pair of counter-rotating swirls are present in the near wake. The main discrepancy in the flow behavior of the cylinders with different aspect ratios can be observed at $\phi = \pi$ and $5\pi/4$, in which the mean recirculation region appears to be suppressed for the cylinder with $L/D = 20$
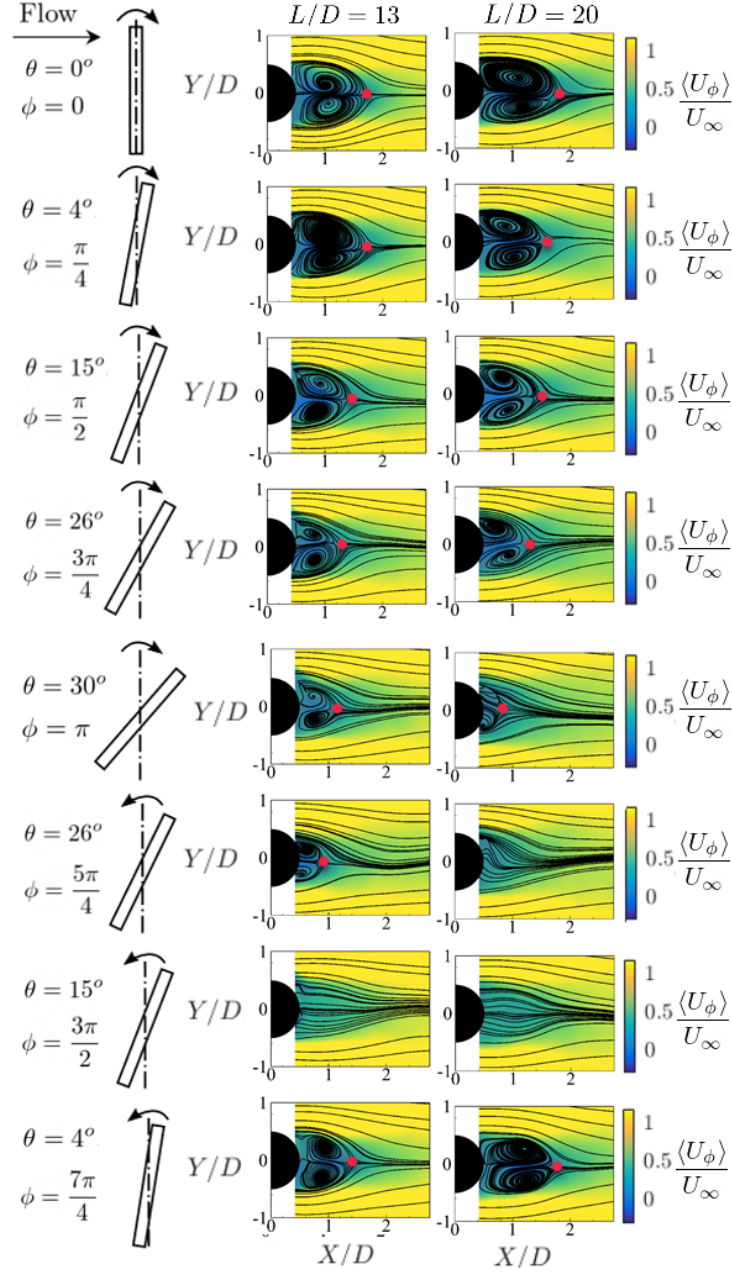
Figure 7.10: Contours of phase-averaged normalized streamwise velocity ($\langle U_\phi \rangle / U_\infty$) overlaid by phase-averaged streamline topology ($\langle \psi_\phi \rangle$) at eight select phases of oscillation with the reduced frequency of $K = 1.3$ for aspect ratios of $L/D = 13$ and 20 at Re $= 5 \times 10^3$ in the mid-span plane. Symbols represent the saddle points.

whereas it exists in the near wake of the cylinder with lower aspect ratio. In Chapters 5 and 6, it was discussed that for the $L/D = 13$ case at $K = 1.3$, the suppression of the mean recirculation region in the mid-span plane occurs at the phase of $\phi = 3\pi/2$. However, it is shown that this flow phenomenon is happening at earlier phases for $L/D = 20$ cylinder. This can be directly related to the previous discussion on the rapid development of positive axial flow along the span of the cylinder in the return cycle by increasing the aspect ratio, as depicted in Figure 7.6 and its impact on the suppression of the mean recirculation region. For both cylinders, the swirl patterns are eliminated at $\phi = 3\pi/2$ and then recovered again at $\phi = 7\pi/4$.

Figure 7.11 shows that for the phases of $\phi = 0$ and $\pi/4$, the counter-rotating swirls can be observed downstream of both cylinders. For $L/D = 13$, from the phase of $\phi = \pi/2$ to $\phi = \pi$, a deformation in the shape of the counter-rotating swirls is seen and the center of the swirls is apparently attached to the base of the cylinder. This deformation occurs due to the presence of the negative vorticity at the mid-span (Figure 7.5) at the corresponding phases. However, at the same phases for $L/D = 20$, the counter-rotating swirls experience weaker deformation and symmetrical swirls can be seen downstream of the cylinder. In the return cycle, for both cylinders, the mean recirculation region in the mid-span plane is shown to be significantly suppressed at all phases.

7.2.2.2   Planes Located Above and Below the Mid-Span

This section is devoted to investigating the near wake flow features in planes biased toward each end of the cylinders with different aspect ratios. Note that the planes considered in this part are located at the same distance from the center of rotation for both cylinders, namely at $Z/L = \pm 0.23$ and -0.35. Since the flow structure is more complex behind the bottom half of the cylinder, two planes are studied closer to the upstream free end of each cylinder. For both cases, the streamline patterns in the symmetry plane are also provided to better understand the three-dimensional flow structure along the span of the cylinder.

Figure 7.12 shows contours of phase-averaged normalized streamwise velocity ($\langle U_\phi \rangle / U_\infty$)
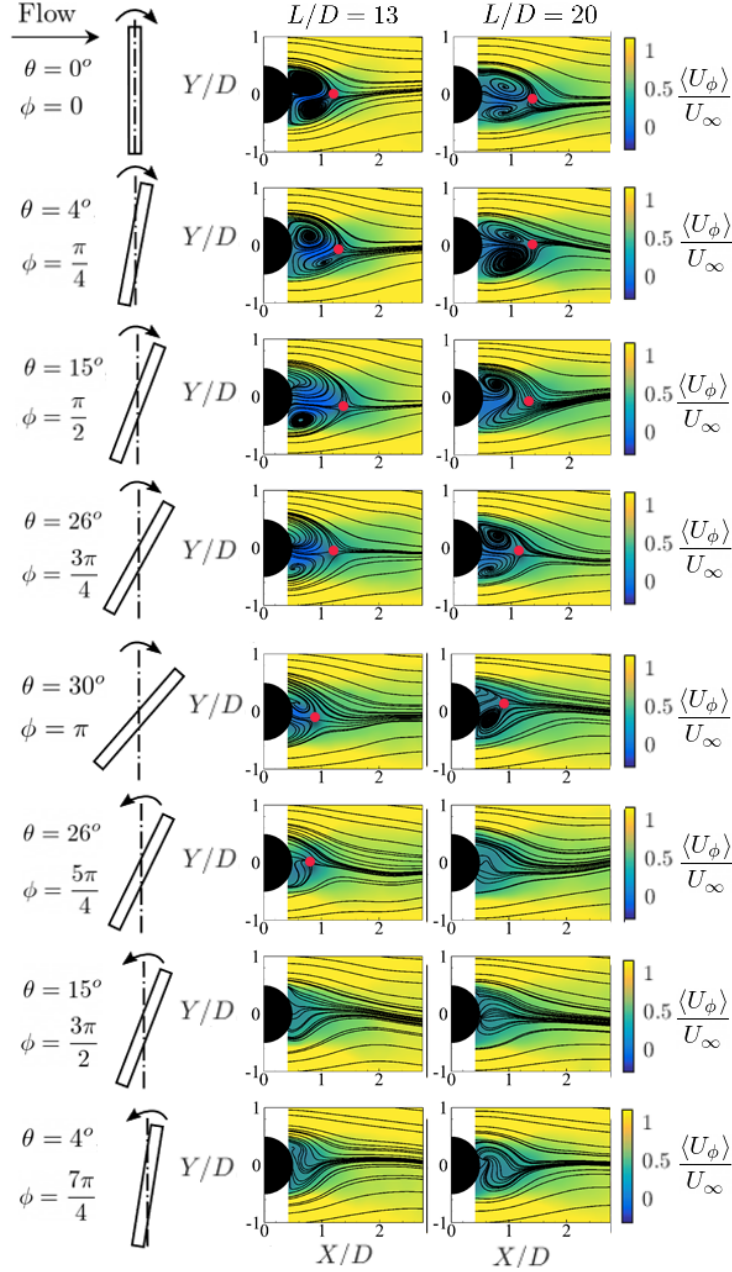
Figure 7.11: Contours of phase-averaged normalized streamwise velocity ($\langle U_\phi \rangle / U_\infty$) overlaid by phase-averaged streamline topology ($\langle \psi_\phi \rangle$) at eight select phases of oscillation with the reduced frequency of $K = 2$ for aspect ratios of $L/D = 13$ and 20 at Re $= 5 \times 10^3$ in the mid-span plane. Symbols represent the saddle points.

overlaid by the phase-averaged streamline topology in the $Z/L = 0.23$ plane at $K = 1.3$ for the two cylinders at $\text{Re} = 5 \times 10^3$. As indicated in this figure, for both cylinders, swirls patterns exist behind the cylinder at $\phi = 0$ and $\pi/4$. As a result of cylinder direction of motion and acceleration, the mean recirculation region is suppressed at $\phi = 3\pi/4$. As discussed earlier in Figure 7.4 for $\phi = 3\pi/4$, the recovery of the mean recirculation region occurs on a larger portion of the near wake for the higher aspect ratio cylinder, hence, the counter-rotating swirls appear downstream the cylinder for this case. In the return cycle, no discrepancy can be detected in the near wake of cylinders with different aspect ratios.

Figure 7.13 shows the flow behavior in the $Z/L = -0.23$ and -0.35 planes. In the first half cycle from $\phi = 0$ to $\phi = 3\pi/4$, the flow in the near wake for both cylinders represents similar behavior, which is the elongation of the counter-rotating swirls further downstream by increasing the yaw angle. Major discrepancies are evident from $\phi = \pi$ onward. At $\phi = \pi$, it can be observed that the counter-rotating swirls are detached from the rear surface of the cylinder in the $Z/L = -0.23$ and -0.35 planes for the $L/D = 13$ cylinder while they are almost
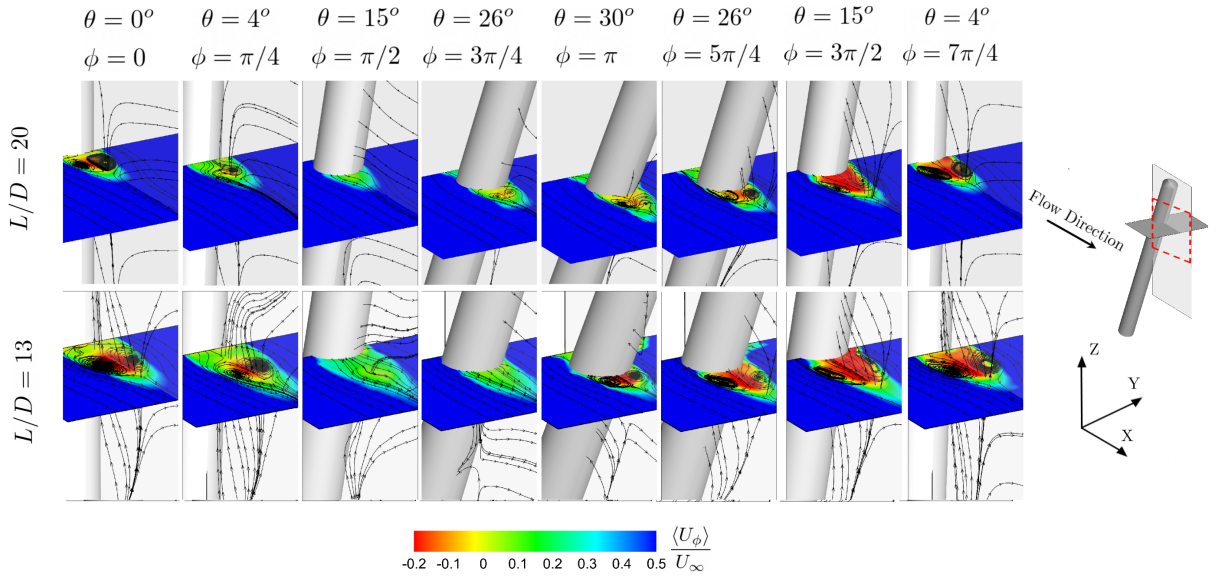
Figure 7.12: Contours of phase-averaged normalized streamwise velocity ($\langle U_\phi \rangle / U_\infty$) overlaid by phase-averaged streamline topology ($\langle \psi_\phi \rangle$) at eight select phases of oscillation with the reduced frequency of $K = 1.3$ for aspect ratios of $L/D = 13$ and 20 at $\text{Re} = 5 \times 10^3$ in the $Z/L = 0.23$ plane.

suppressed in the considered planes for the $L/D = 20$ case. This shows that the separated counter-rotating swirls near the upstream end for $L/D = 20$ cylinder (see Figure 7.4) are located between the studied planes. Therefore, it can be concluded that the size of the detached wake from the surface of the cylinder near the upstream end for the cylinder with a lower aspect ratio is relatively larger. At $\phi = 5\pi/4$, as the detached wake ascends towards the mid-span of the cylinder, the swirl patterns are eliminated in the $Z/L = -0.35$ plane. A small section of the swirls and backflow velocity regions are still visible in the $Z/L = -0.23$ plane for $L/D = 13$ cylinder. However, for the cylinder with $L/D = 20$, no reverse flow and swirls are shown owing to the significant influence of spanwise flow on the suppression of the mean recirculation region in the studied plane. Results at $\phi = 3\pi/2$ reveal that the detached wake is still visible at $Z/L = -0.23$ for the $L/D = 13$ case whereas for the cylinder with a higher aspect ratio the flow is strongly in the positive streamwise direction immediately behind the cylinder under the effect of axial flow, the direction of motion of the cylinder, and the acceleration of the cylinder. At $\phi = 7\pi/4$, the flow in the positive streamwise direction is seen behind the cylinders in both studied planes.

Variations in the shear layers in (X,Y) planes at $Z/L = -0.23$ and -0.35 accompanied by the vorticity field in the (X,Z) plane at $Y/D = 0$ are shown in Figure 7.14. It is apparent that from $\phi = 0$ to $3\pi/4$, the shear layers in the $Z/L = -0.23$ are further curved towards the wake centerline by increasing the yaw angle. However, in the $Z/L = -0.35$ plane, due to the impact of the ascending positive vorticity region, as depicted in the Y/D plane, with increasing yaw angle, the shear layers gradually diverge from the wake centerline. In the return cycle, the effect of the interaction of positive Y-direction vorticity with the shear layers in (X,Y) planes is more pronounced. Comparing the results in the return cycle for the two cylinders indicates that the positive Y-direction vorticity region moves more rapidly towards the middle section of the cylinder for the cylinder with a higher aspect ratio. This can be attributed to the more significant development of the axial flow along the span of the cylinder with increasing the aspect ratio. From $\phi = \pi$ to $\phi = 3\pi/2$, for the cylinder with $L/D = 13$, when the positive Y-direction vorticity in the $Y/D = 0$ plane reaches each plane,
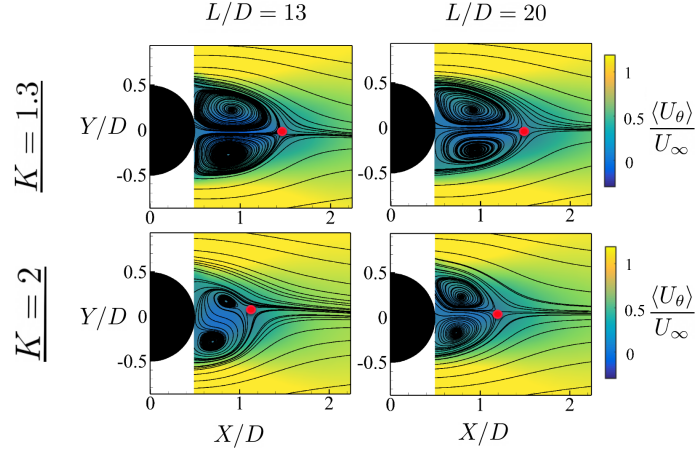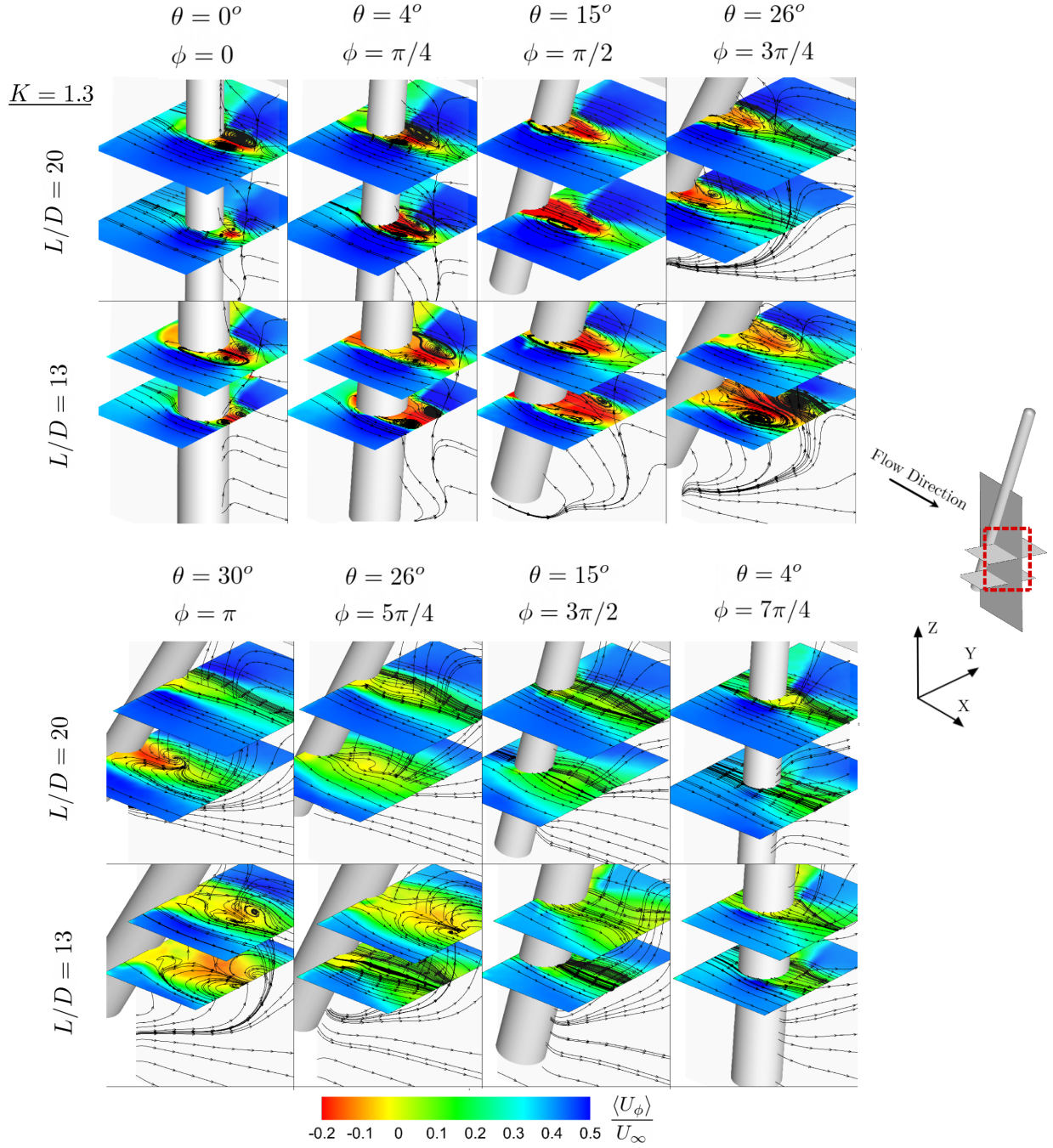
Figure 7.13: Contours of phase-averaged normalized streamwise velocity ($\langle U_\phi \rangle / U_\infty$) overlaid by phase-averaged streamline topology ($\langle \psi_\phi \rangle$) at eight select phases of oscillation with the reduced frequency of $K = 1.3$ for aspect ratios of $L/D = 13$ and 20 at $\mathrm{Re} = 5 \times 10^3$ in the $Z/L = -0.23$ and -0.35 planes.
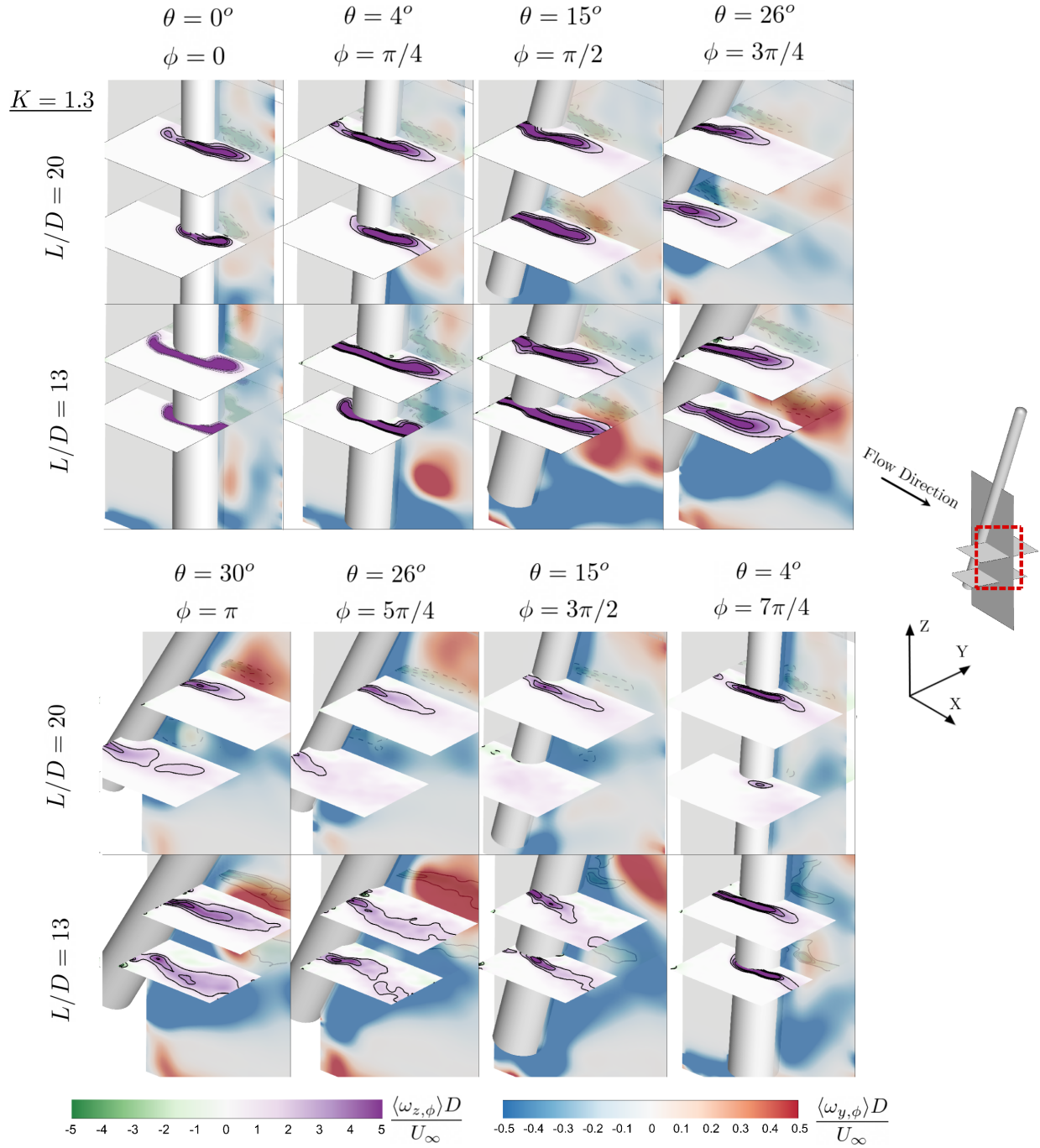
Figure 7.14:   Contours of phase-averaged normalized Z-direction vorticity ($\langle\omega_{y,\phi}\rangle D/U_\infty$) in the in the $Z/L = -0.23$ and -0.35 planes contours of Y-direction vorticity ($\langle\omega_{z,\phi}\rangle D/U_\infty$) in the symmetry plane at eight select phases of oscillation with the reduced frequency of $K = 1.3$ for aspect ratios of $L/D = 13$ and 20 at $\mathrm{Re} = 5\times10^3$

the extent of the vorticity in the shear layers drops and the trajectory of the shear layers significantly diverge from the wake centerline. When the vorticity passes by each plane, the lateral distance of the shear layers gradually decreases as the cylinder returns to the non-yawed position. For $L/D = 20$, the behavior is the same, however, due to the faster motion of the Y-direction vorticity and the higher impact of the axial flow on the near wake, the shear layers are significantly suppressed in the $Z/L = -0.35$ plane.

7.3   Wake Parameters

7.3.1   Wake Closure Length

The spanwise variations of the wake closure length for two yaw-oscillating cylinders at $K = 1.3$ and static yawed cylinders with aspect ratios of $L/D = 13$ and 20 are depicted in Figure 7.15. As shown in this figure, for the static yawed cylinders, the wake closure length is generally shorter along the span of the cylinder with a higher aspect ratio. Notice that the special trend in the variation of wake closure length at $\theta = 15^{\circ}$ occurs for both cases, which was already discussed in Section 6.2. At yaw angles of $\theta = 26^{\circ}$ and 30°, it is shown that the suppression of the mean recirculation region occurs on a larger section of the span of the cylinder with a lower aspect ratio owing to the discrepancy in positive axial flow. Results for the yaw-oscillating cylinder reveal that the trend in the spanwise variation of the wake closure length for yaw-oscillating cylinders with various aspect ratios is remarkably different from what was observed in the static counterpart. Near the top half of the cylinder, the streamwise extent of the mean recirculation region is greater for the cylinder with the lower aspect ratio for nearly all the phases. In the first half of oscillation, near the top half of the cylinder, it is evident that the impact of acceleration/deceleration of the cylinder is more pronounced for the cylinder with $L/D = 20$. For instance, at $\phi = \pi/4$, the suppression of the mean recirculation region occurs from the top end down to around $Z/L = 0.3$ for $L/D = 13$ cylinder while this suppression is extended to around $Z/L = 0.2$ for the $L/D = 20$ case. In the return cycle, behind the top half of the cylinder, the elongation of the wake closure length
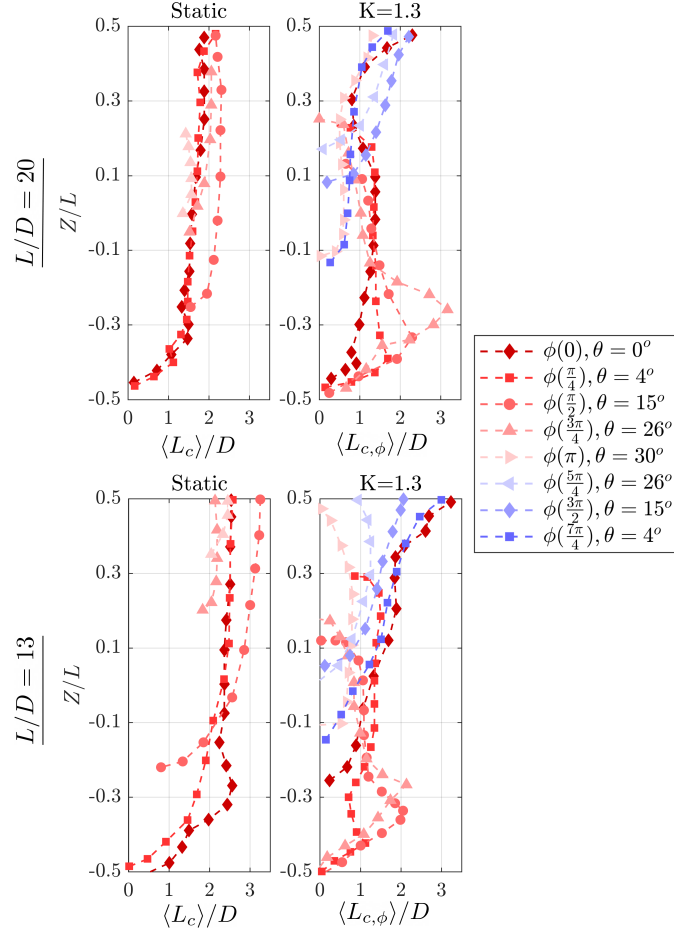
Figure 7.15: Profiles of phase-averaged normalized streamwise velocity ($\langle U_\phi \rangle / U_\infty$) for eight select phases of a yaw oscillation with reduced frequency of $K = 1.3$ for cylinders with aspect ratios of 13 and 20 at a) $Z/L = 0.23$ b) $Z/L = -0.23$ and c) Phase-averaged normalized axial velocity ($\langle V_{A,\phi} \rangle / U_\infty$) in the return cycle at $Z/L = 0.23$. The Reynolds number is 5×10^3.

from $\phi = 5\pi/4$ to $\phi = 3\pi/2$ is more significant for the cylinder with $L/D = 20$. it is evident that the deceleration of the cylinder from $\phi = 3\pi/2$ to $\phi = 7\pi/4$ for the cylinder with a higher aspect ratio leads to a sudden decrease in the wake closure length. Unlike the regions behind the top half, behind the bottom half of the cylinder, the walk closure length is elongated for a cylinder with a higher aspect ratio in the first half of oscillation.

7.3.2   Velocity Profiles

Profiles of $\langle U_\phi \rangle / U_\infty$ on the wake centerline, extracted from the two spanwise planes $Z/L = \pm 0.23$, are presented in Figures 7.16 (a) and (b) for the yaw-oscillating cylinders with $L/D = 13$ and 20 at eight phases from the full oscillation cycle. Notice that these Z/L locations for the two cylinders show the corresponding spanwise locations away from the center of rotation by a fixed percentage of their respective L/D values. When defined in terms of Z/D, these two spanwise planes are the $Z/D = \pm 3$ planes for the cylinder with $L/D = 13$ and the $Z/D = \pm 4.6$ planes for $L/D = 20$. Also, Figure 7.16 (c) represents the variation of $\langle V_{A,\phi} \rangle / U_\infty$ on the wake centerline at $Z/L = 0.23$ for the two cylinders from $\phi = \pi$ to $7\pi/4$ to compare the development of axial flow in their return cycle. Figure 7.16
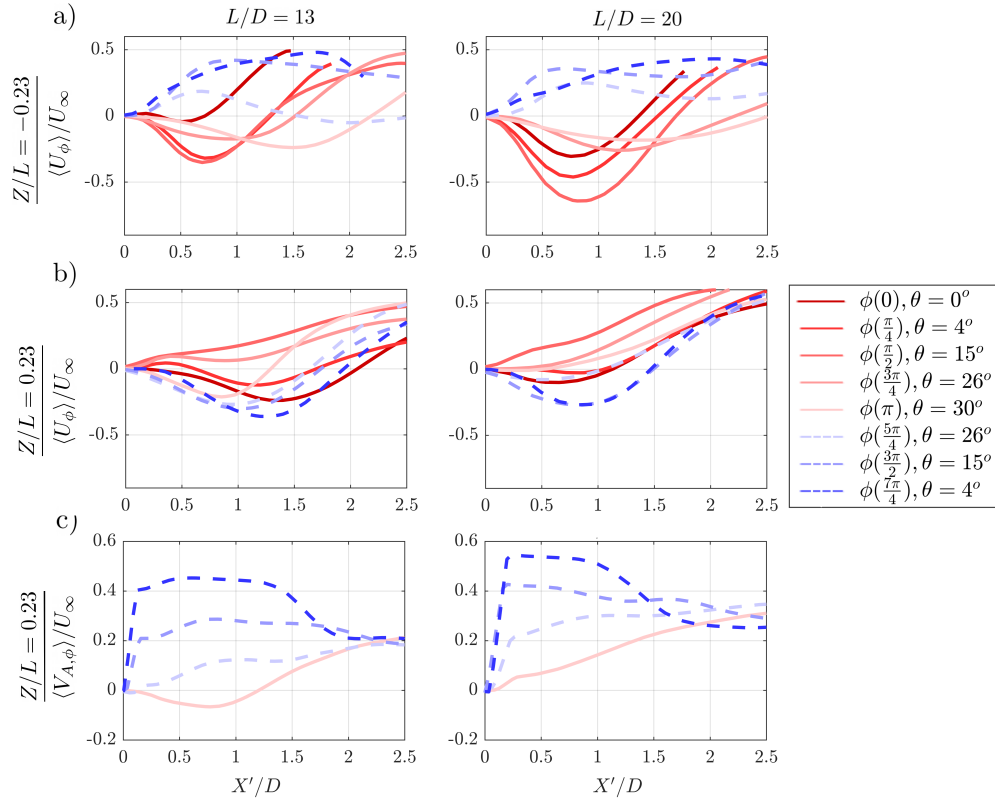
Figure 7.16: Profiles of phase-averaged normalized streamwise velocity ($\langle U_\phi \rangle / U_\infty$) for eight select phases of a yaw oscillation with reduced frequency of $K = 1.3$ for cylinders with $L/D = 13$ and 20 at a) $Z/L = 0.23$ b) $Z/L = -0.23$ and c) Phase-averaged normalized axial velocity ($\langle V_{A,\phi} \rangle / U_\infty$) in the return cycle at $Z/L = 0.23$.

(a) indicates that at $Z/L = -0.23$, as the cylinder accelerates from $\phi = 0$ to $\pi/2$, the peak magnitude of the reverse flow velocity gradually increases for both cylinders and with the acceleration effect being more influential for the larger L/D, relatively higher values are obtained for the cylinder with larger L/D. As the cylinders go from $\phi = \pi/2$ to π, the peak reverse flow velocity decreases for both cylinders under the effect of cylinders' deceleration, and the change in the maximum reverse velocity is more considerable for the larger L/D because of the greater impact of deceleration on the wake of the larger L/D case. In the second half of oscillation from $\phi = \pi$ to $7\pi/4$, the maximum positive velocity at $Z/L = -0.23$ keeps increasing for both L/D as the phase of oscillation advances under the effect of positive X-direction motion of the cylinder. Profiles of $\langle U_\phi \rangle / U_\infty$ at $Z/L = 0.23$, given in Figure 7.16 (b), show for both cylinders a decrease in the peak magnitude of negative streamwise velocity as the phase of oscillation goes from $\phi = 0$ to $\pi/4$ owing to the positive direction of motion of the cylinder's top half with a large acceleration. The reverse flow is weaker at these oscillation phases for the cylinder with larger L/D, again due to the more significant impact from the cylinder acceleration. The accelerating motion of the cylinder in the streamwise direction continues until $\phi = \pi/2$, revoking the reverse flow completely at $\phi = \pi/2$ and leading to a positive streamwise velocity with the higher value obtained for the $L/D = 20$ case. When the cylinder decelerates from $\phi = \pi/2$ to $3\pi/4$, the peak magnitude of the positive streamwise velocity decreases for both cylinders, and this variation is more significant for the cylinder with the higher L/D.

In the return cycle, the peak magnitude of the reverse flow at $Z/D = 0.23$ is generally relatively lower for the cylinder with the higher L/D, suggesting a weaker recirculation region. This behavior can be linked to the spread of the positive axial flow from the lower end of the cylinder over larger spanwise sections in the cylinder wake for the larger length-to-diameter ratio cylinder in its return cycle. The variation of the axial velocity at $Z/L = 0.23$, given in Figure 7.16 (c), further reinforces this observation by depicting that the axial flow is more substantial over the phases of the return cycle for the larger L/D cylinder.

7.4 Vortex Shedding

7.4.1 Static Yawed Cylinder

In order to compare the vortex shedding frequency from the mid-span of the static yawed cylinders with different aspect ratios, the velocity spectra obtained from the streamwise velocity signal at different yaw angles are presented in Figure 7.17 (a) at Reynolds number of 5×10^3. Inspecting Figure 7.17 (a) shows that for both cylinders, narrow-bank peaks associated with the vortex shedding frequency become further broadband with increasing yaw angle accompanied by a reduction in the height and energy of the peak. This can be related to the less organized and mitigated vortex shedding from the cylinder at high yaw angles. Evaluating the impact of L/D in Figure 7.17 (a) reveals that for the cylinder with higher aspect ratio, remarkably narrow-band peaks with higher energy occur at each yaw angle associated with a larger degree of periodic vortex shedding compared to the cylinder with lower L/D. The present results are aligned with the investigation of Benitz *et al.* [67] for the non-yawed cylinder with similar end conditions as the current study. From Figure 7.17 (a), it can also be concluded that unlike the cylinder with $L/D = 13$, increase in the axial flow especially from $\theta = 0^\text{o}$ to 20° has less impact on the vortex shedding of the cylinder with higher L/D as the increase in the width of the peak region by yaw angle is less pronounced.

Figure 7.17 (b) shows the variation of the Strouhal number of vortex shedding with yaw angle for the two cylinders considered in this study. The general trend for both cylinders is a decrease in St with increasing yaw. Moreover, the results indicate that at all yaw angles, the higher Strouhal numbers are obtained for the cylinder with the higher L/D. The discrepancy is more significant at lower yaw angles from $\theta = 0^\text{o}$ to 15° and the unexpected increase in St at $\theta = 15^\text{o}$ does not occur for the higher aspect ratio cylinder. Figure 7.17 (c) indicates the variation of St_N/St_o obtained in Figure 7.17 (b) along with the results of Najafi *et al.* [40] at a comparable range of Reynolds number and L/D. This Figure demonstrates that the Strouhal number of vortex shedding at each yaw angle becomes closer to the prediction of
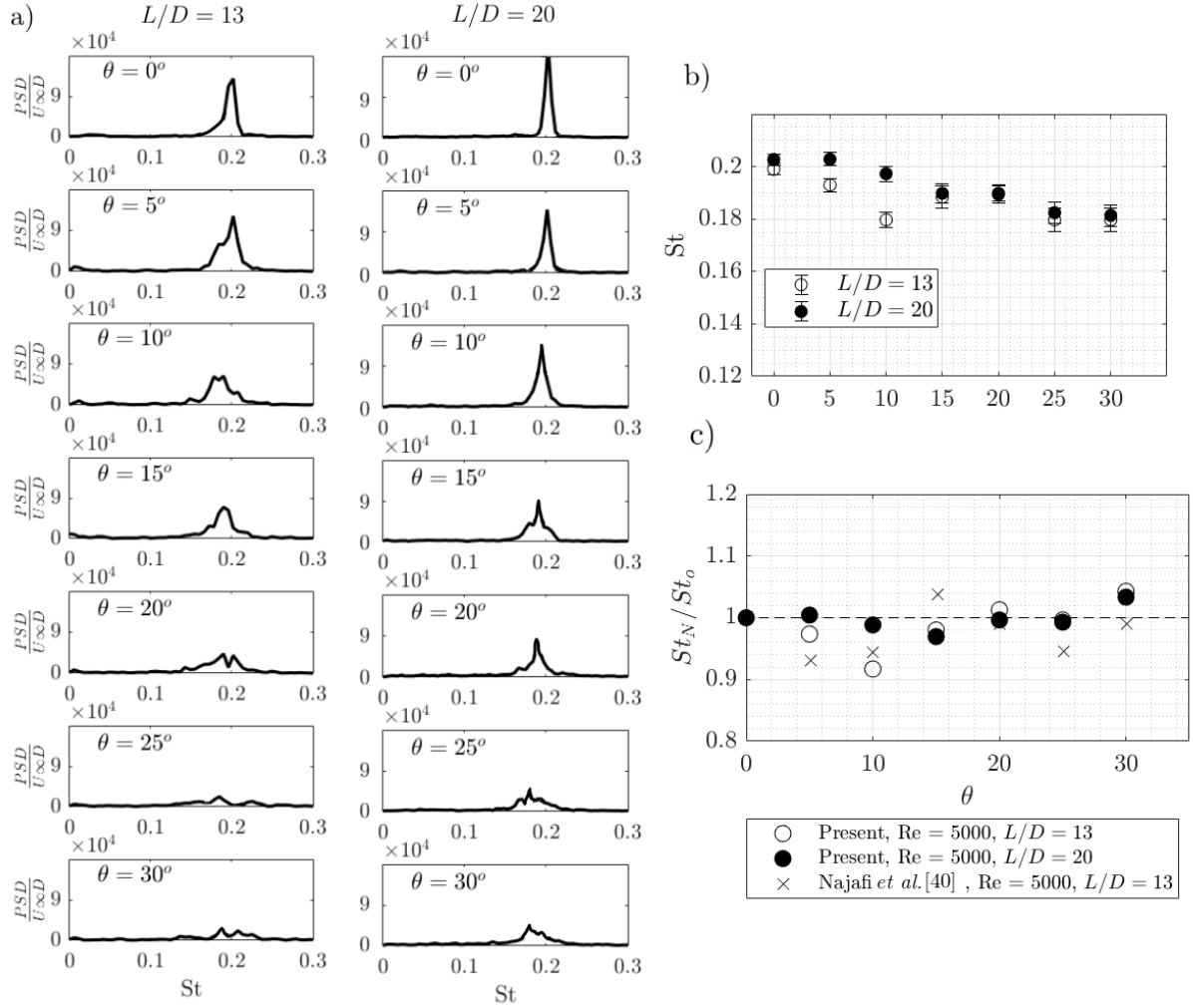
Figure 7.17:   a) Velocity spectra of the streamwise velocity for the static yawed cylinders at different yaw angles. b) Variation of the Strouhal number with yaw angle c) Variation of St_N/St_o with the yaw angle for cylinders with the aspect ratios of 13 and 20 at $\mathrm{Re} = 5 \times 10^3$.

IP by increasing L/D. It can also be observed that the present results for the static yawed cylinder are in agreement with those obtained in the literature.

7.4.2   Yaw-Oscillating Cylinder

Comparative study on the yaw-oscillating cylinders with different aspect ratios is conducted using the yaw-averaged frequency analysis. The velocity spectra of the streamwise velocity for the yaw-oscillating cylinder with reduced frequencies of $K = 1.3$, and 2 are shown for the

159
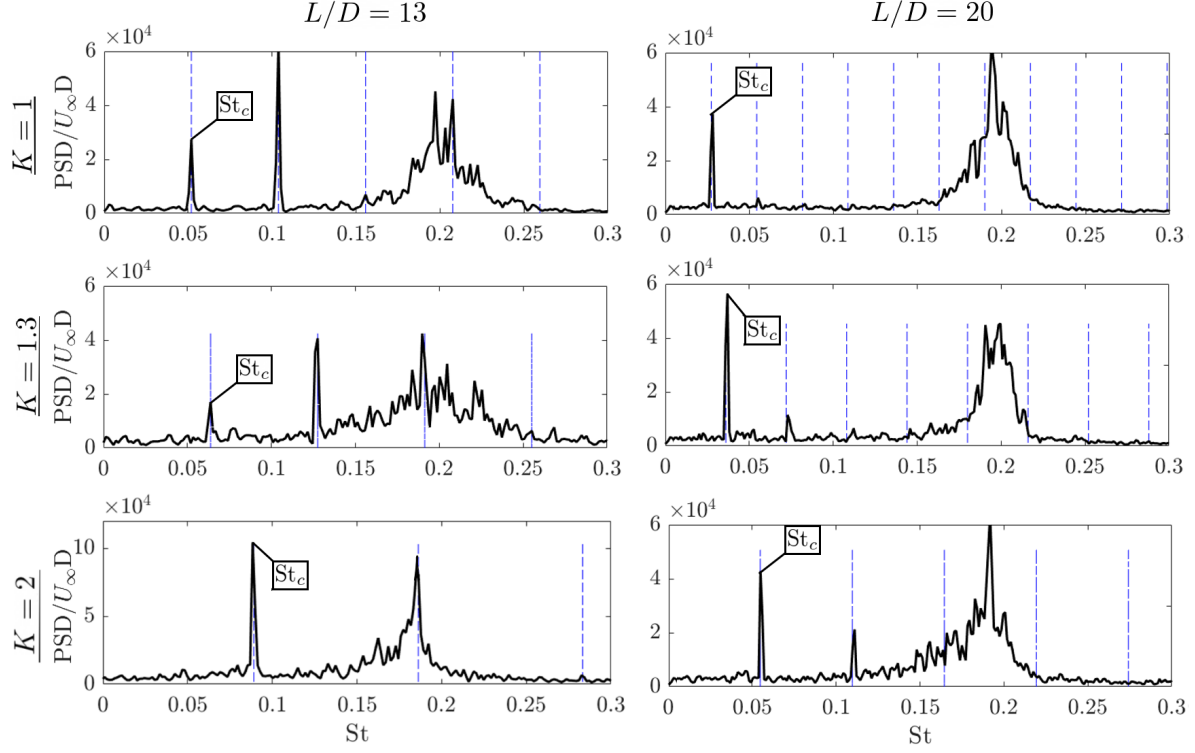
Figure 7.18: Velocity spectra of the streamwise velocity for yaw-oscillating cylinders with aspect ratios of 13 and 20 and reduced frequencies of $K = 1$, 1.3, and 2 at $\mathrm{Re} = 5 \times 10^3$. The Strouhal number of the fundamental frequency of oscillation, which is denoted by St_c, and the corresponding harmonic frequencies are marked by the blue dashed lines.

two studied cylinders at $\mathrm{Re} = 5 \times 10^3$ in Figure 7.18. As previously discussed in Section 6.4, increasing the reduced frequency enlarges the width of the peak region and decreases the peak energy in the spectra. Moreover, it was shown that vortex shedding occurs at lower frequencies by increasing reduced frequencies. For moderate reduced frequencies of $K = 1$ and 1.3, it is apparent that similar to the static cylinder, the peak region in the range of vortex shedding frequency is relatively narrow-band and has higher energy for the cylinder with higher L/D. It can be deduced that more organized and periodic vortex shedding occurs for the yaw-oscillating cylinder with $L/D = 20$ at moderate reduced frequencies. Figure 7.18 also indicates that the oscillation frequency is significantly lower than the range of vortex shedding frequency for the cylinder with higher L/D, hence, lower impact of the harmonic frequencies can be observed in this range of frequencies. At high reduced frequency of $K = 2$,

the peak region in the spectra covers lower range of frequencies for the cylinder with lower L/D. Moreover, for $L/D = 13$, a higher energy peaks are observed at frequency region of $0.15 < \text{St} < 0.17$. This can be associated with the positive Z-direction vorticity region created behind the mid-span of the cylinder that moves downstream by cylinder yaw oscillation, as previously discussed in Section 6.4.2. In the same range of frequencies, the energy of the peak region is lower for $L/D = 20$ presumably due to the absence of such high vorticity region near the mid-span, as previously shown in Figure 7.7.

7.5 Chapter Summary

In this chapter, the effect of the aspect ratio of the cylinder was evaluated by studying the near wake of static and yaw-oscillating cylinders having $L/D = 20$ and comparing the results with those obtained in the previous chapters for the $L/D = 13$ case. The results were compared for $\text{Re} = 5 \times 10^3$.

For the static cylinder, increasing the aspect ratio decreased the wake closure length along the span at all yaw angles. It was also shown that for a larger L/D, the effect of axial flow, particularly at high yaw angles, is diminished and the suppression of the mean recirculation region occurs on a smaller section of the span for the cylinder with $L/D = 20$. Moreover, the vortex shedding behavior at the mid-span of the static cylinders showed that more periodic vortex shedding occurs for a larger L/D case at all yaw angles.

Results for the yaw-oscillating cylinders at $K = 1.3$ showed that the general near wake structure was similar for both cases, however, some variations were observed. The effect of acceleration/deceleration of the cylinder was shown to be more effective on the near wake with increasing L/D. Another discrepancy was related to the development of axial flow along the span of the cylinder, which occurs more rapidly for the cylinder with a larger aspect ratio. The evaluation of vortex shedding behavior for the yaw-oscillating cylinders demonstrated that similar to the static cylinder, the vortex shedding is more organized for the $L/D = 20$ case.

Chapter 8

Conclusions and Future Recommendations

8.1   Conclusions

An experimental study was conducted on a cylinder undergoing yaw oscillation and the baseline flow over the static yawed cylinder at subcritical Reynolds numbers. The motivation of the present research is drawn from sports aerodynamics and particularly the physics of the flow that occurs past a moving limb of an athlete such as in the vicinity of the legs of a cyclist as an example. The circular cylinder is used as a low order model of a limb of an athlete and is subjected to yaw oscillation, which is the dominant motion of the leg of a cyclist while peddling. The present research can provide insight into the understanding of flow past yaw-oscillating bluff bodies that has not received any attention in the literature. The main variables considered in this study are the rate of yaw-oscillation, Reynolds number, and aspect ratio. The flow past the cylinder was measured using two experimental techniques, namely, planar Particle Image Velocimetry (PIV) and Constant Temperature Anemometry (CTA). The case of the static yawed cylinder was used to establish a baseline for comparison with the yaw-oscillating counterpart. For the yaw-oscillating cylinders, the analysis was conducted through ensemble averaging of the flow occurring over the range of yaw angles considered ($\theta =$

0º to 30º), termed yaw-averaged, and at discrete phases using a phase-averaging approach and the results were compared to that of the static case.

For the static yawed cylinder, evaluating the near-wake flow indicated that increasing the yaw angle leads to an increase in the streamwise and spanwise velocity and a decrease in the streamwise extent of the mean recirculation region. Inspecting the vortex shedding behavior at the mid-span of the static cylinder indicated a less periodic vortex shedding at lower frequencies by increasing yaw angle. At the high yaw angles of $\theta = 26$º and 30º considered in the present study, significant suppression of the mean recirculation region and the vortex shedding occurs near the bottom half of the span due to the impact of high-magnitude axial flow that could eventually lead to lower drag. Moreover, evaluating the variation of Strouhal number of vortex shedding with yaw angle indicated the failure of the Independence Principle (IP) at high yaw angles.

Although the static yawed cylinder exhibited relatively more uniform wake flow features along the majority of the span, the phase-averaged analysis of the near wake flow patterns showed that the flow in the near wake of the yaw-oscillating cylinder is highly three-dimensional. The spanwise variation in flow features became more significant as the reduced frequency increased from low ($K = 0.5$) to moderate values ($K = 1$ to 2), and turned being relatively more uniform again at very high reduced frequencies ($K = 4$) due to the delay in the response of the flow to the fast yaw oscillations. The cylinder's direction of motion, its acceleration/deceleration state, and the axial flow developing as the cylinder is yawed during an oscillation period were observed to be important parameters that can impact the flow in the near wake, and which of these parameters remain prominent over different spanwise sections of the wake and their effect depended on whether the reduced frequency of oscillations had a low, moderate or high value. Evaluation of the vortex shedding behavior for the yaw-oscillating cylinders showed that increasing reduced frequency leads to a less organized vortex shedding behind the cylinder and decreases the frequency of vortex shedding.

For low reduced frequencies ($K = 0.5$), the direction of the cylinder's motion is the only dominant factor controlling the near wake flow structure until large yaw angles. This effect

generally adds thrust into the flow from the movement of the cylinder. As half of the cylinder moves in the inflow direction, this movement adds a positive thrust into the flow behind that section of the cylinder, weakening the mean recirculation region and reducing its streamwise extent at those spanwise regions. On the contrary, if the half of the cylinder in question moves opposite to the inflow direction, this effect generates further reverse flow, strengthening the mean recirculation bubble. For example, in the first half cycle of yaw oscillations, as the yaw angle of the cylinder increases from $\theta = 0^{\text{o}}$ to 30°, the top half of the cylinder moves in the direction of the incoming flow, and the induced streamwise thrust on the flow by this movement gradually reduces the reverse flow velocity and its streamwise extent with increasing yaw angle in the top half span. On the other hand, during this same oscillation period, the bottom half of the cylinder moves against the inflow direction. This direction of the cylinder motion generates a gradual increase in the reverse flow velocity, strengthening the mean recirculation bubble in the bottom half of the cylinder up to larger yaw angles. At larger yaw angles, while the direction of the cylinder's motion continues to impact the near wake flow, high-amplitude axial flow velocity, originating from the bottom free end of the cylinder, grows and spreads over larger spanwise sections, and becomes the most prominent element that impacts the near wake flow topology over those spanwise portions. The high-amplitude axial flow is observed to have the general effect of reducing the reverse flow velocity and eventually leading to the suppression of the mean recirculation bubble. For example, the reduction of the streamwise velocity and the subsequent suppression of the recirculation bubble in the bottom half of the span at high yaw angles during the first half cycle of yaw oscillations even though the bottom half of the cylinder continues to move opposite to the inflow are connected to the presence of a more prominent axial flow effect in those regions compared to the impact of the direction of the cylinder's motion. Also, in the second half of the oscillation cycle at large yaw angles, as the lower half of the cylinder moves in the inflow direction, the continued reduction in reverse velocity and even its disappearance over certain sections behind the lower half of the cylinder are a result of the combined effects of the cylinder's motion and the strong axial flow.

For moderate reduced frequency values ($K = 1$ to 2), the acceleration/deceleration in the cylinder motion during its oscillation became another significant effect influencing the near wake flow behavior. Generally speaking, the acceleration of the cylinder motion made the cylinder's direction of motion more influential on the flow; on the contrary, the deceleration weakened the same effect. For instance, as the cylinder's yaw angle increases from $\theta = 0^\text{o}$ to 15°, with the acceleration enhancing the streamwise thrust induced by the cylinder's motion, the reduction in the reverse flow velocity and the spanwise region over which the mean recirculation region is suppressed become much larger in the top half of the cylinder for the moderate K values compared to the lower value of $K = 0.5$. As another example, consider the top half of the cylinder during its deceleration from $\theta = 15^\text{o}$ to 30°. During this movement, although the reverse flow velocity keeps decreasing for $K = 0.5$, the cylinder's forward motion loses its impact on the flow at higher K values, and the reverse flow gradually recovers.

At very high reduced frequencies ($K = 4$), the changes in flow behavior in response to the oscillations occurred with a time-lag. Generally, the direction of motion became the most influential factor in the flow behavior, while due to the delay in the response of the flow to the fast oscillation motion, the effect of deceleration/acceleration of the cylinder on the near wake was eliminated.

The influence of Reynolds number on the near-wake of the static yawed and yaw-oscillating cylinders were evaluated. For the static yawed cylinder, decreasing the Reynolds number results in the elongation of the mean recirculation and a decrease in the reverse flow velocity in the near wake at each yaw angle. Moreover, it was shown that each yaw angle, decreasing the Reynolds number leads to relatively lower axial velocity downstream the cylinder. However, the impact of axial flow on the vortex shedding mitigation and suppression of the mean recirculation region at high yaw angles remained the same. For yaw-oscillating cylinders, results indicated that the flow patterns and the vortex shedding behavior are almost independent of the Reynolds numbers considered. For each phase of oscillation, it was indicated that the existing mean recirculation regions along the span are generally elongated

by decreasing the Reynolds number.

The present study showed that aspect ratio is an important parameter that affects the near wake of static yawed and yaw-oscillating cylinders. For the static yawed cylinders, generally a longer wake closure length was observed for the cylinder with a lower aspect ratio. Moreover, the influence and extent of axial flow on the near wake of the cylinder is reduced by increasing the aspect ratio, thus, the mean recirculation region exists behind a larger section of the span of the cylinder at yaw angles of $\theta = 26º$ and $30º$ for a cylinder with higher aspect ratio. For the yaw-oscillating cylinder, the effect of cylinder aspect ratio on the near wake is more pronounced in the return cycle of oscillation where the axial flow could rapidly expand in the spanwise direction for the cylinder with a higher aspect ratio. Therefore, higher streamwise velocity in the near wake and significant suppression of the mean recirculation region occur behind the lower half of the span for the corresponding phases. The impact of the acceleration/deceleration state of the cylinder on the near-wake flow was enhanced for the larger aspect ratio. For both static and yaw-oscillating cylinders, increasing the aspect ratio led to an increase in the organized periodic vortex shedding and the corresponding frequencies.

8.2 Future Recommendations

The unsteady fluid dynamics of a cylinder undergoing yaw oscillation cylinder is a novel topic concerning the flow past bluff bodies with foundational application for improving the understanding of real complex problems. The present research builds an early understanding of a complex three-dimensional flow structure that occurs behind the cylinder during yaw-oscillation, however, aspects of this problem remain open. The following lists unresolved areas for further exploration:

- *Direct Drag Force Measurements*: One of the important parameters in the investigation of subcrticial flow past circular cylinders is the drag and lift force exerted. Considering the related application of the flow past the limb of an athlete, knowledge concerning the

variation of the total drag force during oscillation can shed further light on the impacts of this motion on aerodynamic performance. The drag measurement was not feasible in the present work due to the limitations and costs of the experimental setup. Although speculations were made on the local drag of the cylinder based on the variation of the mean recirculation region, the total drag of the system has not yet been directly measured.

- *Surface Pressure and Locating Separation Points*: Results in the present study revealed significant variations in the mean recirculation region and the separating shear layers along the span of the yaw-oscillating cylinders based on the reduced frequency and the phase of oscillation indicating variation in the separation point on the surface of the cylinder. Obtaining circumferential pressure distribution on different spanwise locations combined with the flow visualization very close to the cross-section of the cylinder can help estimate the location of separation points and the local force distribution on the cylinder. The information on the possible locations of flow separation points and the variations along the span can be used for flow control purposes.

- *Application to Realistic Limb Models*: The focus of the present study was on the circular cylinder while the realistic models of the limb vary in cross-section in the spanwise direction and possess different end conditions. To extend the knowledge of flow past the yaw-oscillating cylinder to the flow near the real limb of an athlete, a model with a shape of a lower leg, upper leg, and arm of an athlete can be connected to the yawing mechanism in the experimental setup. The size of the model can be chosen to keep the Reynolds number within the range of sports applications. As the shape of these models will not be a perfect circular cylinder, possible discrepancies in the flow behavior from the cylindrical model can be recognized.

- *Passive Flow Control*: Gaining knowledge about the general structure of the flow past a yaw-oscillating cylinder, ideas can be considered to perform a passive flow control over the cylinder to seek any vortex shedding suppression and drag reduction mechanisms.

167

Surface protrusion methods such as using tripwires, axial rods/strakes [93, 94], and grooves [95] on the surface of the cylinder or increasing surface roughness [96, 97] have been widely used in the literature to alter the flow structure in the near wake of a cylinder with the purpose of drag reduction. However, the number of studies on controlling flow past yawed cylinders is significantly limited. Results indicated that the separation points vary along the span of the cylinder and they are also highly dependent on the phase of oscillation. Therefore, using simple axial tripwires or rods on a fixed location might not be properly functional. Therefore, variation in the angle of the wires along the span or at least among a specific section of the cylinder might be required. Finding the appropriate location, size, and shape of the aerodynamic means on the surface of the yaw-oscillating cylinder (or limb model) to suppress the vortex shedding and reduced the drag can be the subject of following research on the topic.

- *Effect of Flow Acceleration/Deceleration*: The flow behavior in the near wake of a yaw-oscillating cylinder was associated with the combination of a cylinder direction of motion and its acceleration/deceleration state. However, the pure impact of acceleration/deceleration on the flow behavior could not be evaluated in the present research. The existing literature on the accelerating/decelerating cylinders is predominantly focused on the impulsively started/stopped non-yawed cylinders [98, 99] whereas studies on the impact of non-impulsive acceleration/deceleration on the near wake of yawed/non-yawed cylinders remain widely unexplored. The effect of this motion parameter is also relevant to athlete motion.

References

[1] C.H.K. Williamson. "Vortex dynamics in the cylinder wake". In: *Annual Review of Fluid Mechanics* 28:1 (1996), pp. 477–539.

[2] B. Forouzi Feshalami, H. Shuisheng, F. Scarano, L. Gan, and C. Morton. "A review of experiments on stationary bluff body wakes". In: *Physics of Fluids* 34.1 (2022), p. 011301.

[3] C.H.K. Williamson and A. Roshko. "Vortex formation in the wake of an oscillating cylinder". In: *Journal of Fluids and Structures* 2.4 (1988), pp. 355–381.

[4] C.H.K. Williamson and R. Govardhan. "A brief review of recent results in vortex-induced vibrations". In: *Journal of Wind Engineering and Industrial Aerodynamics* 96.6 (2008), pp. 713–735.

[5] J. S. Leontini, D. Lo Jacono, and M. C. Thompson. "A numerical study of an inline oscillating cylinder in a free stream". In: *Journal of Fluid Mechanics* 688 (2011), pp. 551–568.

[6] P. Poncet. "Topological aspects of three-dimensional wakes behind rotary oscillating cylinders". In: *Journal of Fluid Mechanics* 517 (2004), pp. 27–53.

[7] J. Carberry, J. Sheridan, and D. Rockwell. "Controlled oscillations of a cylinder: Forces and wake modes". In: *Journal of Fluid Mechanics* 538 (2005), pp. 31–69.

[8] S.E. Ramberg. "The effect of yaw and finite length upon the vortex wakes of stationary and vibrating circular cylinders". In: *Journal of Fluid Mechanics* 128 (1983), pp. 81–107.

[9] D. Cotter and S. Chakrabarti. "Wave force tests on vertical and inclined cylinders". In: *Journal of Waterway, Port, Coastal and Ocean Engineering* 110 (1984), pp. 1–14.

[10] F. Grappe, R. Candau, A. Belli, and D.J. Rouillon. "Aerodynamic drag in field cycling with special reference to the Obree's position". In: *Ergonomics* 40.12 (1997), pp. 1299–1311.

[11] Official 2020 Tokyo Olympic games website. `https://olympics.com/en/olympic-games/tokyo-2020/results/cycling-track/women-s-team-pursuit`.

[12] N. Barry, D. Burton, and J. Sheridan. "Aerodynamic drag interactions between cyclists in a team pursuit". In: *Sports Engineering* 18 (2015), pp. 93–103.

[13] T.N. Crouch, D. Burton, N.A. Brown, M.C. Thompson, and J. Sheridan. "Dynamic leg-motion and its effect on the aerodynamic performance of cyclists". In: *Journal of Fluids and Structures* 65 (2016), pp. 121–137.

[14] L. Brownlie, Y. Aihara, J. Carbo, E. Harber, R. Henry, T. Ilcheva, and P. Ostafichuk. "The use of vortex generators to reduce the aerodynamic drag of athletic apparel". In: *Procedia Engineering, 147 (Supplement C)* (2016), pp. 20–25.

[15] W. Terra, A. Sciacchitano, and F. Scarano. "Cyclist Reynolds number effects and drag crisis distribution". In: *Journal of Wind Engineering and Industrial Aerodynamics* 200 (2020), p. 104143.

[16] M.M. Zdrakovich. *Flow around circular cylinder, Volume 1, Fundamentals.* New York: Oxford University Press, 1997.

[17] R.D. Blevins. *Applied fluid dynamics handbook.* Van Nostrand Reinhold Company, 1984.

[18] R.L. Panton. *Incompressible flow.* eng. 4th ed. Hoboken, N.J.: Wiley, 2013.

[19] A. Ongoren and D. Rockwell. "Flow structure from an oscillating cylinder Part 2. Mode competition in the near wake". In: *Journal of Fluid Mechanics* 191 (1988), pp. 225–245.

[20] W. Ma, J. Liu, Y. Jia, L. Jin, and X. Ma. "The aerodynamic forces and wake flow of a rotating circular cylinder under various flow regimes". In: *Journal of Wind Engineering and Industrial Aerodynamics* 224 (2022), p. 104977.

[21] H.M. Blackburn and R.D. Henderson. "A study of two-dimensional flow past an oscillating cylinder". In: *Journal of Fluid Mechanics* 385 (1999), pp. 255–286.

[22] P.W. Bearman, M.J. Downie, J.M.R. Graham, and E.D. Obasaju. "Forces on cylinders in viscous oscillatory flow at low Keulegan-Carpenter numbers". In: *Journal of Fluid Mechanics* 154 (1985), pp. 337–356.

[23] R. Chengjiao, L. Lin, C. Liang, and C. Tingguo. "Hydrodynamic damping of an oscillating cylinder at small Keulegan–Carpenter numbers". In: *Journal of Fluid Mechanics* 913 (2021), A36.

[24] T.L. Morse and C.H.K. Williamson. "Prediction of vortex-induced vibration response by employing controlled motion". In: *Journal of Fluid Mechanics* 634 (2009), pp. 5–39.

[25] W. Gu, C. Chyu, and D. Rockwell. "Timing of vortex formation from an oscillating cylinder". In: *Physics of Fluids* 6.11 (1994), pp. 3677–3682.

[26] S.F. Hoerner. *Fluid-dynamic drag : Practical information on aerodynamic drag and hydrodynamic resistance.* Alburqueque, 1965.

[27] A. Kozakiewicz, J. Fredsoee, and B.M. Sumer. "Forces on pipelines in oblique attack: Steady current and waves". In: *Proceedings of the 5th ISOPE Conference, Hague, Netherlands.* (1995).

[28] R. King. "Vortex excited oscillations of yawed circular cylinders". In: *Journal of Fluids Engineering* 99 (1977), pp. 495–501.

[29] C.W. VanAtta. "Experiments on vortex shedding from yawed circular cylinders". In: *AIAA Journal* 6 (1968), pp. 931–933.

[30] O.M. Griffin. "A universal Strouhal number for the 'locking-on' of vortex shedding to the vibrations of bluff cylinders". In: *Journal of Fluid Mechanics* 85.3 (1978), pp. 591–606.

[31] O.M. Griffin. "Universal similarity in the wakes of stationary and vibrating bluff structures". In: *Journal of Fluids Engineering* 103.1 (1981), pp. 52–58.

[32] M. Zhao, L. Cheng, and T. Zhou. "Direct numerical simulation of three dimensional flow past a yawed circular cylinder of finite length". In: *Journal of Fluids and Structures* 25 (2009), pp. 831–847.

[33] D. Lucor and G.E. Karniadakis. "Effects of oblique inflow in vortex induced vibrations". In: *Flow, Turbulence and Combustion* 71 (2003), pp. 375–389.

[34] R. Wang, S. Cheng, and D. Ting. "Effect of yaw angle on flow structure and cross-flow force around a circular cylinder". In: *Physics of Fluids* 31 (2019), p. 14107.

[35] A. Thakur, X. Liu, and J.S. Marshall. "Wake flow of single and multiple yawed cylinders ". In: *Journal of Fluids Engineering* 126.5 (2004), pp. 861–870.

[36] J.S. Marshall. "Wake dynamics of a yawed cylinder". In: *Journal of Fluids Engineering* 125 (2003), pp. 97–103.

[37] R. Snarski. "Flow over yawed circular cylinders: Wall pressure spectra and flow regimes". In: *Physics of Fluids* 16 (2004), pp. 344–359.

[38] K.D. Thomson and D.F. Morrison. "The spacing, position and strength of vortices in the wake of slender cylindrical bodies at large incidence". In: *Journal of Fluid Mechanics* 50 (1971), pp. 751–783.

[39] J.D. Hogan and J.W. Hall. "Experimental study of pressure fluctuations from yawed circular cylinders". In: *AIAA Journal* 49 (2011), pp. 2349–2356.

[40] L. Najafi, E. Firat, and H. Akilli. "Time-averaged near-wake of a yawed cylinder". In: *Ocean Engineering* 113 (2016), pp. 335–349.

[41] K. Matsuzaki, M. Shingai, and Y. Haramoto. "Visualization of three-dimensional flow structures in the wake of an inclined circular cylinder". In: *Journal of Visualization* 7.1 (2004), pp. 309–316.

[42] M. Shirakashi, S. Wakiya, and A. Hasegawa. "Effect of the secondary flow on Karman vortex shedding from a yawed cylinder". In: *JSME International Journal Series B* 29 (1986), pp. 1124–1128.

[43] T. Kawamura and T. Hayashi. "Computation of flow around a yawed circular cylinder". In: *JSME International Journal Series B* 37.2 (1994), pp. 229–236.

[44] T. Hayashi and T. Kawamura. "Non-uniformity in a flow around a yawed circular cylinder". In: *Flow Measurement and Instrumentation* 6.1 (1995), pp. 33–39.

[45] A. Jain and Y. Modarres-Sadeghi. "Vortex-induced vibrations of a flexibly mounted inclined cylinder". In: *Journal of Fluids and Structures* 43 (2013), pp. 28–40.

[46] G.R. Franzini, R.T. Gonçalves, J.R. Meneghini, and A.L.C. Fujarra. "One and two degrees-of-freedom vortex-induced vibration experiments with yawed cylinders". In: *Journal of Fluids and Structures* 42 (2013), pp. 401–420.

[47] T. Sarpkaya and M. Isaacson. *Mechanics of wave forces on offshore structures.* Van Nostrand Reinhold, New York, 1981.

[48] C.H.K. Williamson. "Oblique and parallel modes of vortex shedding in the wake of a circular cylinder at low Reynolds numbers". In: *Journal of Fluid Mechanics* 19.206 (1989), pp. 579–627.

[49] C.H.K. Williamson. "Defining a universal and continuous Strouhal-Reynolds number relationship for the laminar vortex shedding of a circular cylinder". In: *Physics of Fluids* 31 (1988), pp. 118–173.

[50] H. Eisenlohr and H. Eckelmann. "Vortex splitting and its consequences in the vortex street wake of cylinders at low Reynolds numbers". In: *Physics of Fluids* 31 (1989), pp. 189–192.

[51] M. Gharib and M. Hammache. "An experimental study of the parallel and oblique vortex shedding from circular cylinders". In: *Journal of Fluid Mechanics* 31 (1991), pp. 567–590.

[52] G.D. Miller and C.H.K. Williamson. "Control of three-dimensional phase dynamics in a cylinder wake". In: *Experiments in Fluids* 18 (1994), pp. 26–35.

[53] P.K. Stansby. "The effects of endplates on the base pressure coefficient of a circular cylinder". In: *Aeronautical Journal* 78 (1974), pp. 36–37.

[54] S. Szepessy. "On the control of circular cylinder flow by endplates". In: *European Journal of Mechanics, B/Fluids* 12 (1993), pp. 217–244.

[55] R. Stager and H. Eckelmann. "The effect of endplates on the shedding frequency of circular cylinders in the irregular range". In: *Physics of Fluids* 3 (1974), pp. 2116–2121.

[56] T.A. Fox and G.S. West. "On the use of endplates with circular cylinders". In: *Experiments in Fluids* 3 (1990), pp. 237–239.

[57]   S. Szepessy and P.W. Bearman. "Aspect ratio and endplate effects on vortex shedding from a circular cylinder". In: *Journal of Fluid Mechanics* 234 (1992), pp. 191–217.

[58]   C. Norberg. "An experimental investigation of the flow around a circular cylinder: influence of aspect ratio". In: *Journal of Fluid Mechanics* 258 (1994), pp. 287–316.

[59]   D. Sumner. "Flow above the free end of a surface-mounted finite-height circular cylinder: A review." In: *Journal of Fluids and Structure* 43 (2013), pp. 41–63.

[60]   D. Farivar. "Turbulent uniform flow around cylinders of finite length". In: *AIAA Journal* 19 (1981), pp. 275–281.

[61]   G. Iungo, L. Pii, and G. Buresti. "Experimental investigation on the aerodynamic loads and wake flow features of a low aspect-ratio circular cylinder." In: *Journal of Fluids and Structures* 28 (2003), pp. 279–291.

[62]   T. Kawamura, S. Mayer, A. Garapon, and L. Sorensen. "Large eddy simulation of a flow past free surface piercing circular cylinder". In: *Journal of Fluids Engineering* 124(1) (2002), pp. 91–101.

[63]   G. Yu, E. Avital, and J. Williams. "Large eddy simulation of flow past free surface piercing circular cylinders". In: *Journal of Fluids Engineering* 130 (2008), p. 101304.

[64]   J. Suh, J. Yang, and F. Stern. "The effect of airwater interface on the vortex shedding from a vertical circular cylinder". In: *Journal of Fluids Engineering* 27 (2011), pp. 1–22.

[65]   M. Inoue, N. Baba, and Y. Himeno. "Experimental and numerical study of viscous flow field around an advancing vertical circular cylinder piercing free-surface". In: *Journal of Kansai Society Naval Architecture* 220 (1993), pp. 57–65.

[66]   P.P. Vlachos and D.P. Telionis. "The effect of free surface on the vortex shedding from inclined circular cylinders". In: *Journal of Fluids Engineering* 130(2) (2008), p. 021103.

[67]   M.A. Benitz, D.W. Carlson, B. Seyed-Aghazadeh, Y. Modarres-Sadeghi, M.A. Lackner, and D.P. Schmidt. "CFD simulations and experimental measurements of flow past free-surface piercing, finite length cylinders with varying aspect ratios". In: *Journal of Computers and Fluids* 136 (2016), pp. 247–259.

[68]   R. Goncalves, G. Franzini, G. Rosetti, J. Meneghin, and A. Fujarra. "Flow around circular cylinders with very low aspect ratio". In: *Journal of Fluids and Structure* 685 (2014), pp. 235–270.

[69]   T. Hayashi, F. Yoshino, R. Waka, and T. Kawamura. "End effect on a yawed circular cylinder in uniform flow". In: *Bluff-Body Wakes, Dynamics and Instabilities. International Union of Theoretical and Applied Mechanics.* (1993).

[70] A. Tayfun. "Controlling the near-wake of a circular cylinder with a single, large-scale tripwire". Ph.D. Dissertation. Canada: University of Toronto, 2014.

[71] A. Prasad and C.H.K. Williamson. "Three dimensional effects in turbulent bluff body wakes". In: *Journal of Fluid Mechanics* 343 (2000), pp. 235–265.

[72] J.M. Yu, T.S. Leu, and J.J. Miau. "Investigation of reduced frequency and freestream turbulence effects on dynamic stall of a pitching airfoil". In: *Journal of Visualization* 20 (2017), pp. 31–44.

[73] J. Westerweel. "Fundamentals of digital particle image velocimetry". In: *Measurement Science and Technology* 8.12 (1997), pp. 1379–1392.

[74] W. Thielicke and E.J. Stamhuis. "Towards user-friendly, affordable and accurate digital particle image velocimetry in MATLAB". In: *Journal of Open Research Software* 2(1) (2014), e30.

[75] M. Raffel, T.C. Willerand, and S. Werely. *Particle image velocimetry: A practical guide.* Springer Press, 2007.

[76] J.R. Taylor. *An introduction to error analysis: the study of uncertainties in physical measurements.* University Science Books, 1997.

[77] I. Lekakis. "Calibration and signal interpretation for single and multiple hot-wire/hot-film probes". In: *Measurement Science and Technology* 7.10 (1996), pp. 1313–1333.

[78] F.E. Jorgensen. *How to measure turbulence with hot-wire anemometers; a practical guide.* Dantec Dynamics, 2002.

[79] J.S. Bendat and A.G. Piersol. *Random data analysis and measurement procedures.* Hoboken, USA, Wiley, 2010.

[80] H. Hu and M.M. Koochesfahani. "Thermal effects on the wake of a heated circular cylinder operating in mixed convection regime". In: *Journal of Fluid Mechanics* 685 (2011), pp. 235–270.

[81] S. Dong, G.E. Karniadakis, A. Ekmekci, and D. Rockwell. "A combined direct numerical simulation–particle image velocimetry study of the turbulent near wake". In: *Journal of Fluid Mechanics* 569 (2006), pp. 185–207.

[82] J.H. Gerrard. "The wakes of cylindrical bluff bodies at low Reynolds number". In: *Philosophical Transactions of the Royal Society of London* 1354 (1978), pp. 351–382.

[83] C. Norberg. "LDV-measurements in the near wake of a circular cylinder". In: *Advances in Understanding of Bluff Body Wake and Vortex Induced Vibration* (1998).

[84] I. Wygnanski, F. Champagne, and B. Marasli. "On the large-scale structures in two-dimensional, small-deficit, turbulent wakes". In: *Journal of Fluid Mechanics* 168 (1986), pp. 31–71.

[85] P.D. Welch. "The use of fast Fourier transform for the estimation of power spectra: A method based on time averaging over short, modified periodograms". In: *IEEE Transactions on Audio and Electroacoustics* 15.2 (1967), pp. 70–73.

[86] H. Liang and R.Q. Duan. "Effect of lateral endplates on flow crossing a yawed circular cylinder". In: *Journal of Applied Sciences* 9(8) (2019), p. 1590.

[87] G.R. Franzini, R.T. Gonçalves, A.L.C. Fujarra, and J.R. Meneghini. "Force measurements on the flow around a fixed and yawed cylinder in the presence of free-surface". In: *Proceedings of the 22th ISOPE Conference, Rhodes, Greece.* (2012).

[88] C.H.K. Williamson. "Oblique and parallel modes of vortex shedding in the wake of a circular cylinder at low Reynolds numbers". In: *Journal of Fluid Mechanics* 206 (1989), pp. 579–627.

[89] A.D. Blackmore. "The use of endplates for a cylinder in the subcritical flow regime". Master's Thesis. Canada: University of Toronto, 2011.

[90] A.A. McKillop and F. Durst. "A laser anemometry study of separated flow behind a circular cylinder". In: *Laser Anemometry in Fluid Mechanics, II, Lisbon, Portugal* (1984), pp. 329–346.

[91] T. Zhou, M. Razali, S. Fatin, Y. Zhou, L.P. Chua, and L. Cheng. "Dependence of the wake on inclination of a stationary cylinder". In: *Experiments in Fluids* 46.6 (2009), pp. 1125–1138.

[92] A. Roshko. "On the wake and drag of bluff bodies". In: *Journal of the Aeronautical Sciences* 22 (1955), pp. 124–132.

[93] M.M. Zdravkovich. "Review and classification of various aerodynamic and hydrodynamic means for suppressing vortex shedding". In: *Journal of Wind Engineering and Industrial Aerodynamics* 7.2 (1981), pp. 145–189.

[94] Y. Lu, X. Yu, Y. Liao, and W. Xu. "The influence of the yaw angle on the VIV fatigue damage of a yawed cylinder with or without helical strakes". In: *Applied Ocean Research* 102 (2020), p. 102295.

[95] C. Zheng, P. Zhou, S. Zhong, X. Zhang, X. Huang, and R.C. So. "An experimental investigation of drag and noise reduction from a circular cylinder using longitudinal grooves". In: *Physics of Fluids* 33.11 (2021), p. 115110.

[96] E. Achenbach. "Influence of surface roughness on the cross-flow around a circular cylinder". In: *Journal of Fluid Mechanics* 46.2 (1971), pp. 321–335.

[97] G. Buresti. "The effect of surface roughness on the flow regime around circular cylinders". In: *Journal of Wind Engineering and Industrial Aerodynamics* 8.1 (2012), pp. 105–114.

[98] Y. Lee, J. Rho, J.H. Kim, and D.H. Lee. "Fundamental studies on free stream acceleration effect on drag force in bluff bodies". In: *Journal of Mechanical Science and Technology* 25 (2011), pp. 695–701.

[99] T. Sarpkaya. "Nonimpulsively started steady flow about a circular cylinder". In: *AIAA Journal* 29 (1991), pp. 1283–1289.

[100] R.J. Adrian. "Particle-imaging techniques for experimental fluid mechanics". In: *Annual Review of Fluid Mechanics* 23(1) (1991), pp. 235–270.

[101] C.E. Willert and M. Gharib. "Digital particle image velocimetry". In: *Experimental Fluids* 10 (1991), pp. 181–193.

[102] D. Michaelis, D.R. Neal, and B. Wieneke. "Peak-locking reduction for particle image velocimetry". In: *Measurement Science and Technology* 27.10 (2016), p. 104005.

[103] F. Scarano and M. Riethmuller. "Advances in iterative multigrid PIV image processing". In: *Experimental Fluids* 29(1) (2000), pp. 51–60.

[104] A. Sciacchitano. "Uncertainty quantification in particle image velocimetry". In: *Measurement Science and Technology* 30.9 (2019), p. 074004.

[105] A. Sciacchitano, D.R. Neal, B.L. Smith, S.O. Warner, P.P. Vlachos, B. Wieneke, and F. Scarano. "Collaborative framework for PIV uncertainty quantification:comparative assessment of methods". In: *Measurement Science and Technology* 26.7 (2015), p. 092001.

Appendices

Appendix A

Uncertainty Analysis

A.1   Sources of Error in PIV Measurement

In PIV measurements, errors are usually originated from three main sources of image acquisition, calibration, and image processing [75]. In the image acquisition, the uncertainty is aminly associated with the camera focus and aperture, particle seeding density, the laser sheet alignment, and image acquisition rate. In the image processing step, the sources of error include selection of interrogation window size, the cross-correlation algorithm, and particle displacement vector computation. In the present experiments, an effort was made to minimize the aforementioned sources of uncertainty as described in the following sections.

A.1.1   Particle Seeding Density

In order to minimize the error related to the density of the particles in the successive images, the literature recommends that at least 10 particles should fit within the interrogation window [100, 101]. In the present experiment, the interrogation window of 32×32 pixel is chosen to ensure that ample numbers of particles are within the selected

interrogation window. More information on the interrogation window size is given in the following sections.

A.1.2 Camera Setting

As previously described in Chapter 3, the camera was located either below or at the side of the water tunnel. The resolution of the images for the bottom view on different planes along the span of the cylinder varies approximately from 0.95 to 0.125 pixels/mm. For the side view analysis, the resolution is around 0.105 pixel/mm. The interrogation windows were selected based on the resolution of the image pairs.

The focus and aperture of the camera play an important role in the effect called pixel-locking in PIV measurement. Briefly, the pixel-locking happens when the diameter of the particle in the image falls below two pixels of the images and results in particle image displacement to be biased towards integer pixel values (see [102] for further details). Assessing the histogram of the particle displacement for various apertures, the F5.6 setting was shown to have a distribution closer to the Gaussian distribution. Blurring the images using the focus of the camera also had positive impacts on pixel-locking improvement. However, it should be noted that the experimental PIV setup used in the water tunnel was not ideal regarding minimizing the pixel-locking effect. As suggested by Raffel *et al.* [75], the average particle diameter is better to be between 3 to 4 pixels. With the F5.6 aperture setting, this requirement is met in the present PIV measurement.

A.1.3 Laser Sheet

The laser sheet thickness is an important factor in PIV measurement as it may contribute to the image acquisition noise and signal-to-noise ratio [100]. The laser sheet has to be sufficiently thick to ensure that the particles do not move out of the plane between the

successive image pairs. Westerweel [73] recommends that to minimize the out-of-plane disparity, the out-of-plane motion between consecutive image pairs has to be lower than 25% of the laser sheet. In the present experiments, the out-of-plane motion of the particles is calculated to be as high as 70% of the freestream velocity. The laser sheet thickness is chosen to be approximately around 2 mm accompanied by the appropriate size of the time interval between each frame to ensure that the maximum out-of-plane displacement is always lower than 0.5 mm.

A.1.4   Interrogation Window Size

Ideally, it is suggested that the velocity gradient within an interrogation window should be lower than half of the particle image diameter from top to the bottom of the interrogation window [100, 101]. The interrogation window size of 32×32 pixel is chosen in the current study to obtain maximum vector resolution in the flow and reduce the errors that can be introduced by the velocity gradient to a minimum. Note that the velocity gradient in the near wake region of the yaw-oscillating cylinder is lower than the maximum recommended by Adrian [100]. Moreover, the interrogation window has to be set in such a way that the maximum particle displacement is always lower than the size of the window. For instance, in a bottom view for the highest Reynolds number in the current study with the velocity of 0.298 mm/s and $\delta t = 1.5$ ms, the maximum free stream displacement is around 4 pixels, which is equal to 1/8th of the window size. However, by using multi-pass cross-correlation algorithms, the in-plane particle displacement disparity is minimized. Adrian [100] also revealed that to minimize the RMS fluctuation in particle displacement, the maximum displacement should be lower than a quarter of the window size, which has been met in the current experiment. Since the multi-grid iterative correlation methods can damp the RMS fluctuations [103], in the image processing of the current experiments, a multi-pass algorithm in the PIVLab program is chosen while 50% overlapping is implemented.

A.1.5 Plane Location at the Mid-span

One of the (X,Y) visualization planes passed through the center of rotation of the cylinder, as marked in Figure 3.3, for both yaw-oscillating cylinder and static cylinder cases. Due to the free surface end condition, an increase in the length of the cylinder exposed to the flow is inevitable with yaw angle. The actual mid-span of the cylinder is slightly closer to the free surface compared to the center of rotation plane with yaw. The discrepancy of the flow in the plane passing from the center of rotation and the plane at the exact mid-span for $\theta = 30^{\text{o}}$ (with the maximum displacement) is evaluated. Figure A.1 represents the profiles of the phase-averaged normalized streamwise velocity ($\langle U_\phi \rangle U_\infty$) at the wake centerline for $Z/L = 0$ (the center of rotation plane), 0.04, and 0.075 (the offset of the mid-span for $\theta = 30^{\text{o}}$) for $K = 1.3$. These profiles show that the deviation of the velocity from the center-of-rotation plane is minor.

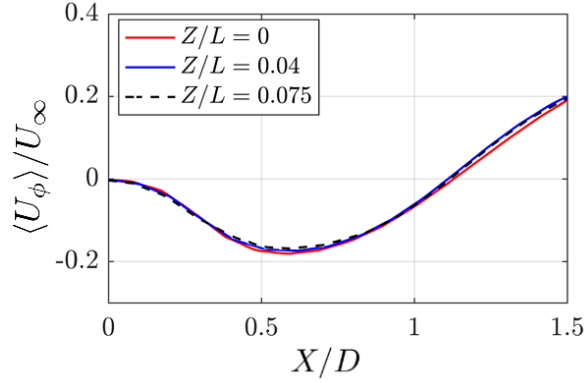Figure A.1: a) Variation of the normalized phase-averaged streamwise velocity profiles along the wake centerline at the planes that are passing from the center of rotation ($Z/L = 0$ plane), the exact mid-span location at phase $\phi = \pi$ ($\theta = 30^{\text{o}}$) ($Z/L = 0.075$), and a plane in between the two ($Z/L = 0.04$) for the yaw-oscillating case at $K = 1.3$ at $\text{Re} = 1.5 \times 10^4$.

A.2 Estimate of PIV Uncertainty

A.2.1 A Priori Approach

This section is devoted to the uncertainty analysis performed in the present thesis to measure the propagation errors during the experiments using a priori approach. According to Taylor [76], assume that x_1, x_2,..., x_n are measured with uncertainties of δx_1, δx_2, ..., δx_n and the measured values are used to compute the function $q(x_1,\ x_2,..., \ x_n)$. If the uncertainties in x_1, x_2,... x_n are independent and random, then the uncertainty in q is:

$$\delta q = \sqrt{(\frac{\partial q}{\partial x_1}\delta x_1)^2 + (\frac{\partial q}{\partial x_2}\delta x_2)^2 + \ ...+ \ (\frac{\partial q}{\partial x_n}\delta x_n)^2}, \tag{A.1}$$

To implement such analysis in the PIV measurement of the current study, the first step is to find the contributing parameters to the uncertainties. In the PIV measurement, the displacement of the illuminated particles is calculated over time. Thus, the velocity field in the field of view can be obtained as follows:

$$u = \frac{\Delta X}{\Delta t}, \tag{A.2}$$

where, u is the velocity of the particle, X is the displacement of the particle, and t is the time interval between the frames. To measure the uncertainty in the velocity field, the uncertainty in the detected particle displacements and time interval between the successive laser pulses should be taken into consideration. Using Equation (A.1), the uncertainty of the velocity field can be expressed as:

$$\delta u = \sqrt{(\frac{\partial u}{\partial \Delta X}\delta \Delta X)^2 + (\frac{\partial u}{\partial \Delta t}\delta \Delta t)^2}, \tag{A.3}$$

According to Raffel *et al.* [75], several factors contribute to the uncertainty for the

particle displacement detection such as seeding density, variation in particle size, sub-pixel displacement, interrogation window, calibration, variation of image quantization level, background noise, *etc.*. Therefore, obtaining the total uncertainty considering all sources of individual errors is highly challenging. In the present work, the uncertainties associated with the calculation of the displacement vector are as follows:

$$\Delta X = MC, \tag{A.4}$$

where M is the magnification factor in mm/pixel and C is the particle displacement obtained from the cross-correlation done in the PIVLab program. Therefore, $\delta\Delta X$ can be calculated as below:

$$\delta\Delta X = \sqrt{(\frac{\partial \Delta X}{\partial M}\delta\Delta X)^2 + (\frac{\partial \Delta X}{\partial C}\delta C)^2}, \tag{A.5}$$

The calibration in the present PIV measurements was conducted using a ruler so that the pixels in the image plane can be related to the real distance covered. The magnification factor (M) can be defined as:

$$M = \frac{d}{n}, \tag{A.6}$$

where d is the reference distance used in the calibration process and n is the number of pixels that fit in the reference distance. Therefore, the uncertainty in the magnification (calibration) process can be obtained as shown below:

$$\delta M = \sqrt{(\frac{\partial M}{\partial d}\delta d)^2 + (\frac{\partial M}{\partial n}\delta n)^2}, \tag{A.7}$$

Partial derivatives obtained in Equations A.2 to A.8 are summarized in Table A.1. Using the above equations and parameters, the values obtained in the uncertainty analysis of both the bottom view and side view PIV measurements are reported in

Table A.1: Partial derivatives and experimental terms obtained for uncertainty calculation

Partial Derivatives	Experimental Terms
$\frac{\partial U}{\partial \Delta X}$	$\frac{1}{\Delta t}$
$\frac{\partial U}{\partial \Delta t}$	$\frac{\Delta X}{(\Delta t)^2}$
$\frac{\partial \Delta X}{\partial c}$	M
$\frac{\partial M}{\partial d}$	$\frac{1}{n}$
$\frac{\partial M}{\partial n}$	$\frac{d}{n^2}$

Table A.2: Calculated values for the uncertainty analysis of PIV measurements

Factor	Side View (X, Z) Planes	Bottom View (X, Y) Planes
d	50.8 mm	50.8 mm
δd	0.1 mm	0.1 mm
n	406 pixels	472 pixels
δn	0.5 pixels	0.5 pixels
M	0.12 mm/pixel	0.10 mm/pixel
δM	0.0018 mm/pixel	0.0024 mm/pixel
δC	0.1	0.1
ΔX	1.52 mm	1.61 mm
$\delta \Delta X$	0.0028 mm	0.0037 mm
δu	6.3 mm/s	9.9 mm/s

Table A.2. As shown in this table, the uncertainty of the velocity field in (X, Y) and (X, Z) planes are $0.021U_\infty$ and $0.033U_\infty$, respectively.

A.2.2 A Posteriori Approach

In this section, a posteriori approach is used to estimate the uncertainty of the PIV results. In this approach, the analysis is made on the obtained image pairs and the corresponding flow fields. Various types of a posteriori approaches for the uncertainty calculation have been proposed in the literature (see, for example, [104]) and in the present project, the particle disparity method [105] is used. The approach is advantageous in estimating the uncertainty in both instantaneous and mean flow fields.

Figure A.2 (a) shows the contours of calculated random errors for the phase-averaged streamwise velocity ($\langle U_\phi \rangle / U_\infty$) of the yaw-oscillating cylinder at $K = 1.0$ in the (X, Y) planes at $Z/D = -3$ and 3. The Reynolds number is 1.5×10^4 and the results are shown at three phases of $\phi = 0$, $\pi/2$, and $5\pi/4$ corresponding to the yaw angles of $\theta = 0^o$, 15°, and 26° to cover different near-wake flow conditions. As shown in Figure A.2 (a), the highest error occurs at two main regions; 1) near the wake closure point, where the shear layers roll up and start shedding, 2) regions immediately behind the cylinder for cases with existing strong axial flow. The first scenario is observable for $\phi = 0$ and $\phi = \pi/2$ in both $Z/D = -3$ and 3 planes due to the presence of the counter-rotating swirls previously shown in Figure 6.4. It is seen that the maximum error of around 8.5% is obtained around the wake closure point. The uncertainty is less further downstream (around 5%) and around 1% in the freestream. The second scenario is seen for $\phi = 5\pi/4$, where the axial flow was already shown to be strong behind the rear surface of the cylinder. The highest uncertainty of around 8% occurs immediately behind the cylinder due to the higher extent of the out-of-plane motion of the particles.

The contours of uncertainty for the phase-averaged streamwise velocity in the (X, Z) symmetry plane at $Y/D = 0$ for the yaw-oscillating cylinder at $K = 1$ are presented in

Figure A.2 (b). Similar to the results for the (X, Y) planes, three phases of $\phi = 0$, $\pi/2$, and $5\pi/4$ corresponding to the yaw angles of $\theta = 0^o$, 15°, and 26° are shown. As evident in Figure A.2 (b), in the (X, Z) planes, the highest errors in the PIV measurement occur near both ends of the cylinder with higher flow interactions. Near the bottom end, the separated flow from the free end interacts with the Karman vortex shedding while the flow behind the top end of the cylinder is under the impact of the turbulent free surface effect. The greatest uncertainty obtained is around 8% for various cases considered.
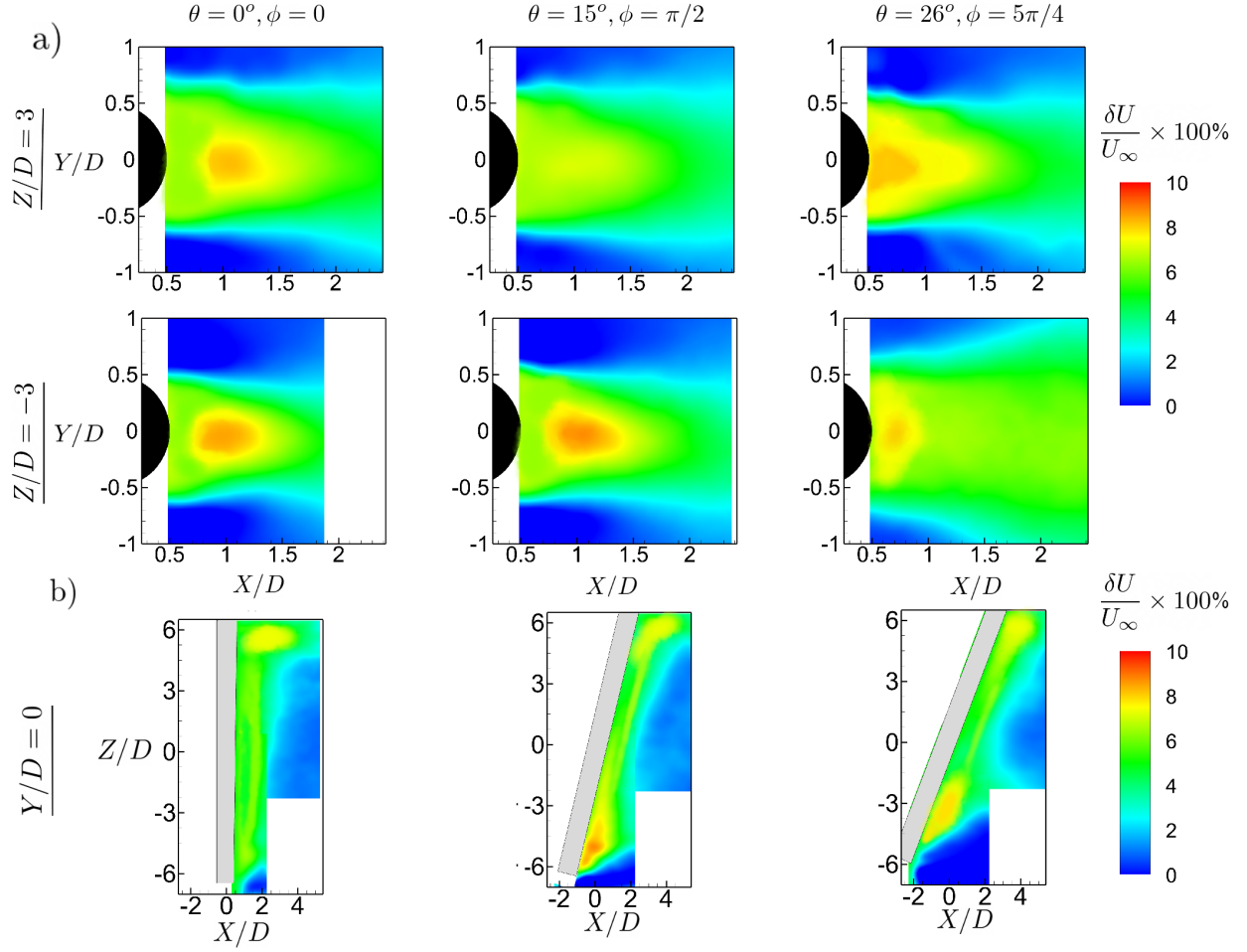
Figure A.2: Contours of random error estimate ($\frac{\delta U}{U_\infty}$) of phase-averaged normalized streamwise velocity for yaw-oscillating cylinder with $K = 1.0$ and aspect ratio 13. Results are shown for $\phi = 0$, $\pi/2$, and $5\pi/4$ corresponding to the yaw angles of $\theta = 0^o$, 15°, and 26° at Re $= 1.5 \times 10^4$ in a) (X,Y) planes b) (X,Z) symmetry plane.